Università
Ca'Foscari
Venezia

Scuola Dottorale di Ateneo
Graduate School

Dottorato di ricerca
in Scienza e Gestione dei Cambiamenti Climatici
Ciclo 29
Anno di discussione 2017

Social Vulnerability and Flood Risk Assessment Using Satellite Remote Sensing
A support for decision making in a changing climate scenario

SETTORE SCIENTIFICO DISCIPLINARE DI AFFERENZA: **ING/INF05**
SECS-P06

Tesi di Dottorato di Fabio Cian, matricola 956095

Coordinatore del Dottorato	**Supervisore del Dottorando**
Prof. Carlo Barbante	**Prof. Carlo Giupponi**

ABSTRACT

The potential of satellite remote sensing (active and passive) has been investigated, with the aim of improving the assessment of flood risk and social vulnerability, for defining the three components of risk: hazard, exposure and vulnerability.

A new method for flood mapping has been developed, based on multi temporal statistics of radar images. Flood depth was estimated using a new method based on a statistical analysis of elevation data along the contours of flooded areas. Taking advantage of Earth observation big data, land cover maps have been derived from data fusion of optical and radar data, allowing urban growth analysis. Population density maps were derived by means of a dasymetric mapping technique, as well as indicators of social vulnerability by means of network analysis. The methodologies have been applied to floods in Italy and Malawi, with the objective of supporting decision makers in a context of climate change adaptation.

ESTRATTO

Con lo scopo di migliorare la valutazione del rischio idrico e della vulnerabilità sociale, si è esplorato il potenziale del telerilevamento satellitare, attivo e passivo, per definire le tre componenti del rischio: *hazard, exposure, vulnerability.*

Si è sviluppato un nuovo metodo per la mappatura di aree inondate basandosi su statistiche multi temporali di immagini radar. La profondità dell'inondazione è stata stimata utilizzando un nuovo metodo basato sull'analisi statistica dell'elevazione lungo i contorni delle aree inondate. Sfruttrando i *big data* di osservazione della Terra (ottici e radar), sono state ricavate mappe di *land cover*, permettendo l'analisi della crescita urbana. Sono state ricavate mappe di densità di popolazione utilizzando tecniche di *dasymetric mapping*, e indicatori di vulnerabilità sociale basandosi sull'analisi delle reti.

Le metodologie sono state applicate a inondazioni successe in Italia e in Malawi, con lo scopo di fornire un supporto ai *decision makers* in un contesto di adattamento ai cambiamenti climatici.

ACKNOWLEDGEMENTS

Some years ago, right after the completion of my Master's degree, I decided that I wanted to become a scientist. Things at the beginning did not go as I expected and I had to face unforeseen difficulties. However, after few years I entered the programme in Science and Management of Climate Change at the Ca' Foscari University of Venice and finally I reached the goal set some years before. Nevertheless, I could not have reached the point where I am standing now, without the help of the many people I encountered along this curvy road, not only during the last three years spent at Ca' Foscari, but also since the day when I made that decision.

I want to thank first of all my supervisor prof. Carlo Giupponi, who guided and helped me constantly during the last three years, inspiring me with new ideas and motivating me by setting new goals. I felt his trust in my efforts growing year after year. This gave me the strength and the confidence to overcome difficulties and doubts. I am also grateful to him because he never limited my ambition and he always supported my initiatives.

During this research, I had the chance to spend some months in three different institutes. In all of them I was lucky to find great atmosphere, inspiration and very nice people. Dr. Mattia Marconcini has been a key figure in my PhD. Without his support, his knowledge, his continuous push for improvement, his patience, his positivity and creativity, I could not have reached all the results I got. Prof. Alexander Fekete has been extremely important in providing inspiration and useful feedbacks that allowed to improve this work. Finally, another very important person has been Dr. Pietro Ceccato, who has been my mentor at the other side of the ocean. His experience and knowledge, his inspiration and kindness, has allowed me to improve my work, to have new perspectives and set new goals.

I want to thank my colleagues and friends, who share beautiful and tough moments during the last three years. Malcolm, Michele, Lili, Vahid, Francesca, Arthur, Silvia R., Kiran, Silvia S.. And the ones met even before but that played a role in this journey. José Manuel, Jolanda, Nicole, Michele, Elisa, Francesco. All of them for some special reason and because together we had fun, thousands of coffees, we share frustration and *frittelle*, we managed to have new ideas and to overcome problems. Federica for her kindness, support and constant help.

A special thank also to Andrew for showing me the most secret spots in Brooklyn, for sharing his passion for science and the craziest ideas about climate science and art, for the hours spent talking in front of a coffee. To Francesco for his inspiration on climate communication and photography, for sharing with me his ideas, experience and kindness. To Marco for being a peaceful, funny and helpful officemate.

Finally, a huge thank to my parents and sisters, who are always there for me and always so proud of everything I do. To my grandmothers for listening to my stories and for sharing theirs. To my grandfathers for being a great example even from far away. To Manu for being a special friend always there for me.

To Elena for the many roles played in this journey, for supporting me in every second, for believing in whatever I do, for inspiring and motivating me, for taking care of me.

Fabio Cian
Venice, December 2016

Table of Contents

List of Figures

List of Tables

Abbreviations

ASTER: Advanced Spaceborne Thermal Emission and Reflection Radiometer

CCA: Climate Change Adaptation

CSK: COSMO-SkyMED

DEM: Digital Elevation Model

DLR: German Aerospace Centre

DRR: Disaster Risk Reduction

EO: Earth Observation

ESA: European Space Agency

EWS: Early Warning System

GEE: Google Earth Engine

GRDH: Ground Range Detected High Resolution

IPCC: Intergovernmental Panel for Climate Change

LC: Land Cover

LU: Land Use

LiDAR: Light Detection and Ranging

NDFI: Normalized Difference Flood Index

NDFVI: Normalized Difference Flood in Vegetated areas Index

NDVI: Normalized Difference Vegetation Index

PCA: Principal Components Analysis

RMSE: Root Mean Square Error

RS: Remote Sensing

SAR: Synthetic Aperture Radar

S1: Sentinel-1

S1A: Sentinel-1A

S1B: Sentinel-1B

SRTM: Shuttle Radar Topography Mission

SVM: Support Vector Machine

TSX: TerraSAR-X

USGS: United States Geological Survey

1. Introduction

1.1 Introduction to the problem context and relevance of the research

Climate science foresees a future where **extreme weather events** could happen with increased frequency and strength as a consequence of anthropogenic activities. Climate change would favor extreme precipitations, which could cause **flooding** to happen more frequently, either riverine, flash or coastal flooding. The probability of these events to happen is exacerbated by land use change and in particular, by urban growth that increases soil sealing and water runoff. The ultimate consequence would be an **increase of impacts**, in terms of either affected people, and economic losses in urban areas, commercial and productive sites, infrastructures and agriculture. Impacts that are constantly increasing since decades as reported by MunichRE (2014) with floods as the main source of losses in the globe.

In the Glossary of Terms of the Intergovernmental Panel for Climate Change (IPCC) (Barros et al., 2012), disaster risk is defined as "*the likelihood over a specified time period of severe alterations in the normal functioning of a community or a society due to hazardous physical events interacting with vulnerable social conditions, leading to widespread adverse human, material, economic, or environmental effects that require immediate emergency response to satisfy critical human needs and that may require external support for recovery*". In this research, flood risk is based on this definition, where flood substitutes disaster. Following the definition in the same document, a flood is "*the overflowing of the normal confines of a stream or other body of water, or the accumulation of water over areas that are not normally submerged. Floods include river (fluvial) floods, flash floods, urban floods, pluvial floods, sewer floods, coastal floods, and glacial lake outburst floods*".

Flood risk and impacts are not sufficiently understood and reported and need to be monitored systematically with improved precision as underlined by the European Flood Directive (European Commision, 2007). This is important to support Climate Change Adaptation (CCA) policies, to develop robust public disaster relief funds, to develop risk profile for financial institutes, risk portfolio for re-insurance companies and risk in supply chain for multinational companies (Mysiak, 2013; UNISDR, 2015). An improved capacity of characterizing risks is vital especially for managing urban areas and planning **economic** activities, not only to save lives, but also to reduce losses and build more resilient livelihoods.

This is even more important if global environmental changes are taken into consideration. Climate change in fact, due to natural internal processes and external forcings (i.e. anthropogenic activities that modify atmosphere composition and land use), is causing environmental changes at global scale, such as modification of precipitation patterns, which influence the occurrence of floods (Oppenheimer et al., 2014; Turner et al., 1990). Therefore, to be able to reduce risks for the future, risk must be assessed under different future scenarios, either climate or emission scenarios. A climate scenario, based on the IPCC definition, is "*a plausible and often simplified representation of the future climate, based on an internally consistent set of climatological relationships that has been constructed for explicit use in investigating the potential consequences of anthropogenic climate change, often serving as input to impact models. Climate projections often serve as the raw material for constructing climate scenarios, but climate scenarios usually require additional information such as about the observed current climate*" (Barros et al., 2012). Instead, an emission scenario is "*a plausible*

representation of the future development of emissions of substances that are potentially radiatively active (e.g., greenhouse gases, aerosols) based on a coherent and internally consistent set of assumptions about driving forces (such as technological change, demographic and socioeconomic development) and their key relationships" (Barros et al., 2012).

Following the definition adopted by the IPCC, in order to assess flood risk, the three components of risk have to be characterized: hazard, exposure and vulnerability (Oppenheimer et al., 2014). In particular, within the Disaster Risk Reduction (DRR) community, flood risk is considered as the expected damage (direct tangible costs) and it is function of the three components above mentioned (Crichton, 1999; Giupponi, 2014).

Hazard refers to the physical and statistical aspects of the event. For a flood, it means its extent, its depth, its duration, its velocity and its return period (Apel, 2009). Maps of the event are needed as detailed and quickly as possible for managing the crisis and for response activities (Martinis, 2009). A map with an accurate flood extent is important to determine the domain of the disaster and understand which areas have been hit by the event. The prompt availability of such a map few hours after the event, can be crucial in order to save lives and assets. In fact, disaster managers need maps in order to plan intervention and manage their resources. An accurate map is also needed for assessing impacts for insurance companies and local authorities, which may need to know in the shortest time possible, how to allocate their resources and budget. Besides flood extent, several parameters need to be monitored during a flood event, such as flow velocity, debris factor and inundation depth. Depth is particularly important since it governs the damage functions (also called vulnerability curves or loss functions), which define the expected damage given a certain flood depth (Mojtahed, 2013; Scorzini, 2015). Retrieving such information could be quite difficult. Especially if the flood has a big extent, the capacity needed in terms of work force and resources for directly assessing the extent and depth could be prohibitive. Even more when the event hits developing or poor countries. Regarding rapid mapping, a direct assess would be too slow to be effective.

Moreover, hazard maps are important also in the frame of flood risk assessment for long-term planning. In this case, obtaining a map in the shortest time possible is not the priority. Still, obtaining maps with an increased precision is very important. This means that all data sources can be exploited, from satellite remote sensing to local sensors, from hydrological and hydraulic models to citizen observations. On the one hand, the availability of more time for gathering and process data could be a great advantage for obtaining an increased precision, on the other hand, if data are not collected immediately during the event or not organized and stored properly for a later use, the more availability of time does not bring advantages. If fact, if satellites are not activated in time, they may not provide observations of the event (even if this is now changing with the increased frequency of observation of the new constellations) or local sensors measurements could be lost or not verifiable, especially in case of developing countries. Finally, in a way, the increased computing capability and easiness of exchanging information are decreasing the differences between near-real time mapping and ex-post mapping. The precision of rapid mapping methodology could result being the one needed also for long-term planning or at least the one needed for calibrating other mapping methodology which make use of models. Vice-versa, the complexity and the quantity of information needed in case of modelling technique, may soon become no more a bottleneck for rapid mapping for emergency management.

Exposure refers to "the presence of people, livelihoods, environmental services and resources, infrastructure or economic, social, or cultural assets in places that could be

adversely affected", as indicated in (Barros et al., 2012). Land cover or land use maps are usually employed for understanding what has been exposed to the flood (Alfieri et al., 2016; Altieri et al. 2014; Apel et al., 2009; Merz et al., 2010; Thieken et al., 2006; Vaz & Nijkamp, 2015). These maps, which are then superimposed to the flood hazard map, report the physical material at the surface of the earth and how it is used, i.e. built-up areas, agricultural areas, forest, etc. Land cover maps are usually produced at time steps of 5 or more years. In the case of Europe, the CORINE Land Cover[1] inventory started in 1990 and has been updated since 2000 every 6 years. The dataset is based on Earth Observation (EO) data and its resolution is somewhat coarse and more suitable for regional studies rather than local ones. Local governments usually dispose of more detailed maps, such as the case for Veneto, a region in the north-east of Italy[2]. Nevertheless, they are updated with similar frequency. Even though land cover in developed countries do not change rapidly, in a 5-year time, changes can be important in terms of built-up areas, infrastructures and distribution of population. When considering developing countries, the fast dynamics of society and economy in the same time step, can create significant changes. Thereby the need of up-to-date products that can allow the assessment of exposed elements. In order to assess the number of people involved in a disaster, data about the population are needed. National statistical institutes collects this information up to building units. However, for developing countries and also for many European ones, they are normally aggregated at the municipality level, if not at bigger scale such as province or county (Batista e Silva, 2013). For assessing the number of people involved in a disaster, most of the time this data need to be disaggregated. To do so, precise information about built-up area are needed, which, again, might not be available or be out of date. Moreover, in poor or developing countries, census data might not exist, be out of date or might be inaccurate. In certain cases, only population estimation may exists: projections based on old census data or from the integration of different datasets. The sum of all these uncertainties can lead to a debatable impact scenario. Therefore, having up to date and precise maps of inhabited areas, together with an effective disaggregation algorithm can significantly increase the capacity of assessing people affected by disasters.

Vulnerability refers to the susceptibility of the exposed elements to suffer from flood damage or "*the propensity or predisposition to be adversely affected*" (Barros et al., 2012). Referring to exposed elements with an economic value, so called damage functions are employed to relate the hazard to the resulting monetary damage by means of a parameter, i.e. flood depth. These depth-damage curves represent the standard in assessing urban flood damages (Merz, 2010; Smith, 1994) even though a large degree of uncertainty is associated in their construction (Jongman et al., 2012). De Moel and Aerts (2011) shows that the most important factor in damage estimation is the uncertainty associated with depth-damage curves and the value of assets. This uncertainty has a stronger effect on the outcome than the one associated to the land use or the hydrological inputs. Nevertheless, there are efforts in improving these limitations, especially for local cases and in particular by adapting existing curves to the economic circumstances of the case under analysis (Amadio et al., 2016; de Moel et al., 2015). Being aware that more efforts are needed to improve depth-damage curves and therefore the representation of vulnerability and the associated estimation of economic damages, at the same time it is also important to improve the precision of depth estimation. Flood depth cannot be directly measured for every asset hit by a disaster and it is usually

[1] http://land.copernicus.eu/pan-european/corine-land-cover

[2] http://idt.regione.veneto.it/app/metacatalog/getMetadata/?id=551

estimated superimposing the flood extent with a Digital Elevation Model (DEM). Thereby the need of precise flood maps and high resolution DEM. The social dimension of vulnerability refers to adaptive capacity, "the ex-ante preparedness of society to combat hazard and reduce its adverse impact", and to coping capacity, "the ex-post skills to cope with and overcome the impacts of the hazard considered" (Giupponi, 2014). It is challenging to characterize and many information are needed, such as socio-economic and demographic data (Cutter, 2003; Fekete, 2009). These datasets might be not easily accessible, not up to date or not available at all, contributing to the overall uncertainty in flood risk assessment. In case of the need of a rapid risk assessment, social vulnerability seems to be the weakest ring of the chain, even more in case of developing countries.

Satellite Remote Sensing (RS) has been used since decades as a source of Earth Observation (EO) data for assessing flood risk, given its synoptic observation capacity and ability to reach inaccessible areas (O'Grady, 2011; Waisurasingha, 2007; Wilson & Rashid, 2005, Martinis 2015). Floods are regularly mapped by means of reliable and well consolidated methodologies that employ multi-spectral and Synthetic Aperture Radar (SAR) data (Bazi, 2005; Brivio, 2002; Mason, 2007; Matgen, 2007; Nico, 2000). For instance, the European Copernicus Emergency Management Service[3] or the International Charter on Space and Major Disaster[4], two of the major operative emergency response centres, are regularly providing flood maps in response to emergencies. Land cover maps have been derived with regularity, from the local the global scale, by means of different source of EO data, with different level of detail and by several institutions (Langanke, 2014; Kovalskyy, 2014, GLC2000, GlobCover, Geoland-2, Copernicus - The European Earth Observation Programme).

Various indicators of vulnerability have been derived from EO data contributing to assess and improve flood risk assessment for different purposes, for rapid assessment of impacts, to support emergency management and for reducing risk in the framework of CCA (De Sherbinin, 2014; Esch et al., 2013; Giupponi & Biscaro, 2015; Wolters & Kuenzer, 2015; Wurm et al., 2009).

Nevertheless, it is only in the last years, namely 2014, with the launch of the Copernicus programme by the European Commission (Copernicus - The European Earth Observation Programme), that EO entered a new era. Images are now coming with unprecedented frequency and free of costs. The 4 Sentinels satellites already in orbit (Sentinel 1A and 1B, Sentinel 2 and Sentinel 3) provide a systematic observation of the whole Earth every week in multi-spectral and radar mode for land and marine services. Adding up to the United States Geological Survey's (USGS) Landsat missions, especially the last Landsat 8 launched in 2013, these data are constituting what it is now called EO big data. In fact, EO data have the 4V features of big data, volume, variety, veracity and velocity (Guo et al., 2014). They represent a great potential toward the observation of global environmental changes and for improving flood risk assessment. In fact, new approaches can now be pursued in data analysis and new services can be developed in support to decision making, to CCA and DRR, for the private and the public sector (Guo et al., 2015).

This research had the aim of exploring the possibility of developing new EO applications for improving flood risk assessment and taking advantage of the new and free EO big data. It developed around a novel methodology for risk assessment that was developed for the EU

[3] http://emergency.copernicus.eu/mapping/
[4] https://www.disasterscharter.org

funded research named KULTURisk, which had the aim of developing a culture of risk prevention (Figure 1). The methodological framework focuses on *(i)* the integration of physical/environmental dimensions with the socioeconomic ones; *(ii)* the consideration of adaptive and coping capacities of reducing risk, *(iii)* the economic valuation of risk that goes beyond the direct tangible costs for decision support on risk mitigation measures, and *(iv)* the integration of CCA in DRR (Giupponi, 2013).

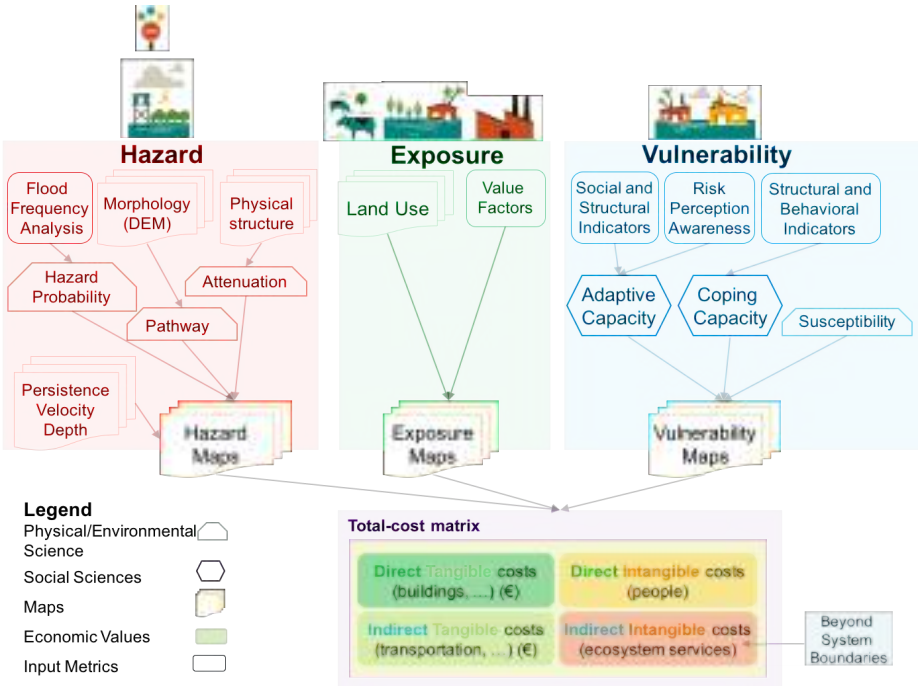

Figure 1 KULTURisk Methodological Framework applied to this research work

At the core of the KULTURisk framework there is the SERRA methodology: Socio-Economic Regional Risk Assessment. SERRA aims at including a socio-economic dimension in the assessment of risk, captured by the vulnerability and exposure dimension. In particular, in the exposure dimension, through the value factors, monetary terms are added allowing a monetization of the non-dimensional terms, hazard and vulnerability (Mojtahed et al., 2013). The assessment of vulnerability in this research follows the one proposed in the SERRA methodology. After the definition of vulnerability indicators, these are firstly normalized and then aggregated following a hierarchical aggregation tree. The KULTURisk framework was applied by Gain et al. (2015) in the assessment of flood risk in the eastern part of Dhaka city in Bangladesh. Direct and indirect tangible costs have been valuated including social dimensions in vulnerability. SERRA was applied to the Vipacco basin in north-east Italy in order to assess the benefits derived from the installation of an Early Warning System (EWS) (Luca et al., 2014). The flexibility and adaptability to different geographical and socioeconomic contexts of SERRA and the KULTURisk framework, has been presented in Ronco et al. (2015), where the methodology was applied to the Sihl River valley including Zurich, Switzerland, and in the case of river flooding, in Longo et al. (2016) where it was applied to the 2002 flood in Eilenburg, Germany.

This research is proposing methodologies based on EO data that can improve each of the three components of risk based on the KULTURisk methodological framework.

The overall research question that has been investigated is:

Can Earth Observation data improve flood risk assessment in a global environmental change scenario?

This imply the following sub-questions:

1) Can flood mapping be improved by means of EO big data?
2) Can flood depth estimation be improved and suitable for rapid assessment of impacts?
3) Can land cover classification be improved and easily up to date?
4) Is it possible to retrieve meaningful indicators of social vulnerability from EO big data?

Question 1 and 2 regard the definition of hazard. Question 3 regards exposure, while question 4 regards vulnerability, as well as question 2. The 4 points face different issues but have a least common denominator, i.e. image classification techniques, which therefore constitute the core of this research. Nevertheless, despite a purely technological nature of the work, the climatic aspect as well as the socio-economic one, has always been kept as the main focus.

1.2 Structure of the thesis

In Chapter 2 the case studies considered in the research are described taking into consideration the climatic and socio-economic context. Three main areas have been considered: i) Veneto region, north-eastern Italy, as an example in a developed country; ii) southern Malawi as an example in a developing country and iii) north-eastern Uganda as an example of operative application.

Chapter 3 presents the methodology of flood mapping developed during the visiting period at the German Aerospace Centre (DLR) in Munich, Germany. An innovative methodology of flood mapping based on statistical analysis of time-series has been developed. A normalized index is computed able to simplify flood mapping and being independent from the type of data used.

Chapter 4 describes the methodology for flood depth estimation, which builds on top of the one presented in Chapter 3. Flood maps are superimposed to a high resolution DEM. From a statistical analysis of elevation values along the contours of flooded areas, the elevation of the water plane is estimated allowing the computation of the depth.

Chapter 5 is developed around a novel land cover classification method based on multi-temporal statistics of optical and SAR data. From the land cover maps so derived, built-up areas are isolated and used for analyzing urban growth, useful not only for characterizing exposure, but also vulnerability.

Chapter 6 will show how the analysis of built-up areas can provide indicators useful to define social vulnerability. These indicators are combined with ancillary socio-economic data for defining an index of social vulnerability.

Chapter 7 will discuss the overall research and will draw conclusions underlining possible way forward.

This work has been conducted at the department of Economics of the Ca' Foscari University of Venice in the frame of the 3-year PhD Program in Science and Management of Climate Change and with the support of the Venice Centre for Climate Studies directed by prof. Carlo Giupponi, which is also the supervisor of this research. Moreover, it is part of a collaboration with other institutes, which provided essential support. In fact, the author has visited the German Aerospace Centre (DLR) for four months supervised by Dr. Mattia Marconcini, the Cologne University of Applied Science for three months supervised by Prof. Alexander Fekete and the International Research Institute for Climate and Society (IRI), Columbia University, New York for three months supervised by Dr. Pietro Ceccato. During these visiting periods, it has been possible to consistently improve the results of this research.

2. Case Studies

Three are the case studies selected for this work. Two of them are considered as the main ones, while the third has been considered only as an example of applicability for the flood mapping methodology.

The first one is the Veneto region, north-east of Italy, where in the recent years many flood events have occurred causing huge impacts, especially from the economic point of view. This area is interesting because rich of data, both geospatial and socio-economic ones. Data that can be used for validating new methodologies and for understanding the added value of new tools and products, such can be EO. All the methodologies developed in this work have been tested in the Veneto region.

The second area considered is southern Malawi, where in 2015 a huge flood caused major problems in the region affecting nearly a million people. This case is the opposite of the previous one, i.e. little data is available and impacts on people are preponderant on impacts on assets. EO has great potential in providing data in area like that, where capacity is little and disasters are vast. In this area, the flood mapping methodology has been applied as well as land cover classification. The absence of a high-resolution DEM prevented the estimation of a flood depth.

Finally, a third case has been considered only for flood mapping. In the framework of the Forecast-based-Financing project of the Red Cross Red Crescent (see paragraph 2.3), a flood alert triggered the humanitarian response in November 2015 and maps were asked for proving the presence of flood in the area.

2.1 Veneto 2010

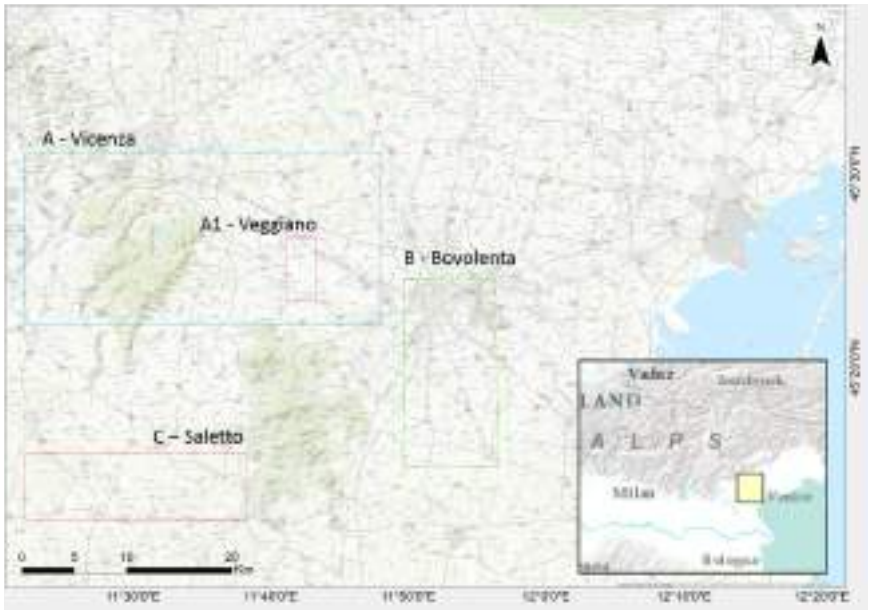

Figure 2 Flood in Veneto 2010 Areas of Interest

From October 31st to November 2nd, in the Veneto Region, northern-eastern Italy, 140 Km^2 of land have been flooded with major damages on properties and infrastructures. The event

was originated by an Atlantic perturbation, which caused intense precipitation over the whole region, with extremes in the Prealps and piedmont areas. Local rainfall accumulation exceeded 500 mm and the average widely surpassed 300 mm, leading to a serious hydraulic stress, especially in the area of Vicenza and the south of Padua. Sirocco wind, persistent on sea and inland, slowed the discharge of rivers into the sea. Early snow melted due to the warm temperature, adding water to the rainfall. The first rupture in the area occurred in the afternoon of November 1st at the south of the city of Vicenza. The flood then propagated southwards until Veggiano, where the Bacchiglione riverbanks have been broken in the night between November 1st and 2nd, Bovolenta and Saletto area. An overall of 262 municipalities were affected leading to roughly half billion Euros damage, three fatalities, 3500 displaced and more the 500 thousand people affected. The flood also triggered hundreds of landslides in the mountainous surroundings, which led to more than 500 warning of instability phenomena received by the province soil protection division (Floris et al., 2012; Scorzini, 2015).

The event is among the three most intense in the record hitting the pre-alps and piedmont area (the rainiest area of Veneto) in the last 50 years, together with the flood of 1966 and 1992. In the surrounding of Vicenza, the maximum precipitation measured during the 2010 flood exceeds by far the previous maximum, such as in the case of Castana – Arsiero, where in two days 431 mm of water have been accumulated in contrast to 326 mm of 1966 and 313 mm in 1992. The precipitation measured have been compared to the historic record for the same area and return periods have been computed with the hypothesis of a Gumbel distribution for annual maxima and using a minimum square method for estimating the parameters of the distribution. Considering the 3 days of the event, for the majority of the recording stations affected by the flood, the return period corresponds to more than 50 years, underlining the magnitude of the event (*Regione del Veneto*, 2010).

Veneto region is one of the most economically competitive and extensively inhabited urban landscape in Europe. In the last two decades, an unstructured development of urban areas occurred in Veneto region due to the increase in population density. In less than 10 years, population has increased by 10 per cent. The main responsible for this growth are Verona, Padua and Venice, which are the major hubs of the region. This rapid change led to an increased soil sealing and urban sprawl, especially within the open space between cities and affecting ecosystems located therein (Vaz & Nijkamp, 2015). The socio-economic changes of the last 50 years, from subsistence agriculture to industrial agro-systems, led to dispersed low-density residential areas and to homogeneously distributed medium-small size productive activities (Fregolent, 2005). Territorial planning have been often short-sighted in the past half-century, with little attention paid to the relationship between environment and urban settlements, affecting the risk connected to natural hazard, in particular floods (Sofia, 2014). In fact, in the diffuse urban landscape of the region, the number of hydraulic dysfunctions have increased due to the spatial and water infrastructure transformation (Ranzato, 2011).

The climate of Veneto is variable with precipitation concentrating mostly on the Prealps. It is often affected by extreme meteorological events, especially in the coast, despite the precipitation being the half of the one occurring in the Prealps. The already critical situation resulting from the combination of land use and extreme events may be exacerbated in the future due to climate change. In fact, projection shows an increase of extreme precipitations, which may lead to an increased frequency of floods (Zollo, 2015).

A commission established by the regional government has assessed the hydraulic risk of the region and presented a mitigation plan. The plan highlighted the numerous measures that need to be taken with urgency to reduce the risk for a total cost exceeding 2.5 billion €. At the

date of the report, end of 2011, only a small part of these measures had already started (for a cost around 100 million €) or their design being funded (for other 100 million €). Moreover, the report exposed the scarce penetration of financial products, such as insurance products, for protecting assets against floods, leaving to local government the burden for ex-post support to population and productive activities (Regione del Veneto, 2011).

This work analysis the 2010 flood, first creating flood maps (Chapter 3) and later estimating flood depth (Chapter 4). The analysis of land cover and the derivation of vulnerability indicators are showed in Chapter 5. The analysis of the 2010 flood concentrates on three main areas as shown in Figure 2: Vicenza and its surrounding (A), Bovolenta area at the south of Padua (B) and Saletto area at the south of Colli Euganei (C). The area of Veggiano indicated as A1, together with area B, is the area where a hydraulic simulation was available allowing a comparison of flood depth results.

2.2 Malawi 2015

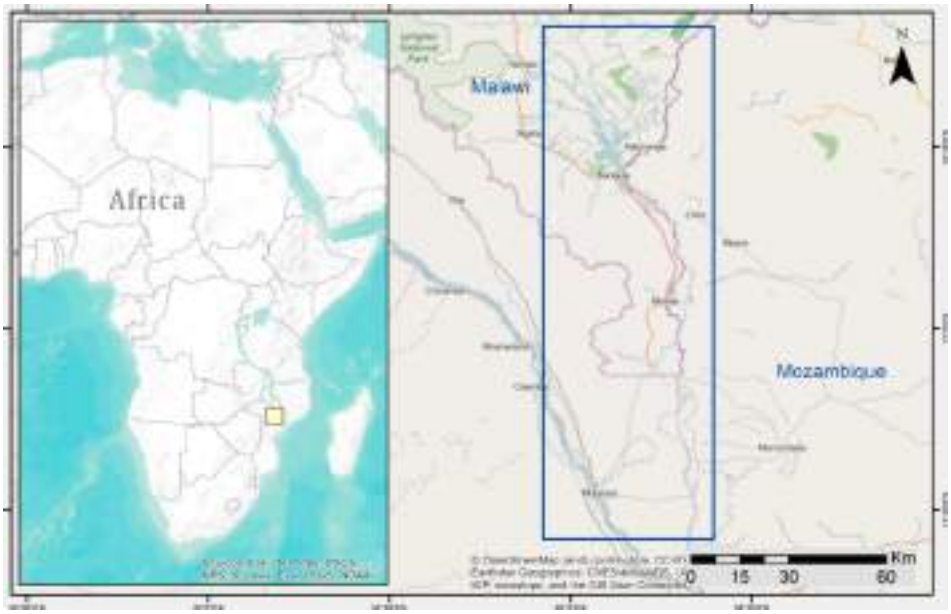

Figure 3 Malawi Flood 2015 Area of Interest

In January 2015, Malawi experienced exceptional rainfall, which led to a disastrous flood especially in the south part of the country that lasted until the end of March. The amount of rainfall was the highest on records and the event constitutes a 1 in 500-year. The already precarious situation for households, was exacerbated by the consequences of the disaster. More than 1 million people were affected, more than 200 thousand displaced, more than 100 killed. On January 13th, 2015, the president of Malawi declared the state of disaster for 15 districts, some of these among the poorest of the country.

The flood impacted on the productivity, public infrastructures and social service sectors. Public and community assets were also affected, livestock was washed away, thousands of building and houses were destroyed. Roads, bridges, school, health facilities and irrigation infrastructures were damaged. In addition, the rainy season was delayed of more than 30 days leading to a shorter growing season, reducing further the crop production already compromised by the disaster, in a country were agriculture is the main driver of economic growth and subsistence. The government estimated a total of 335 million USD in impacts

(approximately 5% of the GDP) and 494 million USD for recovery and reconstruction needs (Malawi PDNA Report, 2015).

Big weather-related losses have occurred in the past too, such as the 1991 flood that caused the highest economic impact or the 1992 drought, which affected 7 million people (Venäläinen et al., 2016). For the future, the climate of the region is expected to increase its variability. Natural hazard, and especially extreme weather events, may increase intensity and frequency. Climate models project warming up to 2° C by 2050 even following a moderate Representative Concentration Pathway RCP4.5. Moreover, changes in seasonal rainfall patterns are indicated, with an increase of rainfall and extreme events during the rainy season and a decrease of rainfall during the dry season (IPCC, 2014).

Also the socio-economic conditions of the country are contributing to the risk scenario. Malawi is one of the poorest country in the world and it is exposed to climate-related disasters. The agricultural sector, dominated by smallholder farmers, rely on flood and drought-prone land and depends on rain-fed agriculture. The majority of the poor population depends heavily on agriculture, therefore poverty reduction is undermined by climate variability (Stringer, 2010). Moreover, population is rapidly growing (2.8% per annum according to 2008 population survey) as well as people living in highly vulnerable regions. Land use and especially urban areas, are strongly affected. This increases the risk of human and economic losses, especially in climate-sensitive sectors such as rain-fed agriculture (Hachigonta, 2013; Venäläinen et al., 2016).

In a country where response to disaster is delayed and ineffective (Tall, 2013), the management of natural hazards, the development of adaptation strategies and the establishment of Early Warning Systems (EWS) has great importance (IPCC, 2012; The World Bank, 2010).

In this work, the 2015 flood is studied in Chapter 3, where flood maps are derived for the southern district of Chikwawa and Nsanje as showed in Figure 3. In chapter 5, land cover maps are derived for the same area.

2.3 Uganda 2015

Figure 4 Uganda Flood 2015 Area of Interest

Forecast-based Financing (FbF) project of the Red Cross Red Crescent Climate Centre consists of a series of preparedness actions to take in order to reduce the impact of possible flood events, after the triggering of a warning system, which is based on the river discharge forecasts of the Global Flood Awareness System (GloFAS). Uganda Red Cross successfully initiated action for the first time in November 2015 following a forecast that triggered the warning system and used the Preparedness Fund provided by the project (Coughlan De Perez, 2015).

To validate the triggering of actions in the Teso region of North Eastern Uganda (Figure 4), several maps have been produced applying the methodology developed in this research to Sentinel-1A data (Chapter 3). The aim was to show the presence of flooded area after the intense precipitation of early November and the following weeks.

The region analysed is swampy and prone to flood during the two rainy seasons of May and October, with farming and livestock raising as main activities. Several floods in recent years caused loss of crops, collapse of houses and latrines, impassable roads and outbreak of waterborne diseases.

3. Normalized Difference Flood Index for rapid flood mapping: taking advantage of EO big data

This chapter describes a new methodology for rapid flood mapping, which aim at exploiting the big amount of data coming from new satellite mission, such as the ones of the Copernicus programme. Starting from a literature review that highlights the main methodological streams of flood mapping, a description of the Normalized Difference Flood Index will follow. The index allows an easy and fast mapping of flooded areas. The chapter has the objective to answer ***research question 1****: "Can flood mapping be improved by means of EO big data?"*

This chapter have been submitted to the journal "Remote Sensing of the Environment" and was under review at the moment of submission of this manuscript. The paper, as well as the chapter, has been written autonomously by the author. The co-authors of the paper are Dr. Mattia Marconcini of the German Aerospace Centre, Germany, who supervised the whole research and Dr. Pietro Ceccato of the International Research Institute of Climate and Society, Columbia University, who helped developing the theoretical part of the research and revised the results.

3.1 Earth Observation Big Data, Climate Change and Flood Mapping

In the era of EO big data, with the new information coming from the recent Sentinels constellation, we are entering a new paradigm for disaster monitoring and EO data exploitation. The European Space Agency (ESA) Sentinel-1 (S1) radar satellite constellation can map entire Earth every 6 days (with interferometric capabilities) giving an unprecedented opportunity to access a huge number of archived scenes, which is of key importance to detect changes and assess economic impacts in case of disasters. The constellation is made of two satellites: Sentinel-1A (S1A) launched in April 2014 and operational since October of the same year, and Sentinel-1B (S1B) launched in April 2016. This big amount of data provided by the constellation opens new frontiers in image processing, giving the possibility to perform statistical analysis on long time-series of data and to develop new approaches in change detection analysis.

In the context of climate change with a foreseen increase in the number of extreme events such as precipitation and consequent flash and riverine floods, it becomes even more important to monitor and map these phenomena with increased accuracy and rapidity. An improved capacity of characterizing risks is vital especially for managing urban areas and planning economic activities, not only to save lives, but also to reduce losses and build more resilient livelihoods. Satellite remote sensing, and especially the data coming from the ESA's Copernicus programme is helping to move toward an improved flood risk assessment.

3.2 Flood Mapping by means of Synthetic Aperture Radar

Synthetic Aperture Radar (SAR) data have been used since decades for flood mapping. Many reliable and well consolidated methodologies have been developed to extract floods from these data (Bazi, 2005; Brivio, 2002; Mason, 2007; Matgen, 2007; Nico, 2000). Moreover, the European Copernicus Emergency Management Service[1] or the International Charter on Space and Major Disaster[2], two of the major operative emergency response centres, are regularly providing flood maps in response to emergencies using SAR data (Martinis 2015).

SAR data are particularly useful in case of floods. SAR microwaves can penetrate clouds allowing the monitoring of land in any weather conditions. Having its own source of illumination, SAR can acquire useful data also during nights and without being affected by the relative position of the sun (O'Grady, 2011; Waisurasingha, 2007; Wilson & Rashid, 2005).

Radar backscattering is influenced by targets' structural, textural and dielectric properties. The first two depend on the relative dimension of targets and wavelength, therefore it's a matter of scale. In case of S1, the C-Band signal (5.405 GHz) has a wavelength of 5.6 cm and it interacts with small branches, leaves and objects with the same scale order. In this interaction, part of the signal will be backscattered towards the satellites that will register an intensity greater than zero, the higher the intensity of the returned signal, the brighter the relative pixel will be. In case of flood or water bodies in general, the smooth surface of the water (compared to the wavelength) reflect the signal to a specular direction. Therefore, the return to the satellite will be theoretically null, letting the pixel representing water to be very dark. Nevertheless, Bragg resonance can happen when regular waves (with comparable size of the

[1] http://emergency.copernicus.eu/mapping/
[2] https://www.disasterscharter.org

wavelength) are present on the water surface, resulting in a high radar backscatter especially when the waves are orthogonal to the radar signal (Schaber, 1997). In partially inundated areas, where vegetation and buildings emerge from the water, the radar signal can interact multiple times with the objects. This "double-bounce" effect (dihedral scattering) results in a very high return to the sensor when the scale of the emerging structure is comparable to the radar wavelength. Considering the case studies presented in this chapter, in particular the flood in Malawi and Uganda, it's important to note that also dry and smooth bare soil can appear very dark in a SAR image since these kind of soils absorb and attenuate microwave radiation and they can be confused with open water (O'Grady et al., 2011; Schaber et al., 1997). The analysis of multi-temporal series of images and in particular the use of the flood index presented in this chapter, allow us to isolate non-permanent water from the rest of the image.

Radar backscatter is also function of the incidence angle. In addition to different layover and shadowing effects, images acquired with different geometry have a different pixel intensity for the same observed object. This problem arises using for example COSMO-SkyMed (CSK) data as shown in this chapter, where the comparison of images acquired with different geometry can lead to less accurate flood maps. With S1 data, given its stable acquisition geometry, this problem does not occur (Boni et al., 2016).

Given the capacity to look through clouds (Schumann et al., 2009), SAR acquisitions during floods can be available with more frequency than optical. However, flood mapping from SAR data can be challenging and errors due to adverse environmental factors can be common. For example, when wind intensity is strong enough, it can lead to a non-smooth water surface; this increases the backscattering and it makes water to appear much brighter than how it normally appears (Bragg resonance). Different soil moisture contents also change the dielectric properties of the surface and can lead to different radar backscattering for the same soil type, even though C-Band signal is not much affected (Paloscia et al., 2013). Presence of vegetation can mask parts of the flood leading to inaccurate maps. With the possibilities to analyse and to extract statistical information from long time-series of images, part of these problems can be solved.

Another typical problem for satellite data is the frequency of acquisition that is given by the satellite revisit time and by the limited duty cycle of SAR sensors (maximum time during which the data can be acquired). Old missions, such as ESA's ENVISAT or the Canadian Radarsat-1, had repeat orbit cycles of a month or more with a duty cycles of 30 minutes per orbit. The chance of acquiring images covering flood events were really low, like the chance to have a reference image of the same area acquired with the same geometry (Martinis, 2013). Newer radar missions like the Italian CSK have a theoretical revisit time of less than 12 hours, optimal for disaster monitoring. In order to achieve such revisit time, the four satellites of the constellation have to be tilted changing the acquisition geometry, a disadvantage for change detection approaches (Pulvirenti et al., 2015). The new S1 mission instead, has a repeat cycle of 6 days and systematically acquires any regions in the world. Even though it has a worse revisit time and resolution compared to CSK, S1 has the advantage of a stable acquisition geometry and provides a large amount of images for every location on Earth freely available through the Copernicus Scientific Data Hub[3] few hours after their acquisition (Torres et al., 2012).

[3] https://scihub.copernicus.eu

Image resolution is a parameter influencing revisit time and therefore frequency of acquisition. A higher resolution means a narrower swath and therefore a higher revisit time leading to less frequent observations, reducing the chance to observe flood events, which usually last for few days. Using low repeat cycle satellites, it is almost impossible to have more than one image per flood (Di Baldassarre et al., 2011). With satellite constellations such as COSMO-SkyMED or the new S1, it is possible to have high resolution and low revisit time (Yan et al., 2015).

The potential of SAR images for near-real time flood mapping has already been demonstrated in the past (Horritt 2001, Henry et al., 2006; Martinis et al., 2009a; Martinis et al., 2015) and it is going to be further improved thanks to the rapidity of data availability, and the frequency of acquisition allowing the analysis of temporal dynamics of floods (Pulvirenti 2013; Serpico et al., 2012).

Different categories of algorithms have been developed in the past decades to derive very detailed flood maps from high-resolution SAR data. Unsupervised classification, active contour models, change detection and thresholding are some of the most used approaches in flood mapping (Bazi et al., 2005; Brivio et al., 2002; Di Baldassarre et al., 2011; Horritt, 1999; Mason et al., 2007; Matgen et al., 2007; Nico et al., 2000; Schumann et al., 2009; Smith, 1997).

Change detection techniques compare pre-event images with images of the event in order to detect the changes (Liu et al., 2004; Lu et al., 2004). The advantage of using identical image geometry is that areas of low backscattering like smooth tarmac and radar shadow can be excluded from the mapping (Giustarini et al., 2013). Image thresholding assumes that all the pixels with a radar intensity lower than a certain value, belong to the water class (Mason et al., 2012; Matgen et al., 2011; Pulvirenti et al., 2012; Schumann, Di Baldassarre et al., 2010). These techniques are computationally not intense, provide reliable results and are ideal for rapid mapping (Brivio et al., 2002; Martinis et al., 2009b).

Operational flood mapping technique used by the International Center on Environmental Monitoring (CIMA foundation), the map provider for the Italian civil protection mainly working with CSK data, follows the approach proposed by Pulvirenti et al. (2014). It uses an automatic algorithm that searches for low backscatter areas after applying an automatic thresholding, then it performs a region growing step. Automatic thresholding is performed looking for a double peak in the image histogram, dark pixel (flood) and areas with higher backscatter. Histogram analysis, an approach followed by many other researchers such as Martinis (2009) for the operative mapping at the German Aerospace Centre (DLR) and Long (2014), creates problems when the extent of the flood is small compared to the dimension of the entire image, something that happen quite often in case of Sentinel-1 data given the large footprint of its images. In such cases, the double peak in the histogram cannot be found and to overcome this problem, these approaches have to add an additional step: image tiling.

An interesting example combining change detection and thresholding is given by (Long et al., 2014). First, the difference between the reference image and the image of the flood is computed, then a threshold is applied to the difference image issued from the computation after the analysis of its histogram. In the difference image, areas appearing dark solely during the flood, still appear dark and correspond to non-permanent water. Dark areas in both images, such as permanent water, instead appear grey in the difference image allowing to isolate flooded areas. Threshold values are decided after the analysis of the histogram distribution (pixel values) of the difference image. To isolate flooded area (low pixel values), the threshold value is found subtracting the standard deviation of the entire image times a coefficient, to the mean pixel value. The same approach is followed to classify water in

vegetated or urban areas (high pixel value due to double-bounce effect). In this case the threshold value is set to the mean pixel value plus the standard deviation of the entire image times another coefficient. The two coefficients are found after several iterations and they can be user-dependent or they can change from case to case.

A tentative to finding optimal thresholds in decibel (dB) to be used in a generic case in order to allow a rapid map of foods (and maybe less user-dependent) was pursued by Manjusree et al. (2012). They studied RADARSAT-2 (RS2) backscatter values for different polarizations (HH, VV, HV) and for different water bodies and they found a set of optimal thresholds for each polarization. The methodology was validated applying the identical thresholds to images of the same area acquired in different dates. Despite the good results shown, the study does not show the validity of the approach for different sensors, different resolutions and different ecosystems.

The new algorithm proposed here, similarly to Long (2014), applies a change detection analysis as a first step, then on the resulting image a threshold is used to extract the flood extent. In this case, the change detection step is based on the computation of an innovative index that allow the identification of non-permanent water bodies easily, with less user-dependency and can be suitably applied even by non-experts. Instead of a simple image differencing between one image of the event of one of reference, we compute the normalised difference of statistics of two time-series of the backscattering σ_0 acquired with the same acquisition geometry, one of reference images (without flood) and one containing images of the flood. On the resulting index image (with values between 0 and 1), a constant threshold is then applied: one to detect flooded areas, and one to detect vegetated flooded areas (flooded areas covered by vegetation, where water plane is below the top of the vegetation); the two threshold values remain constant independently from the dataset used and therefore, the user-dependency of the methodology is decreased. Moreover, it allows the detection of flood in vegetated areas and potentially in urban areas, even with usual limitations typical of these cases (Pulvirenti, 2015). Finally, it shows a new approach of image processing by means of EO big data.

3.3 Case studies

The methodology has been tested in the three case studies described in Chapter 3: i) the flood of January 2015 that occurred in southern Malawi well covered by S1A Ground Range Detected High resolution (GRDH) images; it was the first flood captured by S1A and the huge extent and diversity of environment makes it a challenging flood to map and a good example to show the potential of these new data and methodology; ii) the flood event that occurred in the Veneto region (city of Vicenza and its surroundings) in North Eastern Italy for which multi-temporal COSMO-SkyMed stripmap data have been used; it has been chosen because it represents the typical situation of data availability before the advent of the Sentinels and given our proximity to the area and the amount of data available, it is a perfect test bench for validating the methodology; iii) the flood that occurred in North Eastern Uganda in November 2015 also well covered by S1A GRDH data and it was a first chance to test the methodology for validating a flood warning system (an alert system triggered when the simulated river discharge trespass a certain threshold indicating a risk of flooding).

3.4 Data Used

3.4.1 Malawi

S1A was launched in April 2014 and became operational starting the following October. Even if at the very beginning of its life and not at its full acquisition potential, the frequent observation strategy of the mission allowed an acquisition of many images over southern Malawi prior to the flood occurrence. In the selection of images is important to take into consideration the climate of the region, which is sub-tropical, relatively dry and strongly seasonal. The 95% of the annual precipitation takes place from November to April, the warm-wet season, with peak humidity in January/February. The area analyzed, the Lower Shire Valley, has a low elevation and is particularly prone to floods such as the one occurred in the 1988/89 season. From May to August, the dry winter season has minimum temperature between 4 and 10 degrees Celsius with frost in isolated areas in June and July. From September to October, the hot dry season, temperature vary between 25 and 37 degrees Celsius A hot, dry season lasts from September to October with average temperatures varying between 25 and 37 degrees Celsius and humidity around 50%.

In order to have robust statistics, we considered only the acquisition during the rainy season that starts in November. In only two months, S1A had the availability of more reference images than all SAR sensors used for the Veneto case study after years of operation. Concerning the coverage of the flood, except for the initial phase of the event (unfortunately the most important in order to understand the maximum flood extent), S1A observed the area every 12 days allowing the monitoring of the evolution of the event as shown in Table 1.

Table 1 Malawi 2015 Dataset

Sensor Imaging Mode (Band)	Orbit Rel. Orbit Number (Pol)	Date	Status	Total N. Images
S1A	Ascending	17/11/2014	Reference	2 Reference
GRDH 20 m	101 (VV)	11/12/2014	Reference	2 Flood
(C)		04/01/2015	Flood	
		21/02/2015	Flood	
S1A	Descending	11/11/2014	Reference	3 Reference
GRDH 20 m	6 (VV)	05/12/2014	Reference	5 Flood
(C)		29/12/2014	Reference	
		22/01/2015	Flood	
		03/02/2015	Flood	
		15/02/2015	Flood	
		27/02/2015	Flood	
		23/03/2015	Flood	

3.4.2 Veneto

The event was observed in different dates and resolutions by many SAR sensors. The first image available came from the CSK constellation few hours before the first overflow, at 5:30 am of November 1st 2010. The image covers only the west side of Vicenza and shows a wet environment with little areas of standing water at the south-west of city toward the province

of Verona. At 9:30 of the same day, ENVISAT-ASAR acquired a WideSwath at 150 m resolution, which show the first outflow at the north and south of Vicenza. This image was acquired in HH polarization on the contrary of the usual VV polarization of ASAR acquisitions. No other HH polarized images were found in the archive and therefore we could use it to perform change detection only with another HH image acquired on November 4th. The 2nd of November, RS2 acquired an image at 25 m resolution giving the first precise information about the flood extent. Only on November 3rd, after the activation by the Italian civil protection, CSK was able to acquire the first useful image, after the peak of the flood for the city of Vicenza, but around the peak for the other two areas. CSK acquired one image a day until November 7th, allowing the monitoring of the event. The frequency of acquisition and the very high resolution, 3 m, make these images of great value for a detail flood map. Nevertheless, all the images acquired after the satellite activation have high incidence angles, which makes flood mapping more difficult due to the increasing of shadowing and layover effects and not perfectly suitable for change detection approaches. The use of the proposed index, even though it has been thought for working with images with the same geometry of acquisition, was able to produce very precise maps.

TerraSAR-X (TSX) provided only one image during the event, namely the 6th of November, which matches exactly in term of geometry the only archive image over the area, dated December 2008, allowing a precise and easy flood mapping.

Finally, ASAR provided an image the 12th of November showing the end of the event.

Table 2 Veneto 2010 Dataset

Sensor	Orbit (Pol)	Date	Incidence Angle	Status	Total N. Images
COSMO-SkyMed Stripmap 3 m (X)	Descending (HH)	31/10/2008	27.7-30.8	Reference	2 Reference
		28/04/2010	28.9-31.8	Reference	3 Flood
		03/11/2010	37.4-40.1	Flood	
		04/11/2010	40.1-42.6	Flood	
		06/11/2010	27.7-30.9	Flood	
	Ascending (HH)	29/08/2010	31.1-34.2	Reference	1 Reference
		01/11/2010	31.1-34.2	Flood	2 Flood
		07/11/2010	47.0-49.2	Flood	
TerraSAR-X Stripmap 3 m – (X)	Ascending (HH)	24/12/2008	31.3	Reference	1 Reference
		06/11/2010	31.5	Flood	1 Flood
Radarsat-2 ScanSAR 25 m (C)	Descending (HH)	11/02/2010	30.33	Reference	1 Reference
		02/11/2010	30.28	Flood	1 Flood
	Ascending (HH)	18/09/2010	30.17	Reference	1 Reference
		05/11/2010	30.3	Flood	1 Flood
ENVISAT-ASAR WideSwath 150 m (C)	Ascending (VV)	06/09/2010		Reference	1 Reference
		06/11/2010		Flood	1 Flood
	Descending (VV)	19/09/2010		Reference	2 Reference
		11/10/2010		Reference	1 Flood
		12/11/2010		Flood	
	Descending (HH)	01/11/2010		Reference	1 Reference
		04/11/2010		Flood	1 Flood

Table 2 summarizes the dataset for the flood in Veneto 2010 and show clearly that many sensors had to be used in order to monitor the event, which have acquisitions in different geometries. CSK images with the same acquisition geometry are highlighted. The table also shows that even after years of operation, the reference images covering the area are very few. Finally, in order to retrieve all the data needed, we had to go through different web portals with long processes in order to access the data, except for ESA data, which can be freely downloadable from the web portal (ESA EOLI). TSX, RS2 and CSK were kindly provided respectively by the German Aerospace Center, Canadian Space Agency and the Italian Space Agency.

Table 3 Uganda 2015 Dataset

Sensor (Band)	Orbit Rel. Orbit Number (Pol)	Date	Status	Total N. Images
S1A	Ascending	19/10/2014	Reference	16 Reference
GRDH 20 m	28-29 (VV)	12/11/2014	Reference	2 Flood
(C)		06/12/2014	Reference	
		30/12/2014	Reference	
		16/02/2015	Reference	
		28/02/2015	Reference	
		24/03/2015	Reference	
		17/04/2015	Reference	
		11/05/2015	Reference	
		04/06/2015	Reference	
		28/06/2015	Reference	
		22/07/2015	Reference	
		15/08/2015	Reference	
		08/09/2015	Reference	
		02/10/2015	Reference	
		26/10/2015	Reference	
		19/11/2015	Flood	
		13/12/2015	Flood	
S1A	Descending	26/11/2014	Reference	10 Reference
GRDH 20 m	50 (VV)	20/12/2014	Reference	1 Flood
(C)		13/01/2015	Reference	
		06/02/2015	Reference	
		14/03/2015	Reference	
		07/04/2015	Reference	
		01/05/2015	Reference	
		12/07/2015	Reference	
		29/08/2015	Reference	
		16/10/2015	Reference	
		09/11/2015	Flood	

3.4.3 Uganda

The systematic acquisition over Uganda since the beginning of the S1A mission, resulted in a total of 26 reference images in one year as shown in Table 3. Compared to the pre-S1A scenario, such as the one in Veneto explained above, this is a huge change. The methodology presented is thought for dealing with such big amount of data, as explained in the following paragraph.

Moreover, to process this big amount of data (29 S1A GRDH images) we made use of Google Earth Engine (GEE), which at the time of this work had just ingested the S1A catalog. GEE allowed to process the data and retrieve the results in a matter of minutes. Together with Sentinels data, GEE is a significant improvement for rapid mapping and image processing in general, allowing normal users to perform tasks that were limited to users with high computable capabilities.

3.5 Methodology

S1A is observing the Earth systematically with a revisit frequency of 12 days. With the launch of the second satellite of the constellation on April 2016, Sentinel-1B, the revisit time has decreased to 6 days. This leads to a large amount of reference pre/post event scenes in addition to those acquired during the investigated flood. Sentinel-1 acquires with a stable incidence angle, therefore all the images on the same orbit, descending or ascending, and the same track, can be directly compared as they have the same shadowing and layover effects. The methodology proposed aims at exploiting this huge amount of information, therefore a SAR multi-temporal series of radiometrically calibrated and terrain corrected images is created and a statistical analysis of the backscattering σ0 of each pixel is performed throughout the whole temporal series covering the area of interest. In particular, two stacks are created: one containing only reference images and another one containing also images of the flood under investigation. As a second step, for each pixel we calculate the minimum, maximum and mean value throughout the whole stack of images, either for the stack of reference image and for the one containing the images of the flood. The statistics so computed are used to compute the Normalized Difference Flood Index (NDFI):

$$NDFI = \frac{mean\ \sigma_0(reference) - min\ \sigma_0(flood)}{mean\ \sigma_0(reference) + min\ \sigma_0(flood)} \quad (1)$$

The mean value of each pixel in the reference stack represents its average behaviour. For example, permanent water surfaces will maintain a small mean value even though some pixels could assume medium-high backscatter in one image due to the presence of wind and consequently creating a rough surface. The advantage of a statistical analysis on the time-series is that we can better characterize each pixel. Also smooth surfaces such as road or airport runways will have backscatter mean linear values close to zero. All non-smooth surfaces (urban areas, forest, agriculture, etc.) will have a mean linear value well above zero.
Vice versa, the minimum value is used to capture a specific discontinuity in the time series, i.e. flooded areas, those pixels that during the flood assumed very low backscatter. The difference between the mean value and the minimum highlights those discontinuities, i.e. flooded areas, pixels that during the flood decrease significantly their backscatter values. Normalizing the difference allows us to have values between 0 and 1 and helps to define a threshold in order

to mask flooded areas. Furthermore, all the unchanged features will "disappear" in the index image, i.e. their value will be close to zero. Therefore, computing the index, we get rid of permanent water bodies and we can exclude non-water pixels with low backscattering such as road, dry bare soil, smooth tarmac.

Therefore, NDFI easily allows to categorize as "flooded", those areas solely temporarily covered by water with respect to permanent water bodies and non-water land cover classes.

In order to detect shallow water in short vegetation, a similar index is created aiming at highlighting the increase of backscatter that happens in this circumstances. Using the statistics on the stacks as explained above, the Normalized Difference Flood in Vegetation Index (NDFVI) is compute:

$$NDFVI = \frac{max\ \sigma_0(flood) - mean\ \sigma_0(reference)}{max\ \sigma_0(flood) + mean\ \sigma_0(reference)} \quad (2)$$

In this case the maximum value of the pixels is aiming at highlighting the discontinuity in the time-series caused by shallow water in short vegetation. The difference with the mean value will highlight only those pixels that experience a strong increase in their backscatter.

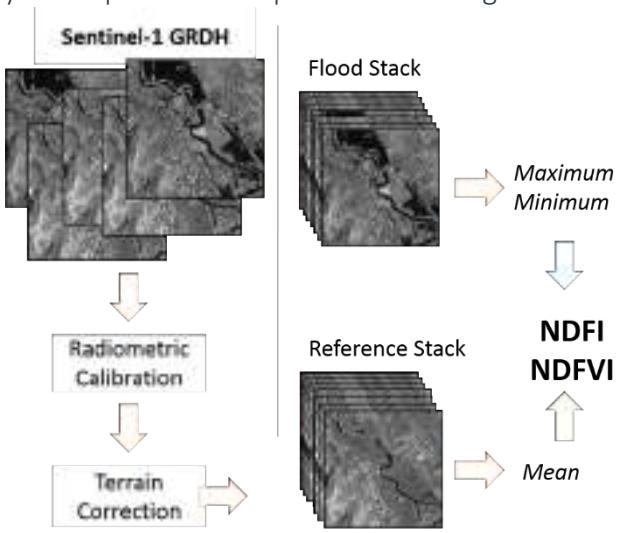

Figure 5 Pre-processing steps and indices calculation workflow

Even though the methodology has been developed having in mind the big data provided by the Sentinel-1 constellation, it can be applied also to other kind of data as it will be shown in the following paragraphs. Figure 5 summarizes the pre-processing steps and workflow for computing the two indices.

As explained in Figure 6, after the computation of the two indices, in order to derive the flood map, a threshold value has to be decided and applied to the resulting indices images in order to include only flooded areas.

(Long et al., 2014) finds the threshold analyzing the histogram of the difference image, i.e. reference image minus the image of the flood. The threshold is the mean value of the whole difference image minus k times the standard deviation:

$$th = \text{mean}\left(\text{NDFI}_{flood}\right) - k * std\ (\text{NDFI}_{flood}) \quad (3)$$

Following a similar approach, we analyzed the NDFI values over surely flooded areas and computed the same metric. The value obtained was 0.7118, obtained using k = 1.5 and with a

mean of 0.845 and a standard deviation of 0.089. Following several trial-error attempts and careful analysis of the statistics computed, the value of 0.7 for NDFI has been decided.

The same approach has been followed for the NDFVI and the resulting threshold was 0.75, using k = 1.5 given by a mean of 0.658 and a standard deviation of 0.187.

$$th_v = \text{mean}\left(\text{NDFVI}_{flood\_veg}\right) + k_v * std\ (\text{NDFVI}_{flood\_veg}) \quad (4)$$

The maps obtained after the thresholding have been filtered following the scheme in Figure 6. Using ENVI®, the classified image is first segmented with a minimum population of 30 and 8 neighbors, then filtered using the dilate morphological filter followed by the closure filtering, both with a window of 3 by 3 pixels. Finally, all the clusters smaller than 10 pixels are excluded as well as all the pixels falling in a slope of more than 5°.

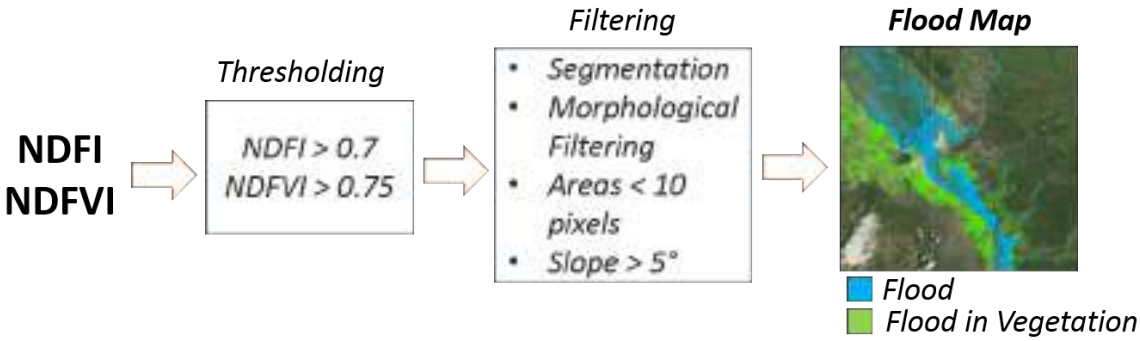

Figure 6 Flood Mapping workflow. From the NDVI and NDFVI indices, a threshold is applied followed by a filtering step in order to obtain the final flood maps.

The threshold value on the NDFI that has been chosen, is conservative in order to obtain a cleaner map. In fact, pixels with NDFI values in the proximity of the threshold can also be found in dry bare soil, shadow or other smooth surfaces mainly due to the effect of the speckle. Decreasing the threshold would result in more false alarms. On the other hand, transitional pixels (pixels at the boarders of flooded area or party inundated ones) can be excluded by the threshold since they could have a smaller value of NDFI. The two morphological filters allow to include in the map those flooded pixels that have slighter lower NDFI value but still with high probability to be part of the flood, i.e. pixels at the boarders of the flooded areas or which are surrounded by flood, without adding noise to the map.

3.6 Results

The methodology has been applied to the three case studies previously described. The results of each case study are presented separately in the following sub-sections.

3.6.1 Southern Malawi 2015

The frequent acquisition of S1 during the flood allowed us to derive 7 flood extent maps using the data listed in Table 1. The maps, Figure 7, show flooded areas and shallow water in short vegetation. They allow to have an overview of the evolution of the flood in the two months of observations, from January 4th, 2015, right before the start of the event, through

January 22nd that is the peak of the flood captured by S1, until March 23rd, at the end of the emergency.

The Copernicus Emergency Management Service (EMS) issued a map produced using the same data we used for the January 22nd map. The two products were compared over the area they overlap. Figure 8 shows the comparison of the two maps highlighting agreement, omission and commission error. It can be noted how the agreement between the two product is quite high. The main source of commission error is due to an area of partial permanent water, as it can be seen in central bottom part of the figure. Copernicus EMS product discarded permanent water bodies using ancillary data, disconnected from the SAR data used to produce the map. Since we did not make use of ancillary data, but instead we based our analysis only on the observations during the rainy season, we reported as flooded all the areas that did not show as covered by water in the reference images. The same thing happens for the omission error: EMS reported as flooded areas that we found already covered by water before the beginning of the flood. These are the main sources of difference between the two products as quantitatively shown by Table 4. The overall accuracy of the map is very good, 96.75%, but the user's accuracy on the flood end up to be low, 65.9%, mainly due to the reasons explained above. The accuracy on the non-flooded areas is very high mainly due the big dimension of the area analyzed.

Table 4 January 22nd 2015 confusion matrix for NDFI based map and Copernicus product

Overall Accuracy (%)	**96.75**		
	Reference (EMS Copernicus)		User's Accuracy (%)
NDFI	No Flood	Flood	
No Flood	17143772	228841	98.7
Flood	370720	715955	65.9
Producer's Accuracy (%)	97.9	75.8	

For a further comparison, we decided to derive a map using Landsat-8 (L8) data. We used all the acquisitions over the area of interest (Landsat Paths 166 and 167, Rows 71, 72 and 73) with a cloud cover lower than 60%. The images were cloud masked and the Normalized Difference Flood Index (NDVI) was computed for each scene. For each pixel, we computed the minimum, maximum and mean of the NDVI throughout the whole stack of images. Finally, a threshold on the three bands was applied in order to derive the flood map. The idea behind this methodology is that whenever there's a flooded surface, the value of NDVI is strongly decreasing. The minimum values aim at capturing this anomaly. In fact, over permanent water bodies the three statistics will be have comparable low values, instead on flooded areas the maximum and the mean will follow the characteristic of the land cover. Therefore, combining the three statistics together we can understand where the flood hit. Of course, in this case we are not able to distinguish in which date the flood hit, but we can see an overview of all the

areas that have been flooded. Figure 9 shows the flood map obtained using this approach and Figure 10 shows a comparison with the NDFI based flood map on the area of Bangula. The main limitation in this case is the cloud coverage and the longer revisit time of L8 (16-day). Differently to SAR data, certain flooded areas could not be observed due to the presence of clouds. Therefore, this product has been though only as a qualitative comparison for our methodology.

3.6.2 Veneto, Italy 2010

A total of 11 flood maps were produced for this flood event. Since we used different sensors, the maps do not offer the same resolution and precision. Only maps derived from CSK and TSX give a very high resolution. Nevertheless, also lower resolution products, such as the one derived from RS-2 and ASAR, are useful to understand the dynamics of the flood. It has to be noted that the images did not always covered the three areas of interests for this flood.

Figure 11 shows the map derived for the area of Vicenza. For November 4th we could derive a map using CSK and one using ASAR and for November 6th one using CSK and one suing TSX. Figure 12 shows in chronological order all the maps produced for Saletto area. For November 4th and 6th respectively 2 and 3 maps were derived thanks to the multiple acquisition from different satellites. Figure 13 shows the maps derived for the area of Bovolenta. In this case, the first image we could use is of November 2nd and the last of November 6th. Also in this case on November 4th and 6th we could make use of two different acquisitions and therefore two maps per day have been derived.

CIMA foundation produced the same maps for the Italian Civil Protection during the event in 2010. In order to validate our methodology, we compared our products with theirs. The comparison of our products and CIMA's obtained with CSK acquisitions can be seen in Figure 14 for November 3rd, Figure 15 and Figure 16 for November 6th and Figure 18 for November 7th.

Table 5, Table 6 and Table 7 show the dispersion matrices for the same products. Figure 17 shows a comparison of the product obtained for the 6th of November using CSK and TSX data. Also in this case, agreement, omission and commission errors can be distinguished in the area of Saletto.

Table 8 shows the dispersion matrix for TSX products and CIMA's for the 6th of November and Table 9 the dispersion matrix for CSK and TSX products based on the NDFI index.

Figure 19 shows one of the errors that affects the dispersion matrix. For the product of the 6th of November, CIMA foundation reported permanent water bodies (in red) most likely using an ancillary dataset. It can be noted how this layer (representing a river) is shifted compared to the SAR image. Flooded areas (in orange) are then reported over the same river, this time in the right position. Having taken CIMA's product has a reference, this kind of error is decreasing the accuracy of our product reported in the dispersion matrix.

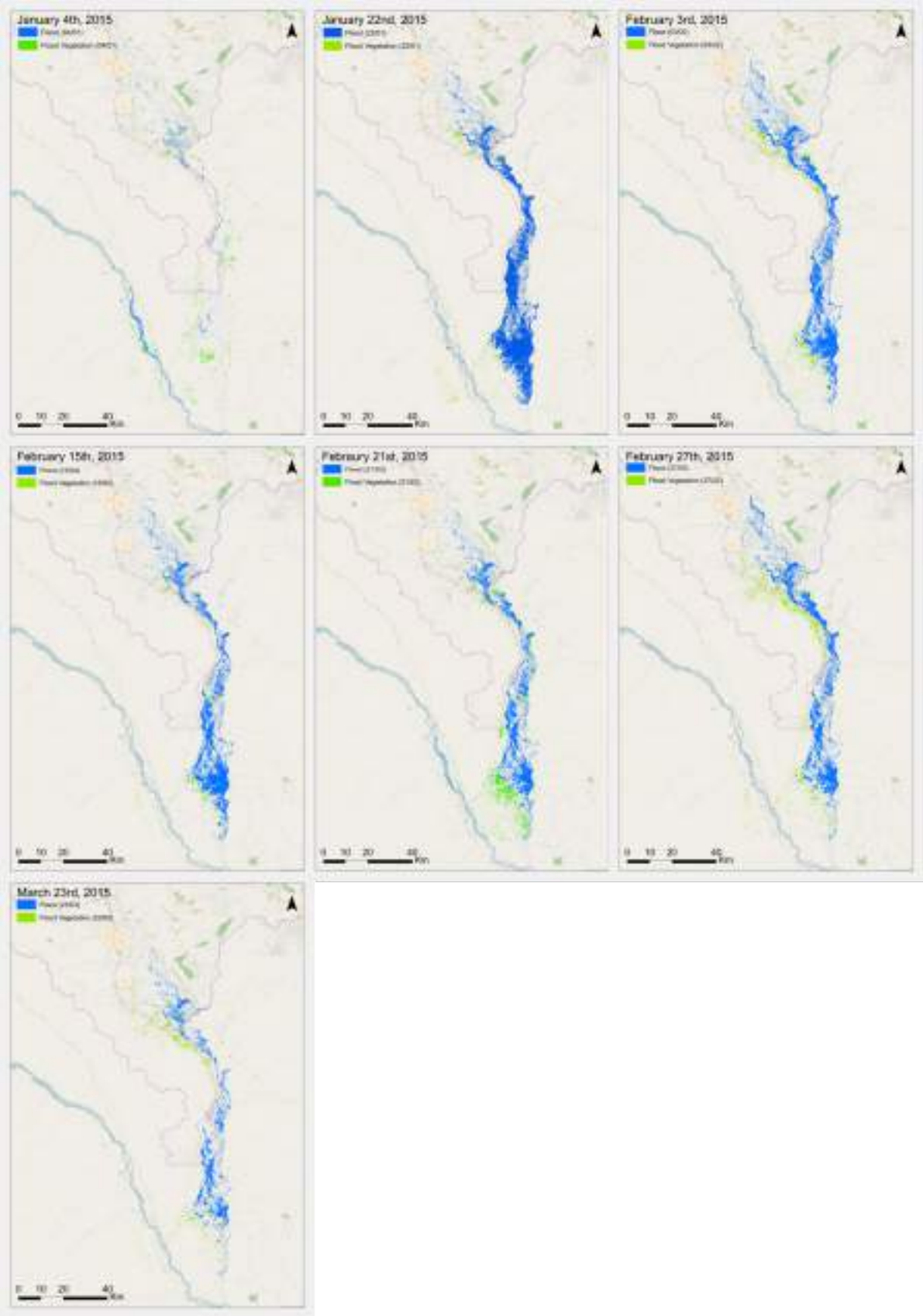

Figure 7 Flood Evolution from January 4th to March 23rd 2015. The maps show also shallow water in short vegetation.

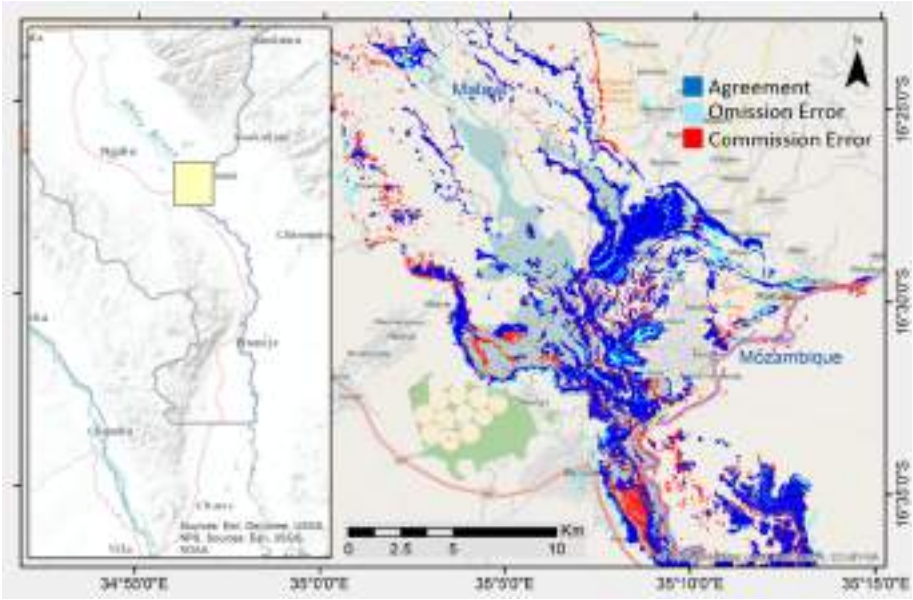

Figure 8 Comparison of the results in the area of the city of Bangula with the map produced by Copernicus Emergency Service for the status of the flood on January 22nd, 2015. The map shows the agreement between the two maps, the omission and commission error. A large commission error can be noted in the central bottom part of the image due to the fact that we did not excluded permanent water bodies using ancillary data. Instead, we used only statistics form the images available during the rainy season.

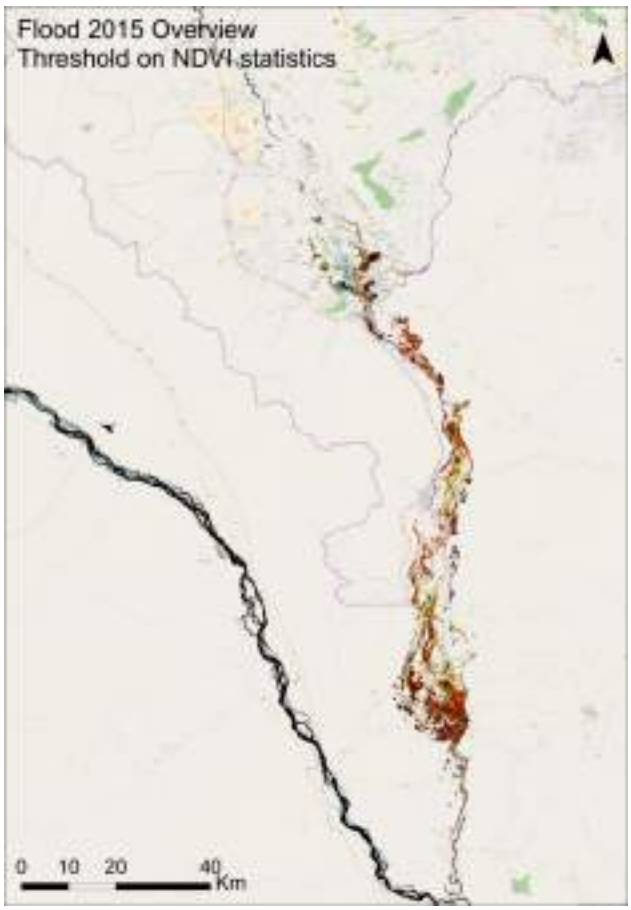

Figure 9 Flood map derived using Landsat-8 date of the entire 2015. Normalized Difference Vegetation Index was computed for all the scenes and its statistics were computed: maximum, minimum and mean value. A threshold on those 3 bands was applied in order to derive the flood extent.

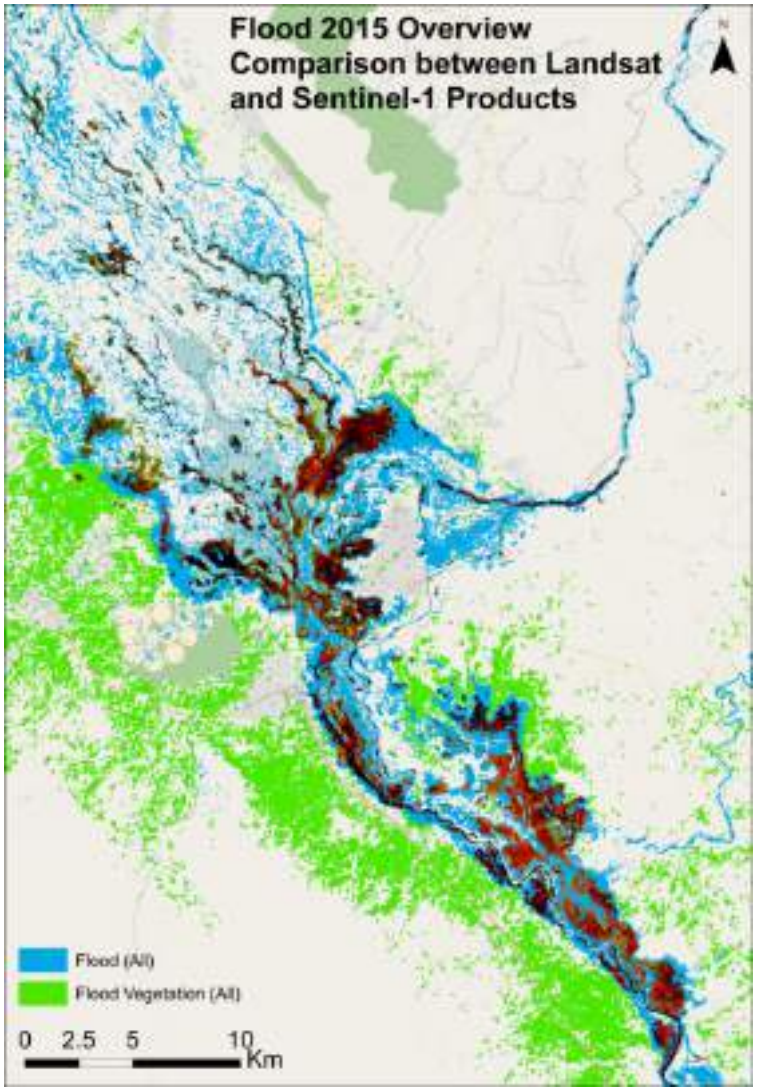

Figure 10 Comparison between flood maps derived using Sentinel-1 data and Landsat-8 data.

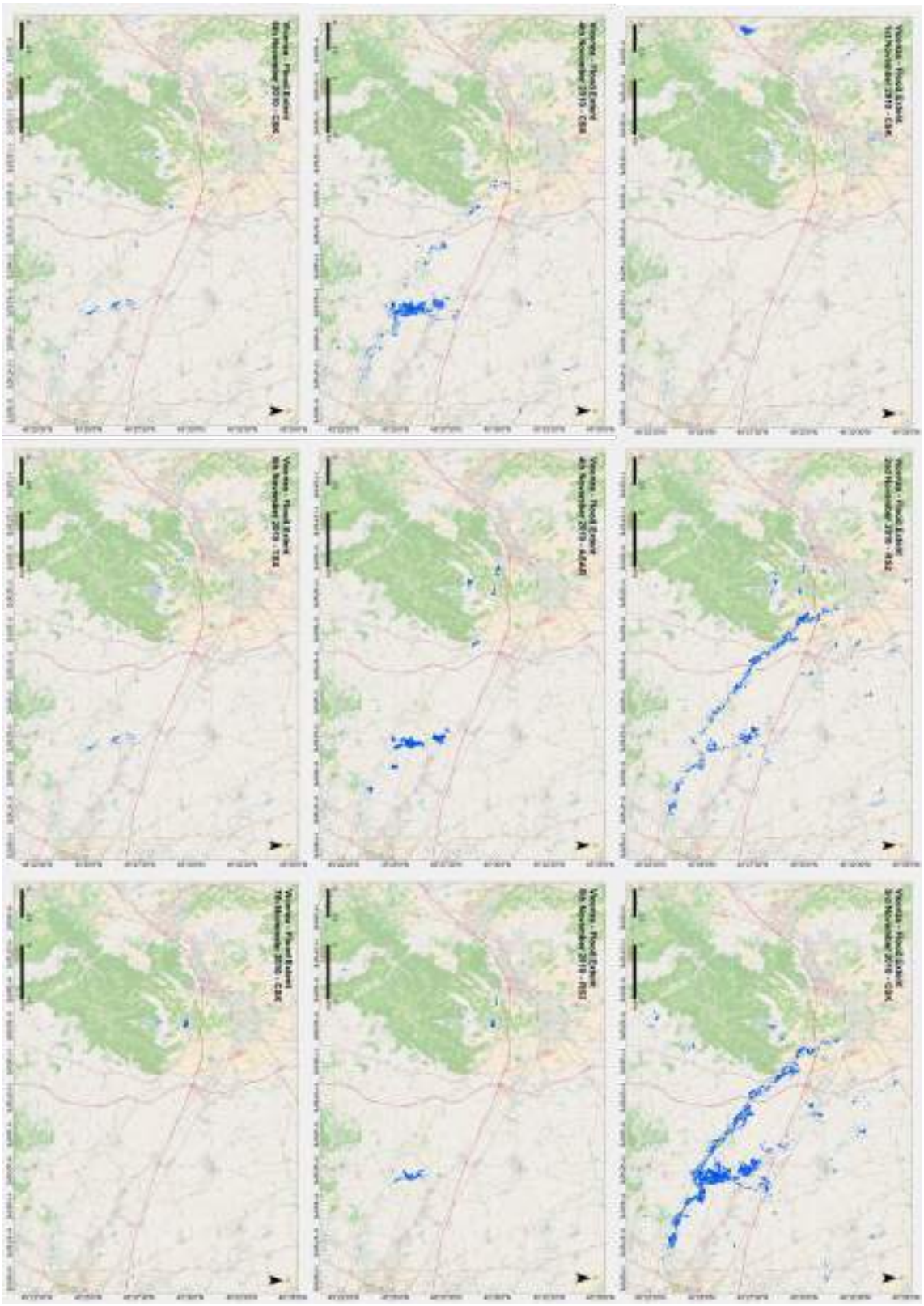

Figure 11 Flood Extent for Vicenza area. Flood evolution from November 1st to November 7th 2010. Since different sensors have been used, on the 4th and 6th of November more than one map has been derived.

Figure 12 Flood Extent for Saletto area. Flood evolution from November 1st to November 12th 2010. Since different sensors have been used, on the 4th and 6th of November more than one map has been derived.

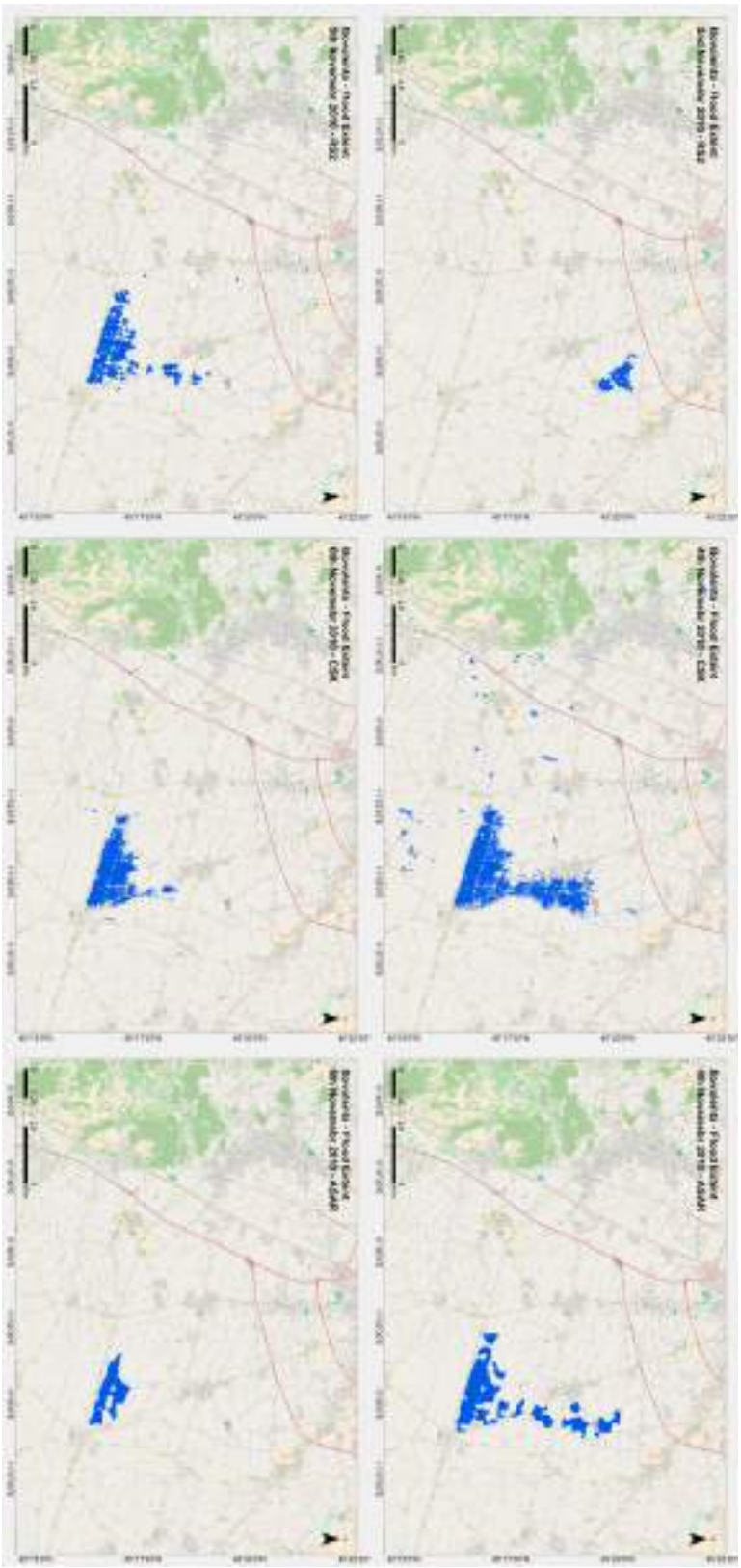

Figure 13 Flood Extent for Bovolenta area. Flood evolution from November 2nd to November 6th 2010. Since different sensors have been used, on the 4th and 6th of November more than one map has been derived.

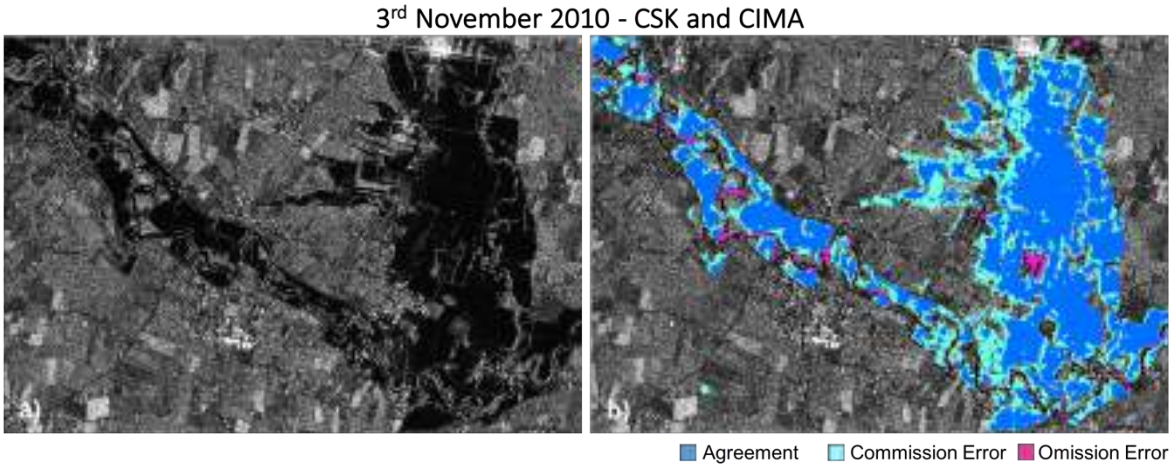

Figure 14 Comparison of results for Bovolenta area with CIMA foundation product for the status of the flood on November 3rd 2010. The map shows the agreement between the two maps, the omission and commission error. What appear as commission error is instead, in most of the cases, a more precise flood mapping using the methodology proposed. Moreover, the omission error are areas of permanent water (river and a small reservoir) indicating the better precision of the presented methodology.

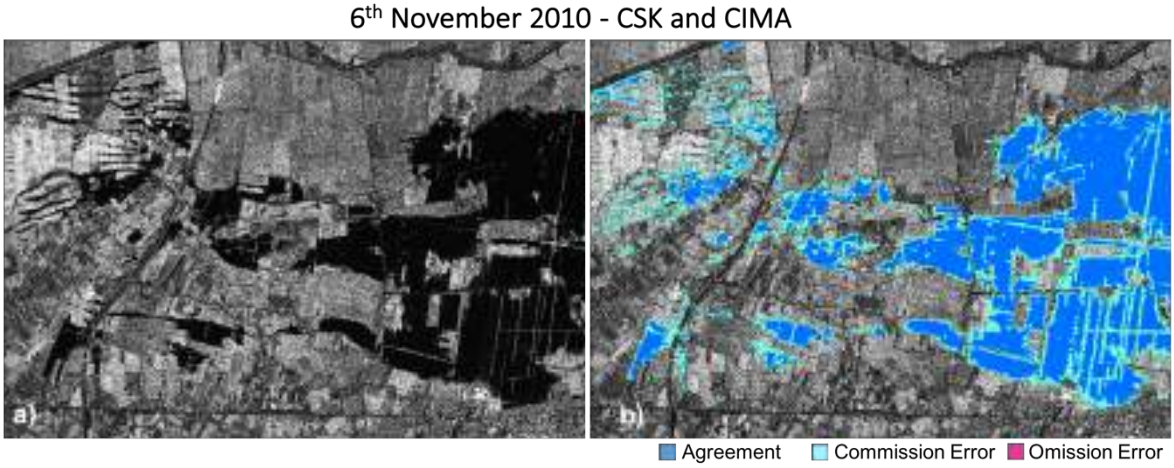

Figure 15 Comparison of results for Saletto area with CIMA foundation product for the status of the flood on November 6th 2010. The map shows the agreement between the two maps, the omission and commission error. Also in this case, it can be appreciated how the omission error are instead a more detail mapping of the flooded areas.

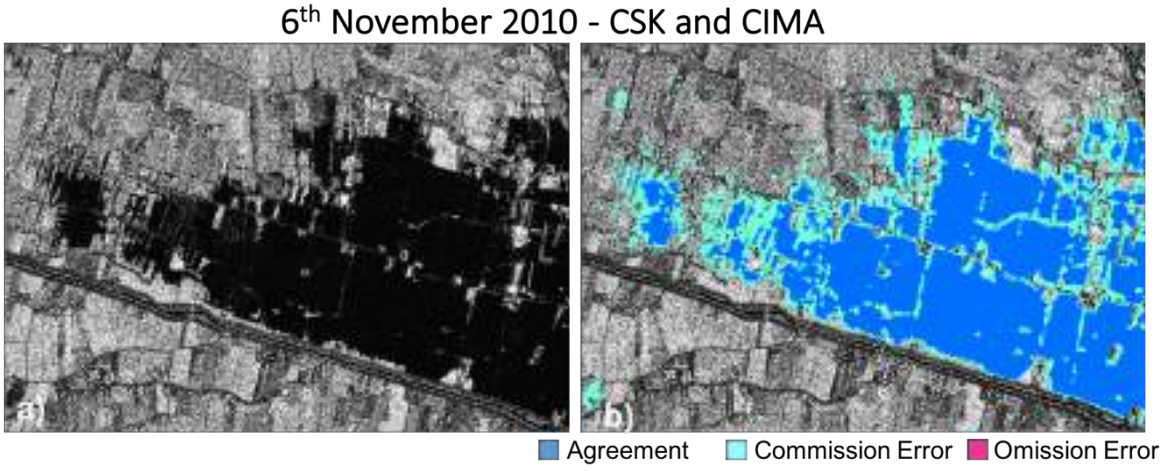

Figure 16 Comparison of results for Bovolenta area with CIMA foundation product for the status of the flood on November 6th 2010. The map shows the agreement between the two maps, the omission and commission error. Also in this case, it can be appreciated how the omission error are instead a more detail mapping of the flooded areas.

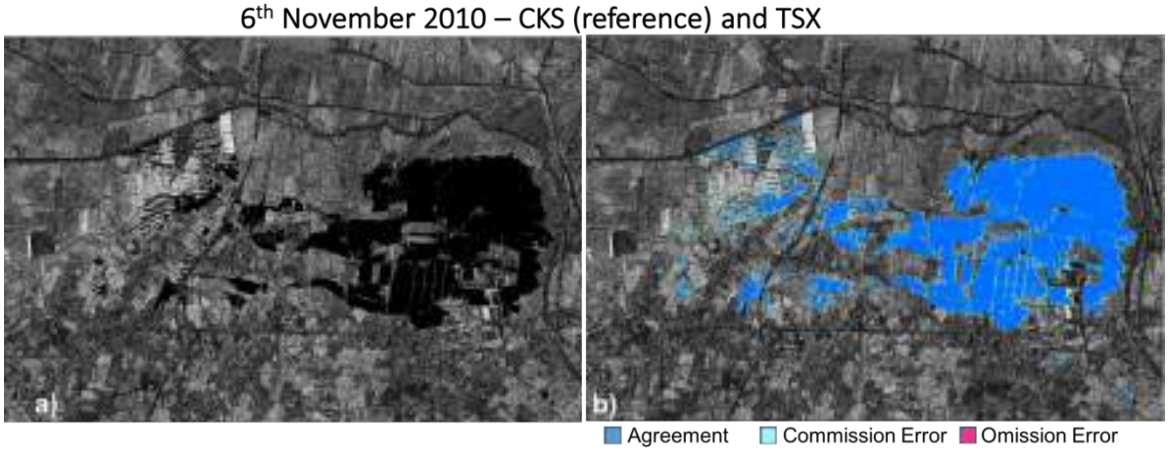

Figure 17 Comparison of results for Saletto area obtained with CSK and TSX data of November 6th 2010. The map shows an almost perfect agreement between the two products.

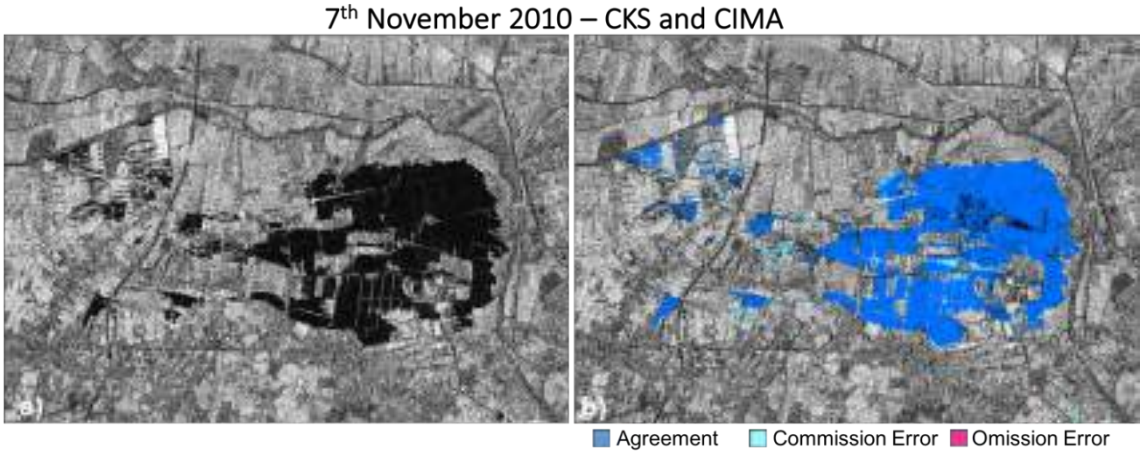

Figure 18 Comparison of results for Saletto area with CIMA foundation product for the status of the flood on November 7th 2010. The map shows the agreement between the two maps, the omission and commission error. Also in this case, it can be appreciated how the omission error are instead a more detail mapping of the flooded areas.

Figure 19 An error in CIMA foundation map of 6th November 2010. Flood area (in orange) are reported over permanent water bodies, in this case a river. In red, pixels labelled as permanent water in CIMA's map. It is clear that these are shifted compared to the SAR data, indicating that probably an external layer for water bodies was used. These errors are affecting the results in the confusion matrix.

Table 5 3rd November 2010 confusion matrix for NDFI based map obtained using CSK data and reference CIMA foundation product

Overall Accuracy (%)	**98.3**		
	Reference (CIMA)		User's Accuracy (%)
NDFI	No Flood	Flood	
No Flood	14286721	33447	99.8
Flood	215878	370569	63.2
Producer's Accuracy (%)	98.5	91.7	

Table 6 6th November 2010 confusion matrix for NDFI based map obtained using CSK data and reference CIMA foundation product

Overall Accuracy (%)	**99.5**		
	Reference (CIMA)		User's Accuracy (%)
NDFI	No Flood	Flood	
No Flood	22376988	23798	99.9
Flood	100190	172290	63.2
Producer's Accuracy (%)	99.6	87.9	

Table 7 7th November 2010 confusion matrix for NDFI based map obtained using CSK data and reference CIMA foundation product

Overall Accuracy (%)	**96.3**		
	Reference (CIMA)		User's Accuracy (%)
NDFI	No Flood	Flood	
No Flood	888941	15987	98.2
Flood	20916	63227	75.1
Producer's Accuracy (%)	97.7	79.8	

Table 8 6th November 2010 confusion matrix for NDFI based map obtained using TSX data and reference CIMA foundation product

Overall Accuracy (%)	**99.6**		
	Reference (CIMA)		User's Accuracy (%)
NDFI	No Flood	Flood	
No Flood	15936509	23157	99.9
Flood	47970	112688	70.1
Producer's Accuracy (%)	99.7	83.0	

Table 9 6th November 2010 confusion matrix for NDFI based maps obtained using CSK and TSX data

Overall Accuracy (%)	**99.7**		
	TSX 06/11		User's Accuracy (%)
CSK 06/11	No Flood	Flood	
No Flood	15509707	8020	99.9
Flood	38040	152638	80.1
Producer's Accuracy (%)	99.8	95.0	

3.6.3 Northern Uganda 2015

Three flood maps were produced for the Uganda flood. This event was not big and not many areas were reported as flooded. The mapping was not easy given also the rapid change of the land cover in this area. We cannot see large flooded areas but the NDFVI index allowed to map shallow water in short vegetation showing that in fact the event hit a wide area as we can see in Figure 20. Figure 21 and Figure 22 show a detail respectively on the North-East of the area of interest (Kapelebyong district) and on the East side (Katakwi district).

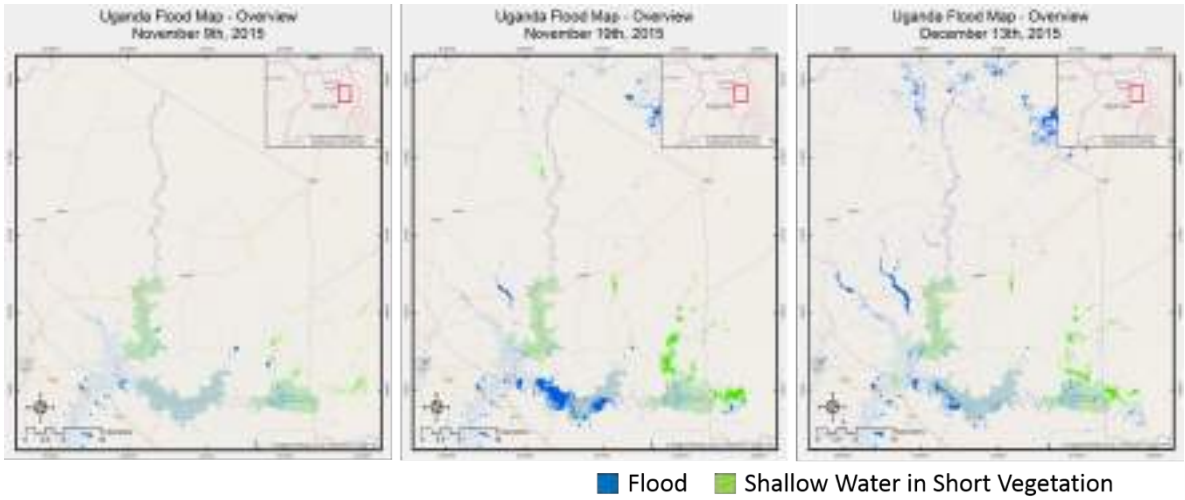

Figure 20 Flood Maps (Overview) for the Uganda flood 2015.

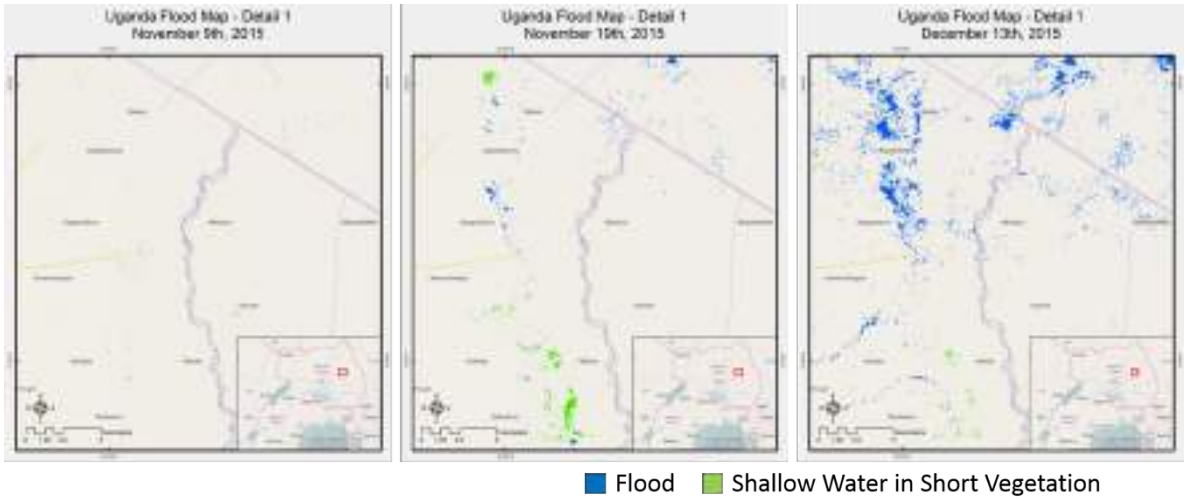

Figure 21 Flood maps detail in the northern East of Uganda, Kapelebyong area.

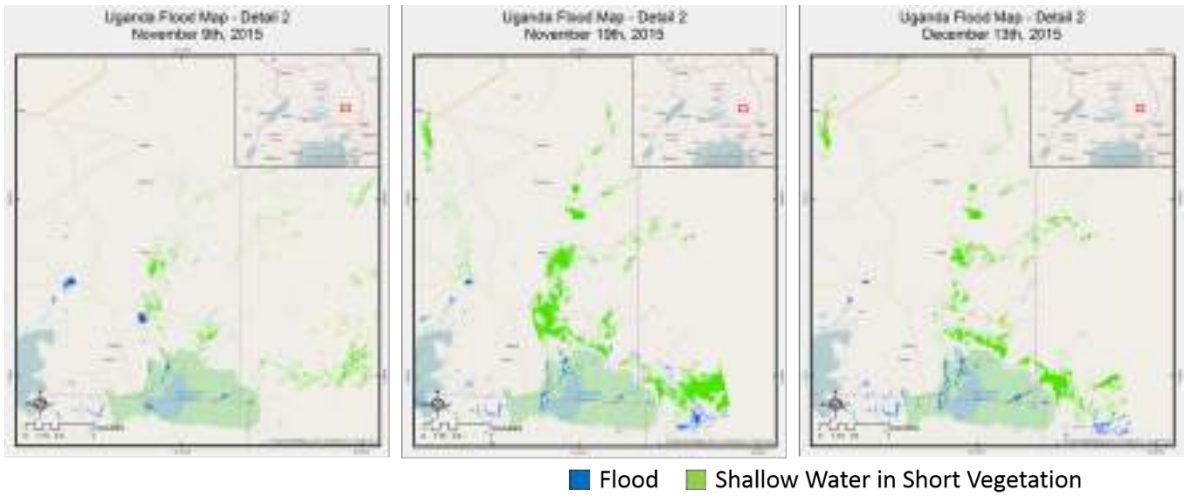

Figure 22 Flood map details in the Eastern side of the area of interest, Katakwi region.

3.7 Discussion

3.7.1 Normalized Difference Flood Index Analysis

Figure 27 shows the range of values assumed by the NDFI index. On the x-axis we have the minimum value of σ^0 in the stack containing the images of the flood, in the y-axis the mean value of σ_0 in the stack of reference images. The colors indicates, for a given couple (σ0min, σ_{0mean}), the correspondent NDFI value.

The plane is divided in two regions by the diagonal; the area below it and marked as (1), corresponds to values of NDFI that are unlikely since we expect the mean value of the reference stack to be always greater than the minimum of the flood image and we can exclude it from our analysis. Negative values of NDFI are actually possible since the mean and the minimum are calculated on two different stacks of images, but this is something unlikely to happen and anyway they are not relevant to the analysis and therefore we can exclude them.

On the diagonal NDFI has value 0, in fact this correspond to equal values of the mean and the minimum throughout the two stacks, i.e. no change between the reference and the flood image. Theoretically here lay also permanent water bodies and stable features such as urban areas, roads, smooth tarmac and desert. In particular, permanent water bodies should lay close to the origin of the plot since they have very low backscatter values. In practice, since small fluctuations of backscatter values can occur caused by speckle and little variations at the surface, permanent water bodies lay on area (2) represented by the yellow triangle. Taking as a reference the values of S1A data for Malawi, σ_0 in this area is less than 0.03 both for reference and flood image. This value has been decided studying the mean value of the backscattering in the stack of reference images. We noted that for $\sigma_0 < 0.015$ only water pixel are detected, which lead to a detection of water bodies that leaves out only their outer borders. Increasing this threshold, dry bare soil pixels starts to be included. When σ_0=0.03, water bodies are delineated very precisely (i.e. the borders of water bodies are also included) but also dry bare soil is included (Figure 25).

Figure 24 zooms on area (2) of the plot considering values of σ_{0mean} from 0 to 0.03. It shows how the threshold applied on the NDFI includes part of this area in the flood map (left side of the threshold line, i.e. for NDFI values greater than 0.7). The area included in the map can be divided in two further areas: (2A) where the mean value of the reference σ_0 is smaller than 0.015 (value representing only water pixel) and area (2B) with mean value of the reference σ_0 greater than 0.015 (water with greater backscattering and dry bare soil). Area (2A) in the NDFI plots represents mainly dry bare soil that decreased its backscatter during the flood and therefore it is correct to include it in the flood map. Area (2B) instead represents permanent water bodies wrongly included in the flood map. Analyzing these values for the Malawi case study as shown in Figure 25, we found that out of 5 million pixels of flooded pixels (NDFI > 0.7, indicated in Figure 25 as “Flood”), only 20 thousand corresponded to area (2B) (indicated in Figure 25 by the red pixels with “$\sigma_{0\,mean} < 0.015$ and NDFI > 0.7”), 0.4% of the total derived flood map and they are barely visible in the figure. The error can be considered negligible. Nevertheless, these pixels can be easily filtered out from the final flood map as explained in the following paragraph 3.4.1.1.

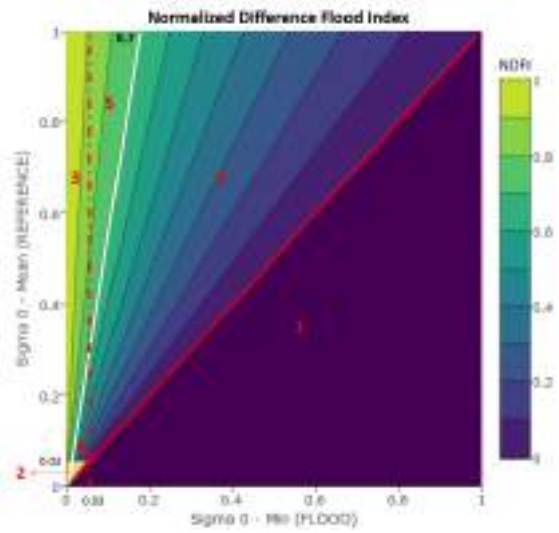

Figure 23 Normalized Difference Flood Index: index values are plotted with reference to the minimum pixels intensity (in linear scale) throughout the "flooded" multi-temporal series (x axis) and the mean pixel values throughout the reference time series (y axis). The white line indicates the threshold value for deriving the flood map.

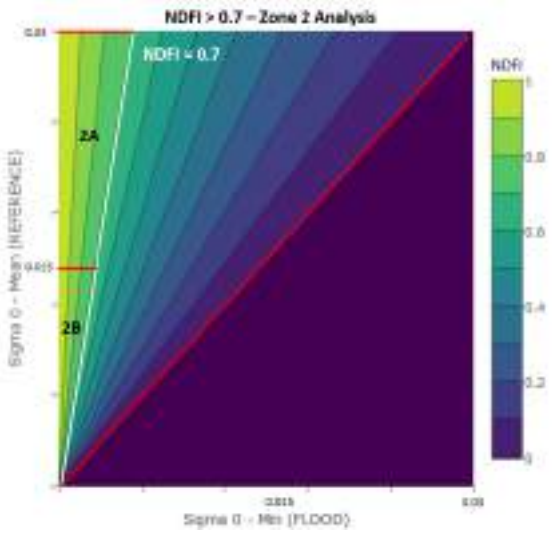

Figure 24 Zoom on the zone 2 of NDFI plot (yellow area in Figure 23). The threshold on the NDFI (0.7) includes part of the permanent water pixels. More precisely area 2A represent dry bare soil that decreased its intensity due to flood, 2B are most likely permanent water wrongly included in the flood map. A careful analysis shows that this error represents only a small percentage of the total flood map.

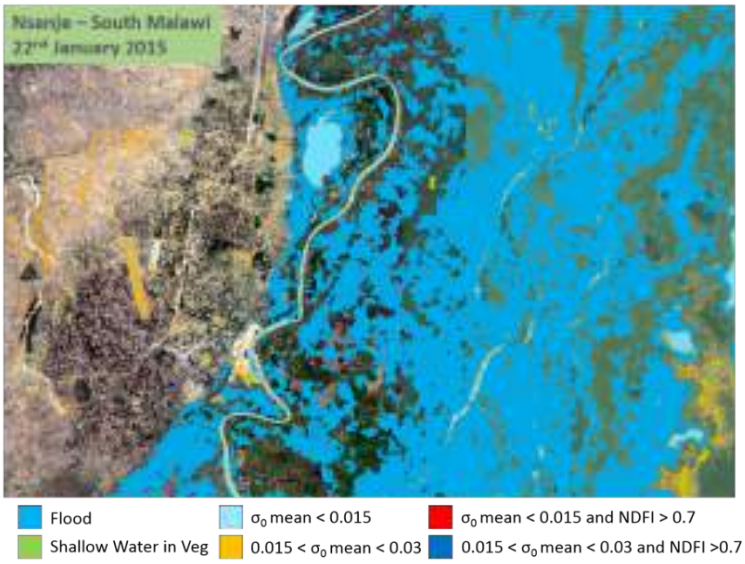

Figure 25 Analysis of σ_0 statistics and correspondent NDFI and NDFVI values on the Nsanje area in southern Malawi for σ_{0mean} values smaller than 0.03, corresponding to Zone 2 of the plot in Figure 24. Light blue pixels represent permanent water bodies. Orange pixels represent mainly the borders of water bodies and dry bare soil. Red and dark blue pixels, barely recognizable, represent the negligible errors in the final flood map corresponding to zone 2A and 2B of the plot in Figure 24.

The dashed-dotted line (σ_{0min} = 0.03) in Figure 23 represents the maximum backscatter for water pixels in the stack containing the images of the flood. Excluding area (2), it creates four additional areas together with the threshold line in the NDFI plot. Area (3) represents non-water pixels (medium-high backscattering, σ_{0mean} > 0.03) that strongly decreased their backscatter during the flood ($\sigma_{0\,min}$ < 0.03), i.e. they are the flooded pixel included in the flood

map. Area (4) represents non-water pixels with low reference backscattering ($0.03 < \sigma_{0mean} < 0.17$) that slightly decreased their backscatter during the flood ($0.015 < \sigma_{0\,min} < 0.03$).

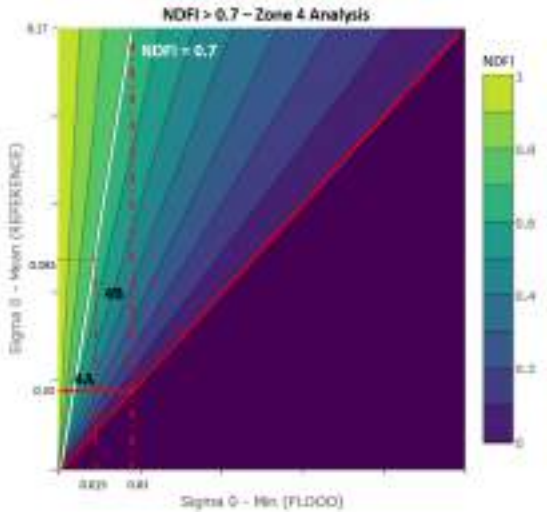

Figure 26 Zoom on the area 4 of NDFI plot. The threshold on the NDFI (0.7) excludes possible flooded areas. A careful analysis shows that this error is compensated by the morphological filtering steps and therefore acceptable.

Figure 26 shows in details this part of the plot. The line $\sigma_{0min} = 0.015$ divides area (4) in two sub-regions. Area (4A) is most probably flood but with a fairly low mean backscattering in the reference. An increase in the NDFI threshold would reduce this uncertainty (on the other hand adding also extra noise). Figure 27 and Figure 28 show that these pixel are eventually included in the flood map thanks to the morphological filtering. Area (4B) are pixels at the boundaries of water surfaces or bare soil that decreased its backscattering during the flood. The same two figures show that these pixels are instead dropped by the final maps, which make sense in most of the cases except in the proximity of flooded areas, where they could be included in the final flood map. The dilatation filter partly adjust this possible error, which is nevertheless acceptable.

Area (5) in Figure 23 represents pixels that could be wrongly included in the final flood map since they did decreased consistently their backscatter during the flood, indicating that something did happen, but not enough to reach a σ0min typical of water pixels. In fact in this area we could include pixels with σ0min equal up to 0.176. Analyzing the results over Malawi, we see that these pixels are only the 1% of the overall pixels that have NDFI greater than 0.7 (53 thousand over 5 million) and the majority of them falls over bare soil and mountainous regions and are eliminated by filtering steps (morphological, area and slope filtering). In fact, after the filtering only the 30% of them (17 thousands) are kept in the final map. Also in this case, an extra filtering step can be applied to get rid of them, as explained in the following paragraph 4.3.1.1. In the Malawi case, the error is negligible as shown in Figure 27 and Figure 28.

Area (6) is correctly eliminated by the index threshold since those are pixels that decreased their backscatter but that are surely not water pixels since their σ0min is too high (σ0min > 0.03). Figure 27 summarizes the concepts for an area North of Nsanje city, Figure 28 for the area of the city of Nsanje.

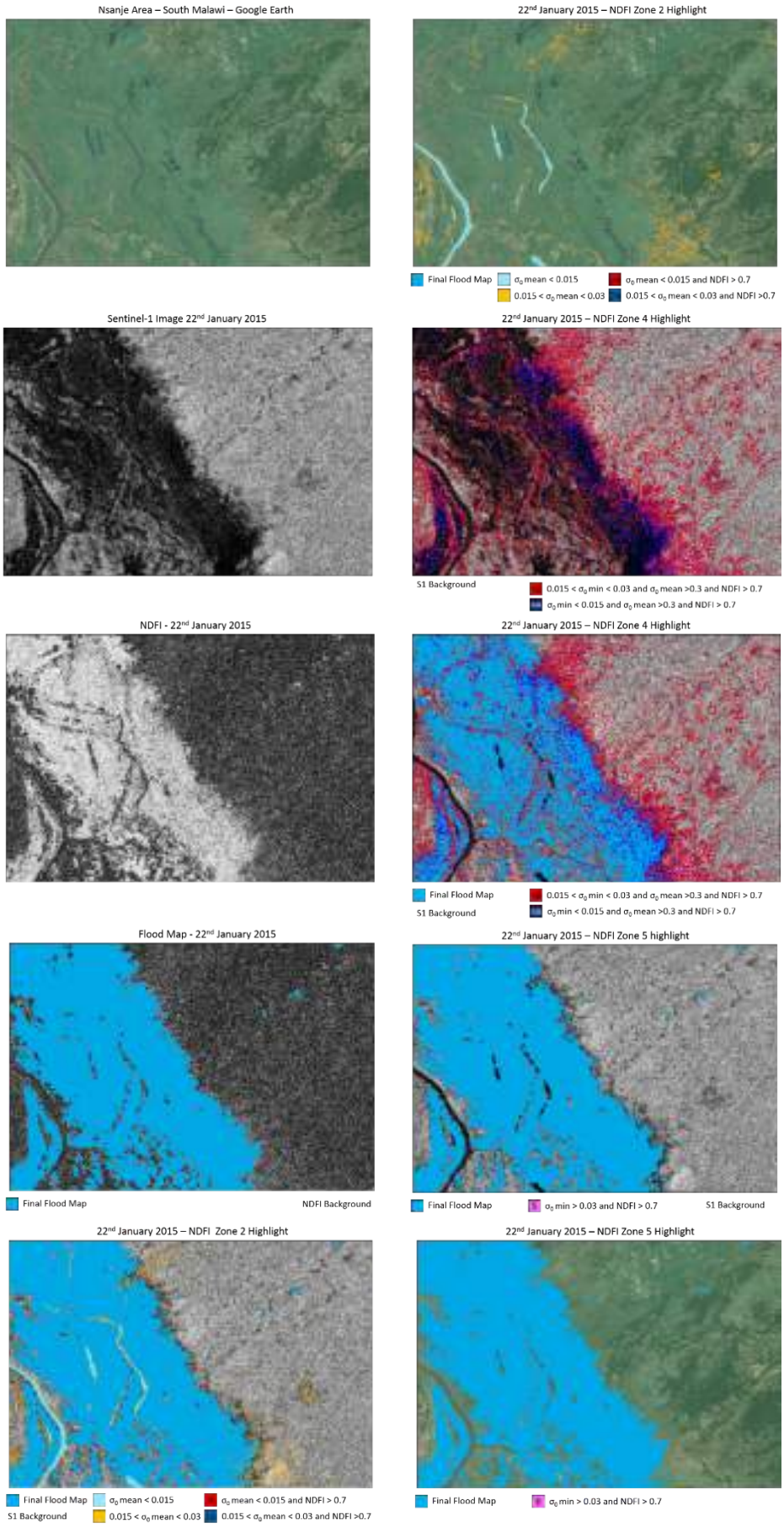

Figure 27 Analysis of NDFI value for an area North of Nsanje.

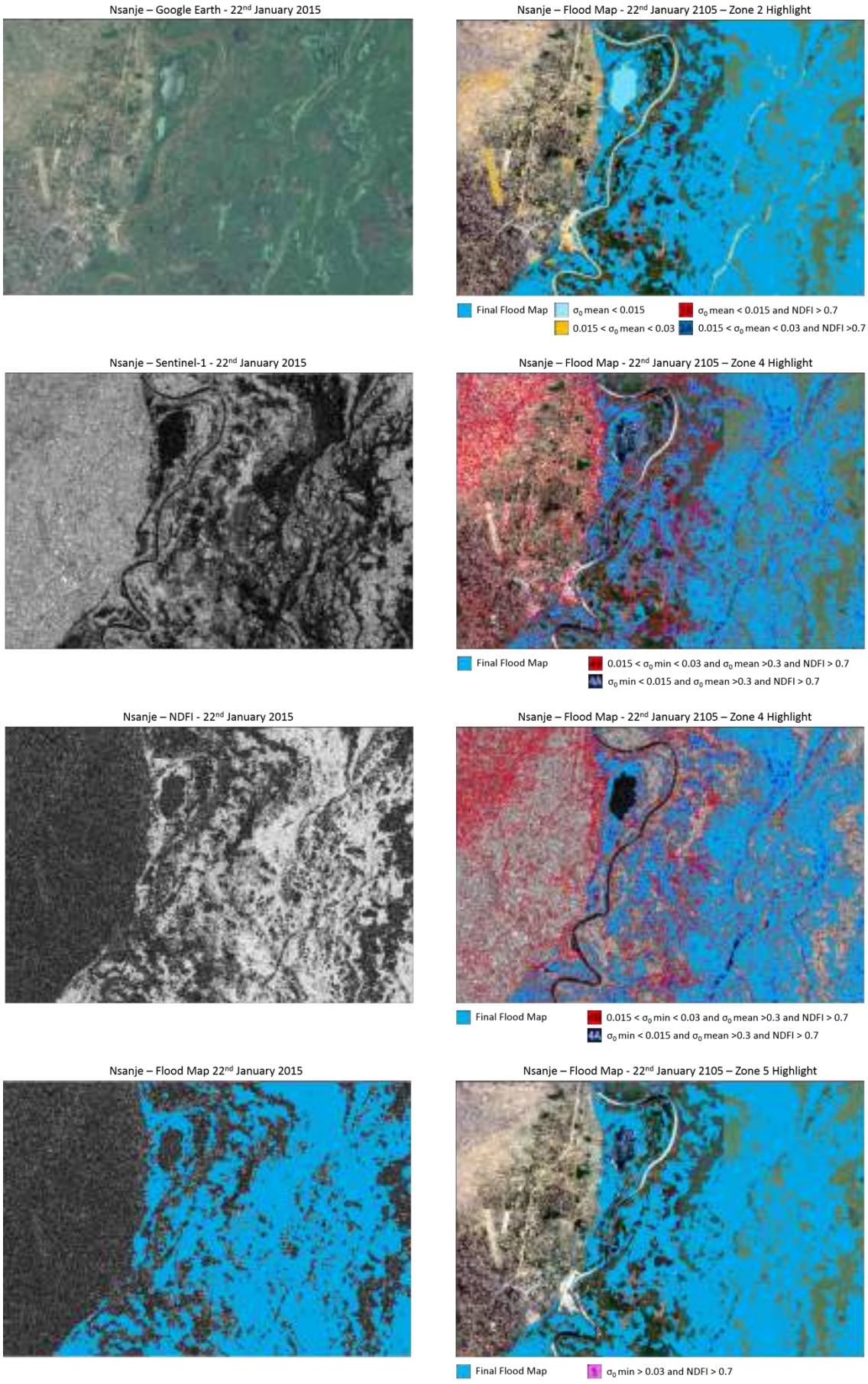

Figure 28 NDFI values analysis over the city of Nsanje

3.7.1.1 Additional filtering to refine the flood map

We showed that choosing a threshold of 0.7 for the NDFI, wrong pixels can be included in the flood map. Specifically, pixels belonging to areas (2) and (5) of the NDFI plane (Figure 23). Even though the errors has been shown to be negligible, we can refine the flood map with a further filtering step as indicated in Figure 29. Firstly, the raster flood map is converted to polygons. Secondly, for each polygons, we compute the mean and standard deviation of the σ0min and σ0mean. The polygons with mean (σ0 mean) < 0.015 (area 2B in the NDFI plot) can be filtered out together with polygons with mean (σ0 min) > 0.03 (area 5 in the NDFI plot).

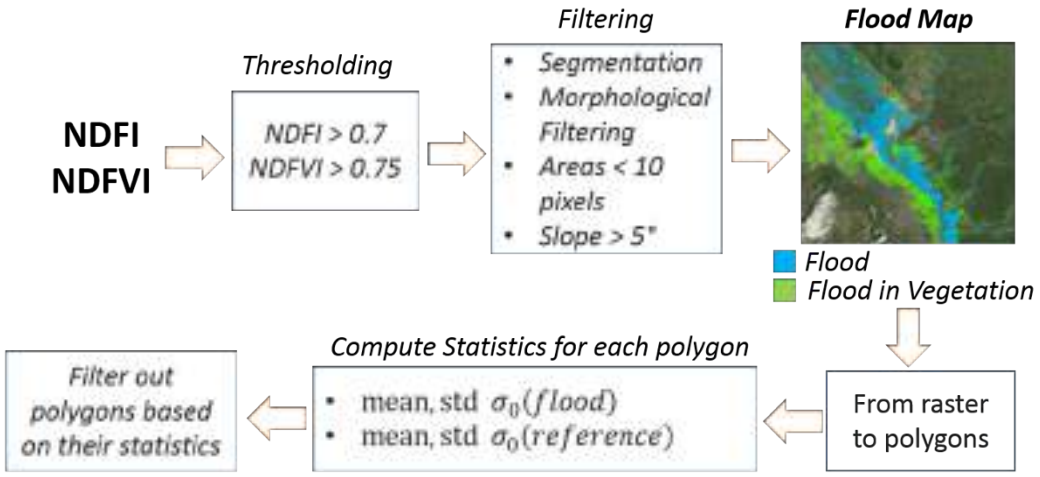

Figure 29 Additional filtering steps in order to refine the flood map and exclude possible misclassified pixels

The use of the statistics in the polygons allowed also to detect false alarms caused by other effects such as replacement of crop (grapes with denser crop such as maize or wheat) or different geometry of acquisition (difference in radar shadows) that occurred in the comparison of CSK images with different incidence angle, as shown in Figure 32. Also the appearance of new constructions can cause false alarms as shown in Figure 31 where a new road was built in the same time frame (14-b), which was not present in 14-a. The new road causes a decrease in radar backscatter and therefore a high value of NDVI, causing some misclassification. In this case a filter in the mean (σ0 min) allowed the detection of the false alarm

The standard deviation can be useful to clean even further the map. Very high values of standard deviation either in the reference or in the flood images, can indicate a false alarm. After several iterations, we found out that a threshold of 2 (in the reference or in the flood image) for the standard deviation allows to detect misclassified areas, but each case has to be analyzed independently.

For example, in the Veneto flood of 2010, there were few CSK archive images available and we had to take an image from 2008 in order to perform the change detection. In the two year time in between the two acquisitions, some changes occurred, which led to some cases of wrong classification. Figure 30 shows one of this cases: a) the image acquired in 2008 shows a large building in construction. The backscattering due to the double-bounce effect is very high. In 13-b) the same building is completed and the steep roof cause some radar shadows. The use of the NDFI highlights this decrease of backscattering letting this area to fall inside the

flood map as shown in 13-c. The use of the standard deviation on the reference image allowed us to filter this polygon and exclude it from the map. In fact, the value of the standard deviation was very high inside the polygon due to the high fluctuation of values.

Figure 30 a) CSK reference image acquire in 2008 with a building in construction b) CSK image acquired during the 2010 flood with the same building completed c) result after the threshold on the NDFI shows the roof shadow as flood d) Google Earth image of the same area

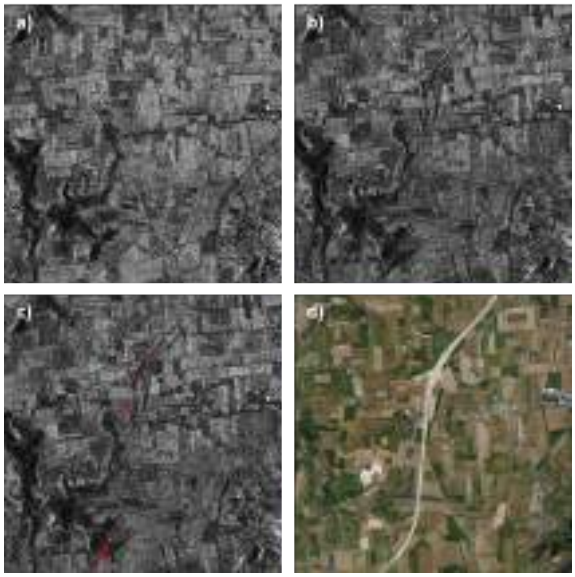

Figure 31 a) CSK reference image acquire in 2008 b) CSK image acquired during the 2010 flood where a new road has appeared c) result after the threshold on the NDFI shows the new road as flood d) Google Earth image of the same area

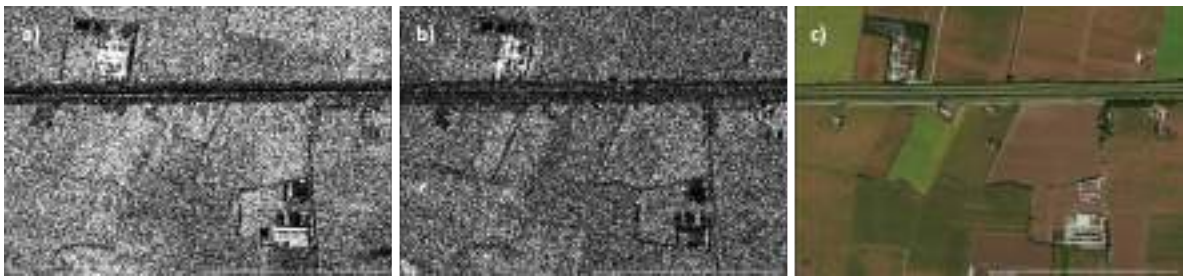

Figure 32 In a) and b) the same area is observed with different incidence angle and it can lead to false alarms due to the different radar shadow.

3.7.2 Normalized Difference Flood in Vegetated areas Index Analysis

The analysis of the NDFVI is easier since the pixels that increase their backscatter during a flood are typically less than the ones decreasing it. Moreover, the reasons for that to happen are also less.

Figure 33 shows the values assumed by the index for a given couple (σ_{0mean}, σ_{0max}). As in the NDFI case, the diagonal divides the plane in two areas where area (1) corresponds to unlikely index values and therefore is exclude from our analysis. Area (2) represents the pixels included in the flood map (NDFVI > 0.75) and area (3) the ones excluded. Figure 34 analyses in detail area (2). Area (2A) represents very dark pixels ($\sigma_{0mean} < 0.015$, most probably water) that increased more or less consistently their backscatter during the flood. Part of this increment is due to fluctuation of the backscattering over permanent water bodies meaning that we would include a very small part of permanent water bodies in the final map, a small error that can be accepted. Instead when the increment is very high, most probably is due to the effect of wind

or vegetation in water surfaces. Analysing the Malawi case study, the pixels falling in the area of the plot and appearing in the final flood map are negligible. Area (2B) represents non-stable water surface or very dry bare soil that increased the backscatter during the flood. Area (2C) and the remaining of area (2) represents herbaceous or shrub areas that experienced the same phenomenon, most probably the effect of shallow water or increased soil moisture. These two areas are correctly included in the map and the Malawi case study confirms that. In fact, more than the 95% of the mapped pixels fall in these two regions and the location of these pixels are contiguous to water surface as expected.

Figure 35 shows the pixels belonging to these areas for the case study of Malawi. It can be noted how the predominant effect is the one of area (2B) and (2C).

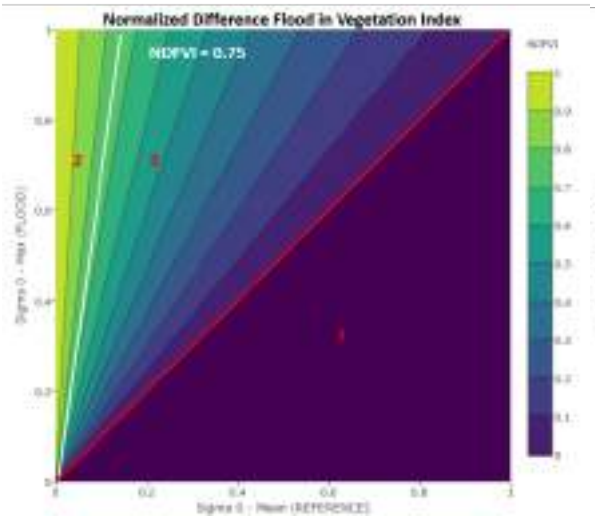

Figure 33 Normalized Difference in Vegetation Flood Index: index values are plotted with reference to the minimum pixels intensity (in linear scale) throughout the reference multi-temporal series (x axis) and the mean pixel values throughout the "flooded" time series (y axis).

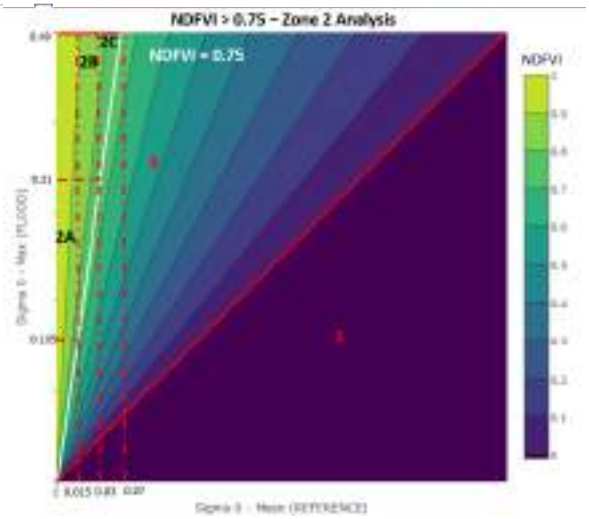

Figure 34 Zoom on the area 2 of NDFVI plot in Figure 9. This region can be divided into other 3 sub-regions depending on the mean backscatter in the reference images allowing to understand what it is mapped as shallow water by means of the threshold on the NDFVI.

Using the methodology proposed, precise flood maps could be derived for the three case studies. The use of the two indices allowed the mapping of open water and shallow water in short vegetation.

The methodology has been tailored for being used with S1 data, i.e. with many archive images to be exploited using pixel statistics. The idea is that such statistics can supply a more robust information on the pre-event conditions. Even though the Malawi case study was not ideal (the first flood captured by S1 with only few archive images due to the short operative life of S1 at the time of the flood), the comparison between our product of January 22nd and Copernicus EMS (the only one matching our products) shows a very good accuracy (overall accuracy of 96.75%) as we can see in the map of Figure 8 and in the dispersion matrix in Table 4. In fact, even though the user's accuracy on the flooded areas resulted in a rather low value (65.9%), it is straightforward to understand that the quality is indeed very high. The main source of differences between the two products comes from a different way of considering

permanent water bodies. In our case, permanent or semi-permanent water bodies are excluded from the map only if they appear in the statistics of

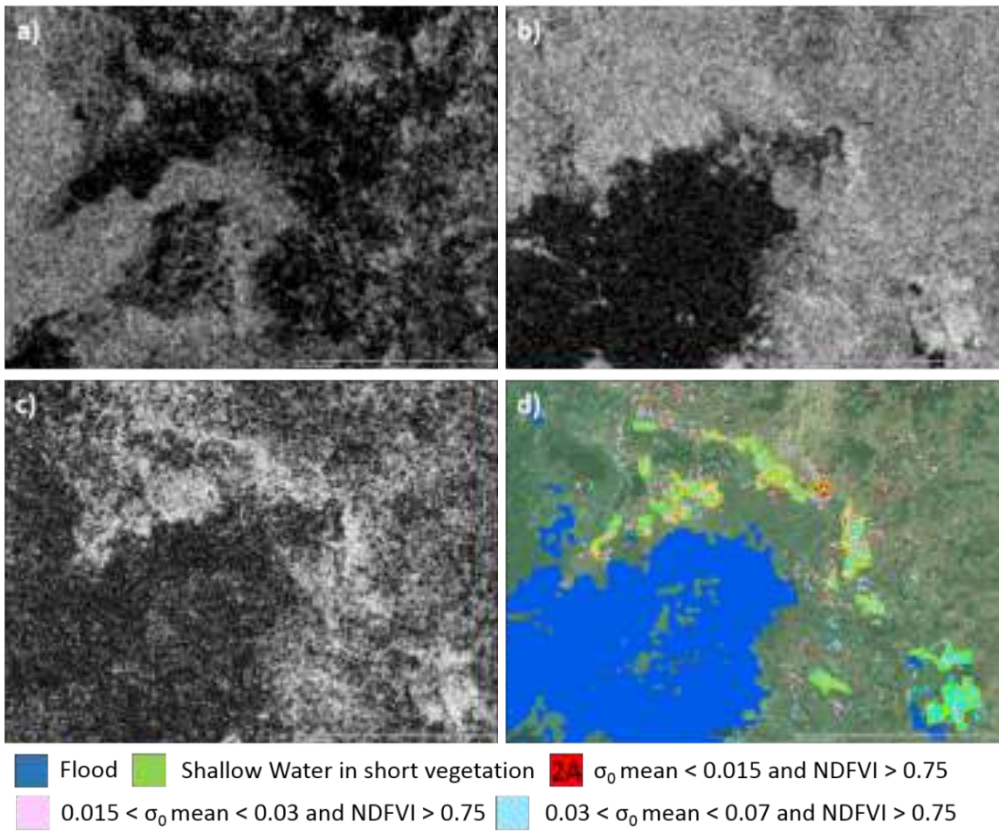

Figure 35 a) Mean backscatter of reference images b) S1 image of the flood on January 22nd, 2015 c) NDFVI computed for the same date d) Pixels that increased their backscatter due to presence of water and captured by a threshold on the NDFVI index. The colors separate the pixels with different backscatter values in the reference images congruently with the legend and the plot in Figure 34.

3.7.3 Discussion of Results

the reference images. EMS product instead takes this information from an external dataset.

Areas of semi-permanent water could be in fact reported as permanent water in the external dataset used by EMS. Therefore, EMS maps excluded this area from the flood map a priori. In our case, the same area is compared with reference images. If the area was dry during the acquisition of reference images, it will show up in the final flood map. The opposite effect can also happen as it can be noted in Figure 8. EMS reported as flooded all the areas showing low backscattering in the images of the event. Part of these areas had low backscattering also in the reference images we used and therefore they are excluded from our map creating an omission error. Taking into account this considerations, the two products are very similar. This prove the goodness of our methodology, which highlight the real changes occurred between ex-ante and ex-post situation.

Furthermore, even if we have no data to validate the products, we are able to report a map of shallow water in short vegetation, an information that is not reported by any

emergency service. These areas appear in proximity of zones of "normal" flooding, where they are more likely to happened and where we were expecting them, suggesting the accuracy of the results. In addition, the flood evolution suggests the validity of this kind of information. In fact, from February 15th to February 21st there's a flood reduction on the south side of the map and, where there was open water, the map is showing shallow water in short vegetation. This suggests that the water has receded and only a small amount of it remained there. On February 27th due to further rainfall, we have a modest increment of flooded area and a consequent reduction of shallow water in short vegetation in the same area.

Also the comparison with the map obtained using L8 data, Figure 10, shows a good correspondence even though the few L8 acquisitions during the event and the limitation of optical sensor with cloud coverage influence this kind of product. Using only the statistics on the NDVI, we are not able to obtain information about shallow water in short vegetation since the amount of vegetation in this kind of situation, and therefore the NDVI values, is comparable to the one before or at the end of the flood. For this reason, we cannot capture any change only using the NDVI.

Nevertheless, the methodology based on the NDVI, here presented very briefly, can be of great value. Figure 9 in fact, shows an overview of the flood that was obtained with few steps. The simplicity and the effectiveness of this approach together with the availability of L8 data in the GEE, makes really easy the mapping of floods in case only a qualitative map is needed.

Flood indices have been developed having in mind EO big data. Nevertheless, we tested the same approach on a typical case study of the past, i.e. with few and diverse acquisitions and almost no archive data useful for change detection. For the Veneto flood of 2010 we tested the method with 4 different sensors at 4 different resolutions: CSK and TSX at 3 meters, RS2 at 25 meters and ASAR at 150 meters. We also had the chance to test it for HH polarization as in the case of ASAR and RS2. The method showed to be robust since the identical processing steps have been followed obtaining in all the cases very good results. The threshold on the NDFI was the same for each dataset. Figure 11, Figure 12 and Figure 13 show the evolution of the flood for the three area of interests of this case study.

In particular, for the 4th and the 6th of November we could derive more than one products due to multiple acquisition from more sensors. This shows how the methodology performs well also at lower resolutions, of course with the expected decrease of details. Given the limited fluctuation of SAR backscattering at these resolutions, the derivation of flood maps was easier and needed less filtering. Finally, we can see how CKS and TSX products are practically identical given their identical resolution, indicating one more the robustness of the method.

The validation in this case has been performed using as a reference the maps produced by CIMA foundation for the Italian Civil Protection during the event. Figure 14, Figure 15, Figure 16 and Figure 18 show clearly how our methodology has comparable, if not better, performances compared to CIMA's products. In fact, comparing with the original SAR data, we can note how our maps are following the flood extent with more precision. The filtering used by CIMA to "clean" the map from small objects and false alarms is also decreasing the details of the map, something not happing in our products.

Table 5, Table 6, Table 7 and

Table 8 show an overall accuracy of 98.3% for November 3rd, 99.5% for November 6th, 96.3% for November 7th and 99.6% for November 6th using TSX data. User's accuracy on flooded areas is instead of 63.2 % for November 3rd, 63.2% for November 6th, 75.1% for November 7th and 70.1% for November 6th using TSX data. The cause of these low values is the

less details of CIMA maps that increase the commission errors and the permanent water bodies wrongly reported by CIMA, which make the omission errors to increase Figure 19.

Table 9 shows that the methodology applied to two different but comparable SAR images, CSK and TSX, give almost identical results, 99.7% overall accuracy. The 80.1% of user's accuracy also shows an improvement in this comparison but also reveal the imperfection of CSK data. In fact, CSK data were noisier compared to TSX. In the derivation of TSX flood map, additional filtering was not necessary and the map resulting after the thresholding was almost in its final version. TSX not only appeared less noisy but also were acquired with identical geometry. Since CSK constellation was activated during the flood in order to obtain more acquisitions (1 a day during the emergency), more false alarms appeared mainly due to differences in radar shadows between images (Figure 32). For the same reason, the NDFVI index was of no help in this case. Few areas, especially along the rivers, showed signs of shallow water in short vegetation, but the resulting maps were too noisy to be trusted and it has been preferred to discard them.

In the Uganda case study, the derivation of flood maps was difficult for several reasons. First of all, it wasn't a big event, in fact the maps were produced for the Red Cross/Red Crescent climate centre in order for them to understand if a real flood occurred or not in the area where their emergency warning system was triggered. The flooded areas are rather small and looking at the maps in Figure 20, we can see how part of these are in fact semi-permanent water bodies as we can understand from their river-shape and from the reference Open Street Map layer. Another difficulty comes from the bimodal rainy season, which lead to a frequent change in the land cover, which made difficult the interpretation of the statistics given that no ground truth was available. Thanks to the high number of reference images, we could rely on the statistics much better than in the other case studies presented.

Radar backscatter during the days when the alerting system was triggered (November 19th, 2015), showed a strong increase compared with the mean value in the reference statistics. The increase, very well captured by the NDFVI index, was non comparable with a simple change in vegetation and therefore allowed us to map shallow water in short vegetation with confidence Figure 36.

3.8 Conclusions

A new methodology based on time-series statistical analysis has been proposed for rapid flood mapping with the aim to exploiting the big EO data coming from the new Sentinels. Two indices are proposed for highlighting flooded areas and for an easy derivation of flood maps: the Normalized Difference Flood Index (NDFI), for mapping open water and the Normalized Difference Flood in Vegetation Index (NDFVI) for mapping shallow water in short vegetation. The two indices are computed comparing two statistics on two different time-series, one with only reference images and one with the images of the flood, therefore performing a change detection: the mean value (reference) with the minimum (flood) for the NDVI, the maximum (flood) with the mean value (reference) for the NDFVI. The mean value aims at capturing the normal condition of the land cover of the area analyzed, the minimum the decreasing in radar backscatter due to the presence of temporary water, the maximum the increasing in radar backscatter due to shallow water in short vegetation. A threshold is then applied to the two indices in order to derive the flood maps, all the pixel above a certain value are classified as

flooded. The maps so extracted are segmented, dilatation and closure morphological filtering is applied, small clusters of pixels are filtered and also pixel above a certain steepness.

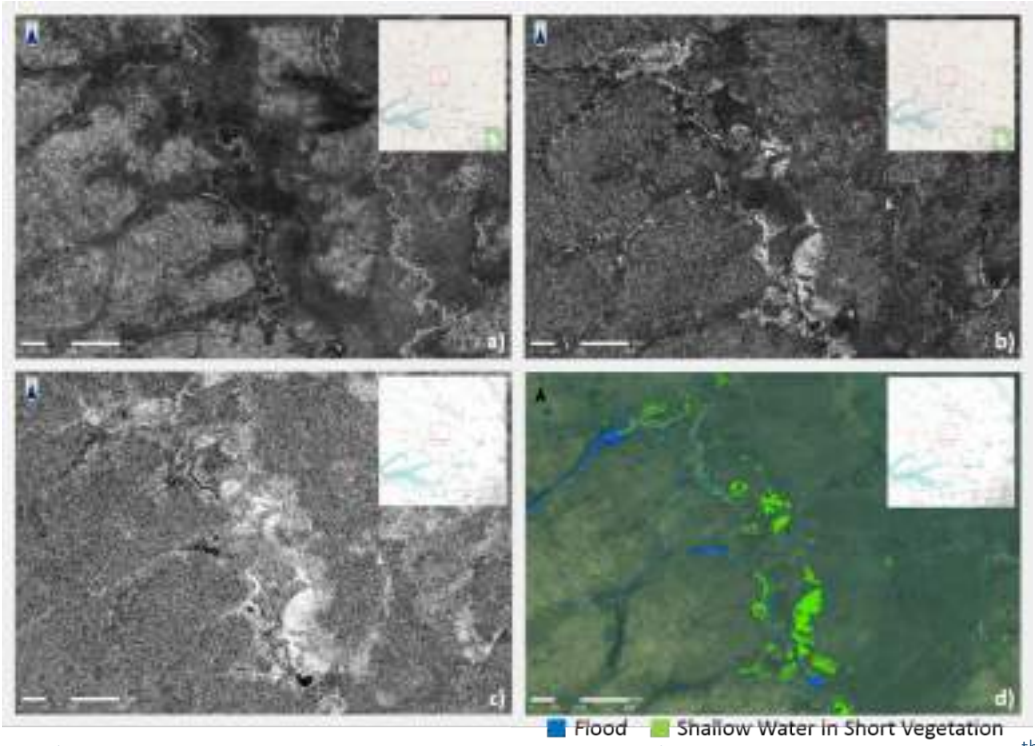

Figure 36 a) Minimum pixel values of the reference stack b) SAR image of November 19th, 2015 c) NDFVI d) resulting flood map

The mean σ_0 over flooded areas increased on average of about 2.5 dB, to an average value of -5 dB. Moreover, the information that came from the field from the Red Cross indicated that the majority of the reported flood was exactly of this kind Figure 37.

Figure 37 Images shot by the Red Cross in Kapelebyong area right after the triggering of the alert (November 13th 2015) showing the kind of flooding that hit the area. https://www.flickr.com/photos/climatecentre/albums/72157660532090507/with/23066963062/

Additional filtering steps are performed in cases where SAR images are noisy or acquired with different geometry in order to reduce false alarms.

The methodology is non-user dependent, it can be easily automated and potentially it can be applied also by non SAR experts. It showed great robustness since the same workflow has been applied to different floods in different environment and using different SAR data (different sensors, polarization and resolution) giving very detailed flood maps, which show good agreement with products produced by third parties. Moreover, shallow water in short vegetation is derived, a product usually non reported by emergency management services. It is suitable for rapid mapping even though there could be a big amount of data to be processed, such as in the case of Uganda. The advent of new cloud computing capability, such as the one offered by GEE, allow a fast analysis and export of the results and allow users with low capacity to perform high quality flood mapping. In fact, in GEE all the S1 catalog is easily accessible online without the need of downloading the original product locally. All the analysis can be performed online and only the final result has to be downloaded.

The methodology presents a new promising approach for flood mapping. Time-series analysis showed great potential also in the case of optical images as briefly showed in paragraph 3.6.1, a methodology that can be further explored.

Nevertheless, there are still some limitation. The use of old SAR data, which usually are sparse and acquired with different geometry, showed to be more complicated and required more filtering steps even though we obtained very good result. In urban areas we could not obtain good results. The resolution of S1 did not allow for detecting changes using only radar intensity and at the moment of this analysis no Single Look Complex data were available on the areas considered in this paper and it remains a possibility for further improvement. CSK could have the potential for showing changes in urban areas but for the flood analyzed in this work the dataset did not allow the detection of floods because the images were acquired with different geometry and therefore the different radar shadow over urban areas did not allow the detection of water.

4. Flood depth estimation by means of high-resolution SAR images and LiDAR data

This chapter presents a methodology for flood depth estimation by means of a high-resolution LiDAR Digital Elevation Model starting from the flood maps derived in the previous chapter. After a literature review, where other approaches to flood depth estimation are presented, it is explained how the elevation of the water plane can be estimated by means of a statistical analysis of the elevation values along the contours of the flooded areas. The methodology has been applied only to the case study of Veneto 2010 because no high-resolution DEM was available for Malawi. The chapter has the objective to answer ***research question 2****: "Can flood depth estimation be improved and suitable for rapid assessment of impacts?"*

This chapter have been submitted to the Journal "Natural Hazard and Earth System Sciences". The paper, as well as the chapter, has been written autonomously by the author. The co-authors of the paper are Dr. Mattia Marconcini of the German Aerospace Centre, Germany, who supervised the whole research and Prof. Carlo Giupponi of the Ca' Foscari University of Venice, who revised the results.

4.1 Flood depth by means of remote sensing for assessing impacts

In order to assess impacts caused by floods, besides flood extent, several parameters need to be monitored, such as flow velocity, debris factor and inundation depth. Depth is particularly important since it governs the damage functions (or vulnerability curves or loss functions), which define the expected damage given a certain flood depth (Mojtahed, 2013; Scorzini, 2015). Therefore, in ex-post assessment deriving flood depth is essential for quantifying impacts and damages and to better characterize flood risk and implement disaster risk reduction measures. It is also important in support to emergency response, to assess accessibility and design a correct plan of intervention, to calculate water volumes and allocate resources for water pumping, to estimate rapidly the costs for intervention and reconstruction.

Remote sensing, and in particular Synthetic Aperture Radar (SAR) data, have been playing a big role in flood monitoring since decades allowing the derivation of flood extent maps during crisis events. Chapter 3, in addition to showing the most popular methodologies of flood mapping, presented a novel approach for mapping floods by means of big EO data. Chapter 4 builds upon the results there presented and shows how flood depth can be derived.

Once the flood extent is available, flood depth can be assessed if a digital elevation model (DEM) is available. Different free global DEMs are available globally. The Shuttle Radar Topography Mission (SRTM) provided in early 2000s the first free global DEM with a resolution of 3" (approximately 90 m) with an absolute height error from 5.6 to 9 m in all continents at 90% confidence level (Farr et al., 2007). Advanced Spaceborne Thermal Emission and Reflection Radiometer (ASTER) Global DEM is another freely accessible dataset at 30 m spatial resolution with an accuracy of 17 m at the 95% confidence level (Tachikawa et al., 2011). A more recent dataset is the TanDEM-X developed by the German Aerospace Centre (DLR) with a spatial resolution of 12 m, vertical accuracy of 2 m and a cost of 100€ per quota, i.e. 7700 Km^2 (Eineder et al., 2012; Schumann et al., 2014). This kind of products are more suitable for regional studies. Local datasets instead can reach much higher resolutions at the cost of much smaller coverage and higher costs. In particular, DEM derived from Light Detection and Ranging (LiDAR) instrument are frequent for many locations. In the case of the Italy, as presented in this chapter, LiDAR DEM is available at 1 m spatial resolution free of costs for non-private purposes[1]. The higher the resolution of a DEM is, the more detailed information about the flood depth can be derived.

Several approaches have been followed in the past, as far as the 80s, for deriving flood depth using flood maps and DEM . Gupta & Banerji (1985) used Landsat Multispectral Scanning System (MSS) to derive the water volume of a dam reservoir in the Himalayas. Water level has been estimated superimposing the contour of the water surface to the topography. Ten years later, Oberstadler et al. (1996) used ERS-1 data to derive flood extent and superimposed the flood map plotted in transparencies to a map with topographic contours. Water stages were registered manually at 500 m steps. Mason et al. (2001) derived the inter-tidal shoreline using several ERS SAR data and heighted them using a hydrodynamic model based on depth-averaged hydrodynamics including the effects of tides and meteorological forcing. Matgen et al. (2007) used ENVISAT-ASAR at 12.5 m resolution and a Light Detection And Ranging (LiDAR) DEM at 2 m to assess water depth for the flood of the Alzette river in Luxembourg in 2003. Flood edges derived from ASAR were intersected with LiDAR data to estimate elevation at the contour. The water surface was computed using two different interpolation modelling: Triangulated

[1] http://www.pcn.minambiente.it/GN/

Irregular Network (TIN) generation and multiple linear regression. Subtracting the DEM to the water elevation, the depth was calculated. This work was improved by Schumann et al. (2007) where the authors computed the water elevation combining the regression model with the TIN generation. The same methodology was used in Schumann et al. (2008) to compare results using different elevation data: LiDAR, topographic contours and Shuttle Radar Topographic Mission (SRTM) DEM. The study showed the best performance of the high-resolution LiDAR data (2 m) but also an acceptable result with SRTM. Zwenzner & Voigt (2008) proposed a similar methodology also based on a model to fit the left and right bank elevation derived from SAR based water map and DEM intersection. A sequence of densely spaced river cross sections is shifted and adjusted individually in order to obtain the correct water level.

These methodologies assume that water level must be the same at the left and at the right of the river cross section, indirectly assuming that the riverbanks are perfectly symmetric and that the river flow dynamics and the dynamics in the flood plain is not conditioning the overflow and the following stream. If on the one hand this assumption takes into consideration the slope of the river and define an equilibrium condition at the ends of the cross-sections, on the other hand it may not fit many types of floods caused by riverbanks ruptures, asymmetric river banks and complex dynamics of the inundation.

More recently, Huang et al. (2014) derived flood depth using Landsat and LiDAR data. The assumption in this case is that if the flooded area is small enough, the water plane can be considered flat. Therefore, they divided the flood extent derived from Landsat data in zones with size 750 x 750 m. For each of these, they "filled" the correspondent DEM up to the level that gave the same flood extent (measured using a Kappa coefficient). Certain zones can be completely covered by water and this method cannot be applied. In order to assign them a water level, the average of the height neighbours is taken. Finally, a water surface is computed using an interpolation method (Kriging) and the depth computed from the difference with the DEM of the same area. A similar approach was followed by Brown et al. (2016). In this case, a flood extent map was derived from SAR using a semi-automated method (thresholding and manual interpretation and correction) and elevation along the flood edges was measured from a LiDAR at 100 m intervals. Elevation points were inspected and in certain cases corrected or added by an operator in order to improve the water surface elevation estimation. The water surface was then created using TIN interpolation.

Instead, Iervolino et al. (2015) describes a SAR backscattering model in case of flood in contrast to a pre-event one and from its inversion, they derive the flood depth. Two methodologies are proposed: Single Image Object Aware *"allowing the evaluation of the water level in the proximity of a selected local building target if the a priori knowledge of the target ground truth and two gauges in its premises is given (Object Aware)"* and Two Images Areas Aware, which "*relies on a couple of images pre- and during/post- event, and permits to retrieve the flood level at a global scale all over the image if an unflooded area in the during/post-event image is available to perform the calibration (Area Aware)".* Even though an interesting and promising approach, the two methods look complex and not applicable by non-experts. Furthermore, ancillary data of difficult retrieval are needed, such as data from gauge stations and information about building affected by the flood.

As already mentioned, flood depth is important not only for emergency response, but also for impact assessment. Purely economic works use flood depth for assessing direct and indirect impacts of floods by mean of depth-damage functions. Depth is usually retrieved from third sources. In certain cases, such as in (Carrera et al., 2013), flood depth information was not available and therefore all possible flood depth values were taken into account in using depth-

damage functions for computing economic impacts. The uncertainty, already intrinsic in the methodology used, was amplified by the lack of depth information, resulting in a huge range of possible damage, roughly 4 billion € in case of minimum flood (1 m) to roughly 10 billion € for the most devastating scenario (6 m). Even though the work considered a quite vast event (1182 Km^2) spreading all over northern Italy, it could have been improved if flood depth was available. In a similar work, Amadio et al. (2016) estimated detailed losses caused by the 2014 flood in Emilia Romagna, Italy. They made use of a simulated max flood depth computed by D'Alpaos et al. (2014) by means of hydraulic models. In this case, depth values allowed a precise impact assessment, but the capacity needed is higher (such as the amount of information for running the model and the time needed) and the uncertainty introduced by the model has to be taken into account, since it may over- or under-estimate the extent and therefore the consequent depth.

The methodologies based on satellite data and the one proposed in this chapter instead, can assist economic impact assessment methods for a rapid estimation of losses (and precise in case of high-resolution elevation data available) as well as the development of emergency plans.

4.2 Flood depth estimation

The methodology is made of three main steps as explained in Figure 38: a) flood map extraction, b) estimation of the elevation of the water surface and c) flood depth calculation.

Flood maps are obtained using a methodology developed by the authors (Cian et al., submitted) based on the multi-temporal statistical analysis of two stacks of images: one containing only reference images and another one containing also images of the event. The mean value of each pixel throughout the reference stack is computed together with the minimum value of each pixel throughout the "flooded" stack. The two statistics are used to derive the Normalized Difference Flood Index (NDFI), which is the normalized difference between the mean (reference) and the minimum (flood) value. The index highlights flooded area and allow to easily separate flooded pixels by non-flooded ones by means of a constant threshold. Additional slope and morphological filtering is used in order to clean the map from spurious flooded areas and false alarms.

Similarly to Huang et al. (2014) and Brown et al. (2016), we supposed that the water surface of the flooded areas is flat. This can be considered a fair assumption in those cases where the slope of the affected area is gentle and the velocity of the stream is modest. More precisely, we do not assume a single constant elevation for each flooded area, but a constant water elevation inside each flooded polygon. Therefore, we do take into consideration the usual decrease of elevation along a river. Under this assumption, if the flood extent map was perfect, along the contour of flooded areas we should read a (quasi) constant value of elevation from the DEM, which would be the elevation of the water surface. In practice, this is not happening because of different sources of errors. On the one hand, there are imperfections in the SAR maps, where the nature of SAR images (speckle, radar shadow, layover…) can lead to false alarms or omission errors and where vegetation or man-made objects can cover or interfere with the flooded area leading to other omission/commission errors. On the other hand, we can have errors in the digital elevation model and misalignment between the SAR data and the DEM. Therefore, if we want to estimate the right elevation of each water surface, on the one hand we should look for the maximum elevation along the contours in order to compensate for omission errors (e.g. flood covered by vegetation), on the other hand we should get rid of outliers, such as high elevation values resulting from SAR and DEM misalignment.

To do that, from the polygons representing the flooded areas, elevation values are extracted along their contours from a high-resolution DEM by means of a script written in Python, which take advantage of the *arcpy* library. For each contour, percentiles are computed and values below the 30th and above the 90th percentile are removed. In fact, we assumed that the values on the tails of the distribution are outliers. For the remaining percentiles in each polygon, the derivative is computed and a condition is applied from the highest percentile toward the lowest. We check if the difference between the nth percentile and the (n-2)th is lower or equal to 10 cm. If the condition is not satisfied, the nth percentile is dropped and the next difference is computed ((n-2)th - (n-4) th, ((n-4)th - (n-6) th,…). Once the condition is satisfied, the estimated water elevation will be the one corresponding to the second to highest percentile satisfying the condition. The adaptive threshold takes care of the different condition of each single polygon and is able to decrease the error compared to the fixed threshold set on the 90th percentile.

Once water surface is computed, we can easily calculate flood depth by subtracting to it the actual terrain elevation value. In few cases, where the geometry of the polygon or the elevation of the area is complex, the estimation of water surface can be wrong. This is easily detectable by looking at the flood depth values. If a polygon contains too many negative values, this indicates that we underestimated the water elevation. If it contains depth values much different from its neighbours or very high value of depth, it indicates that we overestimate the water elevation. Therefore, we select the polygons showing unexpected behaviours and we compare them with a DEM filled with the same water elevation. If the extent does not match, we manually look for the elevation value that best approximated the flood extent and set it as the water elevation. Then we compute again the flood depth and reiterate the steps until we have a satisfying result.

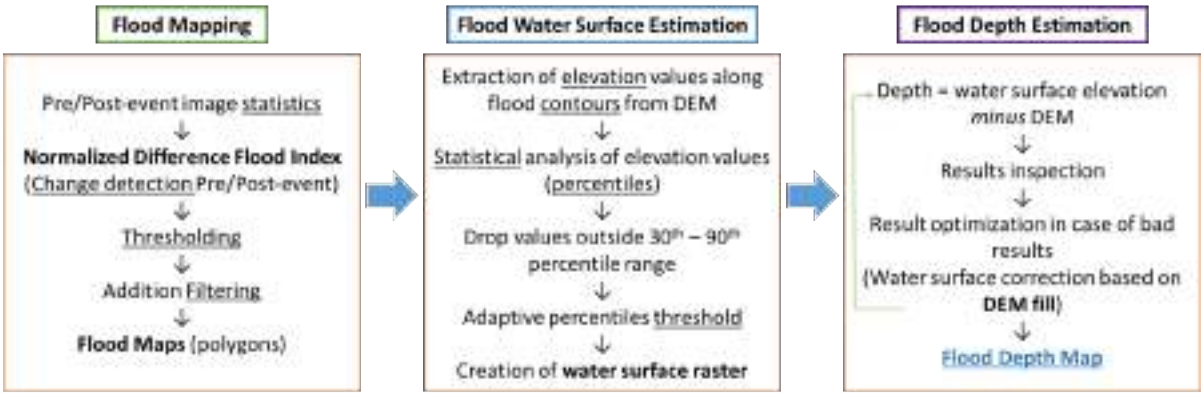

Figure 38 Flood Depth Estimation Methodology

4.3 Case Study: Veneto 2010

The methodology has been applied to the flood occurred in Veneto in November 2010 presented in Chapter 2. Three main flooded areas are considered as shown in Figure 2 in Chapter 2: Vicenza and its surrounding (A), Bovolenta area at the south of Padua (B) and Saletto area at the south of Colli Euganei (C). The area of Veggiano indicated as A1, together with area B, is the area where a hydraulic simulation was available allowing a comparison of results.

4.4 Data Used

Flood maps were derived using COSMO-SkyMED data provided by the Italian Space Agency and following the methodology proposed in Chapter 3. Table 10 shows the complete SAR dataset used. In addition to the SAR data, different DEMs have been used for deriving flood depth. Table 11 shows the dataset. The LiDAR from the Venice River Basin Authority at 2 m resolution have been used for the Vicenza area of interest, the LiDAR from the ministry of Environment at 1 m for the other two areas of study. The DTM at 5 m from the Veneto Region geodatabase was used for the whole area of interest.

In order to validate the results, in absence of proper ground truth, we made use of different datasets that allowed us a qualitative assessment of our maps:

- A simulation of the event by means of a hydrological model were flood depth was obtain as described by (Viero et al., 2013) where flooding extents were estimated using the 2DEF finite elements model (Viero et al., 2014). The flood depth maps were calculated for November 3rd and 4th at the same time of the SAR acquisition
- A set of aerial photographs acquired on November 1st taken by the Firemen Department of Vicenza covering mainly the Vicenza area of interest
- A set of field photographs taken from the Civil Protection of Saletto on November 1st and 2nd covering the area of Saletto.

Table 10 List of SAR data used for deriving flood maps of the event

Sensor	Orbit (Pol)	Date	Incidence Angle	Status	Acquisition Time (UTC)
COSMO-SkyMed	Descending	31/10/2008	27.7-30.8	Reference	17:35
Stripmap 3 m	(HH)	28/04/2010	28.9-31.8	Reference	17:30
(X)		03/11/2010	37.4-40.1	Flood	17:22
		04/11/2010	40.1-42.6	Flood	18:10
		06/11/2010	27.7-30.9	Flood	17:28
	Ascending	29/08/2010	31.1-34.2	Reference	5:01
	(HH)	01/11/2010	31.1-34.2	Flood	5:01
		07/11/2010	47.0-49.2	Flood	5:13

Table 11 List of DEMs used for deriving flood depth

Dataset (Provider)	Resolution (m)	Date of production	Vertical Accuracy
DTM – LiDAR (The Ministry of the Environment and Protection of Land and Sea of Italy)	1 m	2012	20 cm (1σ) 25 cm (2σ)
DTM – LiDAR (Venice River Basin Authority)	2 m	2004	/
DTM (Veneto Region Geoportal)	5 m		/

4.5 Results

The methodology is based on the statistical analysis of elevation values along the contours of the flooded polygons. Figure 39 shows the percentile values of elevation for all the polygons in the Vicenza area of interest on November 3rd. The central part of the profiles (from 30th to 90th percentile) is reasonably flat, on the contrary of their upper and lower part. The upper part is generally steep and it reaches rapidly a plateau below the 90th percentile. The threshold on the 90th percentile cuts out most of the upper outliers. The lower part of the profiles (below the 30th percentile) is more diverse, in most of the cases it is flat but some profiles show a steep increment of elevation or a step-like behaviour. The threshold on the 30th percentile allow to get rid of most of these variations. The adaptive threshold allows setting the water elevation on the correct segment of the profile: it prevents to overestimate water elevation since it gets rid of upper outliers and it prevents to underestimate it posing a limit on the lower percentile and setting a threshold on the slope of the profile. Some irregular profiles can be seen in the plot and for them, the methodology proposed does not always work because of the complex geometry of the polygons or the complex terrain elevation underneath. In those few cases, the elevation increases without showing a predominant value and the resulting maximum elevation does not always represent the correct water elevation. For those few cases, it is necessary to intervene manually as it is not possible to guess the right elevation simply looking at the statistics.

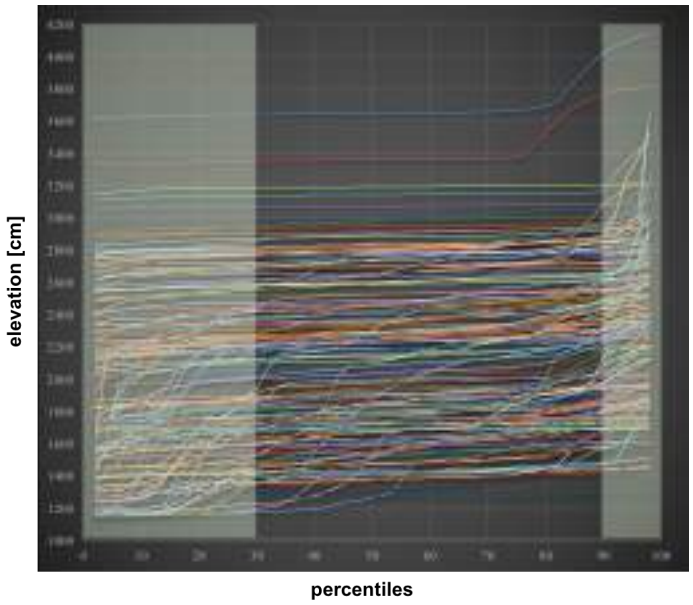

Figure 39 Elevation percentiles for each flood polygon in the Vicenza area on November 3rd. The 90th percentile and the 30th percentile thresholds are highlighted.

Flood maps were restricted to the area covered by LiDAR data and therefore flood depth is reported only limited to this area. LiDAR data covered the whole flood area except for some parts of the flood in the Vicenza area of interest as indicated in Figure 44. Figure 40 shows the results for the Vicenza area of interest. From the images it is possible to appreciate the dynamics of the event, i.e. the receding of water from the 3rd to the 6th of November, where

extent and depth decline gradually. In this case, the flooded area extends for several kilometers along the Bacchiglione river where the terrain elevation decreases gradually from the north-west to the south-east. Since we estimate water elevation for each single polygon, we are able to take into consideration also the slope of the river as shown in the same figure on the top left box. For a flood like this, the hypothesis of a flat water surface inside a single polygon is a good approximation since the flood evolution is slow and therefore water surface can be considered flat. This is especially true in case of the Bovolenta and Saletto area of interest. Figure 41 shows the flood depth for the Bovolenta area of interest on November 4th and 6th. The top right box shows a zoom of the results where the high level of detail can be appreciated. Figure 42 shows the results for the Saletto area on November 3rd, 4th, 6th and 7th. Also in these cases, we can appreciate the receding of the flood and the consequent decreasing of flood depth.

4.6 Discussions

4.6.1 Comparing results: hydrological simulation

Flood depth obtained with the presented methodology has been compared with the one derived by means of a hydrological model provided by (Viero et al., 2013). The simulation was available for the area of Veggiano and Bovolenta on November 3rd and 4th at the same time of the SAR acquisitions over the same areas. Figure 43 in the first and second column, shows the water elevation simulated and the correspondent water depth. The third column shows the difference between the flood depth derived with our methodology and the simulated ones. The fourth column shows the difference between the water levels obtained with our methodology and the simulated ones. Some differences can be seen between the two series of results. The light yellow areas in the difference images indicates that the results are comparable since the $\pm$ 15 cm can be considered a tolerable variance. Water level estimation is very similar between the two methodologies as we can see in the fourth column of Figure 43. In the areas were we notice a bigger difference between the two products, it is clear that our methodology is underestimating the water level. The reason for this is the difference in water extent between the simulation and the SAR based flood maps as highlighted in Figure 44. The model overestimates the extent of the flood leading to a higher water elevation. The third column of Figure 43 shows the difference in water depth. Given the difference in water elevation, we expected a similar difference in water depth. Instead, in certain areas (for example in Bovolenta, bottom right of water depth difference) even if our methodology underestimated the water level, flood depth results to be overestimated. Overall, the two results show good agreement even if the differences in flood depth are greater compared to the difference on water levels. This behaviour indicates that the main source of discrepancies must be the DEM. Table 12 confirms the analysis showing the Root Mean Square Error (RMSE) and the maximum error between the two products. The RMSE on flood depth is 74 cm for November 4th in Bovolenta, 80 and 83 respectively for the November 3rd and 4th for the Veggiano area. The maximum error is 992 cm in Veggiano on November 3rd. If we compare the water elevation instead of the flood depth, the difference between the two methodology is much smaller: the RMSE for Bovolenta on November 4th is only 22 cm, 47 and 69 respectively for Veggiano area on November 3rd and 4th. The maximum error is 475 cm in Veggiano on November 4th.

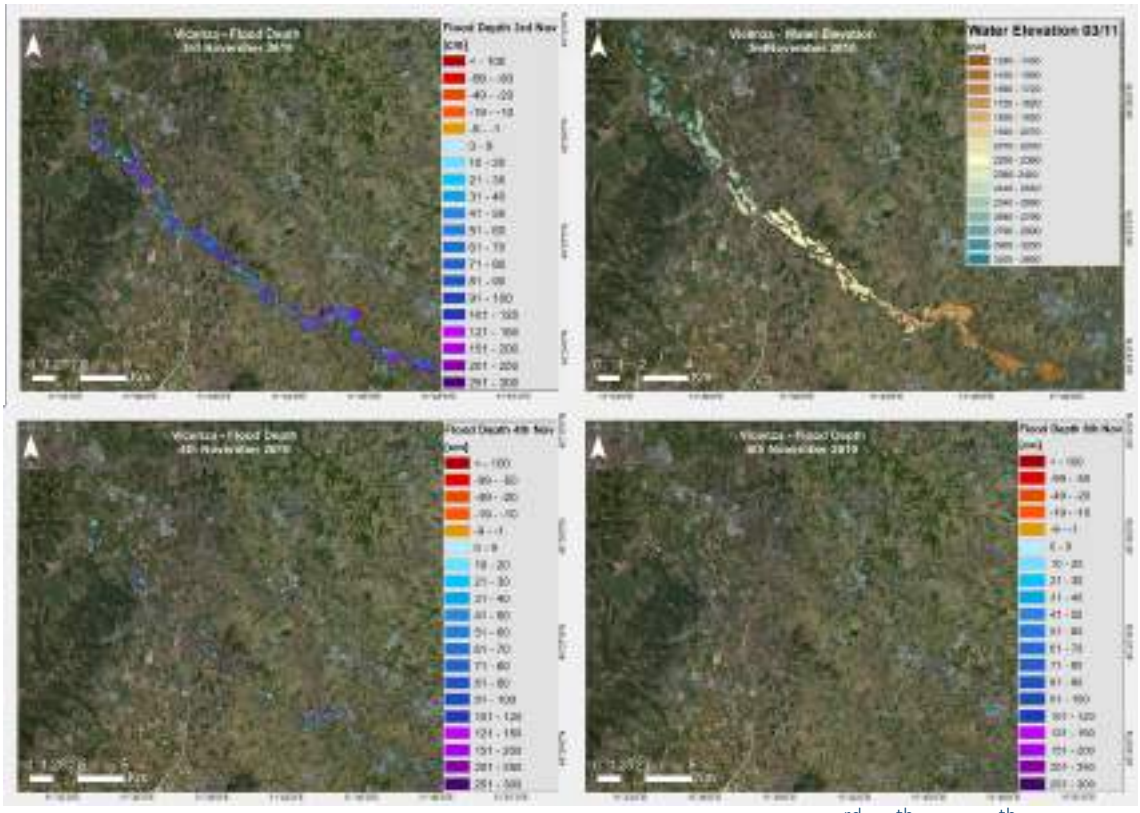

Figure 40 Flood Depth for Vicenza area of interest on November 3rd, 4th and 6th. Red values indicate error in the estimation of the water surface elevation. The top left image shows the water level derived for November 3rd.

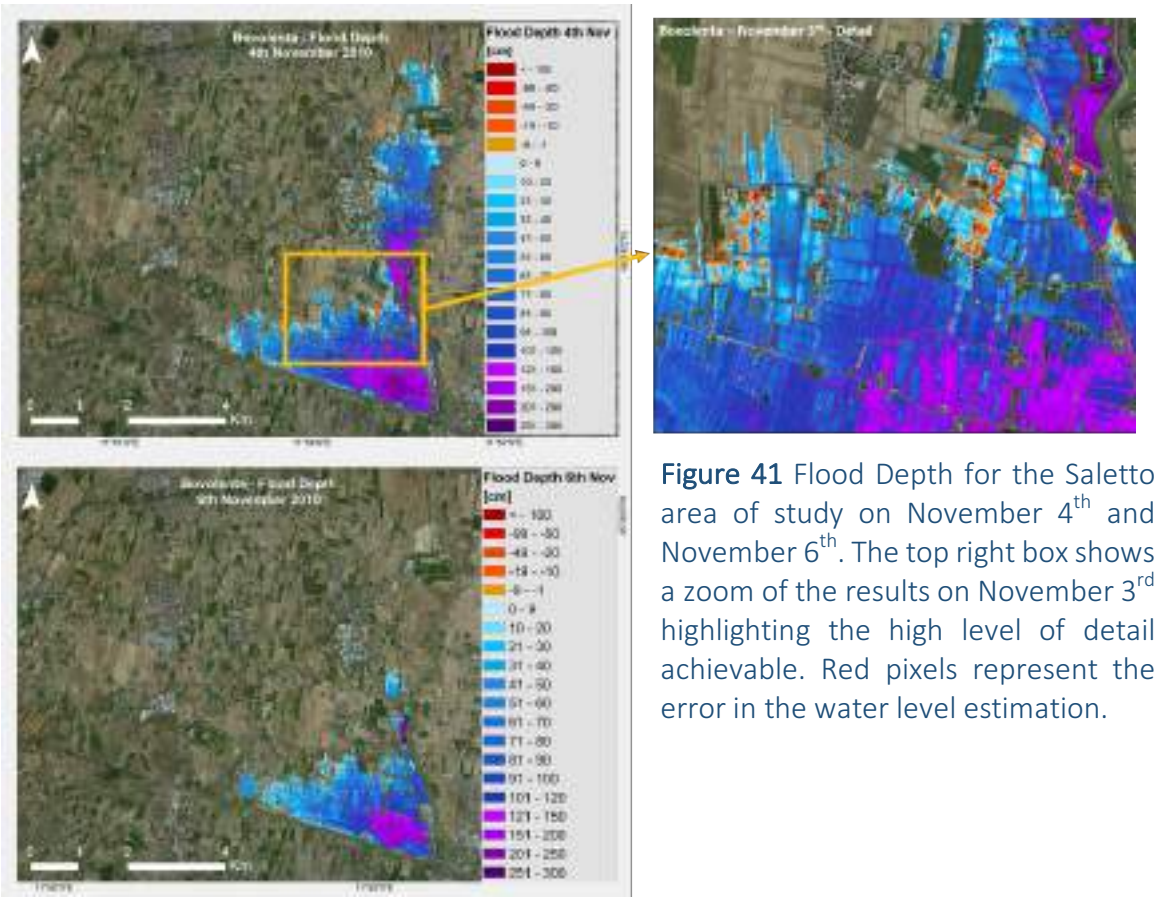

Figure 41 Flood Depth for the Saletto area of study on November 4th and November 6th. The top right box shows a zoom of the results on November 3rd highlighting the high level of detail achievable. Red pixels represent the error in the water level estimation.

Summarizing, the main sources of errors are two: 1) the extent of the flood simulated by the model, which is different from the observed one as we can see in Figure 44 for the Veggiano area on November 3rd, and 2) the difference in the elevation values between the DTM used by the model (the regional DTM at 5 m) and the one used in our methodology (LiDAR at 1 and 2 m).

Table 13 shows the extent comparison between our flood maps and the simulated ones. The assessment has been carried out on the whole area of interest of Veggiano and Bovolenta. Despite a decent overall accuracy for all the maps, the accuracy on flood is quite low. Even if we know that SAR based flood maps are not perfect, they represent with good confidence the ground truth. The model overestimated the flood extent and therefore introduces errors in the computation of water levels and flood depth. In the case of Bovolenta, the overestimation is of 35 Km^2 (69.3 Km^2 against 34.3 Km^2), which introduces the difference in water level estimation.

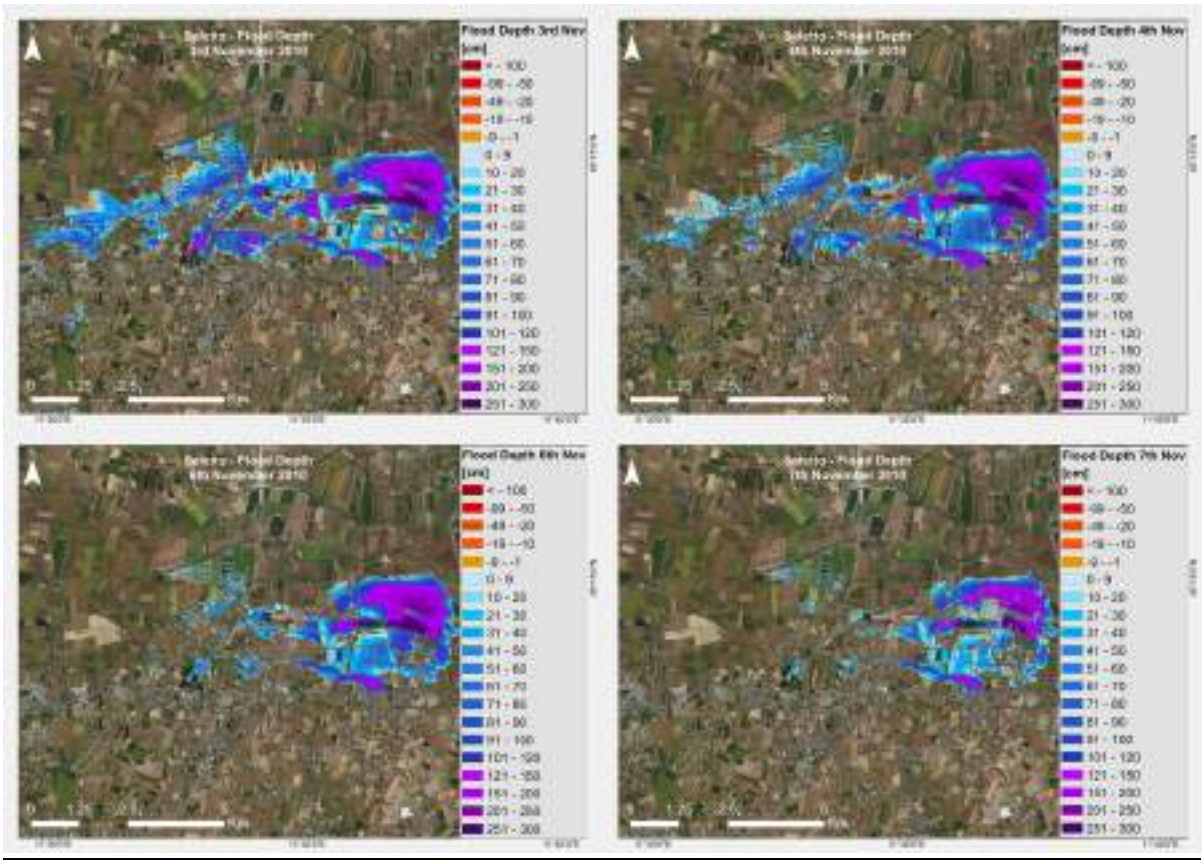

Figure 42 Flood Depth for the Saletto area of interest on November 3rd, 4th, 6th 7th

Table 12 Comparison between water elevation and flood depth obtained with the hydrological model and the proposed methodology

Bovolenta (LiDAR 1m)	RMSE [cm]	Max Error [cm]
4 Nov – Depth	74	370
4 Nov – Water Elevation	22	268
Veggiano (LiDAR 2m)		
3 Nov - Depth	80	992
3 Nov – Water Elevation	47	294
4 Nov - Depth	83	475
4 Nov – Water Elevation	69	174

Table 13 Flood extent assessment: extents comparison between SAR based map and simulated flood. Flood extent accuracy has been calculated as the ration between the agreement in flood extent and the total simulated extent

	Overall Accuracy [%]	Flood Extent Accuracy [%]	Flooded Area Model [Km^2]	Flooded Area SAR based [Km^2]
3 Nov - Veggiano	78	64	6.81	5.86
4 Nov – Veggiano	82.5	57	4.87	3.82
4 Nov - Bovolenta	89.5	45	69.3	34.3

Figure 45 shows the comparison of flood extent obtained from the hydrological simulation (left) with the SAR-based flood map on the same day (right), where the estimated water elevation is shown. Comparing the two products, the simulation is overestimating the extent. The image in the middle of Figure 45 is the LiDAR DEM classified with the same values of the estimated water elevation, where the outline of the SAR-based flood map is overlaid. We can notice the almost perfect correspondence between this map and the SAR-based map: the thresholds on elevation create areas with similar extent as the SAR observation. This confirm that the hydrological model is overestimating the flood.

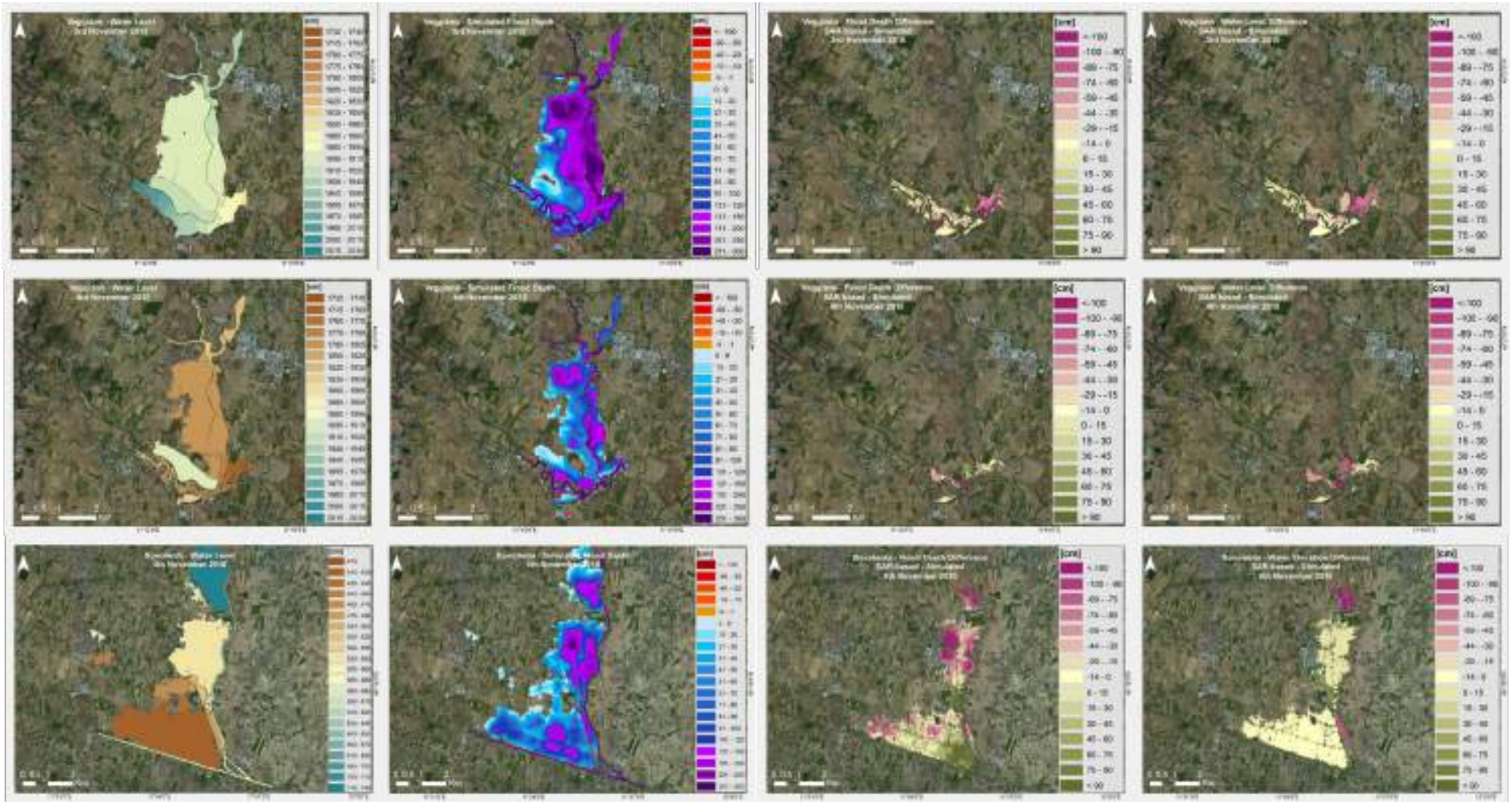

Figure 43 Hydrological model simulation for Veggiano area on November 3rd and 4th and for Bovolenta on November 4th . The first column show the simulated water level, the second column the simulated flood depth, the third column the difference between the SAR based flood depth and the simulated one, the fourth column the difference between the SAR based water elevation and the simulated one.

4.6.2 Comparing results: LiDAR and DTM

Flood depth was computed using the LiDAR DEM (at 1 m resolution for the Bovolenta and Saletto area, and at 2 m resolution for the Vicenza area) and using the regional DTM at 5 m resolution as a comparison. Even though the regional DTM has a good resolution, we noticed big differences between the two products. In fact, in certain points the elevation difference between the two dataset were exceeding 10 m. The quality of the regional DTM does not seem to be comparable with LiDAR products. This is of course affecting the results obtained using the DTM, which are less precise. Figure 46 shows the improvement obtained by using the LiDAR compared to the DTM. Not only the horizontal resolution can be improved, but especially the vertical resolution and therefore the flood depth. Many differences can be noticed in the two products, which highlights the importance of a good DTM in depth estimation.

Table 14 shows the comparison between the flood depth obtained using LiDAR datasets and the DTM at 5 m resolution. For Vicenza area the RMSE exceeds 1 m on November 3rd and 4th and just below this threshold on November 6th. In the case of Bovolenta and Saletto RMSE is lower (from 0.82 in Bovolenta on the 4th of November to 0.54 in Saletto for the 7th of November) but still exceeding half a meter. The analysis shows that the bigger the extent of the flood, the bigger the difference between the two results. This is also confirmed by the comparison of the different DTMs. They have been compared on the area covered by the hydrological model, Veggiano and Bovolenta.

Table 15 shows the RMSE and the maximum difference between the different datasets. The RMSE is 130 cm for the Veggiano area with a maximum error of 460 cm, for the Bovolenta area the RMSE is 136 cm with a maximum error of 1365 cm. The difference between the different DTMs is big and explains the difference in flood depth using the different DTMs. As mentioned in the previous paragraph, it explains also part of the discrepancies in the results obtained with our methodology and the hydrological simulation.

4.6.3 Adaptive Threshold

Adaptive threshold is useful for estimating the correct elevation of the water surface in those cases where flood polygons have a complex geometry, which can overlap complex elevation or can encompass vegetation, roads, built-up areas. Theoretically we expect the elevation along the contour of each polygon to be constant. As already mentioned, due to many sources of error, in practice the elevation would vary along the contour. A static threshold on the 90th percentile would cut out almost all the outliers allowing to estimate as a first guess, the correct elevation of the water surface. Unfortunately, a fixed threshold cannot work for all the flooded areas as well as the same percentile for different case study. Therefore, we made it adaptive in order to take into consideration each single case. Figure 47 shows the flood depth estimated with the fixed and with the adaptive threshold. It can be easily noticed how the adaptive threshold allows to improve the estimation of water depth (A). In the highlighted area, a fixed threshold on the 90th percentile would have estimated higher values of flood depth. Nevertheless, in few cases, the methodology still makes wrong estimation as shown in Figure 47 (B). In this case, too many negative flood depth values, indicates an underestimation of the water elevation, which was corrected manually as explained in the previous paragraphs. Nonetheless, despite some inaccuracies and some manual work needed, the use of the methodology with an adaptive threshold had improved the result over of the area of study.

Finally, the methodology can provide a rapid flood depth map useful for a rapid estimate of flood damages. In the future, the methodology may be further developed in order to automatize the manual steps needed to optimize the results. An integration with a DEM filling algorithm seems to be the right direction to take.

4.6.4 Validation with Aerial Photos

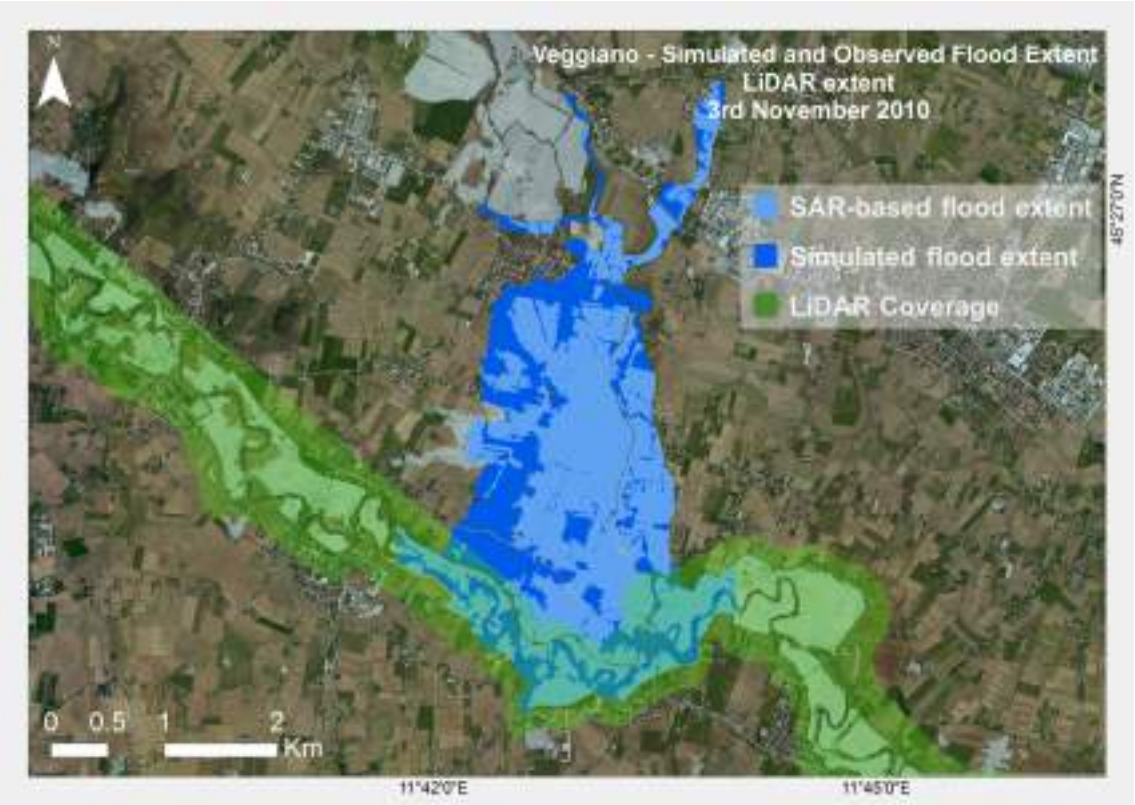

Figure 44 Comparison between SAR-based flood extent and simulated flood extent for the Veggiano area on November 3rd. In green, the coverage of the LiDAR DTM is highlighted.

Ground truth data consist of aerial pictures taken on November 1st, right after the beginning of the event, and of field pictures taken on November 2nd from civil protection. Unfortunately, they do not match the dates of satellite acquisitions.

Nevertheless, given the dynamic of the flood, they can be used to assess the results obtained with the methodology proposed. We compared this ground truth with the flood depth maps of November 3rd.

Figure 48 shows flood depth on November 3rd on the area of Ponti di Debba, south of the city of Vicenza (box 1). Aerial view of the area is from November 1st at 3:45 pm local time (box 2). In between the two dates, the flood in this area receded and in fact is what it can be observed comparing the extent in box 1 with the observation in box 2. The two red

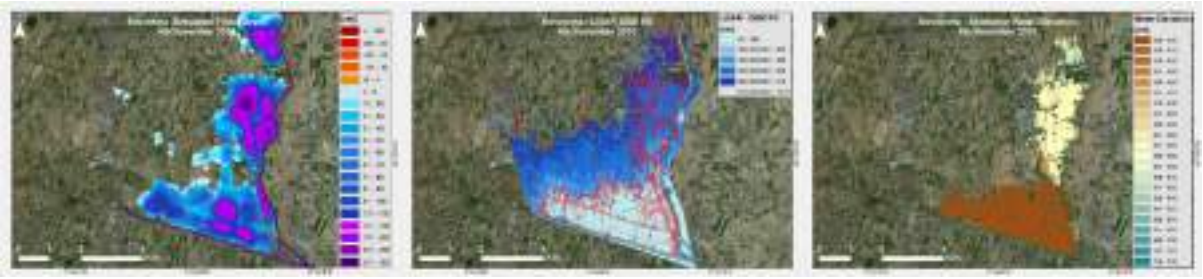

Figure 45 Flood extent comparison for Bovolenta area on November 4th: simulated flood (left), DEM filled extent (centre), SAR based flood map (right)

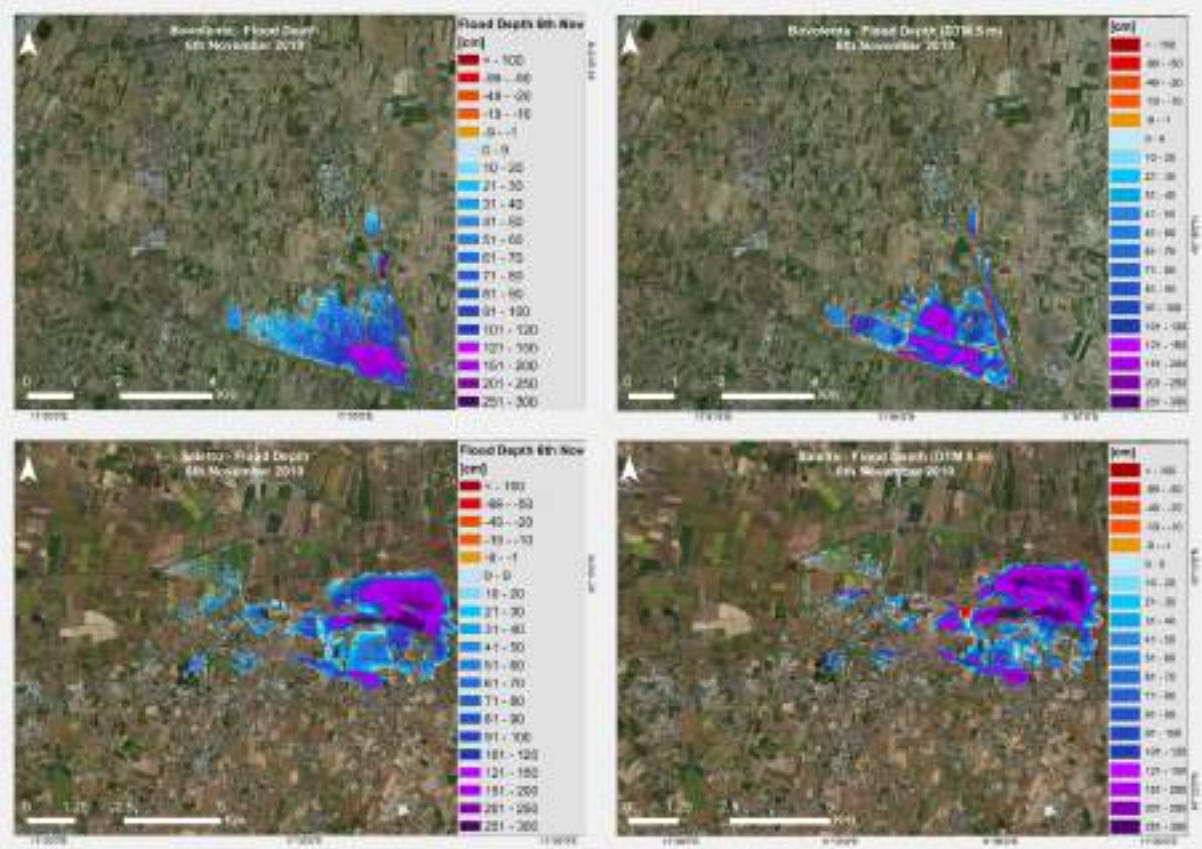

Figure 46 Flood depth estimation by means of LiDAR DTM at 1 m resolution (left) and by means of DTM at 5 m resolution (right) for the Bovolenta and Saletto area on November 6th

squares in box 1 highlight the correspondent street view in box 3 and 4, from where we can see the higher elevation of the road compared to the fields. Moreover, the presence of a white road running along the field boarders can be noticed, which also has higher elevation. Line 1 and its plot in fact, show flood depth around 0 cm (+ 4 to – 6 cm), very shallow water (in accordance to the SAR image that shows a water surface with higher values of backscattering) compared to line 2 where values are between 20 to 30 cm. This makes sense given the elevation of the area and corresponds to the observation, which shows roughly a flood 20 cm deeper in agreement with the dynamics of the event (noticeable comparing the aerial view to the street view). Line 3 shows the depth along the elevation dividing the two fields in the far end in the

image in box 2. Here the depth goes from 20 to 40 cm and it is in agreement with the observation. Line 4 instead is showing big negative values. This error could be due to an error of few pixels in the flood map (due maybe to radar shadow or presence of water on the top of the elevation) plus a possible small misalignment between the DEM and the SAR data.

Table 14 Comparison of flood depth obtained using LiDAR datasets and regional DTM for the areas of interest and for each date.

Bovolenta (LiDAR 1m)	**RMSE [cm]**	**Mean Error [cm]**	**Std [cm]**
4 November	82	14	80
6 November	67	0	67
Saletto (LiDAR 1m)			
3 November	67	30	60
4 November	64	16	62
6 November	57	9	57
7 November	54	-17	51
Vicenza (LiDAR 2m)			
3 November	108	26	105
4 November	106	23	104
6 November	91	-9	91

Table 15 Comparison of LiDAR datasets and regional DTM dataset (Veneto Regione at 5 m resolution) over the areas covered by the hydrological model.

	RMSE [cm]	**Max Error [cm]**
Bovolenta (LiDAR 1 m)	136	1365
Veggiano (LiDAR 2m)	130	460

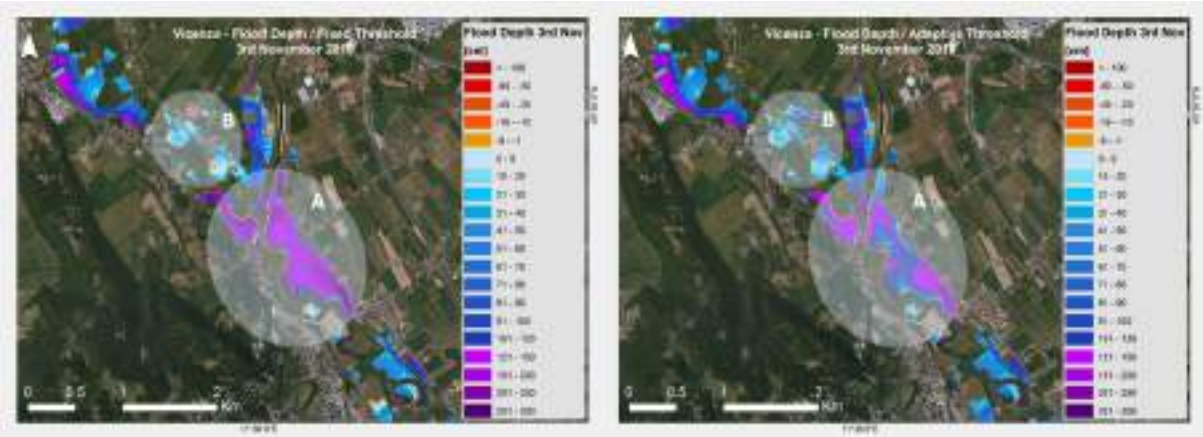

Figure 47 Flood Depth estimated using fixed (left) and adaptive (right) threshold

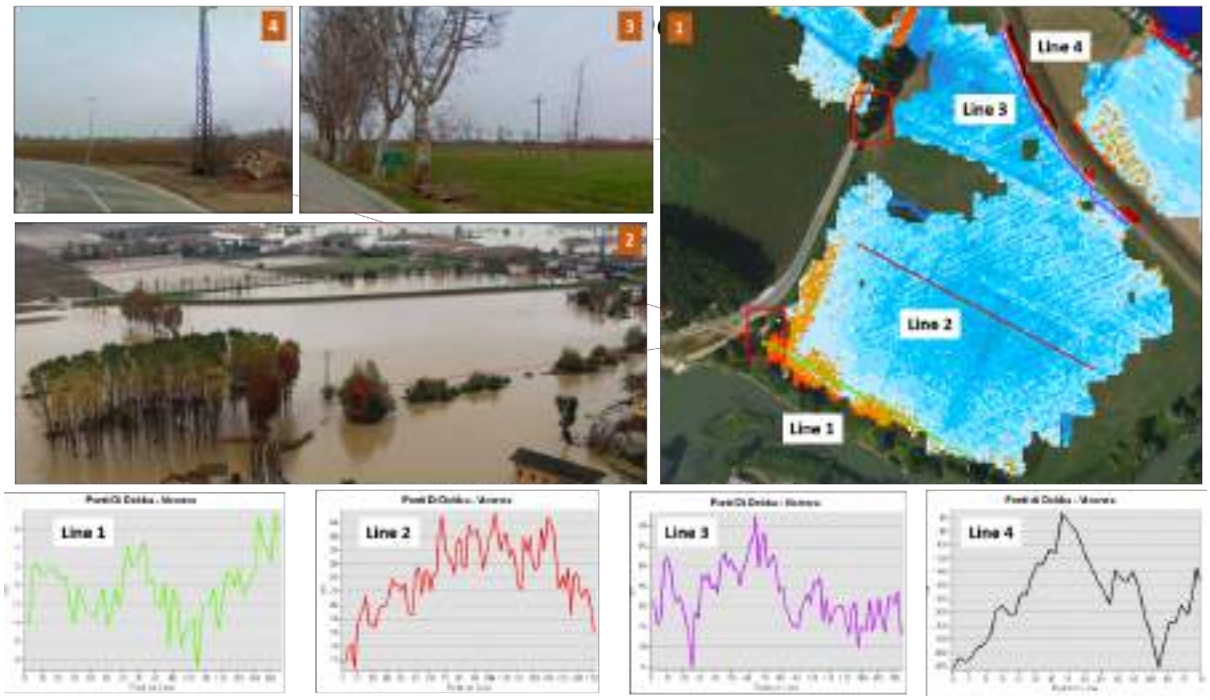

Figure 48 1) Flood Depth on November 3rd over Ponti di Debba in the Vicenza area of interest; 2) aerial view of the event on November 1st at 3:45 pm local time; 3-4) Google Street View of the area analysed; bottom plots: profiles along lines in box 1

Figure 49 shows a comparison between the flood depth map of November 3rd over Cabriani in the Saletto area of study (box 1), and several aerial images acquired during the event on November 1st 2010 at 4:30 pm local time (box 2, 3, 4, 6 and 7). We know that in Saletto area the flood expanded from November 1st to November 3rd. Nevertheless, this part of the Saletto area shows little change from November 2nd to November 3rd in the SAR based flood maps. Therefore, we can consider the aerial images as a good approximation of the flood on November 3rd. In box 1, two points are marked with A and B. On the flood depth map of November 3rd they show respectively depth 59 and 29 cm. On the small canal next to point B (on the left of the road in box 1), depth is between 109 and 130 cm. Comparing image in box 4 (the image acquired during the event on November 1st) with the one in box 5 (a Google Street

View image of the same location), we can see a very good correspondence with these values. Area D and C in box 1 are shown by aerial images in box 2 and 3. The plot named “Line 1” shows the values of depth along the same line in box 1, from left to right. It can be noted an average of 50 cm on the left side of the line and the average of 70 on the right one, reasonable values if compared with the image in box 3. Plot “Line 2” shows flood depth from the bottom to the top of the same line in box 1. It shows no more than 30 cm over the road at the top edge of line 2, confirmed by images in box 2 and 7, where we can observe how water cover only half of the car’s wheels. Box 6 shows the areas in the red rectangle in box 1. Once again, a good correspondence can be noticed between the aerial observations and the computed depth. Here we can also see the limitation of SAR based flood mapping, namely the difficulties in mapping correctly water over urban areas.

Figure 50 shows another part of the Cabriani area covered by the same data. Point A in box 1 does not show water as instead showed in box 3 by the aerial image. This is an error in the flood map due to the limitation of the flood mapping methodology. Point B shows 52 cm of flood depth on November 3rd. In box 5 and 6 we can see the aerial images from where we can estimate roughly 30 cm of water depth. Even though we know that the in the following days the flood expanded, comparing the extent from box 1 and 2, we can see very small differences. As previously said, we can consider the situation the same in the two dates. In this case, our methodology is overestimating the depth of roughly 20 cm.

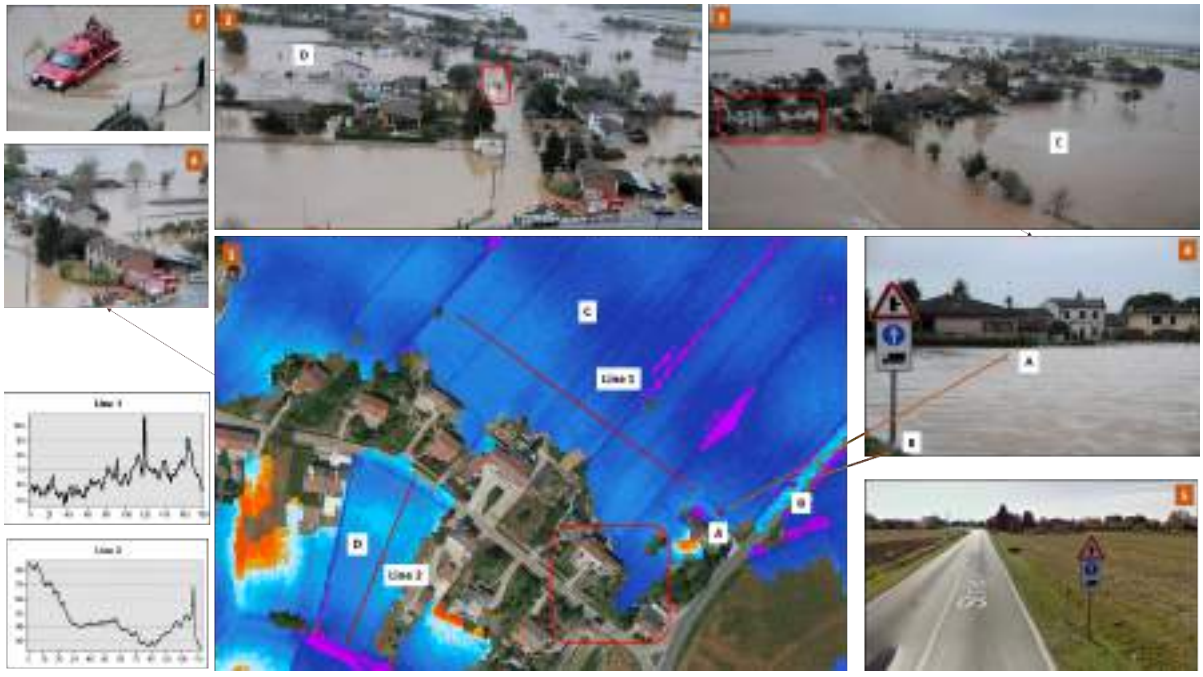

Figure 49 1) Flood Depth on November 3rd over Cabriani area in the Saletto area of interest; 2-3-4-6) Aerial views of the flood taken on November 1st at 16:30 local time; 5) Google Street View corresponding to image 4); 7) Detail of image 2); bottom left: flood depth profiles of line 1 and 2 shown in 1)

The two points marked as C show a depth of 5 cm on the road and 34 cm on the field, similar values of the one that can be estimated in box 2, 5 and 6. The plot on the top right of the image is showing the depth profile along Line 1 in box 1, from to top to bottom. The negative values are indication that there is a little underestimation of few centimetres (max 9 cm) or small errors in the flood map. In fact, from box 2, at the top and right hand side of the orange building in the lower right corner of the image, we can notice that small parts of the terrain are not covered by water. Nevertheless, this indicates that water is shallow in that field as our results are showing, an average of 20 cm of water depth.

Figure 51 shows the flood depth on November 3rd in Via Isole, in the Saletto area of interest, not far from the previous area analysed. The same consideration about the flood dynamics can be done. The situation on the day of the SAR acquisition is more likely to be the one in box 3, taken on November 1st at 4:30 pm, 40 minutes later than the one in box 2. In box 2 in the blue circle, we can note a man standing in the middle of the street. From that, we can estimate roughly 50 cm of water depth. Few hours later the water level increased as we can see in box 3. Comparing box 4 (street view) to 2 and 3, we can estimate an increase of 10 to 20 cm, a total of 60/70 cm of depth. The results from our method, as shown in the plot by the blue circle, says that flood depth is 70 cm. The values along line 1 also look to be reasonable. In fact, we have a maximum of 95 cm on the small canal along the street and a minimum of – 10 at the edges of the flooded area. The negative values are the errors we committed in the estimation, a combination of flood mapping error and DEM and SAR misalignment.

Figure 52 shows an area along Via Roma in Saletto, a couple of kilometres southern than the previous case described. Box 1 shows the result in flood depth estimation, while box 2 and 3 show the images taken on November 2nd by civil protection. The red dot in box 1 corresponds to the building indicated in box 2. The Line 1 plot shows a depth of 25 cm right next to that building. Comparing images in box 4 (street view of the same area) and the images of the event, we can see a good agreement. Especially in box 3, we can note part of the field coming out of the water indicating shallow water, as reported by our results.

Figure 53 shows results along the new motorway on November 3rd, few hundred meters to the north from the previous case (box 1). The images taken on November 2nd during the event are shown through box 3.1 to 4.3. In box 2.1 to 2.3 we see Google Street view of the same area. In box 1 we can see 4 lines, whose correspondent profile plots are shown on the top left side of the image. Plot of Line 1 shows 30 cm depth on the left side of the line. A similar value can be estimated from image in box 3.2, where the height of windowsills should be around 1 m. Line 2 shows depth between 90 to 100 cm on the other side of the yellow building. From street view in box 2.1 we can notice the higher elevation of the building that justify this change in depth. Line 3 shows an average depth of 100 cm with a peak to 170 cm. The peak correspond to the canal parallel to the motorway noticeable in box 2.3, the same that is flooded in box 4.3, the one at the right side of box 4.1. The elevation of the small bridge is 1080 cm, while the one of the canal next to it is around 890 cm from our LiDAR. Water is 30 cm below the surface of the bridge, 1050 cm of elevation. That makes 160 cm of flood depth, just around 10 cm difference with our result. The water elevation in that point in our estimation is 1066 cm, 16 cm higher than what we estimated from field observation. Similarly, box 4.2 shows the bridge at the left side of box 4.1. Here we can see that water had slightly covered the surface of the bridge. The LiDAR in that point indicates an elevation of 1050 cm, exactly the one of the water estimated from the previous image. Right next to the canal, the elevation is around 900 cm. This would lead to 150 cm of depth, only 16 cm less that what we estimated, 166 cm. Line 4 shows lower values of depth.

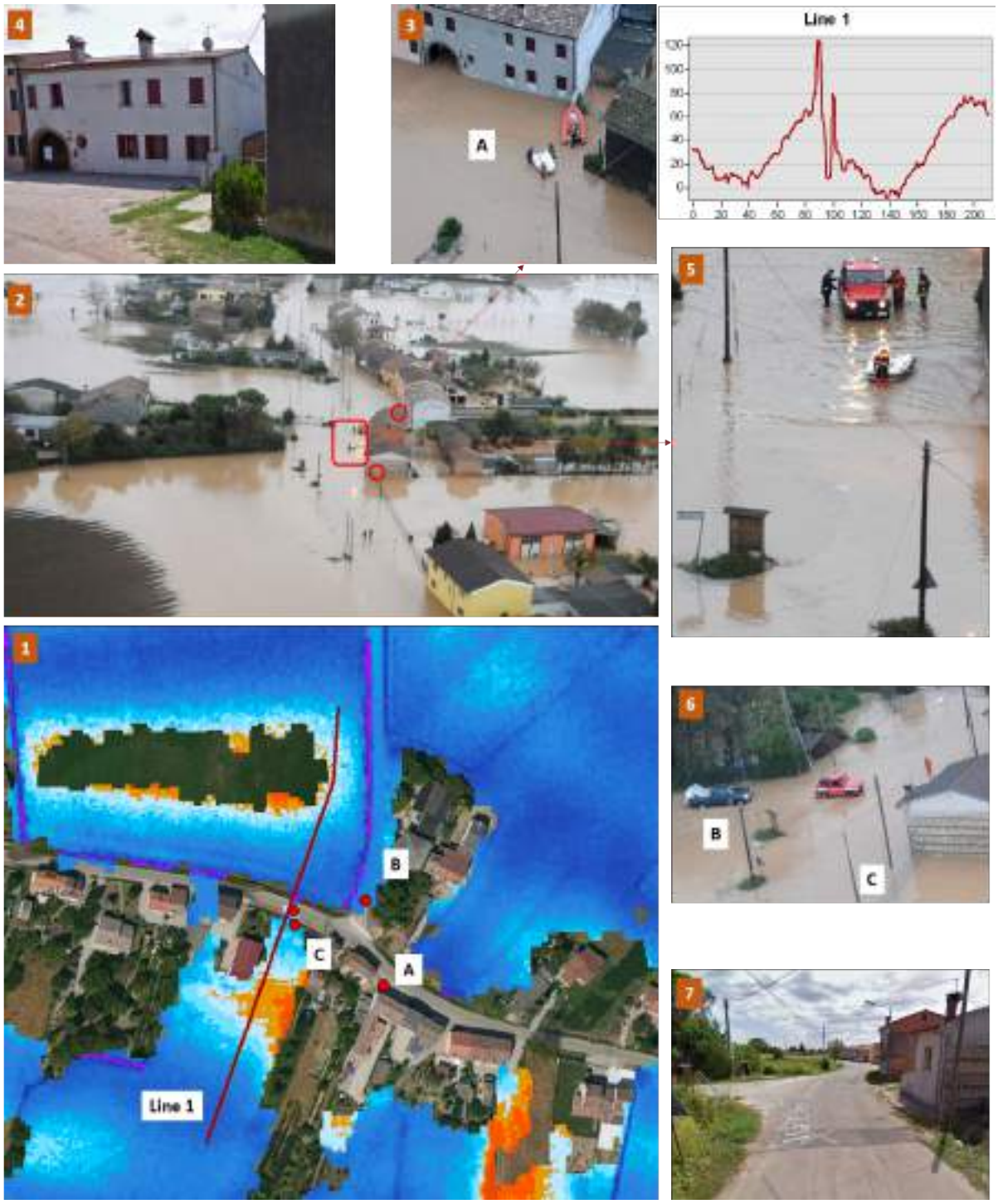

Figure 50 1) Flood Depth on November 3rd over Cabriani area in the Saletto area of interest; 2-3-5-6) Aerial views of the flood taken on November 1st at 16:30 local time; 4-7) Google Street View corresponding respectively to image 3 and 6; top right: flood depth profile of line 1 shown in 1)

This is explained by the difference in elevation between the two fields as we can see in box 2.2. In box 4.1 and box 4.2 we can also see how the crop covered the flood and prevent the flood map to show as flooded that area.

Following the same approach just shown, a total of 150 points were validated trying to select as many different flood polygons as possible. An RMSE of 22.3 cm was found.

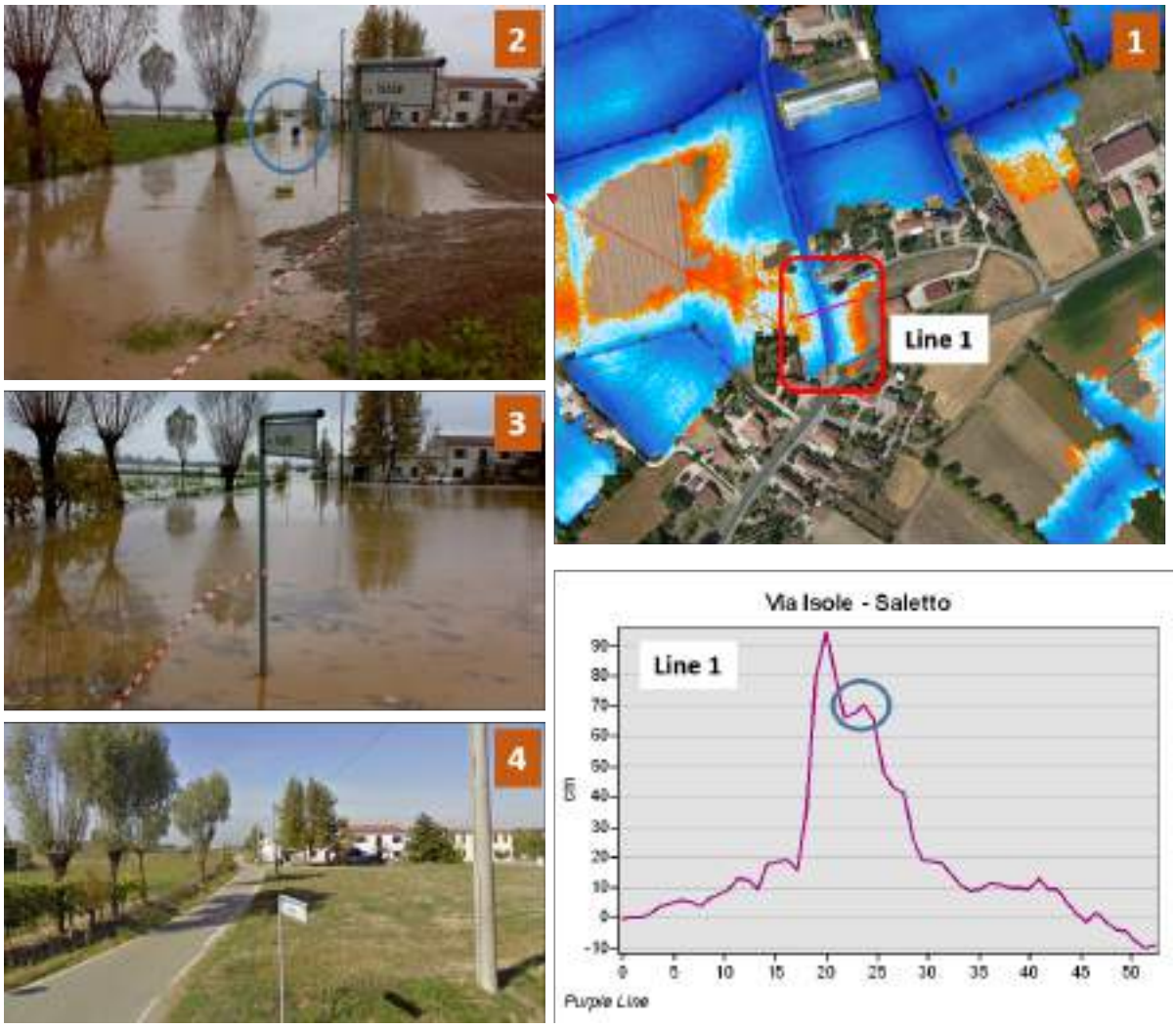

Figure 51 1) Flood depth on November 3rd over Via Isole area in the Saletto area of interest; 2) picture captured by the civil protection at 3:50 pm local time on November 1st; 3) pictures taken at 4:30 pm of the same day showing an increased water level; 4) Google Street View of the same area; bottom right plot: flood depth profile along line 1 in box 1.

4.7 Conclusions

In this chapter, we showed a fast and accurate methodology for assessing flood depth based on a statistical analysis of elevation data along the contours of flooded areas. Starting from flood extent maps and using high resolution DEM, water levels can be estimated and therefore flood depth computed. The RMSE obtained on 150 validation points is 22.3 cm. The methodology could be suitable for operational mode. In fact, it could meet the ideal requirements as indicated by Brown et al. (2016): accurate, simple to use also for non-GIS and RS experts, easily applicable to different satellite data (SAR and optical) and quick to apply.

Figure 52 1) Flood depth on November 3rd in Via Roma in the Saletto area of interest; 2-3) pictures taken by civil protection on November 2nd at 9:30 am local time; 4) Google Street View of the same area; bottom left: flood depth profile along the line in box 1

In comparison to hydrological models, this methodology is more easily implementable since less information is needed, only SAR images of the event and a DEM. Hydrological models need additional information in order to derive depth, such as precipitation volumes, information about the soil, number and location of water pumps, etc. Moreover, the comparison with results obtained with a hydrological model gives very good correspondence, the main difference being the difference in the DEMs used in the two methodologies, 1 or 2m meter and very accurate in our case, 5m with most probably many inaccuracies in the case of the hydrological model. The RMSE on the water elevation is as good as 22 cm in the area of Bovolenta where the flood dynamics was simpler, and 69 cm in the Veggiano area where the flood dynamics was more complex. The comparison of flood depth gave worse results, an RMSE of 74 cm in Bovolenta to 83 cm in Veggiano. Nonetheless, the results of the hydrological simulation cannot be considered as a ground truth given the many approximations introduced for running the model. Models have many sources of uncertainties such as data of gauge stations, parameters of the soils, number of pumps, etc.

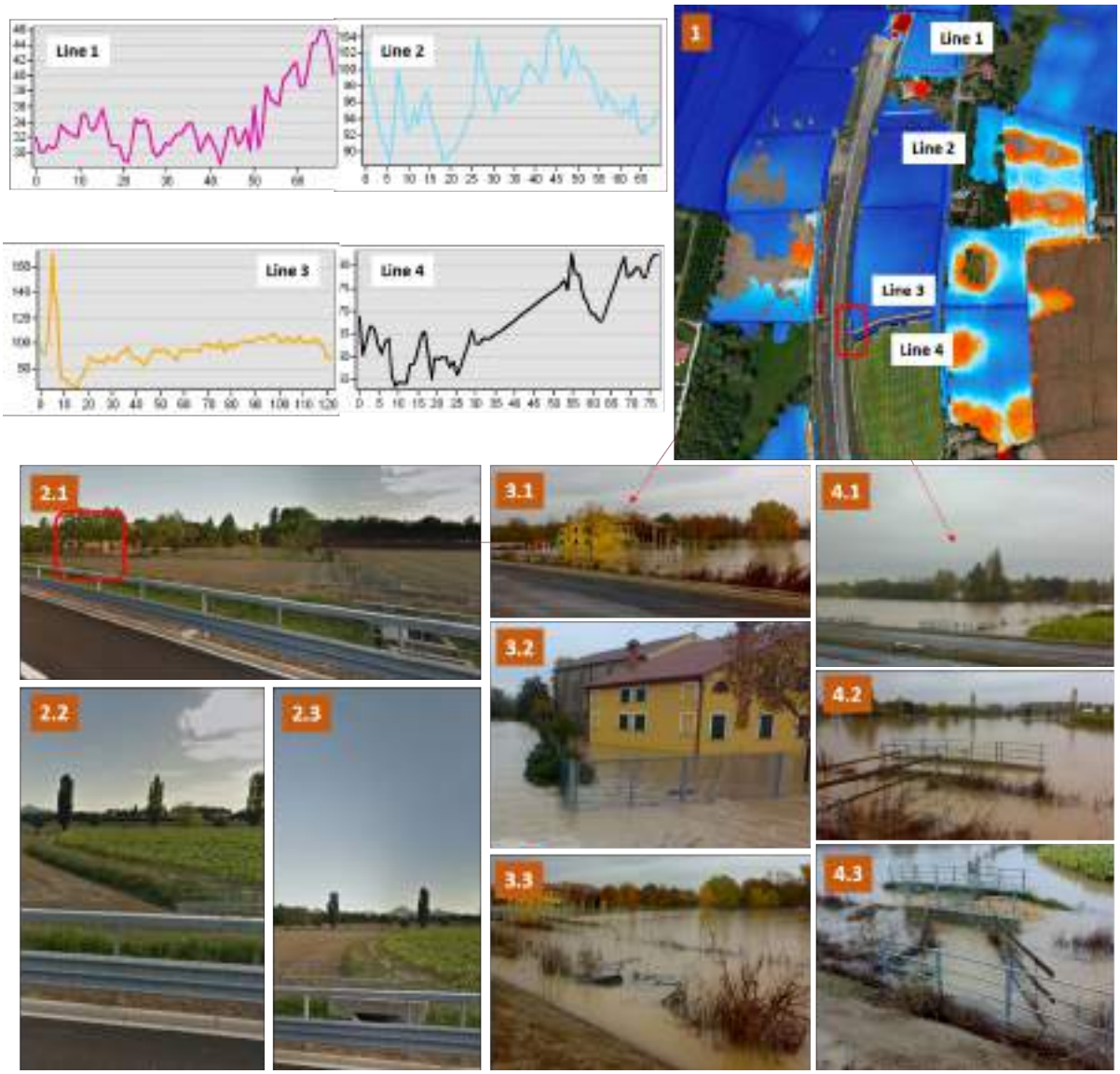

Figure 53 1) Flood depth on November 3rd along the new motorway crossing Saletto area; 2) Google Street View images of the areas in boxes 3 and 4; 3-4) Images taken on November 2nd at 9:30 pm; Top left: flood depth profiles along the lines in box 1

Despite the very good results obtained, the methodology can be further improved and automatized. Future work may consider to integrate a DEM filling procedure for improving water level estimation (Huang et al., 2014). The use of a vegetation index such as NDVI, may be used to exclude wrong points along the contours. In fact, if presence of vegetation is found along the contour, that may indicate an error in the flood map and therefore the correspondent elevation would be an information to be discarded. Similarly, slope can be computed from the DEM and used to exclude errors due to radar shadow or misalignment between SAR and DEM data. In fact, in case the elevation measured is greater than a certain threshold, that may indicate that the point is on a steep area (e.g. river banks) and with high probability the point was wrongly included in the flood map (radar shadow), or the pixel in the flood map does not exactly overlay the DEM. Excluding these possible sources of error would improve the statistics and therefore the estimation of the water level. Another improvement may come from the

method for creating the water elevation plane. Instead of relying simply on the elevation values distribution, the plane that minimize the RMSE could be found using the contours points left after the exclusion of outliers. The plane created could also take into consideration the slope of the river in a better way compared to the current method. By means of a shape index and the relative position between the river and the flooded area, the slope of the polygons can be estimated and imposed to the water plane. This would take into account the slope of the river and therefore the dynamics of the flood allowing to derive better results also for floods with a fast dynamic.

5. SAR and optical data fusion for land cover and urban growth analysis

This chapter presents a methodology for land cover classification. It allows the characterization of exposed elements to natural hazards and the analysis of urban growth, from which landscape metrics will be derived for the characterization of vulnerability.

The need of up to date land cover maps for assessing exposed elements to natural hazards, led to the development of a classification methodology that makes use of the new EO big data coming from the Sentinels satellite. Data fusion of radar and optical data have been found to provide a better classification compared to the use of only optical data. The change in built-up areas has been assessed in order to provide information regarding urban growth, which can be useful not only in terms of exposure to hazards, but also in term of vulnerability.

The chapter has the objective to answer ***research question 3****: "Can land cover classification be improved and easily up to date?" and, partially, to* ***research question 4****: "Is it possible to retrieve meaningful indicators of social vulnerability from EO big data?"*

The chapter will be submitted to the Journal "International Journal of Remote Sensing". The paper (which at the moment of the submission is in preparation) as well as the chapter, has been written autonomously by the author. The co-authors of the paper are Dr. Mattia Marconcini of the German Aerospace Centre, Germany, who supervised the whole research, José Manuel Delgado Blasco of the European Space Agency, who provided support in data processing and results analysis, Dr. Pietro Ceccato who supported the validation of the classification methodology and Prof. Carlo Giupponi of the Ca' Foscari University of Venice, who revised the results.

5.1 An introduction to Land Cover and Land Use

Land Cover (LC) is the physical material at the surface of the Earth; the physical land type such as forest, open water, wetlands, grass, asphalt, trees, bare ground, etc. (Lex Comber et al., 2005). LC data documents how much of a region is covered by land type classes. Instead, Land Use (LU) shows how people use the landscape, whether for development, conservation or mixed uses. For instance, in case of urban areas, LU data shows how these areas are used, if it is residential, commercial or industrial. LU corresponds to "the arrangements, activities and inputs people undertake in a certain LC type to produce, change or maintain it" (FAO/UNEP, 1999; FAO, 1997a). At any one point or place, there may be multiple and alternate LUs.

RS, in particular from satellite, is the most common source of data on LC. The surface of the Earth reflects solar radiation (or in case of active instruments, the Earth reflects the radiation they emit) to sensors that are able to measure the intensity of the reflected radiance at difference frequencies. In fact, depending on the specific characteristic of the surface type, the scattered radiation will have different responses at different wavelength, i.e. different spectral signatures. Different soil types absorb or reflect different part of the spectrum of the incident radiation. Therefore, it is possible to deduct the cover class of the Earth surface from the sensors measurements. Vice versa, it is not always possible to reveal the intended use of the land. However, in some cases, putting together LC with spatial structures and additional attributes, it may be possible to infer the LU (Park & Stenstrom, 2008).

A wide range of methods exists for the interpretation of remote sensing imagery and they can be classified in automated, semi-automated and pure interpretation (Richards, 2012). Automated approaches have the advantage of being fast allowing high temporal resolution and replication, very useful for monitoring rapid changes such as deforestation (Asner, 2009). Instead, supervised techniques and visual interpretation have the advantage of integrating the knowledge of experts, field observations and pattern recognition (Sirén & Brondizio, 2009), but have the drawback of being subjective and therefore dependent on the observer (Foody, 2002). Replication and change detection can therefore result biased. Surveys and census data are also sources of LCLU data, in fact many countries and international agencies collect statistical information on LU, such as agricultural census, which usually contain management information (irrigation, fertilizer use, crop yields, etc.). These sources of data are highly suitable for LU maps production, information that is not possible to retrieve from satellites. Nevertheless, in many cases the focus of census is on economic sectors disregarding data on natural LU. Moreover, "data are often aggregated to the level of administrative units while the original data are not available as result of privacy legislation" (Sabor et al., 2007).

Eventually, even if less frequently used, field survey and cadastral information are other sources of data for LCLU maps (Rambaldi et al., 2007).

The different sources of data above listed have different possible applications. Most advanced instruments with high-resolution capability (such as the one on board of IKONOS, Quickbird, GeoEye-1, WorldView-2 and RapidEye satellites) allow retrieving detailed LC information and the derivation of LU. Nevertheless, high-resolution data have the drawback of being costly and feasibly acquirable and interpretable only for relatively small areas. It follows that for global or continental coverage, medium to coarse resolution is normally used. Among the existing global databases, the Global Land Cover 2000 dataset (GLC2000) was built with SPOT images with 1 km resolution and the GlobCover dataset (GlobCover) with MERIS images with 300 m resolution. Coarser scale allows global coverage but it also means a higher probability of errors in the representation of landscapes. In a LC map, every single pixel is

usually classified as one well-defined cover class. When the resolution is coarse, the area represented by the pixel very often contains different cover types. Therefore, some of them, usually the less dominant, have to be dropped, resulting in an underestimation of the cover class dropped. The appropriate resolution has to be selected carefully depending on the landscape under analysis or some methods have to be employed to report the fractional coverage of each LC within the pixel (Ozdogan & Woodcock, 2006).

The temporal scale also play an important role. In fact, census data and surveys are usually infrequent and changes in sampling schemes and definitions occur between surveys. One the contrary, RS is a more continuous source of data, but suffering from inconsistencies due to improved resolution of sensors over the years and changes in classification schemes, which make difficult to compare products produced in different times or from different institutions. Moreover, cloud cover can represent a limit, especially in humid tropics, which complicate the collection of data over certain areas, a problem that may be partially overcome using SAR data (Berberoglu & Akin, 2009; DeFries, 2008; Freitas et al., 2008; Hansen et al., 2008). Different issues can affect the comparison and integration of different data sources, such as temporal and spatial consistency, scaling bias, thematic differences and inconsistencies, and differences between LC and LU (Verburg, Neumann, & Nol, 2011).

Consistent data over a long period is necessary in case of change detection and time series analysis. Ideally, the data utilized should be derived from the same source and processed with the same techniques. This is of course not the real case; in particular, short-term funding and specific information requirements by the funding agencies have often driven remote sensing projects. Therefore, what it is available is normally a wide variety of data generated with the most diverse techniques, different classification systems and legend classes. It has to be bear in mind that these inconsistencies could be the source of changes in the dataset analyzed, which should be distinguished from “real” changes (Verburg et al., 2011).

Errors in georeferencing of remote sensing data can be a source of spatial inconsistencies between different datasets. Nevertheless, these inconsistencies can be rather small if the georeferencing is performed with accuracy and they can be neglected if compared with inconsistencies coming from different spatial scale and aggregation. In fact, a coarser scale can be a great source of errors especially in the derived statistics. For instance, an area can be classified 100% grassland due to a coarse dataset resolution, neglecting the presence of wetlands or water bodies and having large impact on the estimation of GHGs emissions given the large difference in emission between the two cover classes.

Different data sources have different capacities in capturing specific LCLU types given the characteristics of the observation technique. Each data source will therefore lead to specific categorical uncertainties in the final LCLU data. Moreover, a wide range of definitions is used for the same LC class between different datasets and inventories. For example, the class “forest” can be defined based or not on certain features such as stand height, canopy cover, strip width, inclusion of grasses. As an example, area without trees may be classify as forest cover if the intention is to replant (UK), or areas with many trees may not be classified as forest if the trees are not growing fast enough (Norway and Finland) (Lex Comber et al., 2005). The lack of an international organization responsible for standardize the definitions is one of the causes of thematic inconsistences (Verburg et al., 2011).

One of the major challenges for analyzing land changes is the relation between LC and LU. LC addresses the layer of soils and biomass, including natural vegetation, crops and human structures that cover the land surface. LU in contrast refers to the purposes for which humans exploit the LC. LU is not always easily observable from RS data, but it may be inferred from

observable activities (e.g., grazing) or structural elements in the landscape (e.g., the presence of logging roads). Land abandonment for example, is reported to be decreasing in Europe. This is not observable from RS data. For example, "abandoned" grassland may be used for other functions, such as horse keeping. Even if the LC remains the same, the changing LU has large implications for the functioning of the land and the rural economy (Verburg et al., 2011). Similarly, the decreasing agricultural areas in Europe's mountain areas reported by many authors (MacDonald et al., 2000; Etienne et al. 2003; Tasser et al., 2007), is not observable by RS, which is unable to detect changes in intensity and actual use of the grassland. In fact, there are two major changes in these areas: part of the meadows are more intensively used, while other parts have been converted to pasture or have been abandoned (Mottet, Ladet, Coqué, & Gibon, 2006). Of course, this can lead to a discrepancy with agricultural statistics.

LC maps are a valuable source of vital information in many cases. They provide support to decision makers for natural landscape management when no picture of how the landscape look like is available. As it has already been mentioned, time series allow seeing changes and therefore evaluating past land management decisions. In addition, the effect of current decisions on the land can be monitored by time series, which can also be used as a baseline to understand the effect of possible future decisions before their implementation.

More specifically, LC maps are used to assess urban growth, predict and assess impact of flood or storms, potential impact of see level rise, track wetland losses, prioritizing areas for conservation efforts or purchases, compare LC changes with effect in the environment or to connection with socio-economic changes such as increasing population.

The production of LCLU dataset is limited by several factors and the production of a continental map can take up to 5 years, as it is the case for United States (NOAA) or the European Union (Corine Land Cover (CLC) has a time interval of 6 years). First of all, the acquisition of the imagery can be very slow due to bad weather conditions coupled with the revisiting time of the satellite used. In fact the presence of clouds inhibits the possibility to retrieve LC information, therefore in such a case, the acquisition has to be postponed of an interval equal to the satellite revisiting time, which can be up to a month. Moreover, the radiometric calibration of all the data acquired is a complex and time-consuming step. Different illumination conditions among all the acquisitions have to be taken into account, in addition to the possible different disturbance of atmospheric conditions. Finally, data has to be geometrically calibrated, interpreted and classified, validated and georeferentiated. Therefore, there is a limit in the production of LCLU dataset with a frequent temporal baseline.

There are many existing database of LCLU maps with different characteristics, produced using different sensors and covering different areas with different resolutions. Table 16 shows some of the main important projects and datasets worldwide. In spite of a coarse spatial resolution, global scale datasets are useful for many scientific and managerial applications. Global Land Cover (GLC) mapping is progressing towards higher spatial resolution, increasing the benefit of these data for the near future. GLC maps are commonly validated using higher-quality reference data such as independent validation datasets and regional maps. Currently, there are several independently validated GLC datasets (Table 17), which generation required significant efforts to analyze a large number of satellite images and interpret the LC type. These reference datasets are not always easily accessible to the community and are not used to their full potential despite the scarcity of such datasets. Some of them have been produce and are available at the Global Observation of Forest Cover and Land Dynamics – Land Cover project (GOFC - GOLD).

Table 16 Global Land Cover datasets

Dataset Name	Provider	Coverage
GLC 2000	EC JRC	Worldwide/ 1 Km (SPOT 4)
VHSR	Boston University	Worldwide/ 1 Km (VIIRS)
GlobCover 2005 - 2009	ESA/UCL	Worldwide/ 300 m (MERIS)
CLC 2012	EEA	Europe / 25 m (IRS/RapidEye)
Landsat GLC Map	China	Worldwide/ 30 m (Landsat)
GLCNMO	International Steering Committee for Global Mapping	Worldwide/ 1 Km (MODIS)
LC CCI	ESA	Worldwide/ 300 m (SPOT/MERIS)
FAO FRA	FAO	Worldwide/ 250 m (MODIS/Landsat)
MODIS training (STEP)	Boston University	Worldwide/ 2 km (MODIS)
GEO-WIKI	GEO-WIKI site	Worldwide
VIEW-IT		Worldwide
NELDA dataset	NELDA	Northern Euroasia
TREES	EC JRC	Worldwide
Global Human Settlement Layer	EC JRC	Several Countries / 10-500m (several data)
Global Urban ground truth data	University of Tokyo	Worldwide
MODIS Land Cover (MCD12Q1)	USGS	Worldwide / 500 m (MODIS)

Table 17 Global Land Cover reference datasets

Database	Description
GLC 2000 Database	It is the result of a consolidation work realized on the original GLC 2000 dataset. The original GLC 2000 classes were aggregated following the Aggregated Generalized Legend (AGL) resulting in a set of 11 LC classes.
GlobCover 2005 database	It is the result of a consolidation work realized on the original ESA-GlobCover 2005 dataset. A total of 186 points, associated with a pure LC class, were randomly selected and interpreted according to the GlobCover legend (which counts 22 LC classes). The purpose of this dataset was to validate the global GlobCover 2005 LC map derived from 300 m MERIS time series. Each sample is a 5*5 MERIS pixel window (~225 ha) drawn on Google Earth that was interpreted in terms of FAO-LCCS classifiers by independent experts. The consolidation of the entire dataset is still going on.
System for Terrestrial Ecosystem Parameterization (STEP) database	It was developed and maintained by Boston University between 2000-2013. The major purpose of this database is to train decision tree classifiers that are used by the MODIS Land Cover (MCD12Q1) product. Each site is a polygon (~4-sq km) drawn on Google Earth that is considered a stable example of a specific LC type. Recently STEP attributes were revised to be compliant with the FAO-LCCS and the database was filtered for sites that had been disturbed through time.
Visible Infrared Imaging Radiometer Suite (VIIRS) database	It was derived directly from the Boston VHSR database (under development) in order to meet the validation requirements for the VIIRS Surface Type (ST) product in the summer of 2013. Each VIIRS (~1-km) pixel within each VHSR site was manually interpreted according to the 17-class International Geosphere-Biosphere Programme (IGBP) legend. The database contains primary and secondary IGBP labels at each pixel, a confidence for the first label, and records any LC changes that may have occurred between the date of the imagery and the year 2012. Because of the similarity between the MODIS and VIIRS grids, this database can be used to compare these two LC products.

5.1.1 European state of the art on LCLU

Geoland-2 project started in 2008. Funded by the European Commission within the 7th Framework Program, it ended in 2012. The aim of the project was to provide decision makers with accurate, up-to-date and reliable information on the changing condition of natural resources, given the increasing pressure on natural biodiversity and on human living conditions due to climate change. Geoland-2 was part of the Global Monitoring for Environment and Security (GMES) initiative and it inherited the knowledge and results of previous European projects such as Geoland and BOSS4GMES (Building Operational Sustainable Services for GMES) of the EC, and GSE Land and GSE Forest Monitoring of the European Space Agency (ESA). The aim was to provide cross-border harmonized geo-information at global to local scales in a time- and cost-effective manner (Geoland-2). After its end, the EC decided to start the Copernicus project, a European system for monitoring the Earth. It makes use of different data sources: EO satellites, ground stations, airborne and sea-borne sensors. It is operated by the ESA for the space component and of the European Environment Agency (EEA) and the Member States for the in-situ component.

The services it provides, address six thematic areas: land, marine, atmosphere, climate change, emergency management and security. They support a wide range of applications, including environment protection, management of urban areas, regional and local planning, agriculture, forestry, fisheries, health, transport, climate change, sustainable development, civil protection and tourism. The main users of Copernicus services are policymakers and public authorities who need the information to develop environmental legislation and policies or to take critical decisions in the event of an emergency, such as a natural disaster or a humanitarian crisis.

The land monitoring service provides geographical information on LC and on variables related, for instance, to the vegetation state or the water cycle. It supports applications in a variety of domains such as spatial planning, forest management, water management, agriculture and food security, etc. The service became operational in 2012 and it consists of three main components: global, pan-European and local. The global component, coordinated by the EC Joint Research Centre (JRC), produces data across a wide range of biophysical variables at a global scale (i.e. worldwide), which describe the state of vegetation, the energy budget and the water cycle. The Pan-European component, coordinated by the EEA, will produce 5 high-resolution data sets describing the main LC types: artificial surfaces (e.g. roads and paved areas), forest areas, agricultural areas (grasslands), wetlands, and small water bodies. The pan-European component has also updated the CLC dataset to the reference year 2012. The local component, also coordinated by the EEA, aims to provide specific and more detailed information that is complementary to the information obtained through the Pan-European component. It focuses on "hotspots" which are prone to specific environmental challenges. The local component provides detailed LCLU information over major European cities, which are the first type of "hotspots". In addition to the above-mentioned components, the service also supports the generation of a Pan-European Digital Elevation Model (DEM) (Copernicus - The European Earth Observation Programme).

5.1.2 Upcoming products

The combination of improved sensor technology (Landsat 8, the new Sentinels and EnMAP (Environmental Mapping and Analysis Program)[1]), advanced computational capacity (Google Earth Engine and other cloud computing services) and open data access (Landsat and Sentinel datasets), has fueled the development of improved LC information derived from satellites and it will further enhance opportunities in mapping and modeling ecosystems and their changes over time in the global scale (Udelhoven, 2014). This improved information is transforming this discipline and it is enabling advances in LU science and practical application of social benefit (Justice, 2014).

However, recent data deluge makes it increasingly difficult to identify data of relevance to a given issue and finding useful information often requires cross disciplines expertise. The size and complexity of available RS resources gives rise to the development of data intensive and innovative processing, visualization, analytics and integration of heterogeneous RS data. Moreover, LCLU analysis requires RS affording high temporal, spectral and spatial resolution, which can be provided only by multiple sensors, therefore data fusion methodologies will be needed.

Furthermore, the problem of uncertainty is evident and it is not addressed in recent research. In fact, class definition, subjective of reference data collection, mixed pixel problems, data processing, limitation in statistical methods, are all topic that need to be faced (Udelhoven, 2014).

Another important effort that the LCLU community is facing, is in standardizing the production and use of LCLU data. In fact, GLC datasets still show high degree of disagreement. LCLU classes are often mixed (such as the case of the Corine Land Cover) and defined in too many different ways. The Global Observation of Land Dynamics (GOFC - GOLD) is an international effort that aims at providing the most appropriate databases among the existing ones based on internal quality criteria, fostering the use of recommended practices for LC validation and direct users to the most appropriate dataset according to their needs. Many steps still have to be done, but many improvements have been achieved in the past decade. Two concrete examples come from the two biggest community of LCLU. The NASA funded Web-Enabled Landsat Data (WELD) project has systematically generated 30m weekly, seasonal, monthly and annual composited Landsat mosaics of the United States for more than 10 years. The Landsat moderate spatial resolution is sufficiently resolved to enable chronicling of anthropogenic and natural change at local to global scale and the data are calibrated to enable discrimination between data artifacts and actual land surface changes (Kovalskyy, 2014). This can lead to think, that based on this example, in the near future the LULC community could dispose of such kind of data in a global scale. In fact, also from the European side there are encouraging signals. Although the Corine Land Cover is widely and successfully used, its limitations are also know, in particular the course spatial resolution, mixing of LC and LU classes in its nomenclature and a few problematic mixed classes. More demanding requirements, including increased update frequencies for environmental information, urge for complementary information services. The Copernicus project is currently implementing the mapping of 5 High Resolution Layers (HRLs), 100 m validated resolution, on LC characteristics at pan-European and at local level (imperviousness, forest, permanent grassland, wetlands, permanent water bodies) (Langanke, 2014). The HRLs are part of a trend towards higher spatial

[1] http://www.enmap.org/

and temporal resolution LCLU products. This trend is being enabled partly by better RS data availability, in particular by the new Sentinel-2 data.

5.2 The need of new and detailed land cover maps

The start of the Sentinels missions, Europe's eyes on Earth of the Copernicus programme, set forth a revolution on land monitoring. Commencing from October 2014 when the first satellite of the constellation Sentinel-1A radar mission began its operative phase, followed by its optical twin Sentinel-2A in late 2015, a huge amount of data (Earth Observation big data) are freely available on a weekly basis for every location on the planet. For the first time in history, we now have an opportunity to access diverse data for precision mapping covering the Earth's surface and its dynamics, allowing tracking changes due to human activities or as result of natural disasters.

This in fact is one of EU's response to tackle an era of global changes, in particular climate change, which is threatening our environment from different sources. On the one hand, Earth's biosphere is threatened by temperature rise and human activities; therefore, thereby the need to monitor biodiversity and the effect of policies enforced to control human effects on land use. On the other hand, with a foreseen increasing number of extreme events, such as extreme precipitations and the consequent flash and riverine floods, there is a need to understand what is at stake when these events occur (Mysiak, 2013; MunichRE, 2014; UNISDR, 2011).

Despite the efforts described in the previous paragraph, the need of new and detailed land cover maps is evident. With these motivations, this work has explored the potential of new EO data for the derivation of land cover maps and indicators of exposure and vulnerability useful for flood risk assessment. The data fusion of the new Sentinel-1 and 2 images allowed deriving land cover maps at 20 meter resolutions, which can be seen as an improvement of state-of-the-art products such as CORINE land cover, in terms of accuracy and possibility to be updated more frequently. Moreover, the potential of new cloud computing environments has been exploited for a faster analysis of a big amount of data. Google Earth Engine[2] (GEE) allows a quick access to data, which are available directly in the cloud, and provide a huge computation capacity for a quick and reliable analysis. In fact, for characterized different types of land cover, temporal statistics on time-series of 2 years of observations have been derived online and later classified by means of a Support Vector Machine (Cristianini & Shawe-Taylor, 2000a). Different datasets have been considered to assess the usefulness of data fusion.

Land cover analysis can be used to derive indicators of exposure and vulnerability and in particular we propose indicators extracted from the analysis of urban growth and network analysis of settlements[3].

Two are the areas analysed: i) the Veneto region, North-Eastern Italy, an area that has experienced profound changes in the past decades and has been hit recently by several natural disasters and where local authorities have urgent need of improved land cover maps, more precise and more up-to-date (Floris et al., 2012; De Natale & Pignatti, 2014); ii) southern Malawi, hit by disastrous flood in early 2015, an area lacking any source of data and in need to increase its capacity towards risk reduction and climate change adaptation.

[2] https://earthengine.google.com

[3] Network analysis is explained with more details in the next chapter.

Providing improved indicators of exposure and vulnerability is vital for creating a more resilient environment and livelihood, for better land management, preservation of ecosystems and adaptation to climate change, as well as for disaster risk reduction and protection of human lives and economic activities (de Moel et al., 2015). This work is an attempt to fulfil these requirements and demonstrate the benefit of the new Sentinel constellation, which in future could also be applied at larger scale.

5.3 Land cover classification and urban growth

In order to create a land cover map, remotely sensed images have to be interpreted, assigning to every pixel (or set of measurement associated to the pixel) a specific class (spectral class or land cover class). We can distinguish between two main groups of classification techniques, supervised and unsupervised classification (Angiuli & Trianni, 2013; Verburg et al., 2011). In unsupervised classification or clustering techniques, pixels are automatically grouped based on their position in the multidimensional space of the input features (spectral bands, i.e. radiances, or derived indices, etc.) and associated to a real class (land cover class) (Richards & Jia, 2006). In supervised classification, the class of the pixels is determined based on a-priori statistical information (spectral signature of classes). An analyst select training samples (points or clusters of points that represent distinct sample areas of the different land cover types) to classify the image (Foody, 2002; Sirén & Brondizio, 2009).

There is a vast literature regarding classification techniques for deriving LC maps from RS data and classifiers may come from different disciplines with diverse purposes. There are classifier adopted from statistics, symbolic artificial intelligence, data mining, some that use neural networks or that are ensembles and use regression or clustering approaches. We can also distinguish among several families of classifiers, such as Discriminant Analysis, Bayesian approaches, Neural Networks, Decision Trees, Random Forest, Support Vector Machines and many others. Support Vector Machines (SVMs), which have been selected for this work, have been found to be robust and effective algorithms for land cover classification (Burges, 1998; Cristianini & Shawe-Taylor, 2000; Fernández-Delgado et al., 2014; Mountrakis et al., 2011).

Multi-spectral indices

Multi-spectral data such as the images acquired by Landsat satellites since more than 40-years and by the new Sentinel-2 have been extensively used in land cover classification. These freely accessible datasets have a spatial resolution (30 m for Landsat, 10/20 m for Sentinel-2) that allows the identification of small features on the Earth surface needed for local and global studies and have a spectral resolution that allows the identification of spectral signatures for different land cover classes (Angiuli & Trianni, 2013). Instead of using images' spectral bands, many works make use of combination of bands and more specifically of normalized differences of different bands (Angiuli & Trianni, 2013; Aswatha et al., 2016; Joshi et al., 2016; Patel et al., 2015). In the literature, many indices have been defined as normalized difference of two bands with the aim of highlighting certain features of land cover, such as vegetation, water surfaces, built-up areas, etc. (Aswatha et al., 2016; Li & Chen, 2014; Silleos et al., 2006; Zha et al., 2003; Zhou et al., 2014).

Angiuli & Trianni (2014) introduced the Normalized Difference Spectral Vector (NDSV), which is a vector of 15 elements derived from all the possible bands combinations (normalized difference of band 1 to 6) of Landsat 8 data. The idea was to "extract the information contained in the multispectral image removing errors and ambiguities due to differences in time, space, acquisition, etc." Among the 15 elements of the NDSV, indices already defined in the literature can be found, such as the Normalized Difference Vegetation Index (the normalized difference of band 5 and band 4 for Landsat 8), the Normalized Difference Water Index (the normalized difference of band 4 and band 2 for Landsat 8) or the Normalized Difference Built-up Index (the normalized difference of band 4 and band 5 for Landsat 8). The advantages of this method are that data are intrinsically normalized and consistent globally, the information provided by each index gives the opportunity for analysing the contribution of different features in mixed urban areas and risk of ambiguities are minimized since the lack of each index is compensated by the others. This approach has been found to be effective by several studies (Aswatha et al., 2016; Lopez-Caloca, 2015; Patel et al., 2015; Trianni et al., 2014) and it has been selected as a base for this work.

Data fusion

Given the amount of free multi-spectral and SAR data continuously acquired by the new Sentinels satellites over the whole globe, the fusion of the two types of data has been explored with the aim of improving land cover classification especially concerning built-up areas. In fact, SAR and multi-spectral can be complementary (Tupin, 2010). In the case of vegetation for example, the information derived from multi-spectral data (leaf structure, pigmentation, moisture) can be complemented by the one derived from SAR (size, density, orientation, dielectric properties). In general, optical data can be more suitable for delineating broad land cover classes, while SAR can allow the characterization of land management and modifications thanks to the information on surface roughness and moisture.

Joshi (2016) distinguishes three main groups of image fusion methods: i) pixel-level fusion, the combination of original image pixels; ii) feature fusion, combination of features extracted from the individual datasets; and iii) decision fusion, a separate classification of SAR and optical with a combination of the two outputs to obtain the final result.

Several works have employed data fusion improving classification results (Amarsaikhan et al., 2007; Pereira et al., 2013; Dusseux et al. 2014; Erasmi & Twele, 2009; Joshi et al., 2016; Stefanski et al., 2014; Waske & Van Der Linden, 2008). For example, Amarsaikhan et al., (2010) compared different techniques of data fusion at pixel level for improving urban land cover classification, finding the Brovey transformation to be the one giving better results. Later, features were extracted and the dataset classified using a Bayesian Maximum Likelihood classification. In another work based on feature fusion, ENVISAT-ASAR and Landsat data have been used together for identifying urban areas. Spectral characteristics were retrieved from Landsat bands (normalized difference indices) and spatial characteristics were derived from SAR data. Later, a majority voting method were used to classify the image allowing to identify urban areas with precision (Lopez-Caloca, 2015).

In this work, we make use of features fusion at first, with a successive step of data fusion, as it will be explained more in details in the following paragraph.

Classification

As already mentioned, several are the available techniques of supervised classification. A technique that has been increasingly used in land cover classification is the SVM (Mountrakis et al., 2011), which has been selected for this work. SVMs are suited for RS classification given their robustness and ability to work well even with limited training samples (Mantero et al., 2005) and given their high performances (Fernández-Delgado et al., 2014). SVM has been used by Waske & Van Der Linden (2008) for land cover classification by means of SAR and optical decision fusion, by Dusseux et al. (2014) by means of data fusion and by Dalponte et al. (2008) for classification of complex forest areas by fusion of hyperspectral and LiDAR data. Esch et al. (2009), Huang & Zhang (2009), Inglada (2007), Licciardi et al. (2009) and Song & Civco (2004) used SVMs for classification of impervious surfaces and urban areas. Dixon & Candade (2008), Huang et al. (2008) and Li et al. (2010) used SVMs for general land cover classification obtaining good results. In the next paragraph, a more detailed description of the SVM employed in this work is provided.

Urban Growth

The mapping of built-up areas is a topic that gained increasing interest in the past decades. In fact, the rapid urbanization of many areas of the world has strong impact on the environment, on the economy and society, posing challenges in terms of sustainable development and management of natural resources. Benefits and challenges of urbanization are many and complex and they need to be studied (Dye, 2008; Seto et al., 2011). On the one hand, negative effects of urbanization needs to be monitored, such as the loss of natural habitats and biodiversity, or transportation and traffic problems. On the other hand, urbanization can increase living standards, societal values, education and protection and a support for planning development may be crucial. Moreover, in terms of management of natural disasters and disaster risk reduction, detailed maps of built-up areas and of population are fundamental in order to estimate impacts, create safer settlements and reducing losses in terms of people and assets. The maps currently available not always are detailed enough and do not always allow to detected rapid changes, therefore improved maps of built-up areas are needed in order to study urbanization and its growth (Esch et al., 2014; Potere et al., 2009; Potere & Schneider, 2007; Seto, 2009).

Urbanization has been studied by means of RS since decades, using either optical (Angiuli & Trianni, 2013; Estoque & Murayama, 2015; Patel et al., 2015a; Schneider, 2012; Taubenböck et al., 2012) and SAR data (Dell'Aqua & Gamba, 2010; Esch et al., 2011, 2012; Marconcini, et al., 2013; Taubenböck et al., 2012) or data fusion of the both (Amarsaikhan et al., 2010; Joshi et al., 2016; Lopez-Caloca, 2015; Tupin, 2010). In the years, methods have improved as well as accuracy (Patel et al., 2015a), leading to improvement also in population mapping (Gaughan et al., 2013; "The WorldPop Project," 2014). Moreover, the availability of new sensors and the quantity of free new data opens up new opportunities for urban mapping and urban growth analysis.

5.4 Case Studies

5.4.1 Veneto, North-Eastern Italy

The importance of the region in terms of change, either form the climate and from the socio-economic point of view, has been explained in Chapter 2. Figure 54 shows the Veneto region (shaded-green) and the area considered for the analysis (red box).

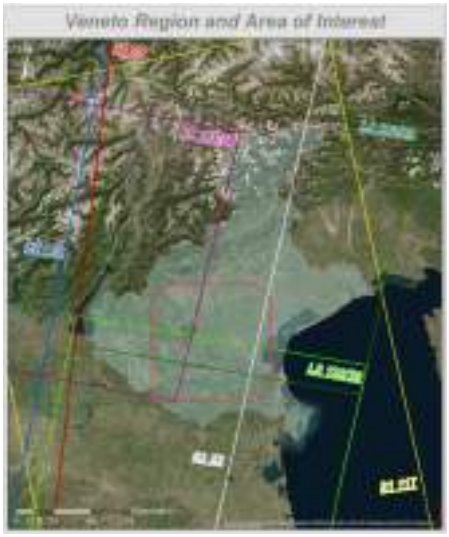

Figure 54 Veneto region (shaded green areas) case study. The red-box corresponds to the area analysis. Footprints of the images are highlighted

5.4.2 Southern Malawi

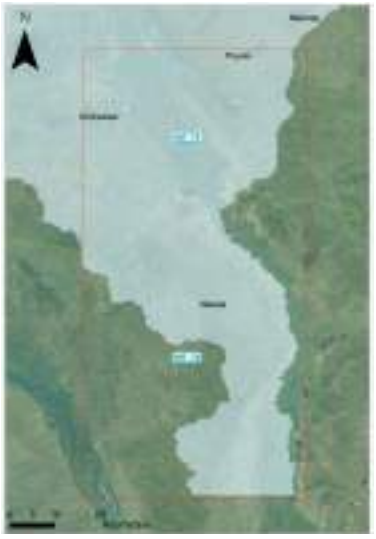

Figure 55 Southern Malawi with Chikwawa, Thyolo and Nsanje districts. The analysis, as shown by the red box, is concentrated in the Nsanje district cover by Landsat Path 167 row 71 and 72.

Figure 55 shows the area of interest for the case of Malawi. The analysis has been concentrated on the Nsanje district over an area of 50 by 100 kilometers as shown by the red box. In Chapter 2, the region has been described with more details highlighting its issues with flood events, climate change and its capacity from the socio-economic point of view.

5.5 Data Used

Land cover classification has been performed for both case studies. We made use of Google Earth Engine for pre-processing the images and therefore, the data there available have been used.

For Veneto, regarding the classification of 2015, we made use of data fusion of S1 and S2 data. For S2, which started the acquisition in July 2015, we made use of all the images available in the archive at the moment of the processing (end of April 2016). We also made use of Landsat 8 (L8) Surface Reflectance for an independent classification to be used as comparison. Since L8 data in GEE where not available with cloud mask and given the lack of a reliable cloud masking algorithm in GEE, a threshold of 70% on the cloud cover was set. For 1995, we considered a period of acquisition of two years given the small amount of observations available. We made use of Landsat 5 Surface Reflectance acquired from January 1994 to December 1995 with a cloud cover threshold of 70%.

For Malawi, at the moment of the processing there were not enough S1 and S2 acquisitions over our area of interest and therefore only Landsat data have been used.

Table 18 summarized the data used and specifies the orbits considered for both case studies.

Table 18 Dataset

	2015	1995	Cloud Cover	Orbit		
				S1	S2	Landsat
Veneto, Italy	**100 L8** from 01/14 to 12/15 **23 S1** from 01/15 to 12/15 **34 S2** from 07/15 to 04/16	**37 L5** from 1/1/94 to 31/12/95	<70% / /	95 D	22 122	192/28-29 193/28
Southern Malawi	**79 L8** from 01/14 to 12/15	/	<70%	/	/	167/71-72

5.6 Methodology

5.6.1 Land Cover Classification

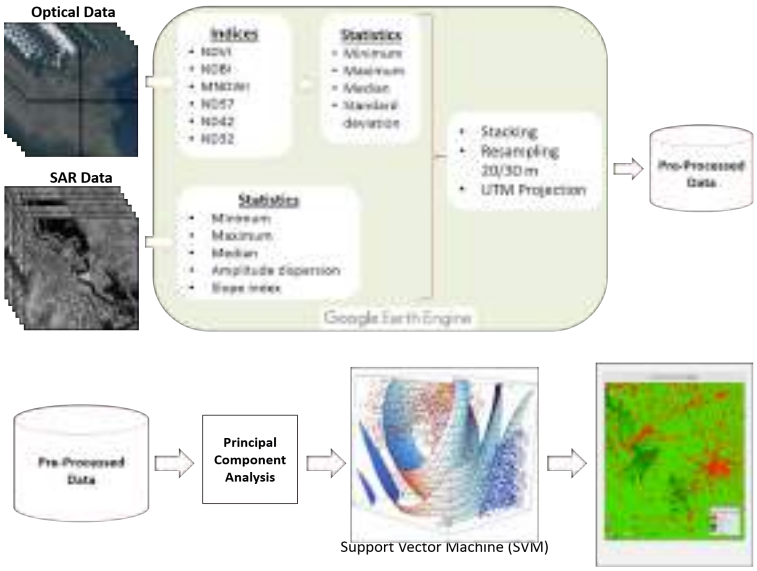

Figure 56 Classification Methodology

In order to perform the land cover classification, several pre-processing steps had to be performed. Given the availability of the data in the GEE and given its ease of use and very high performances, all the pre-processing steps have been performed in its platform as shown in Figure 56. Later, pre-processed data have been transformed by means of Principal Components Analysis (PCA) using the R software and classified using a Support Vector Machine implemented in the PKTools[4].

Pre-processing in Google Earth Engine

The S1 Ground Range Detected High resolution SAR dataset, which comes radiometrically calibrated, thermal noise corrected and terrain corrected, have been statistically analysed and the following feature extracted: i) minimum pixel intensity; ii) maximum pixel intensity; iii) median pixel intensity; iv) amplitude dispersion; v) mean slope index. Each band has been normalised in order to have value from -1 to 1 consistently with the values of the feature derived from optical data.

Amplitude dispersion gives an indication of the stability of the pixel and therefore, of the observed object. It has been computed using the formula (Ferretti, Prati, & Rocca, 2001):

$$AD = \text{standard deviation (Amplitude)} / \text{mean (Amplitude)} \quad (1)$$

Stable and strong scatterers, such as buildings, have small standard deviation with high amplitude resulting in a small amplitude dispersion value (< 0.25). Non-permanent vegetated

[4] http://pktools.nongnu.org (Pieter Kempeneers)

areas, such as agricultural areas, compared to urban areas have higher standard deviation with lower mean amplitude, resulting in a higher value of amplitude dispersion. Therefore, this parameter is useful for discriminating different type of land cover and most of all, it gives an indication of the stability or variation of the land cover (Ferretti et al., 2001).

The mean slope index is defined as:

$$\text{Mean Slope index} = \frac{\sum_{i=1}^{N-1} |x_{i+1} - x_i|}{N-1} \quad (2)$$

where *x* is the pixel intensity value and *N* the number of available observations ordered by date of acquisition. This index gives an indication of the type of variation of scatterers. A stable object, such as a building, has a slope index very close to zero. A scatterer that varies very rapidly and exhibits changes at every acquisitions will have a high value of slope index. The variation registered by the index is not scaled by the intensity of the object observed, i.e. that changes on high reflective scatterers will have the same importance of the changes on low reflective scatterers.

From the optical images, S2 and Landsat, the following indices have been extracted:

Normalized Difference Built-Up Index	$NDBI = \frac{SWIR1 - NIR}{SWIR1 + NIR}$	(3)
Modified Normalized Difference Water Index	$MNDWI = \frac{Green - SWIR1}{Green + SWIR1}$	(4)
Atmospheric Resistant Vegetation Index	$ARVI = \frac{NIR - 2Red + Blue}{NIR + 2Red - Blue}$	(5)
Normalized Difference Vegetation Index	$NDVI = \frac{NIR - Red}{NIR + Red}$	(6)
Normalized Difference B5 - B7	$ND57 = \frac{SWIR1 - SWIR2}{SWIR1 + SWIR2}$	(7)

The Normalized Difference Built-up Index (NDBI) is the normalized difference between the middle infrared (MIR or shortwave infrared 1 (SWIR1) in case of Landsat) and the near infrared (NIR) as reported in equation (3). Built-up areas have higher reflectance in the MIR wavelength compared to the reflectance in the NIR band, allowing the index to highlight them (Zha et al., 2003). However, similar behavior occurs for dry vegetation and water with high suspended matter concentration, which can create noise in a NDBI image (Xu, 2007).

The Normalized Difference Water Index (NDWI) is the normalized difference between the green band and the NIR band as in equation (4). It exploits the high reflectance of water in the green wavelength and the low reflectance in the NIR band. Moreover, it takes advantages of the high reflectance in the NIR by vegetation and soil features. Positive values of NDWI indicates the presence of water, while zero or negative values indicates vegetation or soil features (McFeeters, 1996). However, this index do not work properly in areas with built-up land background, which in fact have positive value of NDWI (Xu, 2006). If instead of the NIR band, the MIR is used, built-up areas can be discriminated from water since their reflectance in this

band is much higher than that of water (Xu, 2006). For this reason, the used of the Modified NDWI (MNDWI) has been chosen.

The Normalized Difference Vegetation Index (NDVI) is the normalized difference between the NIR and red band. The red channel is strongly absorbed by chlorophyll while NIR is strongly reflected by vegetation, allowing the highlight of vegetated areas. NDVI is sensitive to atmospheric effects (Gao, 1996). Similarly, the Atmospherically Resistant Vegetation Index (ARVI) (Kaufman & Tanre, 1992) highlights vegetation comparing the NIR channel with a combination of the red and blues channels, which is less sensitive to the effects of the atmosphere.

ND57 index in equations (7) has been chosen based on its use in the literature and in order to have a representation of the remaining bands of the Landsat sensors (Lu, Mausel, Brondízio, & Moran, 2004).

For each of the five computed index, the following statistics have been derived: i) minimum pixel value; ii) maximum pixel value; iii) mean pixel value; iv) standard deviation; v) slope index, which has been computed using the formula (2). This set of statistics is intended to capture the variability of the land cover throughout the year and allowing a better separation of land cover classes' spectral signature.

The two sets of features created, one derived from SAR and the other from optical data, have been stacked, resample at the same resolution, converted to UTM projection and finally exported from GEE.

Classification using Support Vector Machines

Support Vector Machines (SVMs) is a supervised non-parametric statistical learning technique that in the last years have been increasingly used on RS problems. A training algorithm finds a hyperplane that separates optimally the dataset in a number of predefined classes consistently to the training examples provided. Optimality is obtained setting a margin around the hyperplane (decision boundary) that minimizes misclassifications as shown for the linear case in Figure 57. It is a learning technique because of the iterative process for finding the optimal boundary that separates the training patterns and later, with identical configurations, the dataset.

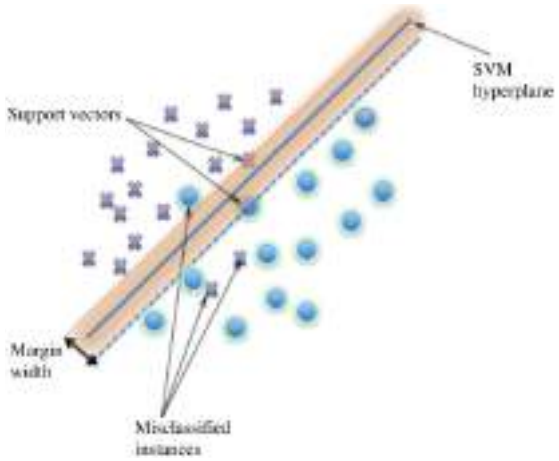

Figure 57 Supper Vector Machine example (linear). Source: (Mountrakis, 2011)

In practical cases, linear separability is difficult since points of different classes overlap each other. The soft margin method or the kernel trick are workarounds that solve the inseparability problem by introducing additional variables or incrementing the space dimensionality.

SVMs work well with small amount of training samples, a typical scenario when working with RS applications, providing high classification accuracy with a finite amount of training patterns. They minimize misclassification without prior assumptions made on the probability distribution of data such as in the case of maximum likelihood estimation. The drawbacks on RS application are the difficulty in choosing the right kernel and the intimidating theory for non-experts (Burges, 1998; Vapnik, 1998; Cristianini et al., 2000; Fernández-Delgado et al., 2014; Mountrakis et al., 2011).

PKTools

We made use of the open source *pktools*[4], a C++ suite of utilities for RS image processing (McInerney & Kempeneers, 2015). It implements a C-SVM (classification SVM) for supervised classification based on the library *libSVM*[5] and it uses a radial basis function (RBF) kernel (Keerthi & Lin, 2003; Lin & Lin, 2003; Vapnik, 1998). Several steps are needed in order to perform the classification: i) the input features composing the dataset to be classified, have to be scaled in order to avoid that attributes in greater numeric ranges dominates those in smaller numeric ranges (e.g. -1 to 1); ii) prepare a training dataset (a shapefile of points) for each class to be classified where each points bear the value of the input features; iii) using the RBF kernel, the optimal parameters C (penalty parameter for wrong classification) and γ (transformation parameter in the kernel) have to be found for allowing the classifier to accurately predict unknown data; iv) finally the classification has to be performed.

Input datasets

The input dataset to the SVM classifier is the stack of SAR and optical data exported from GEE. The stack is composed of 30 bands: 25 bands resulting from the statistical analysis of optical data (5 indices with 5 statistics each) plus 5 resulting from the analysis of the SAR data. Given dimension of such input dataset and given that certain statistics could be redundant, we performed a Principal Component Analysis (PCA) transformation using the *raster package* in the R software environment. With this processing, data fusion of optical and SAR data is performed. We decided to keep the principal components that represents the 99% of information of the original dataset. Only 18 bands were kept form the initial 35 and were used as input for the SVM classifier.

PCA is commonly understood as a technique of data compression used for reducing dimensionality of multidimensional data sets (Richards, 2012). It is a statistical techniques used for image encoding, change detection and multi-temporal dimensionality, which transforms a set of inter-correlated variables into a new set of uncorrelated linear combinations of the original variables (Pohl & van Genderen, 1998). It's implementation in R is easy to use and has very good performances.

[5] https://www.csie.ntu.edu.tw/~cjlin/libsvm/

Training

The training file have been manually created by photointerpretation. We made use of Google Earth images and photos acquired during field work for assessing the land cover type. For the case study of Veneto, an up to date and detailed land cover map were also available and use for creating the training set. After the manual classification, the training set was randomly sampled to partially remove errors and bias. The classes created are:

1: Urban
2: Agriculture
3: Forest
4: Bare Soil
5: Water

We made use of the PKTools function *pkextract*[6] for creating the training dataset needed by the SVM, where each training point bears the values of the input features.

Search of the optimal C and γ parameters

We made use of the PKTools function *pkopt*[7] for finding the optimal C and γ parameters. The function needs as input the range of C and γ among which looking for the optimal ones. Moreover, a cross-validation parameter has to be specified, which is used to divide the training set in *v* subsets of equal size. Iteratively, one subset is tested using the classifier trained on the remaining *v-1* subsets.

First, we look for the optimal C and γ in a coarser grid, and after individuating the best area in the C-γ plane, we look for the optimum in a finer grid.

Classification

The PKTools function *pksvm*[8] is used for classifying the input dataset. The training file is needed as well as the optimal C-γ. The result is a land cover map classified using the classes specified in the training.

5.5.2 Urban Growth Analysis for Veneto case study

As summarized in **Error! Reference source not found.**, land cover maps have been obtained for the year 2015 and the year 1995, allowing to perform a change detection analysis on built-up areas. From each map, built-up areas have been selected and compared. The comparison has been performed at pixel level allowing to obtain a change detection image useful for an overall analysis of change, such as the computation of increment or loss of built-up area. For each study area, administrative units have been used to compute several parameters useful for a further analysis of urban growth. For Veneto, we disposed of three levels of administrative

[6] http://pktools.nongnu.org/html/pkextractogr.html

[7] http://pktools.nongnu.org/html/pkoptsvm.html

[8] http://pktools.nongnu.org/html/pksvm.html

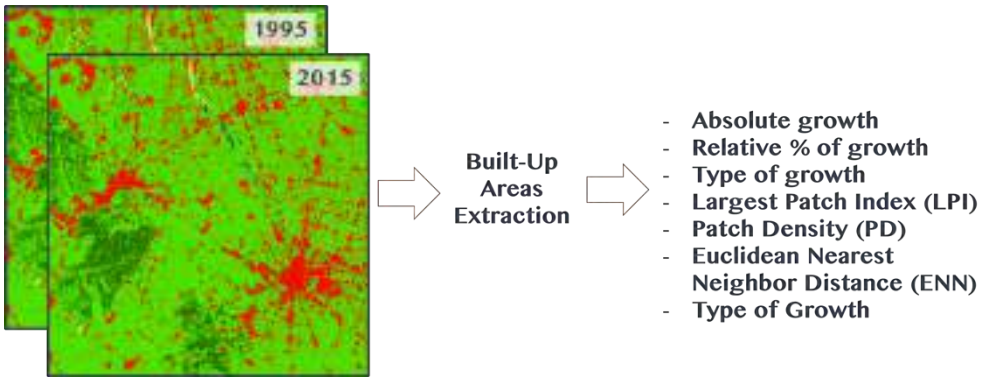

Figure 58 Urban Growth Analysis

units: census cell, municipality and province. Census cells can have dimensions from about 100 m^2 in city centres up to about 100 Km^2 in mountainous areas with little population. Municipalities can be as little as 3 Km^2 for small villages up to several hundreds of Km^2 for cities such as Padua or Vicenza. In order to analyze urban growth, the following parameters have been computed:

Absolute Built-Up Growth	$(\text{Built-Up Area})_{2015}$-$(\text{Built-Up Area})_{1995}$	[m^2]
Relative Built-Up Growth	$\frac{(\mathbf{Built-Up\ Area})_{2015} - (\mathbf{Built-Up\ Area})_{1995}}{(\mathbf{Built-Up\ Area})_{1995}}$	[%]
Largest Patch Index (LPI)	$\frac{\max(\text{patch Area})}{\text{Area}_{\text{unit cell}}}$	[%]
Patch Density (PD)	$\frac{\text{number patches}}{\text{Area}_{\text{unit cell}}} * (10000) * 100$	[Number/100 ha]
Euclidean Nearest Neighbor Distance (ENN)	h_i	[m]
Type of growth	$\frac{\sum \text{imperviouness pixel}_i}{\text{number pixels}_{\text{unit cell}}}$	[%]
Proportion of built-up areas	$(\text{Built-Up Area})_{\text{cell}}$ - $(\text{Area})_{\text{cell}}$	[%]

With the exception of Patch Density and Euclidean Nearest Neighbor Distance, which have been computed only at municipality level, these parameters have been computed at both municipalities and census cells level.

Relative indicators are important in order to satisfy the additivity property as described in Jaeger et al. (2010). In particular, when parameters (such as built-up growth area) are weighted

by their own areas, they became area-proportionately additive and they allow the comparison of patches with different size. Moreover, they allow to compare a local analysis taking into consideration what happen in the whole region (Altieri et al., 2014).

Absolut growth of built-up areas allow a spatial comparison of growth for each unit cell, relative growth on the other hand, allow for a comparison of growth dynamics. The Largest Path Index (LPI) is the percentage of the largest patch in the area of measurement compared to the total area of the unit cell and it describes the dominance of the urban core (McGarigal & Marks, 1994; Taubenböck et al., 2009). Patch Density (PD) of built-up patches inside the unit cell express in hectares and it measures the fragmentation of the settlement pattern (McGarigal & Marks, 1994; K C Seto & Fragkias, 2005). Patch dispersion is measured by means of the Mean Euclidean Nearest Neighbor distance (ENN), where small distances indicates a more compact distribution of built-up areas and large distances a more disperse pattern (Hannes Taubenböck et al., 2011). Type of growth is the average value of imperviousness for the grown built-up area and it gives an indication on the type of built-up areas. It has been calculated following the methodology proposed by Esch et al. (2009). Higher values of this indicators imply a more sealed surface. Proportion of built-up areas allows to compare the intensity of urbanization between areas of different size (Altieri et al., 2014) and can indicate the vulnerability to floods (Nirupama & Simonovic, 2007; Taubenböck et al., 2011).

5.7 Land Cover Classification Results and Discussions

5.7.1 Veneto

Land cover maps have been derived for 1995 and 2015 following the methodology presented in this chapter. As a training input, a minimum of 500 points were selected for each of the 5 classes. The set of points has been randomly extracted from a bigger set selected manually from photointerpretation. The validation of the derived products has been performed using and independent set of ground truth points extracted from photointerpretation and form the land use map available, dated 2012 and provided by the Veneto region. Every validation has been performed using 14.716 points.

Given that S2 mission was at the beginning of its life, the distribution of acquisitions throughout the year was not optimal. For this reason and for the sake of comparison, land cover maps for 2015 has been derived using data fusion of L8 indices statistics and S1 statistics. The two results are shown in Figure 59 (L8 and S1) and Figure 60 (S2 and S1). From a visual inspection, it is possible to see that the two products are very similar. This is confirmed also by Table 25 and Table 20, which show respectively the classification error matrix for the L8 and S1 classification and for S2 and S1 classification. The overall accuracy is of 93% in the case using L8 with K of 0.906. 89% is the overall accuracy in the case using S2, with a K of 0.86. The accuracy for built-up areas shows the greatest difference, 80% in the case of fusion of L8 and S1, 75% in the case of fusion of S2 and S1. This difference is also noticeable in the two land cover maps.

In order to justify the use of the data fusion of optical and SAR and the use of the statistics on the indices, sever products have been derived as a comparison. Table 21 shows the classification error matrix for the land cover obtained using as input dataset only the L8 indices statistics, without SAR data. This gave an overall accuracy of 91% and a value of the coefficient K of 0.88. Table 22 shows the error matrix for the land cover map obtained using as input only

the statistics on the L8 bands, which gave overall accuracy of 88% and K of 0.83. The statistics computed were the same computed on the indices, i.e. maximum, minimum, mean, standard deviation and slope index. Table 23 shows the error matrix for the map obtained using statistics on S2 indices, which gave overall accuracy of 88% and K of 0.84.

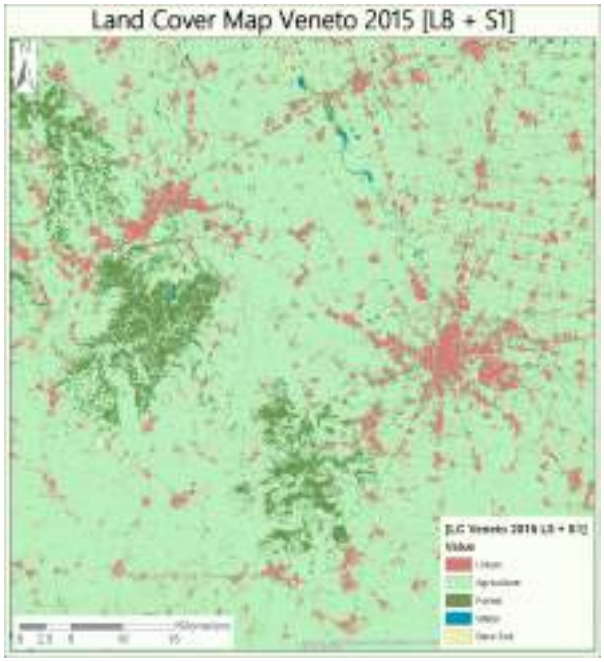

Figure 59 Land Cover for Veneto 2015 obtained from data fusion of L8 Indices statistics and S1 statistics

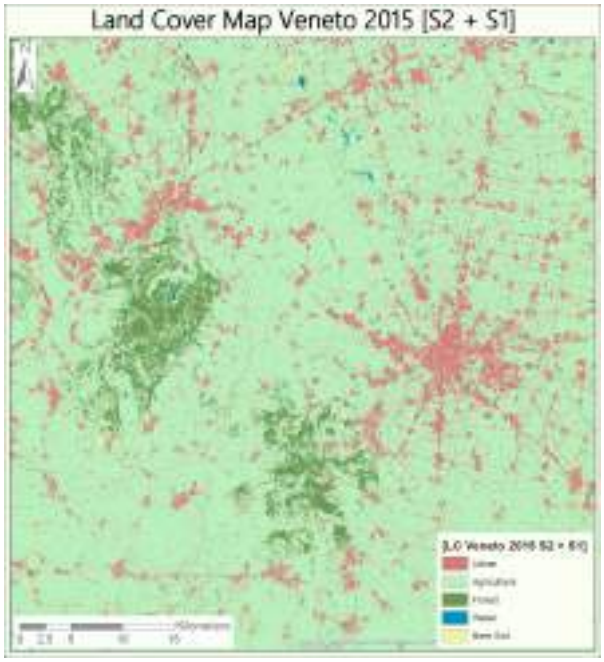

Figure 60 Land Cover for Veneto 2015 obtained from data fusion of S2 Indices statistics and S1 statistics

Table 19

L8 Indices + S1 - Classification Error Matrix

Pixels		Ground Truth [Pixels]					
	Land Cover Class	Urban (1)	Agriculture (2)	Forest (3)	Water (5)	Bare Soil (13)	Total Row
Classification 2015	Urban (1)	2085	5	0	0	42	2132
	Agriculture (2)	48	6148	74	0	78	6348
	Forest (3)	294	158	2522	0	2	2976
	Water (5)	52	17	62	2021	35	2187
	Bare Soil (13)	109	9	7	17	931	1073
	Total Column	2588	6337	2665	2038	1088	14716
	Agreement Accuracy	0.8	0.97	0.95	0.99	0.856	
	Commission Error	0.022	0.031	0.15	0.076	0.132	
	Omission Error	0.19	0.03	0.054	0.008	0.144	
	Overall accuracy	0.93					
	Kappa coefficient	0.906					

Table 20

S2 Indices + S1 - Classification Error Matrix

Pixels		Ground Truth [Pixels]					
	Land Cover Class	Urban (1)	Agriculture (2)	Forest (3)	Water (5)	Bare Soil (13)	Total Row
Classification 2015	Urban (1)	2125	1	0	0	6	2132
	Agriculture (2)	429	5287	419	0	213	6348
	Forest (3)	190	153	2633	0	0	2976
	Water (5)	20	4	2	2161	0	2187
	Bare Soil (13)	81	7	0	8	977	1073
	Total Column	2845	5452	3054	2169	1196	14716
	Agreement Accuracy	0.747	0.97	0.862	0.996	0.817	
	Commission Error	0.003	0.17	0.115	0.012	0.089	
	Omission Error	0.253	0.03	0.138	0.004	0.183	
	Overall accuracy	0.896					
	Kappa coefficient	0.86					

Table 21

Landsat 8 Indices - Classification Error Matrix

Pixels		Ground Truth [Pixels]					
	Land Cover Class	Urban (1)	Agriculture (2)	Forest (3)	Water (5)	Bare Soil (13)	Total Row
Classification 2015	Urban (1)	2128	0	0	0	4	2132
	Agriculture (2)	64	6183	63	0	38	6348
	Forest (3)	464	294	2217	0	1	2976
	Water (5)	108	9	17	2034	19	2187
	Bare Soil (13)	145	10	1	44	873	1073
	Total Column	2909	6496	2298	2078	935	14716
	Agreement Accuracy	0.73	0.95	0.96	0.98	0.93	
	Commission Error	0.002	0.025	0.25	0.07	0.19	
	Omission Error	0.268	0.05	0.03	0.02	0.07	
	Overall accuracy	0.91					
	Kappa coefficient	0.88					

Table 22

Landsat 8 Bands - Classification Error Matrix

Pixels		Ground Truth [Pixels]					
	Land Cover Class	Urban (1)	Agriculture (2)	Forest (3)	Water (5)	Bare Soil (13)	Total Row
Classification 2015	Urban (1)	2130	0	0	0	2	2132
	Agriculture (2)	89	6234	10	0	15	6348
	Forest (3)	1038	26	1912	0	0	2976
	Water (5)	73	28	150	1936	0	2187
	Bare Soil (13)	320	37	0	14	702	1073
	Total Column	3650	6325	2072	1950	719	14716
	Agreement Accuracy	0.58	0.985	0.922	0.993	0.976	
	Commission Error	0.001	0.018	0.357	0.115	0.346	
	Omission Error	0.48	0.014	0.077	0.007	0.024	
	Overall accuracy	0.877					
	Kappa coefficient	0.83					

Table 23

S2 Indices - Classification Error Matrix

Pixels		Ground Truth [Pixels]					
	Land Cover Class	Urban (1)	Agriculture (2)	Forest (3)	Water (5)	Bare Soil (13)	Total Row
Classification 2015	Urban (1)	2081	31	0	0	20	2132
	Agriculture (2)	567	5546	31	0	204	6348
	Forest (3)	405	235	2336	0	0	2976
	Water (5)	28	7	1	2151	0	2187
	Bare Soil (13)	170	21	1	8	873	1073
	Total Column	3251	5840	2369	2159	1097	14716
	Agreement Accuracy	0.64	0.95	0.986	0.996	0.80	
	Commission Error	0.024	0.126	0.215	0.016	0.19	
	Omission Error	0.36	0.05	0.014	0.004	0.2	
	Overall accuracy	0.88					
	Kappa coefficient	0.84					

5.7.2 Malawi

For Malawi, the training has been created by photointerpretation using Google Earth images and photos collected by field work. Among the all points created, a minimum of 500 points were randomly selected for each of the 7 classes of land cover and use to train the classifier. The validation has been performed against the land cover map of 2010 available in the Malawi Spatial Data Portal (MASDAP)[9] using a total of 10.355 points.

Figure 61 show the resulting land cover map. In this classification we distinguished perennial agriculture from annual agriculture and we used the class sparse vegetation for shrub land, grassland and very sparse trees. The resulting map looks quite detailed and is able to detect settlements even if they are very challenging to classify. In fact, there are no big cities in the area analysed, which is mainly characterized by rural settlements. With the spatial resolution offered by Landsat (30 m), detecting the presence of small buildings is not easy. The map reports many forested areas along the Shire river on the North side of the area. Technically this is not a mistake given that the images clearly show the presence of thick vegetation in this area. Nevertheless, this area is reported in other maps as wetland as indicated in Figure 62 (left and right). This area is known to be covered by water periodically and both classification may be correct. Figure 62 shows the comparison of our result over the north side of the Nsanje district with the land cover map of 2010 available in the MASDAP portal and the open street map. It can be clearly seen that settlements have a very good correspondence with the open street map layer. Instead, land cover of MASDAP appears less accurate and certainly not up to date. In fact, the big area of permanent agriculture at the North of the city of Bangula is not present in this map.

Table 24 shows the error matrix computed using the MASDAP land cover as a reference. As already mentioned, this map is dated 2010 and therefore does not report recent changes. Moreover, from a qualitative analysis it does not seem as detailed as the result that is presented here. The lack of other products, prevented other comparisons. The validation with this map using 10.355 points shows an overall accuracy of 76% with a K coefficient of 0.52. Even though these numbers do not indicate outstanding performances, given the circumstances explained above, they can be considered very good.

[9] www.masdap.mw

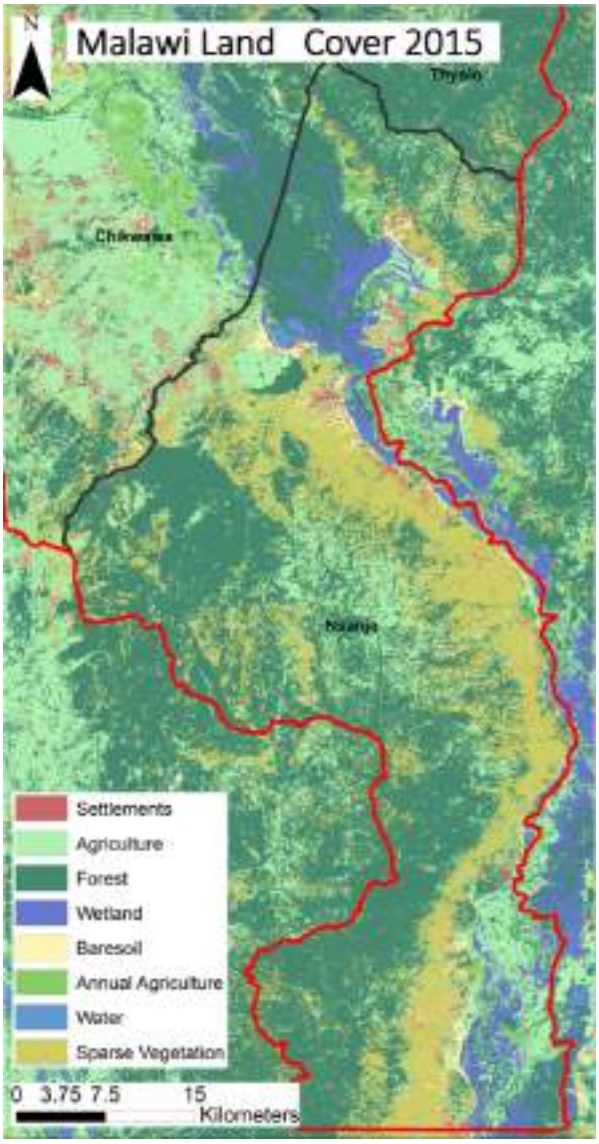

Figure 61 Malawi Land Cover Map 2015 obtained using data fusion of Landsat 8 and Sentinel 1 images statistics

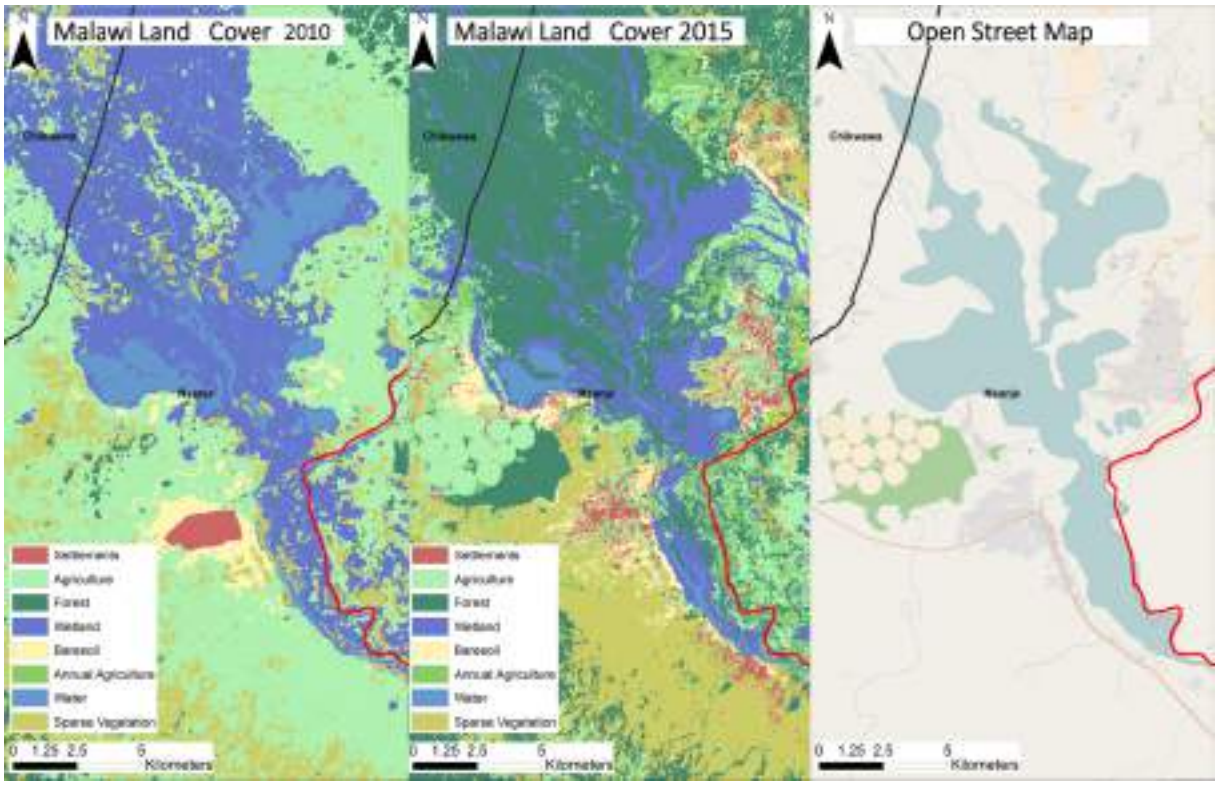

Figure 62 A zoom of different products over the North side of the Nsanje district: Land cover map of 2010 available in the Malawi Spatial Data Portal (left); Malawi Land Cover map of 2015 (centre); Open Street Map (right)

Table 24

		L8 + S1 Indices - Classification Error Matrix							
	Pixels	Ground Truth [Pixels]							
	Land Cover Class	Urban (1)	Agricult. (2)	Forest (3)	Wetland (4)	Water (5)	Bare Soil (6)	Sparse Veg. (7)	Total Row
Classification 2015	Urban (1)	*165*	*42*	*0*	*0*	*0*	*3*	*4*	*214*
	Agriculture (2)	*0*	*4025*	*239*	*79*	*0*	*0*	*988*	*5331*
	Forest (3)	*1*	*16*	*1693*	*84*	*3*	*0*	*6*	*1803*
	Wetland (4)	*0*	*8*	*0*	*1052*	*314*	*0*	*167*	*1541*
	Water (5)	*0*	*0*	*0*	*8*	*942*	*0*	*6*	*956*
	Bare Soil (6)	*0*	*221*	*0*	*0*	*0*	*9*	*49*	*279*
	Sparse Vegetation (7)	*0*	*223*	*2*	*0*	*0*	*0*	*6*	*231*
	Total Column	*166*	*4535*	*1934*	*1223*	*1259*	*12*	*1226*	*10355*
	Agreement Accuracy	*0.99*	*0.89*	*0.87*	*0.86*	*0.75*	*0.75*	*0.005*	
	Commission Error	*0.23*	*0.24*	*0.06*	*0.31*	*0.01*	*0.96*	*0.97*	
	Omission Error	*0.01*	*0.11*	*0.12*	*0.93*	*0.25*	*0.25*	*0.86*	
	Overall accuracy	0.76							
	Kappa coefficient	0.52							

5.7.3 Discussions

The results show the strength of the methodology proposed and the usefulness of the metrics derived from indices. The highest accuracy has been obtained using the fusion of L8 and S1, 93% overall accuracy with K of 0.9. The use of only L8 indices gives a lower accuracy, 91%, and a lower K, 0.88. Adding statistics derived from S1 SAR data improve the results. The fusion of Sentinel-2 and Sentinel-1 gave slightly lower accuracy, 89% of overall accuracy and K of 0.86. As already mentioned, the reason for this is a sub-optimal distribution of the acquisition throughout the year and an overall lower number of acquisition of S2 image, which do not allow to build a statistics as robust as in the case of L8. The use of S2 would allow to obtain land cover maps with an increased resolution, 20 m against the 30 m of the Landsat. Once the S2 archive will be enough populated, it will be possible to derive more robust statistics and obtain more precise results. Also in the case of S2, the use of only optical data allows to have a result with lower accuracy, 88% overall accuracy and K of 0.84.

The fusion of SAR and optical data and the use of the metric proposed is justified by these results.

For each land cover class considered, the spectral signature has been plotted as shown in Figure 63. The plots show clearly how the statistics allow to discriminate form one class to the other. In the case of forest and agriculture, we can see very similar signatures. The use of the mean value for each index would not allow to discriminate accurately the two classes. The use of the other statistics, in particular the minimum, plus the use of SAR statistics improve the capability of separating forest from agriculture.

Table 25

L8 Indices + S1 (full input features) - Classification Error Matrix

Pixels		Ground Truth [Pixels]					
	Land Cover Class	Urban (1)	Agriculture (2)	Forest (3)	Water (5)	Bare Soil (13)	Total Row
Classification 2015	Urban (1)	2101	5	0	0	26	2132
	Agriculture (2)	5	6202	88	0	53	6348
	Forest (3)	320	52	2604	0	0	2976
	Water (5)	12	17	111	2038	9	2187
	Bare Soil (13)	109	4	3	5	952	1073
	Total Column	2547	6280	2806	2043	1040	14716
	Agreement Accuracy	0.825	0.987	0.928	0.997	0.915	
	Commission Error	0.014	0.023	0.125	0.068	0.113	
	Omission Error	0.175	0.012	0.072	0.002	0.085	
	Overall accuracy	0.94					
	Kappa coefficient	0.92					

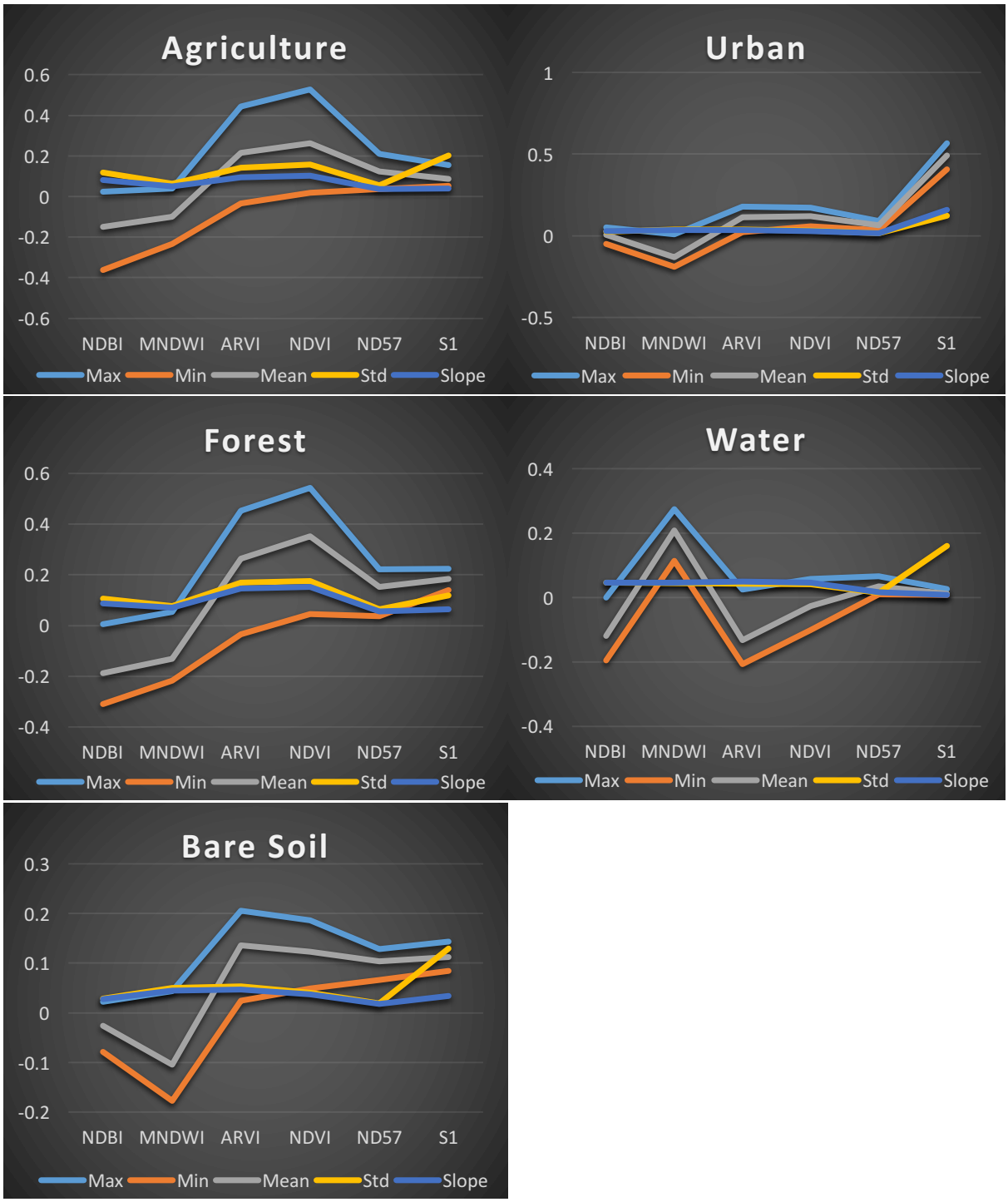

Figure 63 Spectral signatures of the five land cover classes.

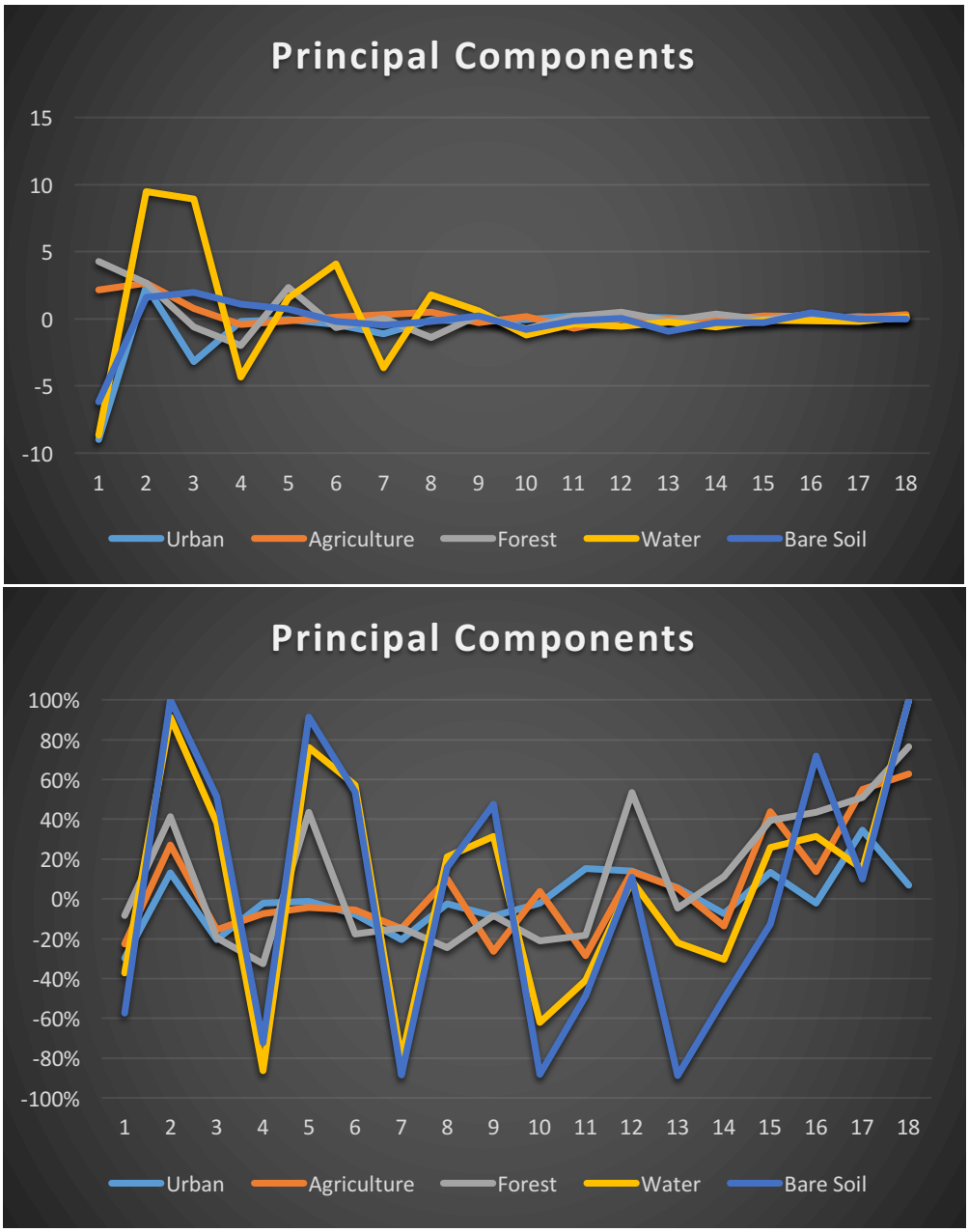

Figure 64 Spectral Signatures for each land cover class in the principal component domain

The use of Principal Component Analysis allowed to reduce the input features from 30 to 18, improving the efficiency of the classification methodology. The PCA analysis showed that the first 18 components allowed to keep the 99% of the original information. In order to prove that the reduction would not compromise the accuracy of the classification, we derived a land cover map using as input the original L8 statistics plus the S1 statistic. The classification error matrix shown in Table 25, indicates that the overall accuracy 94% with a K 0f 0.92. The quality of the result is comparable with the one obtained with the reduced dataset, showing that the efficiency obtained in terms of computation is not at the expense of the accuracy. In fact, the classification process was much faster with the reduced dataset, either regarding the SVM optimization step and the classification step. Moreover, once the principal component

reduction is performed, there is an advantage also in term of size of files. If the area analysed is not small, the full statistics file could be challenging to handle. Figure 64 shows spectral signatures for each land cover class in the principal component domain. The upper part of the image shows the values of each component for every land cover class, the lower part shows the same values but in a relative percentage form. This plot shows that also the last components provided useful information for discriminating each class.

5.8 Veneto Urban Growth Results and Discussions

The first product computed in order to analyse urban growth has been the change detection map shown in Figure 65. Built-up areas in 1995 have been compared with the ones in 2015. The resulting map shows reddish pixels, which represent unchanged built-up areas, yellow pixels, which are the new built-up areas, and light blue pixels, which are the built-up areas present in 1995 and which have changed to another land cover type in 2015.

Table 26 shows that from 1995 to 2015 the area has gained 402.1 km^2 of new built-up areas losing 70.4 km^2 of the older one, resulting in a net gain of 331.7 km^2 (64.8 %). From the map we can clearly see the construction of new roads and the expansion of the existing towns. The city of Padua, centre right of the image shows a fairly big expansion toward the south-east, with a remarkable expansion of the industrial area (east side of the city centre).

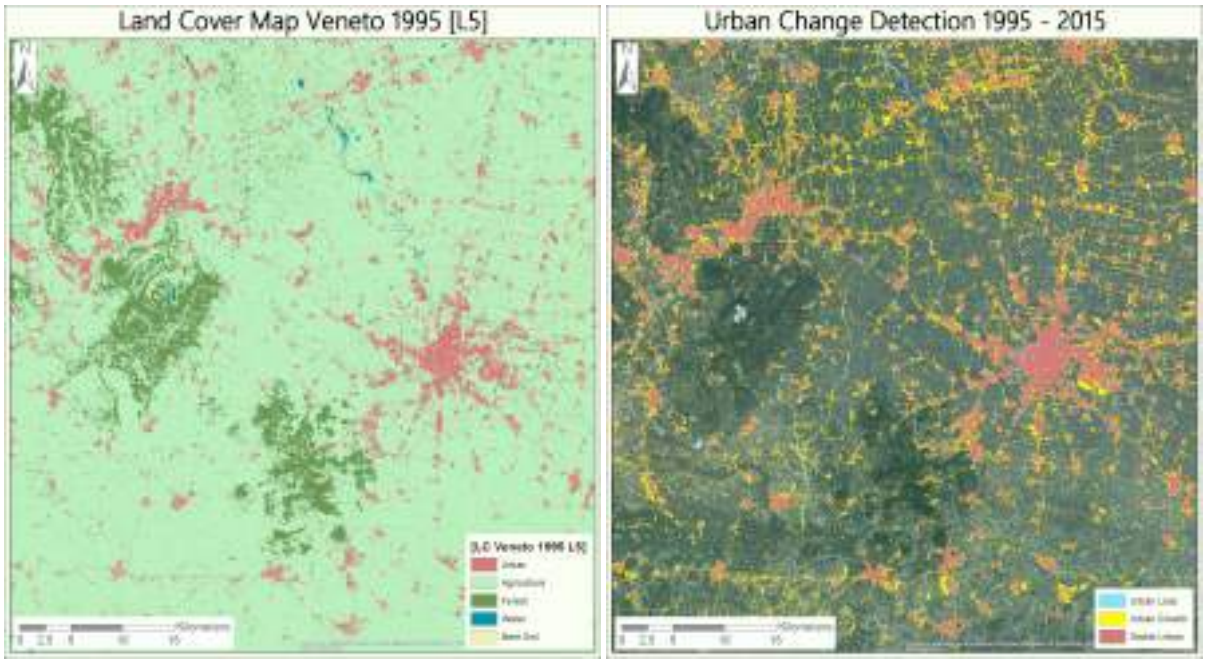

Figure 65 Change detection between built-up area in 1995 and 2015 over the region of interest of Veneto. Red pixels represent stable built-up areas, yellow pixels represent new built-up areas, while purple pixels represent built-up areas present in 1995 and which has disappeared in 2015.

Based on administrative subdivision of the area analysed, parameters of urban growth have been computed for municipalities and for census cells. Figure 66 shows absolute (left) and relative (right) growth aggregated at municipalities (top) and census cells (bottom) level. It can be noted that the two main cities in the area, Vicenza (North-West) and Padua (centre-East), show the highest level of growth in absolute terms. In relative terms, though, they don't not show relevant changes. Vice versa, the municipalities in the piedmont area (North/North-East), such as Castelfranco Veneto and Cittadella, show a significant increase of built-up areas, either in absolute and in relative terms, indicating a more significant impact of built-up growth on this area. Moreover, looking at the level of municipalities, it can be observed how this growth is more concentrated in certain specific locations, which in general excludes city centres and highlights urban sprawl. The analysis at census cells level highlights changes that are not so evident at the municipality level. This is evident in the south side of the area, where the smaller resolution of census cells, exposes the quite intense growth of this area.

Table 26 Built-Up areas analysis 1995 – 2015 for Veneto

		2015					
		Built-Up		Non-Built-Up			
		Pixel	Area (km²)	Pixel	Area (km²)	Total Built-Up 1995 Pixel	Total Built-Up 1995 Area (km²)
1995	Built-Up	490327	441.3	78257	70.4	568584	511.7
	Non-Built-Up	446805	402.1	5442623	4898.4		
	Total Built-Up 2015	937132	843.4				

	1995	2015
% Built-Up on total area	8.8%	14.5%
% of absolute built-up growth	/	5.7%
% Built-Up growth compared to 1995	/	78.6%
% Built-Up Loss compared to 1995	/	13.8%

The comparison of built-up areas in 1995 and 2015 is shown in the plot of Figure 67 (left) highlighting a general growth of built-up areas at municipality level. As expected, in absolute terms, the bigger the original built-up area was, the more it has increased. At census cells level, data show a more diverse behaviour, which was also expected given the small dimensions of many cells, but on average it confirms the same general trend. The right side of the figure shows instead the comparison between absolute and relative growth at municipality level. Even if the polynomial regression has a low coefficient of determination, the plot shows that the higher relative growths correspond to small absolute growths. In other words, the municipalities that experience the major development, are the smaller ones. This is confirmed also in the maps of

Figure 66, as explained above, and in the plot at the bottom right of in Figure 67, which shows the relative growth versus the area of each municipality.

Figure 68 shows the Patch Density for municipalities in 1995, 2015 and the difference between the two dates. Generally, municipalities corresponding to bigger cities or municipalities in the outskirt of these, experienced a decrease of PD or a very little change, highlighting the fact that these have become more compacted in terms of urbanizations. Municipalities corresponding to smaller towns, experienced instead an increase of PD indicating a more scattered development. The plot in Figure 69 shows that there is a general decrement of PD and the bigger decrement tend to occur to municipalities that were originally more scattered.

Figure 70 shows the Largest Patch index computed for municipalities and census cells in 1995 and 2015. Its difference shows that the major changes occurs mainly in North part of the area confirming what has been found in the other parameters, i.e. that the piedmont area has gone through a significant urban expansion. The analysis at census cell level in this case allow to have a better understanding of the process, showing in fact that the major increment of LPI occurred in the outskirt of the urban centres. The plots in Figure 71 confirm the general increment of LPI, either at municipality and at census cell level. At census cell level a more scattered behaviour is observed, due to the small size of many of these cells.

Figure 72 shows the difference in the mean Euclidean Nearest Neighbours distance, computed between 1995 and 2015 at municipality level. The map shows a general decrease of this parameters confirmed by the plot in the same figure. This indicates a more compact distribution of built-up areas, as expected given the generalized growth of built-up areas.

Figure 73 shows the mean value of imperviousness for the new built-up areas at municipality and at census cell level. If the analysis at municipality level can give a general idea about the increment of imperviousness in the area, the analysis at census cell level is very interesting since it can show the type of expansion that occurred. In fact, the mean value of the imperviousness in cells of such small dimensions, can be correlated to the dominant type of growth. As an example, the dark red area at the east side of Padua (centre-East side of the map) correspond to a high value of imperviousness compared to the average in the area of study. This correspond to the expansion of the industrial area of the city, which has a much higher imperviousness compared to new residential areas built in the same time frame.

Finally, Figure 74 shows the proportion of built-up areas at municipality and census cell level. It can be seen that there is an overall increase of this parameter in the whole area of study, which is more consistent in the north side of the areas and in the surroundings of the two main cities, Padua and Vicenza.

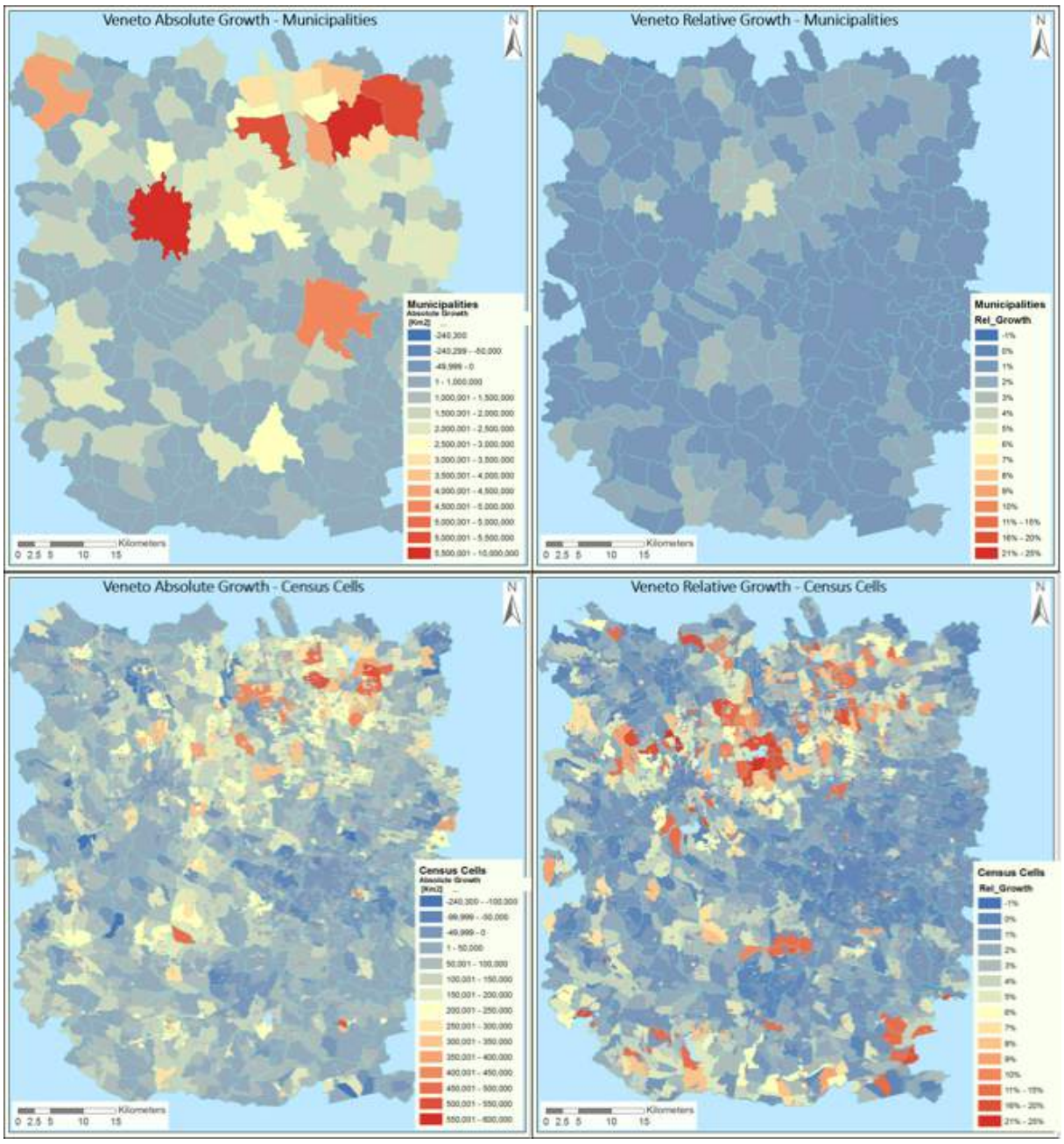

Figure 66 Absolute and Relative growth of built-up areas computed for municipalities and census cells

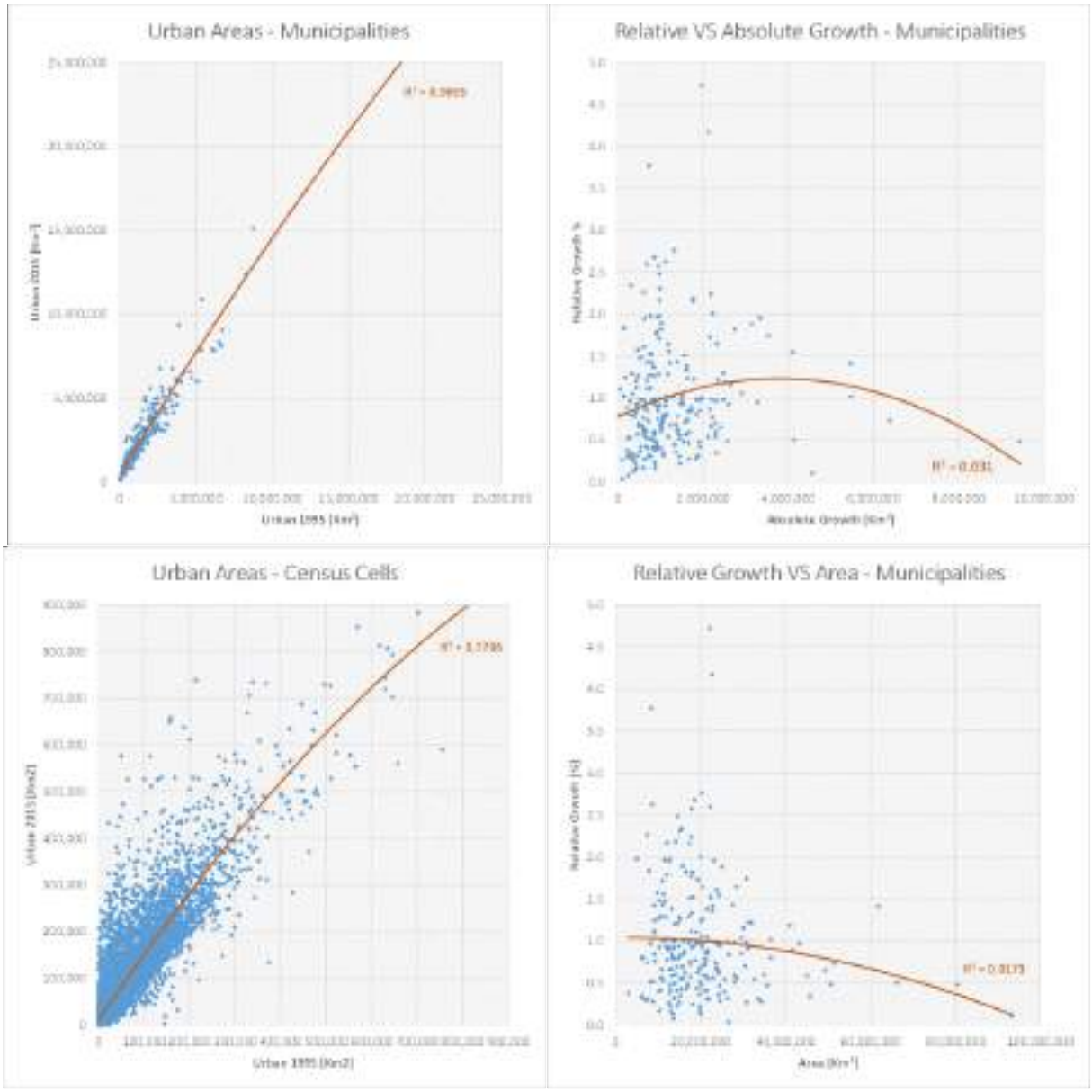

Figure 67 Comparison of built-up areas in 1995 and 2015 at municipality and census cells level (left); comparison of absolute and relative growth computed at municipalities (top right) and comparison of relative growth and area computed at census cells level (bottom right)

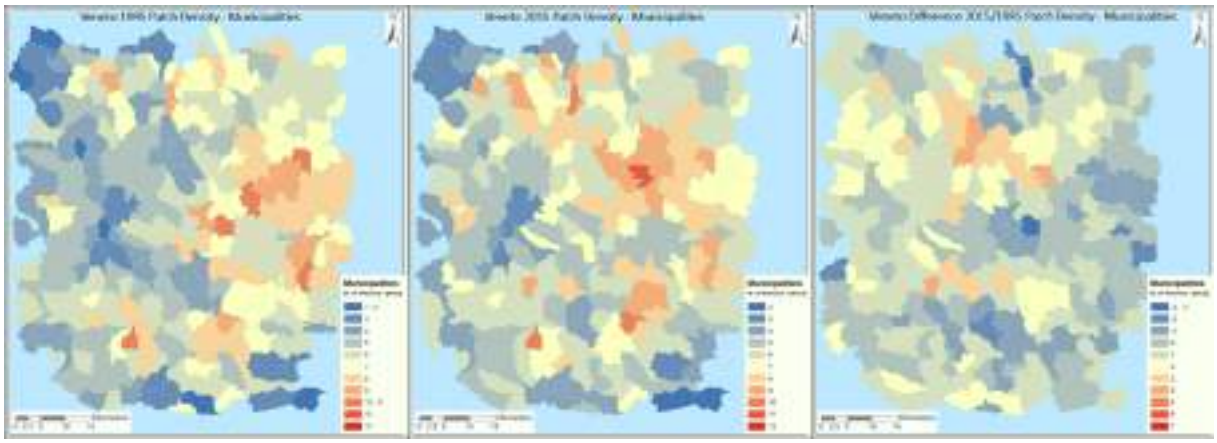

Figure 68 Patch Density index computed for municipalities in 1995, 2015 and its difference

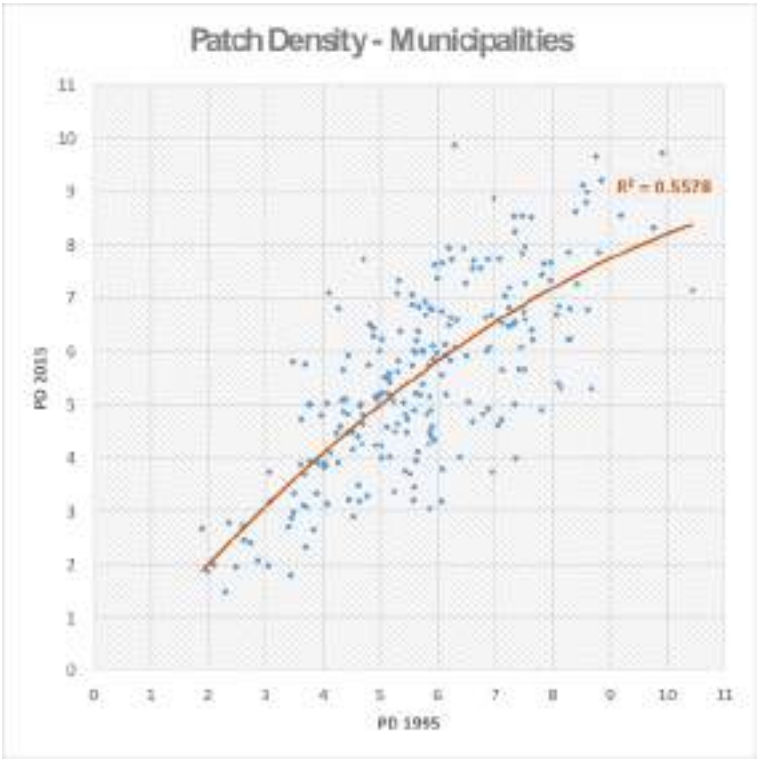

Figure 69 Comparison of Patch Density in 1995 and 2015 computed at municipalities level

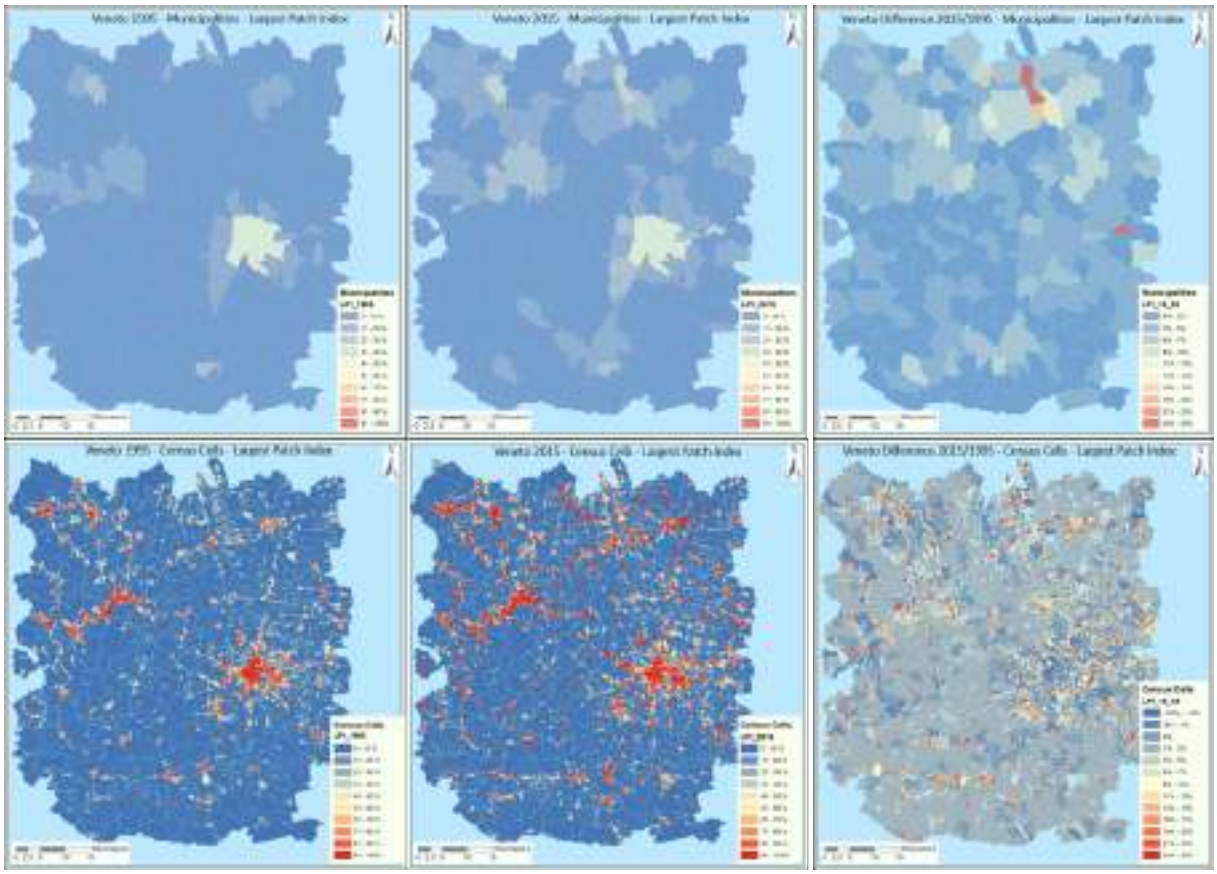

Figure 70 Largest Patch Index computed for municipalities and census cells in 1995, 2015 and its difference

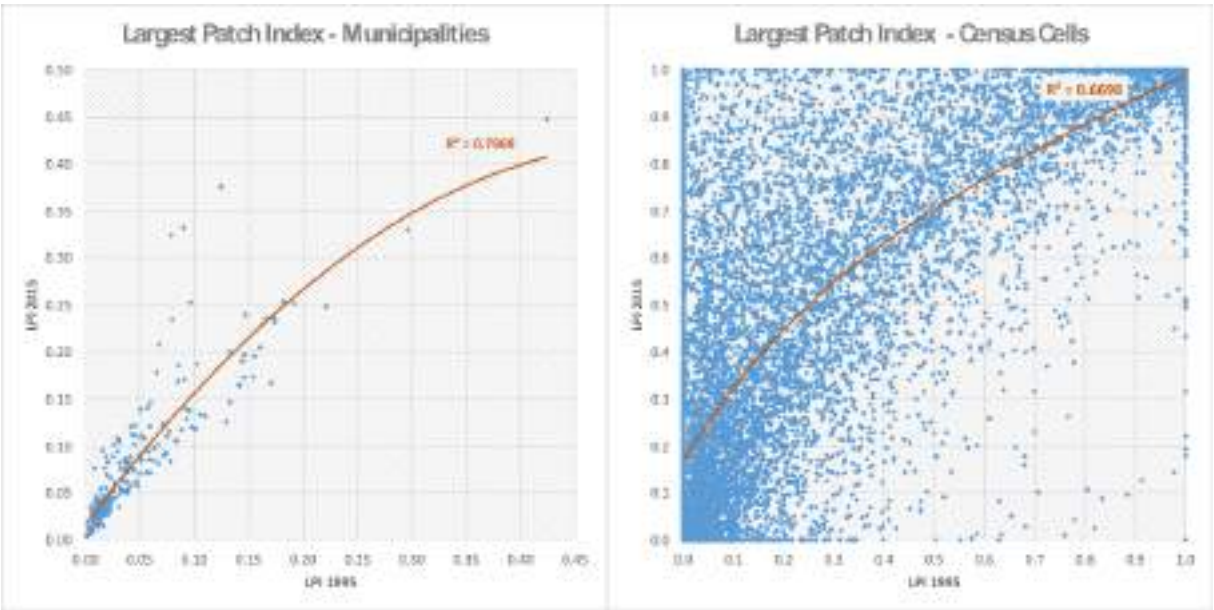

Figure 71 Comparison of Largest Patch Index in 2015 and 1995 computed at municipalities and census cells level

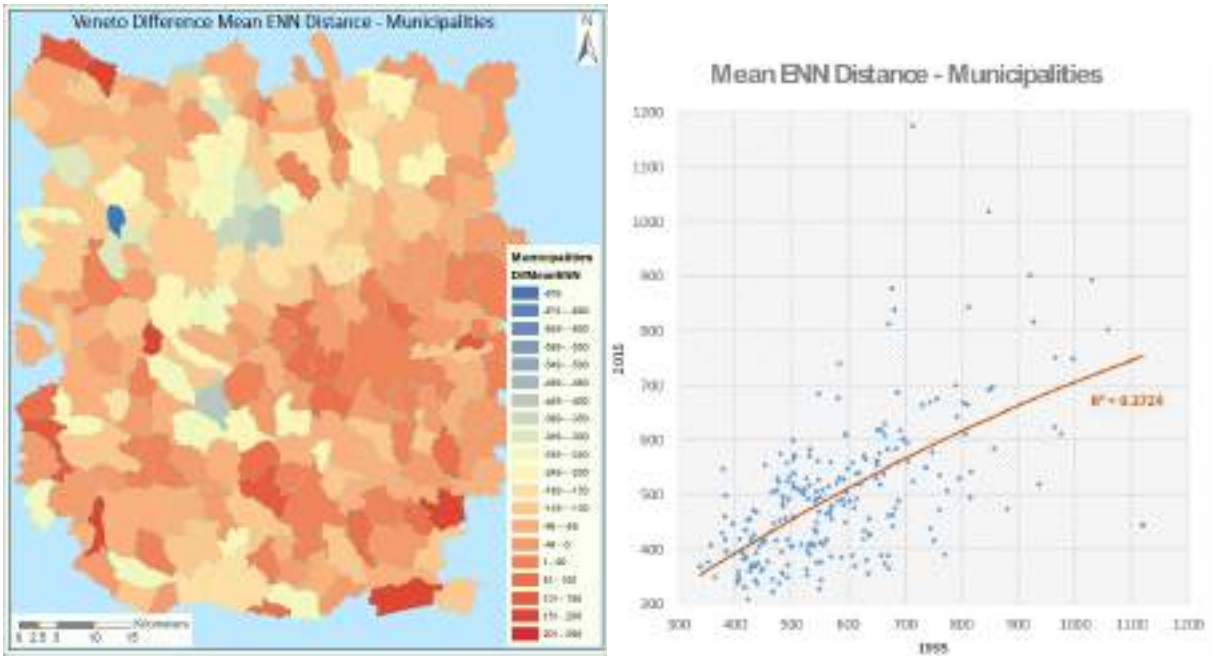

Figure 72 Difference of Mean Euclidean Nearest Neighbors distance computed for municipalities between 1995 and 2015 (left) and comparison of Mean Euclidean Nearest Neighbors distance in 1995 and 2015 computed at municipality level (right)

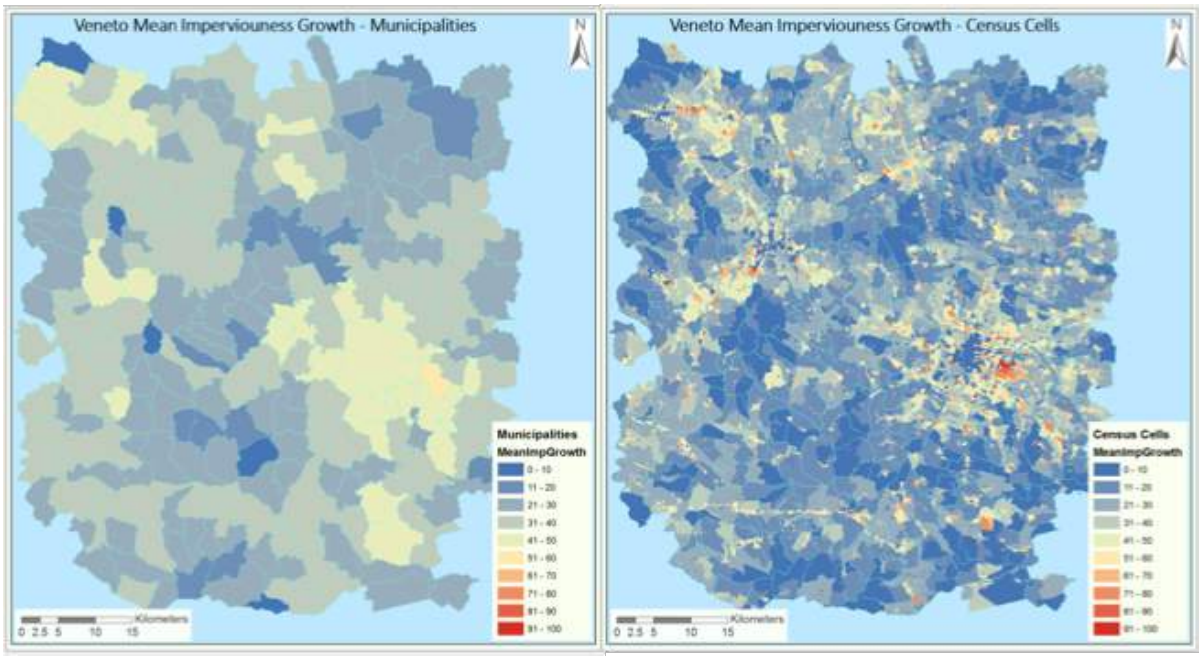

Figure 73 Mean imperviousness of new built-up areas computed for municipalities and census cells

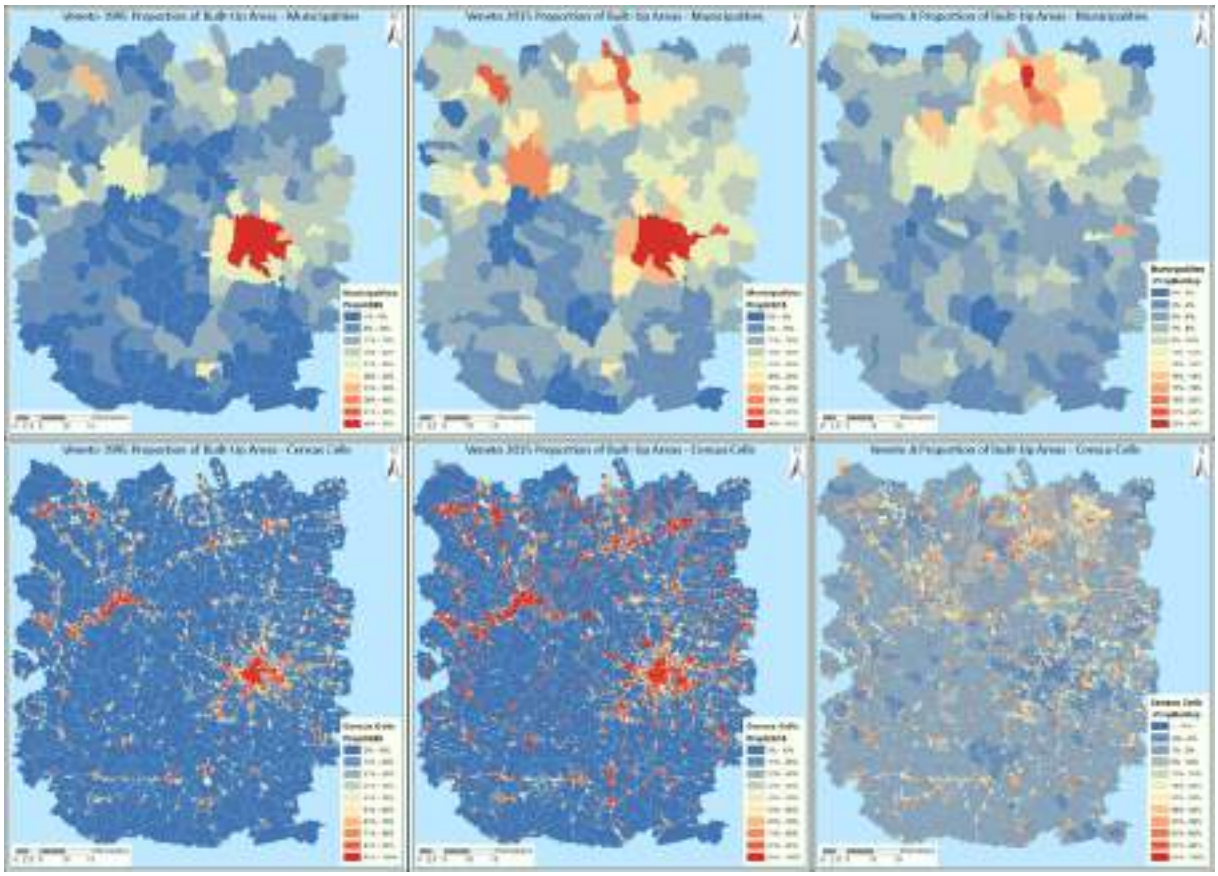

Figure 74 Proportion of built-up areas for municipalities and census cells

5.8 Conclusions

In this chapter, a classification method based on data fusion of radar and optical images has been presented and tested in the area of Veneto and Malawi, the same hit by the flood events presented in the previous chapters. The classification methodology has been proven to be fast (thanks to the capability of the GEE and the PKTools-SVM), reliable (good performances with different datasets) and accurate. Data fusion has increased the accuracy of the results. Worse performance has been obtained using Sentinel-2 data, only because the satellite has been operative for less than a year at the moment of data processing and acquisitions over the overall phenological cycle were not available. Most of the inaccuracy occurred over agricultural areas classified as urban or forest, forested areas classified as agriculture or urban, and bare soil classified as urban. A time-series over the whole year, which is possible already available for 2016, will improve the classification, not only in terms of classification accuracy but also in terms of spatial resolution. The use of SAR data made the classifier training easier compared to the case of only optical images, especially for urban areas where SAR response is very stable.

Therefore, new and up to date land cover maps can be produced in case of needs with the purpose of a rapid impact assessment following a disaster. Moreover, the methodology could be totally implemented in the GEE, using the built-in classifier available or programming a new one. This could eventually speed up the process even more.

In the second part of the chapter, a methodology for assessing urban growth has been presented, proposing a series of parameters that could be used as indicators of vulnerability. The analysis, applied to the case study of Veneto, showed interesting information about the development of built-up areas in the region, allowing to highlighting sprawls, more scattered settlements or more connected one. The analysis and the parameters proposed could be useful for ecology- or biodiversity-based study, for studying ecological corridors or the effect of conservation policies on biodiversity. Moreover, this analysis may be the base for a dasymetric mapping technique for distributing population data at pixel level, an information that would be very useful in the framework of disaster impact assessment and risk reduction.

6. Social Vulnerability Index: use of remote sensing and census indicators

This chapter presents a methodology for computing a social vulnerability index by means of remote sensing and census data. Based on the KULTURisk methodological framework, the three components of vulnerability will be defined: adaptive capacity, coping capacity and susceptibility. Network analysis is employed for describing the distribution of urban areas in the area of study, aiming at providing indicators for vulnerability.

The chapter has the objective to answer ***research question 4****: "Is it possible to retrieve meaningful indicators of social vulnerability from EO big data?"*

The chapter will be submitted to the Journal "Natural Hazard and Earth System Sciences". The paper (which at the moment of this thesis submission, is in preparation) as well as the chapter, has been written autonomously by the author. The co-author of the paper is Prof. Carlo Giupponi of the Ca' Foscari University of Venice, who helped developing the methodology and supervised the whole work.

6.1 Introduction

Damages deriving from floods can have different dimensions depending on the degree of monetization and level of physical contact of the hazard. Therefore, we can have four different categories of impacts: direct tangible, indirect tangible, direct intangible and indirect intangible (Giupponi et al., 2014). Tangible costs are the damage to receptors with a market value, while intangible costs are the one with only an intrinsic value. The majority of available methods for flood impact assessment, focuses only on direct tangible ones and only few try to go beyond this limit (Balbi et al., 2013; Jonkman et al., 2008; Merz et al., 2010). The KULTURisk framework, introduced in Chapter 1, was created with the precise goal of assessing also indirect and intangible damages, as shown in the case of Dhaka City, Bangladesh (Gain et al., 2015), where socioeconomic factors have been considered in addition to physical ones especially for the characterization of vulnerability.

Vulnerability is the variable that allows to assess damages given the hazard and the exposed elements. This chapter addresses this topic for the case study of Veneto, considering only direct impacts, finalizing the aim of this research, i.e. to show the potential of satellite remote sensing in assessing each component of flood risk and therefore assessing the related impacts.

The definition of vulnerability can vary significantly depending on the community addressing it. The IPCC, with its Special Report on Managing the Risks of Extreme Events and Disasters to Advance Climate Change Adaptation (IPCC-SREX, 2012), made an effort for harmonizing the definition of vulnerability among the communities of Disaster Risk Reduction (DRR) and Climate Change Adaptation (CCA). The KULTURisk framework is based on the definition of the IPCC and brings innovations in terms of (a) integration of the physical/environmental dimension and the socio-economic ones, and (b) in terms of considering social capacities of risk reduction, other than the already mentioned four dimensions of impacts (Giupponi, 2013). More precisely, KULTURisk considers vulnerability as "the propensity of predisposition of exposed receptors to be negatively affected by hazard events" (IPCC-SREX, 2012) and it considers both the physical and human dimensions. The physical dimension is the susceptibility of man-made structures, namely their predisposition of being negatively affected by hazards. The human dimension is made of two components: adaptive capacity (ex-ante) that is "the ability to anticipate and transform structure, functioning, or organization to better survive hazards", and coping capacity (ex-post) that is "the ability to react to and reduce the adverse effects of experienced hazards" (Gain et al., 2015).

Another aspect of vulnerability, which is difficult to capture, is its dynamics. As explained in Adger et al. (2013), Di Baldassarre et al. (2013) and Di Baldassarre et al. (2015) the dynamics of vulnerability is intertwined with the occurrence of extreme events. In particular, Adger et al. (2013) investigated what changes happen in the context of social contract when the status quo is disrupted by extreme events such as floods. The study found out that the direct experience of flooding, influences the perception of future risk and the responsibility to act. One of the case study presented showed that people that already experienced a flood had a propensity to believe that they would be affected again in the future. Moreover, these people showed a stronger sense of personal duty and willingness to adapt.

A very effective attempt to frame the interplay between physical and social processes intrinsic to flood risk, was presented by Di Baldassarre et al. (2015). The first type of dynamics relates to the observed decreasing social vulnerability linked to the frequent occurring of floods, i.e. the so-called "adaptation effect" (Mechler & Bouwer, 2015; Penning-Rowsell, 1996; Wind et al., 1999). During an experience of flooding, a community gains coping and adaptive capacity, which may reduce vulnerability. Moreover, the government or local authorities may intervene after an event by means of flood risk management policies (e.g. EWS, flood risk awareness programs or land use planning regulations), which may also reduce vulnerability (Johnson et al., 2005; Pahl-Wostl et al., 2013; Penning-Rowsell et al., 2006). Another type of dynamics of vulnerability relates to the observed increasing social vulnerability linked to the non-occurrence of frequent flooding, i.e. the so-called "levee effect" (Montz & Tobin, 2008), which is possibly caused by flood protection structures such as levees. There are many examples in the literature reporting an empirical evidence of increased social vulnerability and flood risk due to flood control structures. In fact, measures taken in order to prevent flooding may lead to a shift from frequent but small flooding, to rare but catastrophic ones (Bohensky & Leitch, 2014; Burton & Cutter, 2008; Di Baldassarre et al., 2013; Kates et al., 2006; Ludy & Kondolf, 2012).

The dynamics of vulnerability are not captured by most of the many methodologies of vulnerability and flood risk assessment in the literature. Changes in risk are usually assessed by comparing scenarios of climate change and socioeconomic development (Apel et al., 2009; Winsemius et al., 2013). Flood policies are considered an external forcing to the physical system and the impacts triggered by the physical systems are considered as an external forcing to the human system, therefore missing to capture the dynamics explained above (Di Baldassarre et al., 2015).

Figure 75 shows how vulnerability is considered in this work. The physical dimension, which weights for the 40%, is the susceptibility and it is given by the properties of the buildings and the value of imperviousness of the area. The social dimension, which weights for the 60%, is made of coping capacity (weighting for the 60%) and of adaptive capacity (weighting for the 40%). Coping capacity takes into consideration demography, the urban growth and the characteristics of the urban environment. Adaptive capacity takes in to consideration the skills of the society, such as employment and income level.

For the three main components of vulnerability, different indicators have been identified and data from RS and census have been used for a quantitative analysis. The appropriate indicators have been selected from the generalized list of indicators proposed by Giupponi et al. (2013) and Mojtahed et al. (2013) for the three components of vulnerability. The selection has been based on data availability, and on characteristic and spatial extent of the area of study.

One of the limitation of the proposed methodology is that it does not capture the dynamics of vulnerability. This was in fact out of the scope of this research, where the focus is to show how EO can provide added value to the existing methodologies, rather than develop a new methodological framework. Nevertheless, this work is intended to be the base for future research where the interplay between the physical and social processes of vulnerability will be at the core of the activity.

Paragraph 6.2 lists the available census data and the useful parameters of the urban growth analysis. Paragraph 6.3 shows the methodology used to compute each component of

vulnerability. Paragraph 6.4 shows results and discusses them. Paragraph 6.5 draws conclusions and the way forward.

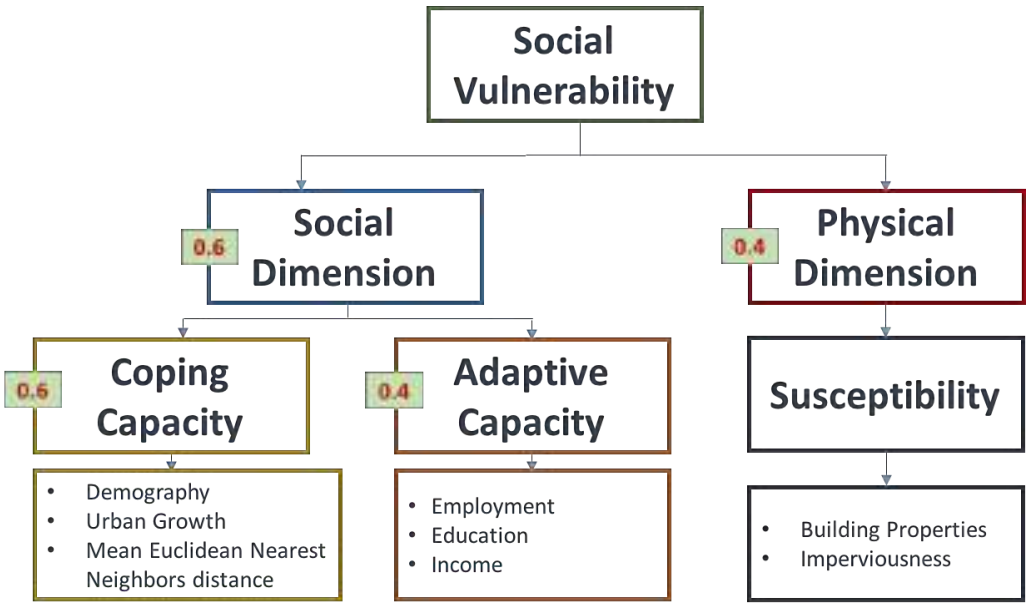

Figure 75 Vulnerability

6.2 Indicators of social vulnerability

6.2.1 Census Data

Census data for Italy comes every ten years. Based on the analysis performed on the hazard and exposure dimensions, the census of 1991 and 2011 are the one useful for this analysis. They provide a wide range of information about demography, education, employment, characteristic of buildings. Data are aggregated at census cell, which are very detailed sub-divisions of municipalities. Their dimensions can go from few hundreds square meters in case of densely populated city centres, to several tens of square kilometers for mountainous area with little population.

Concerning coping capacity, census data provide useful indicators:

- Demography
  - Population divided by age groups and gender
  - Family status
  - Education divided by gender
  - Commuters
  - Foreigners divided by age groups and region of provenience
  - Number of families made of 1, 2, 3, 4, 5 or 6+ people

Concerning adaptive capacity, census data provide the following indicators:

- Employment divided by gender
- Families in rented houses
- Families in property houses

Concerning susceptibility, census data provide useful information about buildings, aggregated at census cell:

- Number of buildings divided by type: commercial, residential, etc.
- Buildings occupied by at least one person
- Empty Buildings
- Type, age, material
- Status of conservation
- Number of storeys, number of apartments per storey

Moreover, the census gives indication about economic activities with the following parameters:

- Activity sector
- Number of units for each company
- Number of employees
- Number of other workers (not employees but working for the company)
- Volunteers

Income of each family is also collected by the census and it would be a useful indicator of the capacity of each family to take adaptation actions. Unfortunately, these data are not freely accessible due to privacy reasons and therefore they could not be used. Nevertheless, given the level of wealth in the area analyzed, this is not a limitation and it has been hypothesized that a similar discriminant in terms of adaptive capacity can be the percentage of rented houses.

6.2.2 Urban Growth Analysis

From urban growth analysis of Chapter 5, the following parameters are available:

Absolute Built-Up Growth	$(\text{Built-Up Area})_{2015}\text{-}(\text{Built-Up Area})_{1995}$	[m²]
Relative Built-Up Growth	$\frac{(\text{Built}-\text{Up Area})_{2015}-(\text{Built}-\text{Up Area})_{1995}}{(\text{Built}-\text{Up Area})_{1995}}$	[%]
Largest Patch Index (LPI)	$\frac{\max(\text{patch Area})}{\text{Area}_{\text{unit cell}}}$	[%]

Patch Density (PD)	$\frac{\text{number patches}}{\text{Area}_{\text{unit cell}}} * (10000) * 100$	[Number/100 ha]
Euclidean Nearest Neighbor Distance (ENN)	h_i	[m]
Type of growth	$\frac{\sum \text{imperviouness pixel}_i}{\text{number pixels}_{\text{unit cell}}}$	[%]
Proportion of built-up areas	$(\text{Built-Up Area})_{\text{cell}} - (\text{Area})_{\text{cell}}$	[%]

Moreover, a geometrical network for built-up areas has been created based on the methodology proposed by Marconcini et al. (2015). Each isolated cluster of pixel is transformed in a polygon. For each polygon, its centroid is computed. Starting for the centroid location, edges are constructed in order to connect neighbouring polygons in a radius of 5, 4, 3, 2 and 1 km (Figure 76).

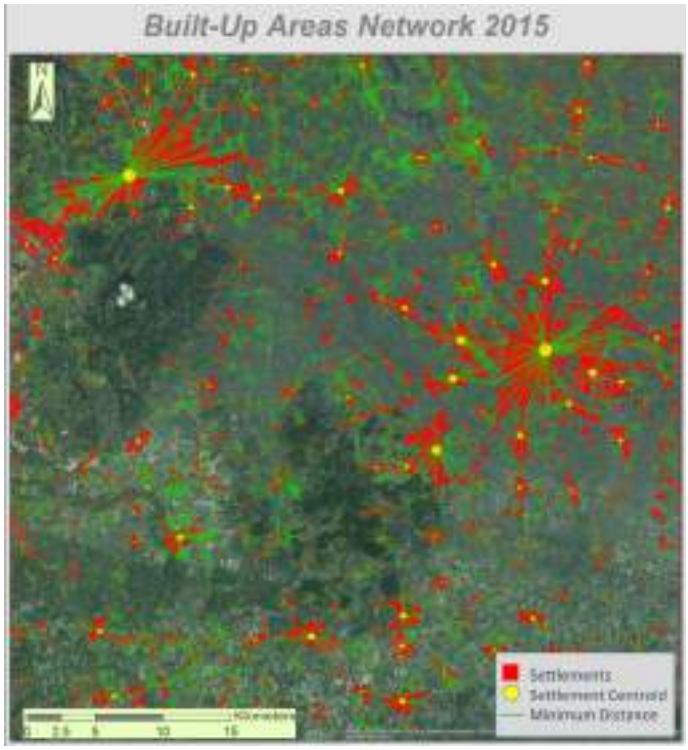

Figure 76 Network of built-up areas for the Veneto case study

This allowed us to extract several additional parameters that could be useful for the definition of vulnerability:

- Edges
  - Euclidean Nearest Neighbour Distance

- Minimum distance between each polygon
- Centroid distance

- Nodes
  - Degree centrality of each polygon (number of neighbours) in a radius of 5, 4, 3, 2 and 1 km.
  - Sum of areas of all neighbours in a radius of 5, 4, 3, 2 and 1 km

- Polygons
  - Area
  - Perimeter
  - Outer perimeter
  - Compactness

Network analysis is important in order to take into consideration the location of each settlement in its region and therefore allow to perform an analysis that is not only local, but also regional. For example, degree centrality gives a measure of the importance of a node in the network and how much information can be shared among the population in the area.

6.2.3 Indicators of social vulnerability

Table 27 shows the list of indicators of social vulnerability used in this work and their description.

Table 27 List of indicators used in the assessment of vulnerability

Variable	Indicators / Proxies	Definition
COPING CAPACITY		
Dependency Ratio	total labor force / total population [%]	Population with higher DR leads to lower CC and therefore increase vulnerability
Literacy Ratio	literate / total population [%]	Population with higher LR leads to higher CC and therefore decrease vulnerability
Population Age	(people > 74 yo + people < 5 yo) / total population [%]	Population with higher percentage of children or elderly have lower CC and therefore increase vulnerability

Foreigners	(Non-EU immigrant resident) / total population [%]	A higher number of foreigners leads to lower CC and increase vulnerability
New comers	Relative built-up areas growth [%]	Relative built-up area growth is used as a proxy of new comers. Higher percentage of new comers leads to lower CC and increase vulnerability
Compactness of urban areas	Mean Euclidean Nearest Neighbors distance [m]	It used a proxy for intervention capacity in case of disaster. An urban area more scattered will need more capacity in case of intervention, therefore this reduce CC and increase vulnerability
ADAPTIVE CAPACITY		
Employment	Active labor force / total population [%]	It is used as a proxy for income level. Given that in the area analyzed it can be hypnotized that everyone with an income have capacity to adapt, a higher percentage of employment increases AC and decreases vulnerability
Education	People with high school diploma / total population [%]	Higher percentage of educated people leads to an increased AC and decreases vulnerability
House Property	Rented houses / total houses	A higher percentage of rented houses lead to a decrease of AC and increase vulnerability
SUSCEPTIBILITY		
Building Age	[0.75*(Building older than 45 yo) + 0.25*(Building between 25 and 45 yo) + 0.05*(Buildings between 25 and 15 yo)] / total number of buildings	A higher percentage of old building increases susceptibility. The degree of susceptibility increases with the age of the building

Conservation Status	(0.25 * bad condition) + (0.75 * very bad condition) / number of buildings [%]	A higher percentage of buildings in bad condition increases susceptibility
Number of multi-storey buildings	Building with more than one storey / total number of buildings [%]	A higher percentage of building with more than one storey decrease susceptibility
Empty buildings	Number of empty buildings / Number of total buildings [%]	Social vulnerability does not apply to empty building, therefore this indicator is used to reduce vulnerability to only occupied buildings
Imperviousness	Mean value of imperviousness of the new built-up areas [%]	Increased imperviousness leads to an increased susceptibility

6.3 Social Vulnerability Index

To aggregate indicators, they need to be normalized. The generalized approach of value function has been followed, which is a mathematical representation of human judgements through the determination of a an upper and lower threshold and different levels of performance depending on the defined goals (Beinat & Nijkamp, 1998; Thieken et al., 2005). Normalized indicators have been then categorized into five classes as presented in Table 28, following the methodology presented in Giupponi et al. (2014).

Table 28 Definition of normalized scores

Normalized Value	Vulnerability Level
0	Not Vulnerable
0.25	Slightly Vulnerable
0.5	Highly Vulnerable
0.75	Extremely Vulnerable
1	Fully Vulnerable

Aggregation has been performed applying weighted average (WA) method (Birkmann et al., 2010), with weights as indicated in Figure 75 for coping capacity, adaptive capacity and susceptibility. For coping and adaptive capacity, equal weights have been given to each indicator:

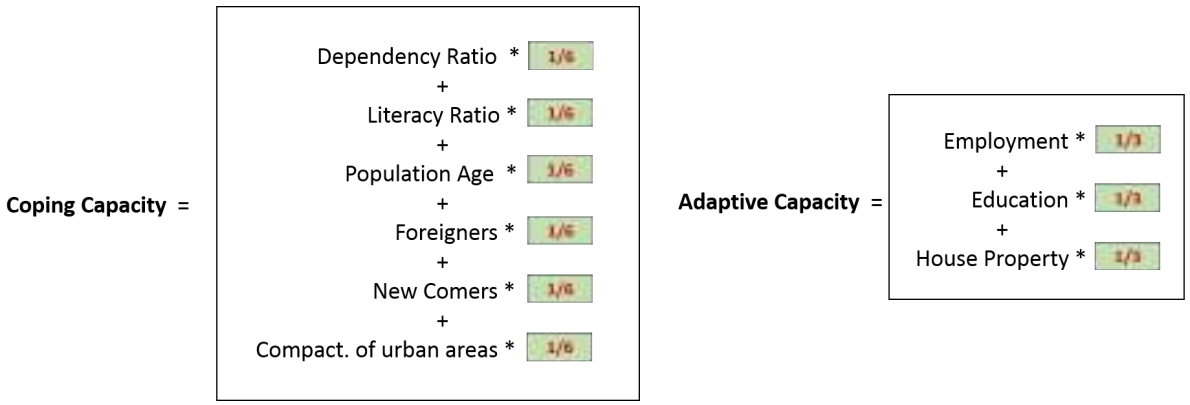

For susceptibility, the characteristics of the building have been first aggregated together using equal weights, then reduced by the percentage of empty buildings. To this component, which has a weight of 0.75, imperviousness has been added with a weight of 0.25:

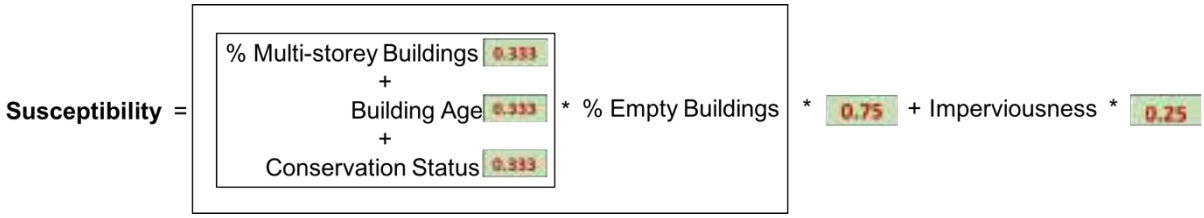

Summarizing, the final formula for the Social Vulnerability Index (SVI) is:

$$SVI = \sum_{i=1}^{n}\left[\left(\sum_{j=1}^{m_i}(x_{ij} * w_{ij}) * W_{ij}\right)\right]$$

where *i* is the number of the *n* principal components of vulnerability (coping capacity, adaptive capacity and susceptibility), *j* is the number of the *m* indicators in each component, *x* the indicator, *w* the weight assigned to the *j* indicator and *W* the weight assign to the i^{th} component. SVI has been computed for 1995 and 2015. In the case of 1995, which is used as a baseline, the indicator "New Comers" has not been used and therefore the weights used in the computation of cooping capacity is 1/5 instead of 1/6.

Each indicator has been normalized following the schemes presented in Figure 77. Following this methodology, the final Social Vulnerability Index is obtained with a score between 0 and 1, where 1 represent high vulnerability and 0 no vulnerability.

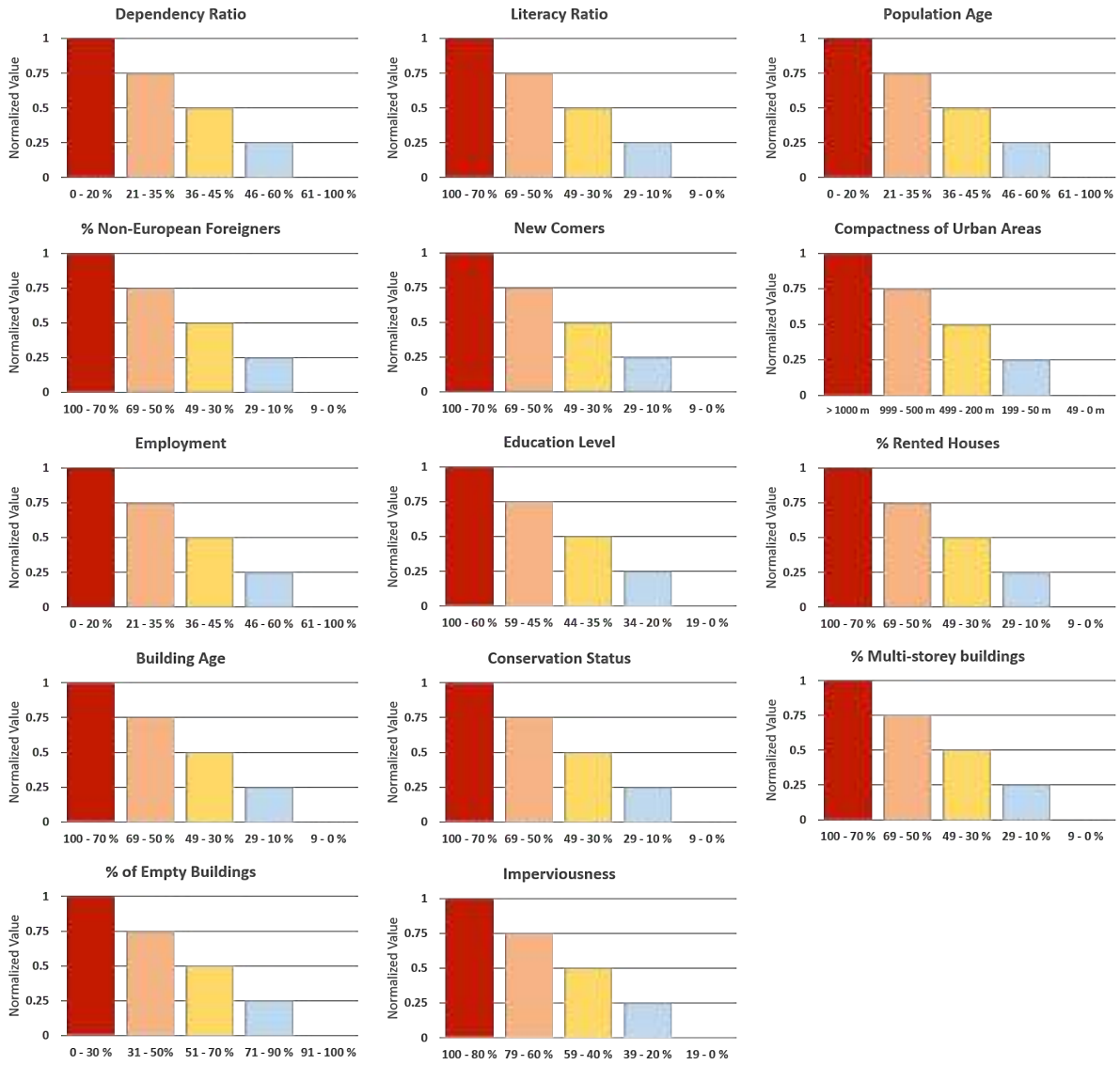

Figure 77 Normalization Functions

6.4 Results and discussions

Figure 78 shows coping capacity, adaptive capacity and susceptibility computed for year 1995 and 2015 at census cells level. Coping and adaptive capacity have to be read with inverse meaning, i.e. high value of them indicate higher vulnerability, lower values of capacity indicate lower vulnerability. Vulnerability connected to coping capacity is lower in cities and in more compact urban areas. A slightly increase of this component of vulnerability can be seen between 1995 and 2015. Looking in details to the data, we can see that the vulnerability connected to dependency ratio has increased on average by 2% and the one connected to the percentage of children and elderly has increased on average by 6%, mainly due to the decrease in percentage of children and teen-agers and the increment of elderly in the population. The vulnerability connected to the literacy ratio decreased on average by 3.5% and the one connected to the percentage of foreigners from non-EU countries increased on average of 1.8%.

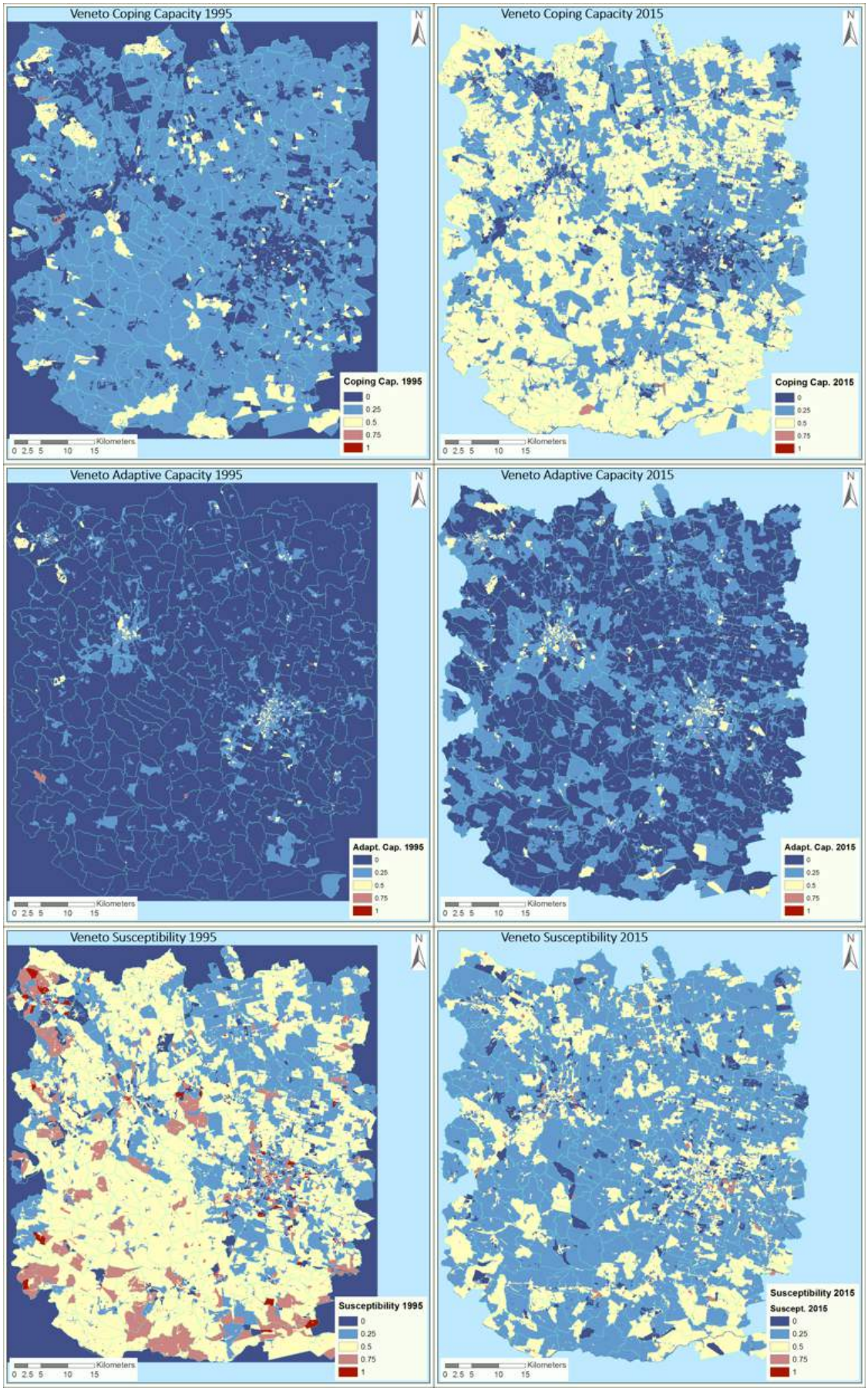

Figure 78 Coping capacity, adaptive capacity and susceptibility for 1995 and 2015

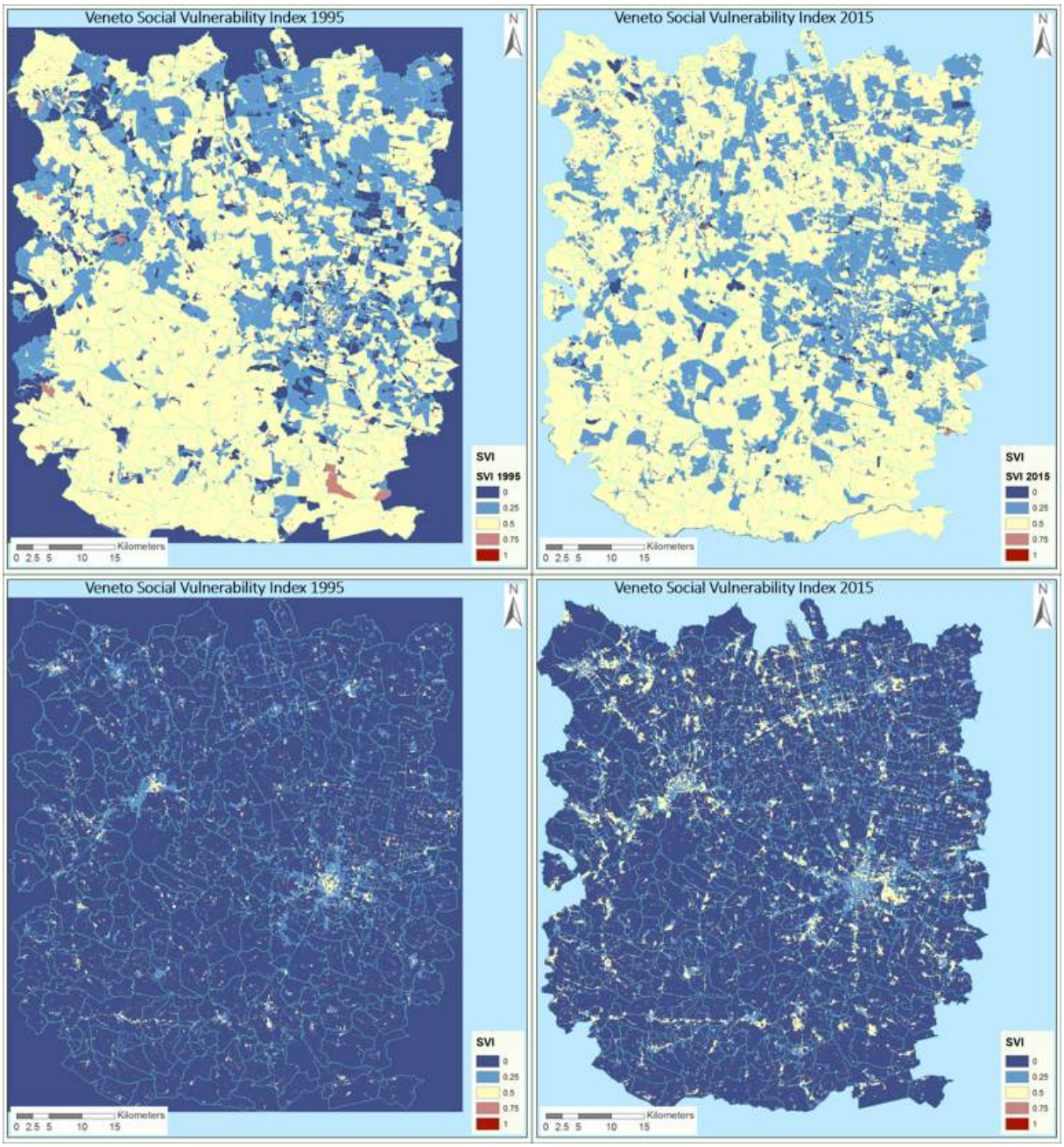

Figure 79 Social Vulnerability Index for 1995 and 2015 at census cell level (top) and reduced for only built/up areas (bottom)

Finally, the vulnerability connected to the compactness of the urban areas has decreased by 30%, to the new comers it has increased by 60%. Therefore, from the one hand a more compact built-up scenario can lead to a lower vulnerability, to the other hand a big increment of urban areas increases vulnerability, and this last one is the main responsible to this increment of vulnerability associated to coping capacity.

Regarding vulnerability connected to adaptive capacity, we can observe a more diverse behavior even if a slightly increase is noticeable in the rural areas. In this case, employment rate has decreased (0.6% on average) increasing vulnerability, education has also increased (13%) decreasing vulnerability, the percentage of rented house has decreased (3%) increasing

vulnerability. Education is the predominant factor in adaptation capacity and despite it decreasing effect in vulnerability, a general increment is noticed because of the non-homogeneous behavior of this indicator between cities and rural areas, in particular associated to the other two indicators.

Regarding susceptibility, we can notice a substantial reduction in vulnerability. The census data of 1991 did not report information about the status of conservation of the building and the number of storey for each building. Therefore these two components do not enter in the computation of vulnerability, with the result that building age receive full weight in the computation of susceptibility. Nevertheless, these two factors in 2011 has a very low weight since the percentage of building in bad and very bad conditions is negligible as well as the percentage of building with only one storey. The number of empty buildings is the one having the major effect, in fact there is an increment of almost 5% of empty buildings, reducing susceptibility. The increase of imperviousness (an average of 19%) has also a very low weight in the final computation of susceptibility.

Figure 79 shows the values of the SVI for 1995 and 2015. The results are also reported for built-up areas only. It can be observed a general slight increase of SVI, which can be attributed mainly to the widespread increase of vulnerability connected to coping capacity.

Finally, analyzing the value of SVI over the areas affected by the flood occurred in 2010 analyzed in Chapter 2 and 3, we find an increase of SVI of 7.6% (from 0.296 to 0.372).

6.5 Conclusions

This chapter presented a methodology for assessing social vulnerability to floods, which has been applied to the case study of Veneto. The combined use of socio-economic and remote sensing data allowed to characterize the three dimensions of vulnerability: coping and adaptive capacity for the social dimension, and susceptibility for the physical dimension. The analysis is showing an increased vulnerability in the area from 1995 to 2015, mainly due to the growth of built-up areas. Moreover, the increase of vulnerability in the same time frame, is shown also in the areas where the flood of 2010 occurred, highlighting the increased predisposition to damage and losses in the area.

Of the long list of data and indicators available from census and from urban growth analysis, only a subset of this has been used for the sake of simplicity. Nevertheless, more information could have been used. For example, the data about commuters could be useful for differentiating vulnerability during day and night time. The data about the population are aggregated at the level of census cell. Even though the cells are generally quite small, in some cases they are not. Moreover, their dimension is different from one census to the other, not allowing the direct comparison of certain parameters. For example, one cannot simply compute the difference of population between two different census for the same cell. This expose the need of a technique of dasymetric mapping which would allow to distribute population data at the pixel level. This is even more important in the case of developing country, such as Malawi. In this case in fact, there are no reliable or up to date data about population and the only data

available may be aggregated in cells of some square kilometres (for example the one provided by CIESIN which comes in cells of 12 by 12 Km)[1].

Moreover, the methodology was not applied to Malawi for the lack of reliable socio-economic data. Using as a starting point the analysis presented here, in the future a dasymetric mapping technique may be developed using the built-up area classification methodology, the urban growth analysis and settlement pattern analysis. This would allow to have disaggregated population data, which would allow to assess vulnerability to disaster with an increased precision.

This methodology for vulnerability assessment, even with some limitations, showed the potential of EO data to improving flood risk assessment. As already mentioned, one of the main limitations of the methodology is that it does not capture the dynamic of vulnerability, i.e. adaptation and levee effects (Di Baldassarre et al., 2015). Nevertheless, the use of new EO products is promising especially if coupled with the use of socio-economic data and embedded in emerging frameworks. In fact, new interdisciplinary approaches are emerging (e.g. complex system theories, socio-hydrology or socioecological systems), which are considering the dynamics of risk through the modelling of continuous interactions and mutual feedbacks between flooding and society (Di Baldassarre et al., 2013; Liu et al., 2007; Montanari et al., 2013; Ostrom, 2009; Srinivasan et al., 2012; Werner & McNamara, 2007). This research can be a starting point for new investigations with the aim of capturing the dynamics of vulnerability and exploring the impact of global changes on floodplains or urbanizing deltas. In fact, as reported by Di Baldassarre et al. (2015), there is the need to go beyond traditional scenarios and capture relevant dynamics driving changes in flood risk. EO data can play a key role in this framework and to help gaining further insights into the interplay between physical and social processes.

[1] http://sedac.ciesin.columbia.edu/data/sets/browse?facets=theme:population

7. Conclusions

.

This research had the aim of exploring the possibility of developing new EO applications for improving social vulnerability and flood risk assessment and taking advantage of the new and free EO big data. The idea was to provide new tools to the climate change adaptation community for monitoring disasters and planning disaster risk reduction measures. In chapter 1, the following research question has been posed:

Can Earth Observation data improve flood risk assessment in a global environmental change scenario?

In order to reply to this question, the three components of risk, hazard, exposure and vulnerability, have been investigated separately. Each component has been analysed and characterized using EO data. In the same chapter, the research question has been divided in four sub-questions. The first one was: "Can flood mapping be improved by means of EO big data?"

Chapter 3 dealt with this problem and presented a new methodology for flood mapping. The Normalized Difference Flood Index was developed by means of a statistical analysis of time-series of archive images and images of the event. The index allows a precise extraction of flooded area from SAR images and of areas with the presence of shallow water in short vegetation. The methodology is much less user-dependent than common flood mapping techniques, it can be easily automated and it is very robust since it performs equally well independently from the type of data used and the environment under analysis. In fact, floods in completely different regions have been analysed using different type of SAR data (different sensors, polarization and resolution). The obtained results show good agreement with products produced by third parties. Moreover, shallow water in short vegetation is derived, a product that usually is not reported by emergency management services.

The methodology is suitable for rapid mapping even though there could be a big amount of data to be processed, such as in the case of Uganda. The advent of new cloud computing capability, such as the one offered by Google Earth Engine, allows a fast analysis and export of the results and allows users with low capacity to perform high quality flood mapping. In fact, in Google Earth Engine all the S1 catalog is easily accessible online without the need of downloading the original products on a local computer. All the analysis can be performed online and only the final result has to be downloaded.

The methodology is suitable also as a support to flood risk assessment for long-term planning. The precision of the resulting maps is valuable in this framework, as well as for calibrating hydrological models.

One of the main limitations of the flood mapping methodology is that it did not improve flood mapping in urban areas. The resolution of S1 did not allow for detecting changes using only radar intensity and at the moment of the analysis no Single Look Complex data were available on the areas considered in this research. Therefore, it was not possible to exploit radar coherence to investigate the possibility of mapping floods in urban areas. Despite the very high resolution of CSK data, also in this case it was not possible to detect changes in urban areas. The main problem in this case was that the images were acquired with different incidence

angles introducing different geometrical distortions. Radar shadow over urban areas did not allow the detection of water. Nevertheless, the methodology is very promising and it leaves room for further investigations. Improving the methodology in urban areas is one of the potential development of this research.

The second sub-question posed in the introduction was: "Can flood depth estimation be improved and suitable for rapid assessment of impacts?"

Chapter 4 described the methodology for flood depth estimation, which builds on top of the one presented in Chapter 3. Flood maps obtained using the Normalized Difference Flood Index are superimposed to a high-resolution DEM. From a statistical analysis of elevation values along the contours of flooded areas, the elevation of the water plane is estimated allowing the computation of flood depth. The RMSE obtained on 150 validation points is 22.3 cm.

In comparison to hydrological models, this methodology is more easily implementable since less information is needed, only SAR images of the event and a DEM. Hydrological models need additional information for deriving flood extent and then depth, such as precipitation volumes, information about the soil, number and location of water pumps, etc.

Despite the very good results obtained, the methodology can be further improved and automatized. Future work may consider to integrate a DEM filling procedure for improving water level estimation (Huang et al., 2014). The use of a vegetation index such as NDVI, may be used to exclude wrong points along the contours. In fact, if presence of vegetation is found along the contour, that may indicate an error in the flood map and therefore the correspondent elevation would be an information to be discarded. Similarly, slope can be computed from the DEM and used to exclude errors due to radar shadow or misalignment between SAR and DEM data. Finally, the slope of the river could be taken into consideration during the estimation of water level allowing to derive better results for floods with fast dynamics.

The methodology presented answered the question that was posed at the beginning. Flood depth estimation can be obtained with a precision in the order of centimetres, when a high-resolution DEM is available. This could be a support both for rapid assessment of impacts, given the little amount of data needed and the fast computation required, and for long-term planning given the accurate derivation of depth values. Moreover, with a further development of the methodology, especially for what concerns automatization, it could also become an operative tool to be use in disaster management activities.

Together with the methodology presented in chapter 3, it improves the characterization of the hazard component in the flood risk assessment.

The third sub-question was: "Can land cover classification be improved and easily up to date?"

Chapter 5 is developed around a novel land cover classification method based on multi-temporal statistics of optical and SAR data. These statistics have been merged using Principal Component Analysis as a technique of data fusion. Finally, using a Support Vector Machine classification methodology, land cover maps have been derived for Veneto and Malawi. The use of statistics allows to distinguish spectral signatures of different land cover classes. The analysis of a big amount of data allows to create more robust statistics and improve the results. The data fusion step, not only allows to exploit information from both radar and optical data, but it also allows to reduce the size of the input dataset and improve the algorithm performances. The availability of new EO data, such as the data acquired by the Sentinel

constellation, allow to obtain land cover maps with an increased resolution and accuracy. Their frequency of acquisition allows to create updated maps whenever it is needed. Even though the accuracy obtained with the use of S2 data was slightly worse compared to the one obtained using Landsat 8 data (due to a sub-optimal distribution of acquisitions during the year), the big amount of data that S2 is providing now that it is fully operational, will allow, employing the methodology presented, to improve existing land cover maps, which can be a great advantage for flood risk assessment.

Therefore, chapter 5 answered to the third sub-question showing how the characterization of the exposure component of flood risk can be improved.

The fourth sub-question was: "Is it possible to retrieve meaningful indicators of social vulnerability from EO big data?"

The second part of chapter 5 presented a methodology for assessing urban growth and proposed a series of parameters that could be used as indicators of vulnerability. The analysis, applied to the case study of Veneto, showed interesting information about the development of built-up areas in the region, allowing to highlighting sprawls, more scattered settlements or more connected one. The analysis and the parameters proposed, other than being useful for characterizing vulnerability, could be useful for ecology- or biodiversity-based studies, for studying ecological corridors or the effect of conservation policies on biodiversity. Moreover, this analysis may be the base for a dasymetric mapping technique for distributing population data at pixel level, an information that would be very useful in the framework of disaster impact assessment and risk reduction.

Chapter 6 showed how social vulnerability can be defined using census data, the indicators derived in Chapter 5 from urban growth analysis and settlement patterns analysis. The methodology has been applied to the Veneto case study and both the physical component of vulnerability was considered as well as the social dimension, i.e. coping and adaptive capacity.

This methodology for vulnerability assessment, even with some limitations, showed the potential of EO data to improving social vulnerability and flood risk assessment. As mentioned in the chapter, one of the main limitations of the methodology is that it does not capture the dynamic of vulnerability, i.e. adaptation and levee effects (Di Baldassarre et al., 2015). Nevertheless, the use of new EO products is promising especially if coupled with the use of socio-economic data and embedded in emerging frameworks. Therefore, also this part of the research leaves rooms for further developments.

This research showed some of the potential of EO data in the framework of vulnerability and flood risk assessment. The methodologies developed have been applied to different case studies showing the big impact that EO can have either in data-reach and in data-poor contexts. In fact, in the case of Veneto, EO allows to increase the precision of the analysis, while in the case of Uganda or Malawi, the methodologies allow to derive information that is otherwise not existent of very difficult to retrieve.

Finally, given the focus of the research and the available resources in terms of time, it was not possible to develop all the aspects of social vulnerability. In particular, in chapter 6, the limits in terms of vulnerability dynamics have been highlighted as well as the need to capture "adaptation effect" and "levee effect". It seems promising to continue this work following emerging interdisciplinary frameworks that proposes to capture vulnerability dynamics, such as complex system theories, socioecological systems or socio-hydrology. With a vision to

contribute to the research activities of Ca' Foscari University and in particular of the Department of Economics and the Venice Centre of Climate Studies, these are fields that would put together the expertise of established scientists in the institute and for which the institute would benefit from new contributions (Balbi et al., 2013; Balbi et al., 2016; Giupponi et al., 2013; Mojtahed et al., 2016). In fact, agent-based modelling is a method that has got increasing momentum in social science. This kind of modelling prescribes interaction rules to individual and/or institutions (agents) and allow to include heterogeneity. The models compute agents' interaction at mircolevel and allow to observe behaviour at higher levels (Evans & Kelley, 2004; Gilbert, 2008; Gilbert & Terna, 2000). Another method that is increasingly used in the literature is the use of sets of differential equations that describe fundamental processes and systems behaviour. There are studies in neoclassic economic models or social science that make use of differential equations for dynamic modelling in order to understand complex systems (Di Baldassarre et al., 2015; Liu et al., 2015; Nefedov, 2003; Turchin & Korotayev, 2006; Van Emmerik et al., 2014). In particular, Di Baldassarre et al. (2015) proposed an approach for capturing dynamics of flood and societies using a set of differential equations. The human-flood interaction is conceptualized in a way where a community settles and develops in a flood-prone area to gain economic benefits. The occurrence of flood makes the memory of the community to change, which in turn modify population density or the protections to flood. The tendency to resettle and increase population density again resumes as the memory decays with time (Viglione et al., 2014).

The integration of these emerging methods with the techniques based on EO data presented in this work, can have an impact in the community of climate change adaptation and disaster risk reduction. This research created a solid base in the application of EO products in the field of risk and climate change adaptation, and it may become the starting point for future activities, with the aim to fill the gaps that emerged and to connect with new research frontiers.

8. REFERENCES

CHAPTER 1

Alfieri, L., Feyen, L., Salamon, P., Burek, P., & Thielen, J. (2016). Modelling the socio-economic impact of river floods in Europe. *Natural Hazards and Earth System Sciences Discussions*, 1–14. http://doi.org/doi:10.5194/nhess-2015-347

Altieri, L., Cocchi, D., Pezzi, G., Scott, E. M., & Ventrucci, M. (2014). Urban sprawl scatterplots for Urban Morphological Zones data. *Ecological Indicators*, *36*, 315–323. http://doi.org/10.1016/j.ecolind.2013.07.011

Amadio, M., Mysiak, J., Carrera, L., & Koks, E. (2016). Improving flood damage assessment models in Italy. *Natural Hazards*, *82*(3), 1–14. http://doi.org/10.1007/s11069-016-2286-0

Apel, H., Aronica, G. T., Kreibich, H., & Thieken, A. H. (2009). Flood risk analyses - How detailed do we need to be? *Natural Hazards*, *49*(1), 79–98. http://doi.org/10.1007/s11069-008-9277-8

Barros, V., Stocker, T. F., Qin, D., Dokken, D. J., Ebi, K. L., Mastrandrea, M. D., … Tignor, M. (2012). *IPCC, 2012 - Glossary of Terms*. *Managing the Risks of Extreme Events and Disasters to Advance Climate Change Adaptation*.

Batista e Silva, F., Gallego, J., & Lavalle, C. (2013). A high-resolution population grid map for Europe. *Journal of Maps*, *9*(1), 16–28. http://doi.org/10.1080/17445647.2013.764830

Bazi, Y., Bruzzone, L., & Melgani, F. (2005). An unsupervised approach based on the generalized Gaussian model to automatic change detection in multitemporal SAR images. *Geoscience and Remote Sensing, IEEE Transactions on*, *43*(4), 874–887. http://doi.org/10.1109/TGRS.2004.842441

Brivio, P. A., Colombo, R., Maggi, M., & Tomasoni, R. (2002). Integration of remote sensing data and GIS for accurate mapping of flooded areas Integration of remote sensing data and GIS for accurate mapping of ooded areas. *International Journal of Remote SensingOnline) Journal International Journal of Remote Sensing Int. J. Remote Sensing*, *233*(3), 143–1161. http://doi.org/10.1080/01431160010014729

Copernicus - The European Earth Observation Programme. Retrieved from http://www.copernicus.eu

Crichton, D. (1999). Natural Disaster Management: A Presentation to Commemorate the International Decade for Natural Disaster Reduction (IDNDR).

Cutter, S. L., Boruff, B. J., & Shirley, W. L. (2003). Social Vulnerability to Environmental Hazards n. *Social Science Quarterly*, *84*(2), 242–261. http://doi.org/10.1111/1540-6237.8402002

de Moel, H., & Aerts, J. C. J. H. (2011). Effect of uncertainty in land use, damage models and inundation depth on flood damage estimates. *Natural Hazards*, *58*(1), 407–425. http://doi.org/10.1007/s11069-010-9675-6

de Moel, H., Jongman, B., Kreibich, H., Merz, B., Penning-Rowsell, E., & Ward, P. J. (2015). Flood risk assessments at different spatial scales. *Mitigation and Adaptation Strategies for Global Change*, (June). http://doi.org/10.1007/s11027-015-9654-z

De Sherbinin, A. M. (2014). *Mapping the unmeasurable? Spatial analysis of vulnerability to climate change and climate variability*. http://doi.org/10.3990/1.9789036538091

Esch, T., Taubenböck, H., Tal, A., Feigenwinter, C., & Parlow, E. (2013). Exploiting Earth Observation in Sustainable Urban Planning and Management - the GEOURBAN Project, *856*, 13–16.

EU 2007. Directive 2007/60/EC of the European Parliament and of the Council. *Official Journal of the European Union*, *288*(2455), 27–34. http://doi.org/English

Fekete, A. (2009). Validation of a social vulnerability index in context to river-floods in Germany. *Natural Hazards and Earth System Science*, *9*(2), 393–403. http://doi.org/10.5194/nhess-9-393-2009

Gain, A. K., Mojtahed, V., & Biscaro, C. (2015). An integrated approach of flood risk assessment in the eastern part of Dhaka City. *Natural Hazards*, *79*(3), 1499–1530. http://doi.org/10.1007/s11069-015-1911-7

Geoland-2. http://www.copernicus.eu/projects/geoland2

Giupponi, C., & Biscaro, C. (2015). Vulnerabilities — bibliometric analysis and literature review of evolving concepts. *Environmental Research Letters*, 0. http://doi.org/10.1088/1748-9326/0/0/000000

Giupponi, C., Mojtahed, V., Gain, A. K., & Balbi, S. (2013). Integrated Assessment of Natural Hazards and Climate Change Adaptation : I . The KULTURisk Methodological Framework, (6).

Giupponi, C., Mojtahed, V., Gain, A. K., Biscaro, C., & Balbi, S. (2014). Integrated Risk Assessment of Water Related disasters, 163–200.

Giupponi, C., Paron, P., & Di Baldassarre, G. (2014). Integrated risk assessment of water-

related disasters. *Hydro-Meteorological Hazards, Risks, and Disasters, Elsevier*, 163–200.
Global Land Cover 2000. Retrieved from http://bioval.jrc.ec.europa.eu/products/glc2000/glc2000.php
GlobCover. Retrieved from http://due.esrin.esa.int/globcover/
Guo, H.-D., Zhang, L., & Zhu, L.-W. (2015). Earth observation big data for climate change research. *Advances in Climate Change Research*, *6*(2), 108–117. http://doi.org/10.1016/j.accre.2015.09.007
Guo, H., Wang, L., Chen, F., & Liang, D. (2014). Scientific big data and Digital Earth. *Chinese Science Bulletin*, *59*(35), 5066–5073. http://doi.org/10.1007/s11434-014-0645-3
Jongman, B., Kreibich, H., Apel, H., Barredo, J. I., Bates, P. D., Feyen, L., … Ward, P. J. (2012). Comparative flood damage model assessment: Towards a European approach. *Natural Hazards and Earth System Science*, *12*(12), 3733–3752. http://doi.org/10.5194/nhess-12-3733-2012
Kovalskyy, V. et al. (2014). Web-Enabled Landsat Data (WELD) For Monitoring Contemporary Terrestrial Change Nearly Everywhere. In *Frontiers in Earth Observation for Land System Science*. Berlin.
Langanke, T. et al. (2014). Improving Observation of Land Transformations: Copernicus Land Services in Europe. In *Frontiers in Earth Observation for Land System Science*. Berlin.
Longo, E., Aronica, G. T., Baldassarre, G. Di, & Mukolwe, M. (2016). Assessing fluvial flood risk in urban environments : a case study, *11007*, 4–8.
Luca, C. De, Mojtahed, V., Gain, A., Balbi, S., Ferri, M., & Giupponi, C. (2014). Socio-Economic Regional Risk Assessment (SERRA) application to flood risk in the Vipacco Basin (north-east Italy). *7th Intl. Congress on Env. Modelling and Software, San Diego, CA, USA*.
Martinis, S., Kersten, J., & Twele, A. (2015). A fully automated TerraSAR-X based flood service. *ISPRS Journal of Photogrammetry and Remote Sensing*, *104*, 203–212. http://doi.org/10.1016/j.isprsjprs.2014.07.014
Martinis, S., Twele, a., & Voigt, S. (2009). Towards operational near real-time flood detection using a split-based automatic thresholding procedure on high resolution TerraSAR-X data. *Natural Hazards and Earth System Science*, *9*(2), 303–314. http://doi.org/10.5194/nhess-9-303-2009
Mason, D. C., Horritt, M. S., Dall'Amico, J. T., Scott, T. R., & Bates, P. D. (2007). Improving river flood extent delineation from synthetic aperture radar using airborne laser altimetry. *IEEE Transactions on Geoscience and Remote Sensing*, *45*(12), 3932–3943. http://doi.org/10.1109/TGRS.2007.901032
Matgen, P., Schumann, G., Henry, J.-B., Hoffmann, L., & Pfister, L. (2007). Integration of SAR-derived river inundation areas, high-precision topographic data and a river flow model toward near real-time flood management. *International Journal of Applied Earth Observation and Geoinformation*, *9*(3), 247–263. http://doi.org/10.1016/j.jag.2006.03.003
Merz, B., Kreibich, H., Schwarze, R., & Thieken, a. (2010). Review article "assessment of economic flood damage." *Natural Hazards and Earth System Science*, *10*(8), 1697–1724. http://doi.org/10.5194/nhess-10-1697-2010
Mojtahed, V., Giupponi, C., Biscaro, C., Gain, A. K., & Balbi, S. (2013). Integrated Assessment of Natural Hazards and Climate Change Adaptation : II . The SERRA Methodology, (7).
MunichRE. (2014). *Loss events worldwide 2014 Percentage distribution*.
Mysiak, J. et al. (2013). Towards a potential European flood impact database. *EEA – JRC – ETC/CCA Joint Technical Paper*.
Nico, G., Pappalepore, M., Pasquariello, G., Refice, a., & Samarelli, S. (2000). Comparison of SAR amplitude vs. coherence flood detection methods - a GIS application. *International Journal of Remote Sensing*, *21*(8), 1619–1631. http://doi.org/10.1080/014311600209931
O'Grady, D., Leblanc, M., & Gillieson, D. (2011). Use of ENVISAT ASAR Global Monitoring Mode to complement optical data in the mapping of rapid broad-scale flooding in Pakistan. *Hydrology and Earth System Sciences*, *15*(11), 3475–3494. http://doi.org/10.5194/hess-15-3475-2011
Oppenheimer, M., Campos, M., Warren, R., Birkmann, J., Luber, G., O'Neill, B. C., & Takahashi, K. (2014). *Emergent risks and key vulnerabilities. In: Climate Change 2014: Impacts, Adaptation, and Vulnerability. Part A: Global and Sectoral Aspects. Contribution of Working Group II to the Fifth Assessment Repor t of the Intergovernmental Panel on Climate Change*. Cambridge University Press, Cambridge, United Kingdom and New York, NY, USA.
Ronco, P., Bullo, M., Torresan, S., Critto, A., Olschewski, R., Zappa, M., & Marcomini, A. (2015). KULTURisk regional risk assessment methodology for water-related natural hazards - Part 2: Application to the Zurich case study. *Hydrology and Earth System Sciences*, *19*(3), 1561–1576. http://doi.org/10.5194/hess-19-1561-2015
Scorzini, A. R., & Frank, E. (2015). Flood damage curves : new insights from the 2010 flood in Veneto , Italy, 1–12. http://doi.org/10.1111/jfr3.12163
Smith, D. I. (1994). Flood damage estimation - a review of urban stage-damage curves and loss functions. *Water SA*.

Thieken, A. H., Müller, M., Kleist, L., Seifert, I., Borst, D., & Werner, U. (2006). Regionalisation of asset values for risk analyses. *Natural Hazards and Earth System Science*, *6*(2), 167–178. http://doi.org/10.5194/nhess-6-167-2006
Turner, B. L., Kasperson, R. E., Meyer, W. B., Dow, K. M., Golding, D., Kasperson, J. X., … Ratick, S. J. (1990). Two types of global environmental change. Definitional and spatial-scale issues in their human dimensions. *Global Environmental Change*, *1*(1), 14–22. http://doi.org/10.1016/0959-3780(90)90004-S
UNIDSR. (2015). *Making Development Sustainable: The Future of Disaster Risk Management. Global Assessment Report on Disaster Risk Reduction*.
Vaz, E., & Nijkamp, P. (2015). Gravitational forces in the spatial impacts of urban sprawl : An investigation of the region of Veneto , Italy. *Habitat International*, *45*, 99–105. http://doi.org/10.1016/j.habitatint.2014.06.024
Waisurasingha, C., Aniya, M., Hirano, A., Kamusoko, C., & Sommut, W. (2007). APPLICATION OF C-BAND SYNTHETIC APERTURE RADAR DATA AND DIGITAL ELEVATION MODEL TO EVALUATE THE CONDITIONS OF FLOOD-AFFECTED PADDIES: CHI RIVER BASIN, THAILAND.
Wilson, B. a, & Rashid, H. (2005). Monitoring the 1997 flood in the Red River valley. *Canadian Geographer*, *49*(1), 100–109.
Wolters, M. L., & Kuenzer, C. (2015). Vulnerability assessments of coastal river deltas - categorization and review. *Journal of Coastal Conservation*. http://doi.org/10.1007/s11852-015-0396-6
Wurm, M., Taubenböck, H., Krings, S., Birkmann, J., & Roth, A. (2009). Derivation of population distribution for vulnerability assessment in flood-prone German cities using multisensoral remote sensing data, *7478*(0), 1–12. http://doi.org/10.1117/12.830318

CHAPTER 2

Coughlan De Perez, E., Van Den Hurk, B., Van Aalst, M. K., Jongman, B., Klose, T., & Suarez, P. (2015). Forecast-based financing: An approach for catalyzing humanitarian action based on extreme weather and climate forecasts. *Natural Hazards and Earth System Sciences*, *15*(4), 895–904. http://doi.org/10.5194/nhess-15-895-2015
Field, C.B., V.R. Barros, D.J. Dokken, K.J. Mach, M. D. M., T.E. Bilir, M. Chatterjee, K.L. Ebi, Y.O. Estrada, R.C. Genova, B. Girma, E.S. Kissel, A.N. Levy, S. M., & P.R. Mastrandrea, and L. L. W. (2014). Summary for polycimaker. *Climate Change 2014: Impact, Adaptation, and Vulnerability*, *Part A: Gl*, 1–32.
Floris, M., D'Alpaos, a., De Agostini, a., Stevan, G., Tessari, G., & Genevois, R. (2012). A process-based model for the definition of hydrological alert systems in landslide risk mitigation. *Natural Hazards and Earth System Science*, *12*, 3343–3357. http://doi.org/10.5194/nhess-12-3343-2012
Fregolent, L. (2005). *Governare la dispersione*. (Franco Angeli, Ed.). Milano.
Hachigonta, S., Nelson, G., Thomas, T., & Sibanda, L. (2013). Southern African agriculture and climate change – A comprehensive analysis. *International Food Policy Research Institute (IFPRI), Washington, DC*, 370 pp.
IPCC. (2012). *Managing the Risks of Extreme Events and Disasters to Advance Climate Change Adaptation - SREX*. (C. B. Field, V. Barros, T. F. Stocker, & Q. Dahe, Eds.). Cambridge: Cambridge University Press. http://doi.org/10.1017/CBO9781139177245
Malawi PDNA Report (2015). *Malawi 2015 Floods Post Disaster Needs Assessment Report*, Malawi Government
Ranzato, M. (2011). Integrated water design for a decentralized urban landscape, Doctoral Thesis, Doctoral School in Environmental Engineering, University of Trento.
Regione del Veneto. (2011). Veneto. La Grande Alluvione.
Regione del Veneto (2010), Scheda Evento "Pluvio": 31 Ottobre - 02 Novembre 2010. Centro Funzionale Decentrato, Regione del Veneto (2010).
Scorzini, A. R., & Frank, E. (2015). Flood damage curves: New insights from the 2010 flood in Veneto, Italy. *Journal of Flood Risk Management*, 1–12. http://doi.org/10.1111/jfr3.12163
Sofia, G., Prosdocimi, M., Dalla Fontana, G., & Tarolli, P. (2014). Modification of artificial drainage networks during the past half-century: Evidence and effects in a reclamation area in the Veneto floodplain (Italy). *Anthropocene*, *6*, 48–62. http://doi.org/10.1016/j.ancene.2014.06.005
Stringer, L., Mkwambisi, D., Dougill, A., & Dyer, J. (2010). Adaptation to climate change and desertification: Perspectives from national policy and autonomous practice in Malawi. *Climate and Development*, *2*, 145–160.
Tall, A., Patt, A., & Fritz, S. (2013). Reducing vulnerability to hydro-meteorological extremes in Africa. A qualitative assessment of national climate disaster management policies: Accounting for heterogeneity. *Weather and Climate Extremes*, *1, 4-16*.
Vaz, E., & Nijkamp, P. (2015). Gravitational forces in the spatial impacts of urban sprawl: An investigation of the region of Veneto, Italy. *Habitat International*, *45*(P2), 99–105. http://doi.org/10.1016/j.habitatint.2014.06.024
Venäläinen, A., Pilli-sihvola, K., Tuomenvirta, H., Ruuhela, R., Kululanga, E., Mtilatila, L., … Nkomoki, J. (2016). Analysis of the meteorological capacity for early warnings in Malawi and Zambia, *5529*(May). http://doi.org/10.1080/17565529.2015.1034229

Washington, D. T. I. B. for, & Reconstruction and Development/The World Bank. (2010). Natural hazards, unnatural disasters: The economics of effective prevention. *The World Bank and The United Nations*.
Zollo, A. L., Rillo, V., & Bucchignani, E. (2015). Extreme temperature and precipitation events over Italy : assessment of high-resolution simulations with COSMO-CLM and future scenarios. http://doi.org/10.1002/joc.4401

CHAPTER 3

Bazi, Y., Bruzzone, L., & Melgani, F. (2005). An unsupervised approach based on the generalized Gaussian model to automatic change detection in multitemporal SAR images. *Geoscience and Remote Sensing, IEEE Transactions on*, *43*(4), 874–887. http://doi.org/10.1109/TGRS.2004.842441
Boni, G., Ferraris, L., Pulvirenti, L., Squicciarino, G., Pierdicca, N., Member, S., … Pagliara, P. (2016). A Prototype System for Flood Monitoring Based on Flood Forecast Combined with COSMO-SkyMed and Sentinel-1 Data, 1–12.
Brivio, P. A., Colombo, R., Maggi, M., & Tomasoni, R. (2002). Integration of remote sensing data and GIS for accurate mapping of flooded areas Integration of remote sensing data and GIS for accurate mapping of ooded areas. *International Journal of Remote SensingOnline) Journal International Journal of Remote Sensing Int. J. Remote Sensing*, *233*(3), 143–1161. http://doi.org/10.1080/01431160010014729
Di Baldassarre, G., Schumann, G., Brandimarte, L., & Bates, P. (2011). Timely Low Resolution SAR Imagery To Support Floodplain Modelling: A Case Study Review. *Surveys in Geophysics*, *32*(3), 255–269. http://doi.org/10.1007/s10712-011-9111-9
ESA EOLI. Retrieved from https://earth.esa.int/web/guest/eoli
Giustarini, L., Hostache, R., Matgen, P., Schumann, G. J., Bates, P. D., & Mason, D. C. (2013). A Change Detection Approach to Flood Mapping in Urban Areas Using TerraSAR-X. *IEEE Transactions on Geoscience and Remote Sensing*, *51*(4), 2417–2430. http://doi.org/10.1109/TGRS.2012.2210901
Henry, J. B., Chastanet, P., Fellah, K., & Desnos, Y. L. (2006). Envisat multi-polarized ASAR data for flood mapping. *International Journal of Remote Sensing*, *27*(9–10), 1921–1929. http://doi.org/Doi 10.1080/01431160500486724
Horritt, M. S. (1999). A statistical active contour model for SAR image segmentation. *Image and Vision Computing*, *17*(3–4), 213–224. http://doi.org/10.1016/S0262-8856(98)00101-2
Horritt, M. S., Mason, D. C., & Luckman, a. J. (2001). Flood boundary delineation from Synthetic Aperture Radar imagery using a statistical active contour model. *International Journal of Remote Sensing*, *22*(October 2014), 2489–2507. http://doi.org/10.1080/01431160152497691
Liu, Y., Nishiyama, S., & Yano, T. (2004). Analysis of four change detection algorithms in bi-temporal space with a case study. *International Journal of Remote Sensing*, *25*(11), 2121–2139. http://doi.org/10.1080/01431160310001606647
Long, S., Fatoyinbo, T. E., & Policelli, F. (2014). Flood extent mapping for Namibia using change detection and thresholding with SAR. *Environmental Research Letters*, *9*(3), 35002. http://doi.org/10.1088/1748-9326/9/3/035002
Lu, D., Mausel, P., Brondízio, E., & Moran, E. (2004). Change detection techniques. *International Journal of Remote Sensing*, *25*(12), 2365–2401. http://doi.org/10.1080/0143116031000139863
Manjusree, P., Prasanna Kumar, L., Bhatt, C. M., Rao, G. S., & Bhanumurthy, V. (2012). Optimization of threshold ranges for rapid flood inundation mapping by evaluating backscatter profiles of high incidence angle SAR images. *International Journal of Disaster Risk Science*, *3*(2), 113–122. http://doi.org/10.1007/s13753-012-0011-5
Martinis, S., Kersten, J., & Twele, A. (2015). A fully automated TerraSAR-X based flood service. *ISPRS Journal of Photogrammetry and Remote Sensing*, *104*, 203–212. http://doi.org/10.1016/j.isprsjprs.2014.07.014
Martinis, S., Twele, A., Strobl, C., Kersten, J., & Stein, E. (2013). A multi-scale flood monitoring system based on fully automatic MODIS and terraSAR-X processing chains. *Remote Sensing*, *5*(11), 5598–5619. http://doi.org/10.3390/rs5115598
Martinis, S., Twele, a., & Voigt, S. (2009). Towards operational near real-time flood detection using a split-based automatic thresholding procedure on high resolution TerraSAR-X data. *Natural Hazards and Earth System Science*, *9*(2), 303–314. http://doi.org/10.5194/nhess-9-303-2009
Mason, D. C., Horritt, M. S., Dall'Amico, J. T., Scott, T. R., & Bates, P. D. (2007). Improving river flood extent delineation from synthetic aperture radar using airborne laser altimetry. *IEEE Transactions on Geoscience and Remote Sensing*, *45*(12), 3932–3943. http://doi.org/10.1109/TGRS.2007.901032
Mason, D. C., Schumann, G. J. P., Neal, J. C., Garcia-Pintado, J., & Bates, P. D. (2012). Automatic near real-time selection of flood water levels from high resolution Synthetic Aperture Radar images for assimilation into hydraulic models: A case study. *Remote*

Sensing of Environment, *124*, 705–716. http://doi.org/10.1016/j.rse.2012.06.017
Matgen, P., Hostache, R., Schumann, G., Pfister, L., Hoffmann, L., & Savenije, H. H. G. (2011). Towards an automated SAR-based flood monitoring system : Lessons learned from two case studies. *Physics and Chemistry of the Earth*, *36*(7–8), 241–252. http://doi.org/10.1016/j.pce.2010.12.009
Matgen, P., Schumann, G., Henry, J.-B., Hoffmann, L., & Pfister, L. (2007). Integration of SAR-derived river inundation areas, high-precision topographic data and a river flow model toward near real-time flood management. *International Journal of Applied Earth Observation and Geoinformation*, *9*(3), 247–263. http://doi.org/10.1016/j.jag.2006.03.003
Nico, G., Pappalepore, M., Pasquariello, G., Refice, a., & Samarelli, S. (2000). Comparison of SAR amplitude vs. coherence flood detection methods - a GIS application. *International Journal of Remote Sensing*, *21*(8), 1619–1631. http://doi.org/10.1080/014311600209931
O'Grady, D., Leblanc, M., & Gillieson, D. (2011). Use of ENVISAT ASAR Global Monitoring Mode to complement optical data in the mapping of rapid broad-scale flooding in Pakistan. *Hydrology and Earth System Sciences*, *15*(11), 3475–3494. http://doi.org/10.5194/hess-15-3475-2011
Paloscia, S., Pettinato, S., Santi, E., Notarnicola, C., Pasolli, L., & Reppucci, A. (2013). Soil moisture mapping using Sentinel-1 images: Algorithm and preliminary validation. *Remote Sensing of Environment*, *134*, 234–248. http://doi.org/10.1016/j.rse.2013.02.027
Pulvirenti, L., Chini, M., Marzano, F. S., Pierdicca, N., Mori, S., Guerriero, L., … Candela, L. (2012). Detection of floods and heavy rain using Cosmo-SkyMed data: The event in Northwestern Italy of November 2011. *International Geoscience and Remote Sensing Symposium (IGARSS)*, (November 2011), 3026–3029. http://doi.org/10.1109/IGARSS.2012.6350788
Pulvirenti, L., Chini, M., Member, S., Pierdicca, N., Member, S., & Boni, G. (2015). Use of SAR Data for Detecting Floodwater in Urban and Agricultural Areas : The Role of the Interferometric Coherence, (OCTOBER), 1–13. http://doi.org/10.1109/TGRS.2015.2482001
Pulvirenti, L., Marzano, F. S., Pierdicca, N., Mori, S., & Chini, M. (2014). Discrimination of water surfaces, heavy rainfall, and wet snow using COSMO-SkyMed observations of severe weather events. *IEEE Transactions on Geoscience and Remote Sensing*, *52*(2), 858–869. http://doi.org/10.1109/TGRS.2013.2244606
Pulvirenti, L., Pierdicca, N., Chini, M., & Guerriero, L. (2013). Monitoring flood evolution in vegetated areas using cosmo-skymed data: The tuscany 2009 case study. *IEEE Journal of Selected Topics in Applied Earth Observations and Remote Sensing*, *6*(4), 1807–1816. http://doi.org/10.1109/JSTARS.2012.2219509
Schaber, G. G., McCauley, J. F., & Breed, C. S. (1997). The use of multifrequency and polarimetric SIR-C/X-SAR data in geologic studies of Bir Safsaf, Egypt. *Remote Sensing of Environment*, *59*(2), 337–363. http://doi.org/10.1016/S0034-4257(96)00143-5
Schumann, G., Bates, P. D., Horritt, M. S., Matgen, P., & Pappenberger, F. (2009). Progress in integration of remote sensing-derived flood extent and stage data and hydraulic models. *Reviews of Geophysics*, *47*(3). http://doi.org/10.1029/2008RG000274
Schumann, G., Di Baldassarre, G., Alsdorf, D., & Bates, P. D. (2010). Near real-time flood wave approximation on large rivers from space: Application to the River Po, Italy. *Water Resources Research*, *46*(5), 1–8. http://doi.org/10.1029/2008WR007672
Serpico, S. B., Dellepiane, S., Boni, G., Moser, G., Angiati, E., Rudari, R., … Rudari, R. (2012). Remote Sensing Images for Flood Monitoring and Damage Evaluation. *Proceedings of the IEEE*, *100*(10), 2946–2970. http://doi.org/10.1109/JPROC.2012.2198030
Smith, L. C. (1997). Satellite remote sensing of river inundation area, stage, and discharge: A review. *Hydrological Processes*, *11*(10), 1427–1439. http://doi.org/10.1002/(sici)1099-1085(199708)11:10<1427::aid-hyp473>3.0.co;2-s
Torres, R., Snoeij, P., Geudtner, D., Bibby, D., Davidson, M., Attema, E., … Rostan, F. (2012). GMES Sentinel-1 mission. *Remote Sensing of Environment*, *120*, 9–24. http://doi.org/10.1016/j.rse.2011.05.028
Waisurasingha, C., Aniya, M., Hirano, A., Kamusoko, C., & Sommut, W. (2007). APPLICATION OF C-BAND SYNTHETIC APERTURE RADAR DATA AND DIGITAL ELEVATION MODEL TO EVALUATE THE CONDITIONS OF FLOOD-AFFECTED PADDIES: CHI RIVER BASIN, THAILAND.
Wilson, B. a, & Rashid, H. (2005). Monitoring the 1997 flood in the Red River valley. *Canadian Geographer*, *49*(1), 100–109.
Yan, K., Di Baldassarre, G., Solomatine, D. P., & Schumann, G. J.-P. (2015). A review of low-cost space-borne data for flood modelling: topography, flood extent and water level. *Hydrological Processes*, n/a-n/a. http://doi.org/10.1002/hyp.10449

CHAPTER 4

Amadio, M., Mysiak, J., Carrera, L., & Koks, E. (2016). Improving flood damage assessment models in Italy. *Natural Hazards*, *82*(3), 1–14. http://doi.org/10.1007/s11069-016-2286-0

Brown, K. M., & Brownett, J. M. (2016). Progress in operational flood mapping using satellite synthetic aperture radar (SAR) and airborne light detection and ranging (LiDAR) data. http://doi.org/10.1177/0309133316633570

Carrera, L., Standardi, G., Bosello, F., & Mysiak, J. (2013). Assessing direct and indirect economic impacts of a flood event through the integration of spatial and computable general equilibrium modelling. *CMCC Research*, *63*, 1–27. http://doi.org/10.1016/j.envsoft.2014.09.016

D'Alpaos, L., Brath, A., & Fioravante, V. (2014). Relazione tecnico-scientifica sulle cause del collasso dell ' argine del fiume Secchia avvenuto il giorno 19 gennaio 2014 presso la frazione San Matteo.

Eineder, M., Fritz, T., Abdel Jaber, W., Rossi, C., & Breit, H. (2012). Decadal Earth topography dynamics measured with TanDEM-X and SRTM. In *International Geoscience and Remote Sensing Symposium (IGARSS)* (pp. 1916–1919). http://doi.org/10.1109/IGARSS.2012.6351130

Farr, T. G., Rosen, P. A., Caro, E., Crippen, R., Duren, R., Hensley, S., … Alsdorf, D. E. (2007). The shuttle radar topography mission. *Reviews of Geophysics*, *45*(2). http://doi.org/10.1029/2005RG000183

Gupta, R. P., & Banerji, S. (1985). Monitoring of reservoir volume using LANDSAT data. *Journal of Hydrology*, *77*(1–4), 159–170. http://doi.org/10.1016/0022-1694(85)90204-5

Huang, C., Chen, Y., Wu, J., Chen, Z., Li, L., Liu, R., & Yu, J. (2014). Integration of remotely sensed inundation extent and high-precision topographic data for mapping inundation depth. *2014 The 3rd International Conference on Agro-Geoinformatics, Agro-Geoinformatics 2014*, 1–4. http://doi.org/10.1109/Agro-Geoinformatics.2014.6910580

Iervolino, P., Guida, R., Iodice, A., & Riccio, D. (2015). FloodingWater Depth Estimation With High-Resolution SAR, *53*(5), 2295–2307.

Mason, D. C., Davenport, I. J., Flather, R. a., Gurney, C., Robinson, G. J., & Smith, J. a. (2001). A Sensitivity Analysis of the Waterline Method of Constructing a Digital Elevation Model for Intertidal Areas in ERS SAR scene of Eastern England. *Estuarine, Coastal and Shelf Science*, *53*(6), 759–778. http://doi.org/10.1006/ecss.2000.0789

Matgen, P., Schumann, G., Henry, J.-B., Hoffmann, L., & Pfister, L. (2007). Integration of SAR-derived river inundation areas, high-precision topographic data and a river flow model toward near real-time flood management. *International Journal of Applied Earth Observation and Geoinformation*, *9*(3), 247–263. http://doi.org/10.1016/j.jag.2006.03.003

Mojtahed, V., Giupponi, C., Biscaro, C., Gain, A. K., & Balbi, S. (2013). Integrated Assessment of Natural Hazards and Climate Change Adaptation : II . The SERRA Methodology, (7).

Oberstadler, R., H??nsch, H., & Huth, D. (1996). Assessment of the mapping capabilities of ERS-1 SAR data for flood mapping: A case study in Germany. *European Space Agency, (Special Publication) ESA SP*, *11*(383), 247–252. http://doi.org/10.1002/(SICI)1099-1085(199708)11:10<1415::AID-HYP532>3.0.CO;2-2

Schumann, G., Hostache, R., Puech, C., Hoffmann, L., Matgen, P., Pappenberger, F., & Pfister, L. (2007). High-resolution 3-D flood information from radar imagery for flood hazard management. *IEEE Transactions on Geoscience and Remote Sensing*, *45*(6), 1715–1725. http://doi.org/10.1109/TGRS.2006.888103

Schumann, G. J. P., Bates, P. D., Neal, J. C., & Andreadis, K. M. (2014). Measuring and Mapping Flood Processes. In *Hydro-Meteorological Hazards, Risks, and Disasters* (pp. 35–64). http://doi.org/10.1016/B978-0-12-394846-5.00002-3

Schumann, G., Matgen, P., Cutler, M. E. J., Black, A., Hoffmann, L., & Pfister, L. (2008). Comparison of remotely sensed water stages from LiDAR, topographic contours and SRTM. *ISPRS Journal of Photogrammetry and Remote Sensing*, *63*(3), 283–296. http://doi.org/10.1016/j.isprsjprs.2007.09.004

Scorzini, A. R., & Frank, E. (2015). Flood damage curves : new insights from the 2010 flood in Veneto , Italy, 1–12. http://doi.org/10.1111/jfr3.12163

Tachikawa, T., Kaku, M., & Iwasaki, A. (2011). ASTER GDEM Version 2 Validation Report. *International Geoscience and Remote Sensing Symposium (IGARSS)*, 1–24.

Viero, D. P., Peruzzo, P., Carniello, L., & Defina, A. (2014). Integrated mathematical modeling of hydrological and hydrodynamic response to rainfall events in rural lowland catchments. *Water Resources Research*, *50*(7), 5941–5957. http://doi.org/10.1002/2013WR014293

Viero, D. Pietro, D'Alpaos, A., Carniello, L., & Defina, A. (2013). Mathematical modeling of flooding due to river bank failure. *Advances in Water Resources*, *59*, 82–94. http://doi.org/10.1016/j.advwatres.2013.05.011

Zwenzner, H., & Voigt, S. (2008). Improved estimation of flood parameters by combining space based SAR data with very high resolution digital elevation data. *Hydrology and*

Earth System Sciences Discussions, *5*, 2951–2973. http://doi.org/10.5194/hessd-5-2951-2008

CHAPTER 5

Altieri, L., Cocchi, D., Pezzi, G., Scott, E. M., & Ventrucci, M. (2014). Urban sprawl scatterplots for Urban Morphological Zones data. *Ecological Indicators*, *36*, 315–323. http://doi.org/10.1016/j.ecolind.2013.07.011

Amarsaikhan, D., Blotevogel, H. H., van Genderen, J. L., Ganzorig, M., Gantuya, R., & Nergui, B. (2010). Fusing high-resolution SAR and optical imagery for improved urban land cover study and classification. *International Journal of Image and Data Fusion*, *1*(September 2013), 83–97. http://doi.org/10.1080/19479830903562041

Amarsaikhan, D., Ganzorig, M., Ache, P., & Blotevogel, H. (2007). The integrated use of optical and InSAR data for urban land-cover mapping. *International Journal of Remote Sensing*, *28*(6), 1161–1171. http://doi.org/10.1080/01431160600784267

Angiuli, E., & Trianni, G. (2013). Urban Mapping in Landsat Images Based on Normalized Difference Spectral Vector. *IEEE Geoscience and Remote Sensing Letters*, *11*(3), 661–665. http://doi.org/10.1109/LGRS.2013.2274327

Asner, G. P. et al. (2009). Automated mapping of tropical deforestation and forest degradation: CLASlite.

Aswatha, S. M., Mukhopadhyay, J., & Biswas, P. K. (2016). Spectral Slopes for Automated Classification of Land Cover in Landsat Images.

Berberoglu, S., & Akin, A. (2009). Assessing different remote sensing techniques to detect land use/cover changes in the eastern Mediterranean. *International Journal of Applied Earth Observation and Geoinformation*, *11*(1), 46–53. http://doi.org/10.1016/j.jag.2008.06.002

Burges, C. J. C. (1998a). A tutorial on support vector machines for pattern recognition. *Data Mining and Knowledge Discovery*, *2*(2), 121–167. http://doi.org/10.1023/A:1009715923555

Burges, C. J. C. (1998b). A tutorial on support vector machines for pattern recognition. *Data Mining and Knowledge Discovery*, *2*(2), 121–167. http://doi.org/10.1023/A:1009715923555

Copernicus - The European Earth Observation Programme. (n.d.). Retrieved from http://www.copernicus.eu

Cristianini, N., & Shawe-Taylor, J. (2000a). *An introduction to Support Vector Machines*. *History* (Vol. 47). http://doi.org/0521780195

Cristianini, N., & Shawe-Taylor, J. (2000b). *An introduction to Support Vector Machines*. *History* (Vol. 47). http://doi.org/0521780195

Dalponte, M., Bruzzone, L., & Gianelle, D. (2008). Fusion of Hyperspectral and LIDAR Remote Sensing Data for Classification of Complex Forest Areas. *IEEE Transactions on Geoscience and Remote Sensing*, *46*(5), 1416–1427. http://doi.org/10.1109/TGRS.2008.916480

de Moel, H., Jongman, B., Kreibich, H., Merz, B., Penning-Rowsell, E., & Ward, P. J. (2015). Flood risk assessments at different spatial scales. *Mitigation and Adaptation Strategies for Global Change*, (June). http://doi.org/10.1007/s11027-015-9654-z

De Natale, F. (INEA), & Pignatti, G. (2014). Aree agricole ad alto valore naturale Approccio della copertura del suolo Veneto.

De Oliveira Pereira, L., Da Costa Freitas, C., Anna, S. J. S. S., Lu, D., & Moran, E. F. (2013). Optical and radar data integration for land use and land cover mapping in the Brazilian Amazon. *GIScience and Remote Sensing*, *50*(3), 301–321. http://doi.org/10.1080/15481603.2013.805589

DeFries, R. (2008). Terrestrial Vegetation in the Coupled Human-Earth System: Contributions of Remote Sensing. *Annual Review of Environment and Resources*, *33*(1), 369–390. http://doi.org/10.1146/annurev.environ.33.020107.113339

Dell'Aqua, F., & Gamba, P. (2010). Radar Remote Sensing of Urban Areas. *Remote Sensing and Digital Image Processing*, 1567–3200. http://doi.org/10.1007/978-90-481-3751-0_2

Dixon, B., & Candade, N. (2008). Multispectral landuse classification using neural networks and support vector machines: one or the other, or both? *International Journal of Remote Sensing*, *29*(4), 1185–1206. http://doi.org/10.1080/01431160701294661

Dusseux, P., Corpetti, T., Hubert-Moy, L., & Corgne, S. (2014). Combined use of multi-temporal optical and Radar satellite images for grassland monitoring. *Remote Sensing*, *6*(7), 6163–6182. http://doi.org/10.3390/rs6076163

Dye, C. (2008). Health and urban living. *Science (New York, N.Y.)*, *319*(5864), 766–769. http://doi.org/10.1126/science.1150198

Erasmi, S., & Twele, a. (2009). Regional land cover mapping in the humid tropics using combined optical and SAR satellite dataa case study from Central Sulawesi, Indonesia. *International Journal of Remote Sensing*, *30*(10), 2465–2478 ST–Regional land cover mapping in the. http://doi.org/10.1080/01431160802552728

Esch, T., Himmler, V., Schorcht, G., Thiel, M., Wehrmann, T., Bachofer, F., … Dech, S. (2009). Large-area assessment of impervious surface based on integrated analysis of single-date

Landsat-7 images and geospatial vector data. *Remote Sensing of Environment*, *113*(8), 1678–1690. http://doi.org/10.1016/j.rse.2009.03.012
Esch, T., Marconcini, M., Marmanis, D., Zeidler, J., Elsayed, S., Metz, A., … Dech, S. (2014). Dimensioning urbanization – An advanced procedure for characterizing human settlement properties and patterns using spatial network analysis. *Applied Geography*, *55*, 212–228. http://doi.org/10.1016/j.apgeog.2014.09.009
Esch, T., Schmidt, M., Breunig, M., Felbier, A., Taubenböck, H., Heldens, W., … Data, S. (2011). IDENTIFICATION AND CHARACTERIZATION OF URBAN STRUCTURES USING VHR SAR DATA Department of Remote Sensing , Institute of Geography and Geology , University of Würzburg , Am Hubland , 1413–1416.
Esch, T., Taubenböck, H., Roth, A., Heldens, W., Felbier, A., Thiel, M., … Dech, S. (2012). TanDEM-X mission—new perspectives for the inventory and monitoring of global settlement patterns. *Journal of Applied Remote Sensing*, *6*(1), 61702–1. http://doi.org/10.1117/1.JRS.6.061702
Estoque, R. C., & Murayama, Y. (2015). Classification and change detection of built-up lands from Landsat-7 ETM+ and Landsat-8 OLI/TIRS imageries: A comparative assessment of various spectral indices. *Ecological Indicators*, *56*, 205–217. http://doi.org/10.1016/j.ecolind.2015.03.037
FAO. (1997). No Title. In *FAO, 1997a: State of the World's Forests. Food and Agriculture Organization, Rome, Italy*.
FAO/UNEP. (1999). FAO/UNEP, 1999: Terminology for Integrated Resources Planning and Management. In *FAO/UNEP, 1999: Terminology for Integrated Resources Planning and Management. Food and Agriculture Organization/United Nations Environmental Programme, Rome, Italy and Nairobi, Kenya.*
Fernández-Delgado, M., Cernadas, E., Barro, S., Amorim, D., & Amorim Fernández-Delgado, D. (2014). Do we Need Hundreds of Classifiers to Solve Real World Classification Problems? *Journal of Machine Learning Research*, *15*, 3133–3181.
Ferretti, A., Prati, C., & Rocca, F. (2001). Permanent scatterers in SAR interferometry. *IEEE Transactions on Geoscience and Remote Sensing*, *39*(1), 8–20. http://doi.org/10.1109/36.898661
Floris, M., D'Alpaos, a., De Agostini, a., Stevan, G., Tessari, G., & Genevois, R. (2012). A process-based model for the definition of hydrological alert systems in landslide risk mitigation. *Natural Hazards and Earth System Science*, *12*, 3343–3357. http://doi.org/10.5194/nhess-12-3343-2012
Foody, G. M. (2002). Status of land cover classification accuracy assessment. *Remote Sensing of Environment*, *80*(1), 185–201. http://doi.org/10.1016/S0034-4257(01)00295-4
Freitas, C. da C., Soler, L. de S., Sant'Anna, S. J. S., Dutra, L. V., dos Santos, J. R., Mura, J. C., & Correia, A. H. (2008). Land Use and Land Cover Mapping in the Brazilian Amazon Using Polarimetric Airborne P-Band SAR Data. *IEEE Transactions on Geoscience and Remote Sensing*, *46*(10), 2956–2970. http://doi.org/10.1109/TGRS.2008.2000630
Gao, B. (1996). NDWI A Normalized Difference Water Index for Remote Sensing of Vegetation Liquid Water From Space, *266*(April 1995), 257–266.
Gaughan, A. E., Stevens, F. R., Linard, C., Jia, P., & Tatem, A. J. (2013). High Resolution Population Distribution Maps for Southeast Asia in 2010 and 2015. *PLoS ONE*, *8*(2). http://doi.org/10.1371/journal.pone.0055882
Geoland-2. (n.d.).
Global Land Cover 2000. (n.d.). Retrieved from http://bioval.jrc.ec.europa.eu/products/glc2000/glc2000.php
GlobCover. (n.d.). Retrieved from http://due.esrin.esa.int/globcover/
GOFC - GOLD. (n.d.). Retrieved from http://www.gofcgold.wur.nl/sites/gofcgold_refdataportal.php
Hansen, M. C., Roy, D. P., Lindquist, E., Adusei, B., Justice, C. O., & Altstatt, A. (2008). A method for integrating MODIS and Landsat data for systematic monitoring of forest cover and change in the Congo Basin. *Remote Sensing of Environment*, *112*(5), 2495–2513. http://doi.org/10.1016/j.rse.2007.11.012
Huang, X., & Zhang, L. (2009). Road centreline extraction from high-resolution imagery based on multiscale structural features and support vector machines. *International Journal of Remote Sensing*, *30*(8), 1977–1987. http://doi.org/10.1080/01431160802546837
Huang, X., Zhang, L., & Li, P. (2008). A multiscale feature fusion approach for classification of very high resolution satellite imagery based on wavelet transform. *International Journal of Remote Sensing*, *29*(20), 5923–5941. http://doi.org/10.1080/01431160802139922
Inglada, J. (2007). Automatic recognition of man-made objects in high resolution optical remote sensing images by SVM classification of geometric image features. *ISPRS Journal of Photogrammetry and Remote Sensing*, *62*(3), 236–248. http://doi.org/10.1016/j.isprsjprs.2007.05.011
Jaeger, J. A. G., Bertiller, R., Schwick, C., & Kienast, F. (2010). Suitability criteria for measures of urban sprawl. *Ecological Indicators*, *10*(2), 397–406. http://doi.org/10.1016/j.ecolind.2009.07.007
Joshi, N., Baumann, M., Ehammer, A., Fensholt, R., Grogan, K., Hostert, P., … Waske, B.

(2016). A review of the application of optical and radar remote sensing data fusion to land use mapping and monitoring. *Remote Sensing*, *8*(1), 1–23. http://doi.org/10.3390/rs8010070
Justice, C. (2014). Advances in Land Cover and Land Use Science Using Earth Observation. In *Frontiers in Earth Observation for Land System Science*. Berlin: EARSel; NASA.
Kaufman, Y. J., & Tanre, D. (1992). Atmospherically resistant vegetation index (ARVI) for EOS-MODIS. *IEEE Transactions on Geoscience and Remote Sensing*, *30*(2), 261–270. http://doi.org/10.1109/36.134076
Keerthi, S. S., & Lin, C.-J. (2003). Asymptotic behaviors of support vector machines with Gaussian kernel. *Neural Computation*, *15*(7), 1667–89. http://doi.org/10.1162/089976603321891855
Kovalskyy, V. et al. (2014). Web-Enabled Landsat Data (WELD) For Monitoring Contemporary Terrestrial Change Nearly Everywhere. In *Frontiers in Earth Observation for Land System Science*. Berlin.
Langanke, T. et al. (2014). Improving Observation of Land Transformations: Copernicus Land Services in Europe. In *Frontiers in Earth Observation for Land System Science*. Berlin.
Lex Comber et al. (2005). What Is Land Cover? *Environment and Planning*, (32), 199–209.
Li, H., Gu, H., Han, Y., & Yang, J. (2010). Object-oriented classification of high-resolution remote sensing imagery based on an improved colour structure code and a support vector machine. *International Journal of Remote Sensing*, *31*(6), 1453–1470. http://doi.org/10.1080/01431160903475266
Li, S., & Chen, X. (2014). A new bare-soil index for rapid mapping developing areas using landsat 8 data. *International Archives of the Photogrammetry, Remote Sensing and Spatial Information Sciences - ISPRS Archives*, *40*(4), 139–144. http://doi.org/10.5194/isprsarchives-XL-4-139-2014
Licciardi, G., Pacifici, F., Tuia, D., Prasad, S., West, T., Giacco, F., … Gamba, P. (2009). Decision fusion for the classification of hyperspectral data: Outcome of the 2008 GRS-S data fusion contest. *IEEE Transactions on Geoscience and Remote Sensing*, *47*(11), 3857–3865. http://doi.org/10.1109/TGRS.2009.2029340
Lin, H., & Lin, C. (2003). A study on sigmoid kernels for SVM and the training of non-PSD kernels by SMO-type methods. *Neural Computation*, (2), 1–32. http://doi.org/10.1.1.14.6709
Lopez-Caloca, A. A. (2015). Data fusion approach for Urban area identification using multisensor information, 1–4. http://doi.org/10.1109/Multi-Temp.2015.7245783
Lu, D., Mausel, P., Brondízio, E., & Moran, E. (2004). Relationships between forest stand parameters and Landsat TM spectral responses in the Brazilian Amazon Basin. *Forest Ecology and Management*, *198*(1–3), 149–167. http://doi.org/10.1016/j.foreco.2004.03.048
MacDonald, D., Crabtree, J. ., Wiesinger, G., Dax, T., Stamou, N., Fleury, P., … Gibon, A. (2000). Agricultural abandonment in mountain areas of Europe: Environmental consequences and policy response. *Journal of Environmental Management*, *59*(1), 47–69. http://doi.org/10.1006/jema.1999.0335
Mantero, P., Moser, G., & Serpico, S. B. (2005). Partially supervised classification of remote sensing images through SVM-based probability density estimation. *IEEE Transactions on Geoscience and Remote Sensing*, *43*(3), 559–570. http://doi.org/10.1109/TGRS.2004.842022
Marconcini, M., Esch, T., Felbier, A., & Heldens, W. (2013). High-Resolution Global Monitoring of Urban Settlements Mattia Marconcini, Thomas Esch, Andreas Felbier, Wieke Heldens, *4*(May), 20–23.
McFeeters, S. K. (1996). The use of the Normalized Difference Water Index (NDWI) in the delineation of open water features. *International Journal of Remote Sensing*, *17*(7), 1425–1432. http://doi.org/10.1080/01431169608948714
McGarigal, K., & Marks, B. J. (1994). FRAGSTATS: spatial pattern analysis program for quantifying landscapesStructure. *General Technical Report PNW-GTR-351. U.S. Department of Agriculture, Forest Service, Pacific Northwest Research Station. Portland, OR*, *97331*(503), 134.
McInerney, D., & Kempeneers, P. (2015). *Open source geospatial tools: Applications in Earth observation*. *Open Source Geospatial Tools: Applications in Earth Observation*. http://doi.org/10.1007/978-3-319-01824-9
Michel Etienne, C. L. P. and M. C. (n.d.). A Step-by-step Approach to Building Land Management Scenarios Based on Multiple Viewpoints on Multi-agent System Simulations. JASSS. Retrieved from http://jasss.soc.surrey.ac.uk/6/2/2.html
Mottet, A., Ladet, S., Coqué, N., & Gibon, A. (2006). Agricultural land-use change and its drivers in mountain landscapes: A case study in the Pyrenees. *Agriculture, Ecosystems & Environment*, *114*(2–4), 296–310. http://doi.org/10.1016/j.agee.2005.11.017
Mountrakis, G., Im, J., & Ogole, C. (2011). Support vector machines in remote sensing: A review. *ISPRS Journal of Photogrammetry and Remote Sensing*, *66*(3), 247–259. http://doi.org/10.1016/j.isprsjprs.2010.11.001
MunichRE. (2014). *Loss events worldwide 2014 Percentage distribution*.

Mysiak, J., Jrc, E. E. A., Cca, E. T. C., & Technical, J. (2013). Towards a potential European flood impact database. *EEA – JRC – ETC/CCA Joint Technical Paper*.
Nirupama, N., & Simonovic, S. P. (2007). Increase of flood risk due to urbanisation: A Canadian example. *Natural Hazards*, *40*(1), 25–41. http://doi.org/10.1007/s11069-006-0003-0
NOAA. (n.d.). Retrieved from http://www.csc.noaa.gov/digitalcoast/data/ccapregional/faq
Ozdogan, M., & Woodcock, C. E. (2006). Resolution dependent errors in remote sensing of cultivated areas. *Remote Sensing of Environment*, *103*(2), 203–217. http://doi.org/10.1016/j.rse.2006.04.004
Park, M.-H., & Stenstrom, M. K. (2008). Classifying environmentally significant urban land uses with satellite imagery. *Journal of Environmental Management*, *86*(1), 181–92. http://doi.org/10.1016/j.jenvman.2006.12.010
Patel, N. N., Angiuli, E., Gamba, P., Gaughan, A., Lisini, G., Stevens, F. R., … Trianni, G. (2015a). Multitemporal settlement and population mapping from Landsat using Google Earth Engine. *International Journal of Applied Earth Observations and Geoinformation*, *35*, 199–208. http://doi.org/10.1016/j.jag.2014.09.005
Patel, N. N., Angiuli, E., Gamba, P., Gaughan, A., Lisini, G., Stevens, F. R., … Trianni, G. (2015b). Multitemporal settlement and population mapping from landsatusing google earth engine. *International Journal of Applied Earth Observation and Geoinformation*, *35*(PB), 199–208. http://doi.org/10.1016/j.jag.2014.09.005
Pohl, C., & van Genderen, J. L. (1998). Multisensor image fusion in remote sensing: Concepts, methods and applications. *International Journal of Remote Sensing*, *19*(5), 823–854. http://doi.org/10.1080/014311698215748
Potere, D., & Schneider, A. (2007). A critical look at representations of urban areas in global maps. In *GeoJournal* (Vol. 69, pp. 55–80). http://doi.org/10.1007/s10708-007-9102-z
Potere, D., Schneider, A., Angel, S., & Civco, D. (2009). Mapping urban areas on a global scale: which of the eight maps now available is more accurate? *International Journal of Remote Sensing*, *30*(24), 6531–6558. http://doi.org/10.1080/01431160903121134
Rambaldi, G., Muchemi, J., Crawhall, N., & Monaci, L. (2007). Through the Eyes of Hunter-Gatherers: participatory 3D modelling among Ogiek indigenous peoples in Kenya. *Information Development*, *23*(2–3), 113–128. http://doi.org/10.1177/0266666907078592
Richards, J. A. (2012). *Remote Sensing Digital Image Analysis: An Introduction [Hardcover]*. Springer; 5th ed. 2013 edition. Retrieved from http://www.amazon.com/Remote-Sensing-Digital-Image-Analysis/dp/3642300618
Richards, J. a, & Jia, X. (2006). *Remote Sensing Digital Image Analysis: An Introduction*. *New York*. http://doi.org/10.1007/978-3-642-30062-2
Sabor, A. a., Radeloff, V. C., McRoberts, R. E., Clayton, M., & Stewart, S. I. (2007). Adding uncertainty to forest inventory plot locations: effects on analyses using geospatial data. *Canadian Journal of Forest Research*, *37*(11), 2313–2325. http://doi.org/10.1139/X07-067
Schneider, A. (2012). Monitoring land cover change in urban and peri-urban areas using dense time stacks of Landsat satellite data and a data mining approach. *Remote Sensing of Environment*, *124*, 689–704. http://doi.org/10.1016/j.rse.2012.06.006
Seto, K. C. (2009). Global urban issues - a primer. In & M. H. (Eds. . P. Gamba (Ed.), *Global mapping of human settlements e Experiences, datasets, and prospects*. Taylor & Francis.
Seto, K. C., & Fragkias, M. (2005). Quantifying spatiotemporal patterns of urban land-use change in four cities of China with time series landscape metrics. *Landscape Ecology*, *20*(7), 871–888. http://doi.org/10.1007/s10980-005-5238-8
Seto, K. C., Fragkias, M., Guneralp, B., & Reilly, M. K. (2011). A Meta-Analysis of Global Urban Land Expansion. *Current Science*, *101*(11), 1435–1439. http://doi.org/10.1371/Citation
Silleos, N. G., Alexandridis, T. K., Gitas, I. Z., & Perakis, K. (2006). Vegetation Indices: Advances Made in Biomass Estimation and Vegetation Monitoring in the Last 30 Years. *Geocarto International*, *21*(4), 21–28. http://doi.org/10.1080/10106040608542399
Sirén, A. H., & Brondizio, E. S. (2009). Detecting subtle land use change in tropical forests. *Applied Geography*, *29*(2), 201–211. http://doi.org/10.1016/j.apgeog.2008.08.006
Song, M., & Civco, D. (2004). Road Extraction Using SVM and Image Segmentation. *Photogrammetric Engineering and Remote Sensing*, *70*(12), pp 1365-1371.
Stefanski, J., Kuemmerle, T., Chaskovskyy, O., Griffiths, P., Havryluk, V., Knorn, J., … Waske, B. (2014). Mapping Land Management Regimes in Western Ukraine Using Optical and SAR Data. *Remote Sensing*, *6*(6), 5279–5305. http://doi.org/10.3390/rs6065279
Tasser, E., Walde, J., Tappeiner, U., Teutsch, A., & Noggler, W. (2007). Land-use changes and natural reforestation in the Eastern Central Alps. *Agriculture, Ecosystems & Environment*, *118*(1–4), 115–129. http://doi.org/10.1016/j.agee.2006.05.004
Taubenböck, H., Esch, T., Felbier, a., Wiesner, M., Roth, a., & Dech, S. (2012). Monitoring urbanization in mega cities from space. *Remote Sensing of Environment*, *117*, 162–176. http://doi.org/10.1016/j.rse.2011.09.015
Taubenböck, H., Esch, T., Wiesner, M., Felbier, A., Marconcini, M., Roth, A., & Dech, S. (2011). Spatial Dynamics and Patterns of Urbanization.

Taubenböck, H., Wegmann, M., Roth, A., Mehl, H., & Dech, S. (2009). Urbanization in India - Spatiotemporal analysis using remote sensing data. *Computers, Environment and Urban Systems*, *33*(3), 179–188. http://doi.org/10.1016/j.compenvurbsys.2008.09.003
Taubenböck, H., Wurm, M., Netzband, M., Zwenzner, H., Roth, A., Rahman, A., & Dech, S. (2011). Flood risks in urbanized areas – multi-sensoral approaches using remotely sensed data for risk assessment. *Natural Hazards and Earth System Science*, *11*(2), 431–444. http://doi.org/10.5194/nhess-11-431-2011
The WorldPop Project. (2014). Retrieved from http://www.worldpop.org.uk/
Trianni, G., Angiuli, E., Lisini, G., & Gamba, P. (2014). Human settlements from Landsat data using Google Earth Engine. *Geoscience and Remote Sensing Symposium*, 1473–1476. http://doi.org/10.1109/IGARSS.2014.6946715
Tupin, F. (2010). *Fusion of optical and SAR images*. *Remote Sensing and Digital Image Processing* (Vol. 15). http://doi.org/10.1007/978-90-481-3751-0_6
Udelhoven, T. (2014). The Use of Long-Term RS Data Archives For LUCC Studies: Challenges and Opportunities. In *Frontiers in Earth Observation for Land System Science*. Berlin.
Unisdr. (2011). *Global Assessment Report on Disaster Risk Reduction*. *2011 Global Assessment Report on Disaster Risk Reduction*. Geneva.
Vapnik, V. N. (1998). *Statistical Learning Theory*. *John Wiley & Sons*. http://doi.org/10.2307/1271368
Verburg, P. H., Neumann, K., & Nol, L. (2011). Challenges in using land use and land cover data for global change studies. *Global Change Biology*, *17*(2), 974–989. http://doi.org/10.1111/j.1365-2486.2010.02307.x
Waske, B., & Van Der Linden, S. (2008). Classifying multilevel imagery from SAR and optical sensors by decision fusion. *IEEE Transactions on Geoscience and Remote Sensing*, *46*(5), 1457–1466. http://doi.org/10.1109/TGRS.2008.916089
Xu, H. (2006). Modification of normalised difference water index (NDWI) to enhance open water features in remotely sensed imagery. *International Journal of Remote Sensing*, *27*(14), 3025–3033. http://doi.org/10.1080/01431160600589179
Xu, H. (2007). Extraction of Urban Built-up Land Features from Landsat Imagery Using a Thematic- oriented Index Combination Technique, *73*(12), 1381–1391.
Zha, Y., Gao, J., & Ni, S. (2003). Use of normalized difference built-up index in automatically mapping urban areas from TM imagery. *International Journal of Remote Sensing*, *24*(3), 583–594. http://doi.org/10.1080/01431160304987
Zhou, Y., Yang, G., Wang, S., Wang, L., Wang, F., & Liu, X. (2014). A new index for mapping built-up and bare land areas from Landsat-8 OLI data. *Remote Sensing Letters*, *5*(10), 862–871. http://doi.org/10.1080/2150704X.2014.973996

CHAPTER 6

Adger, W. N., Quinn, T., Lorenzoni, I., Murphy, C., & Sweeney, J. (2013). Changing social contracts in climate-change adaptation. Nature Climate Change, 3(4), 330–333. http://doi.org/10.1038/nclimate1751
Apel, H., Aronica, G. T., Kreibich, H., & Thieken, A. H. (2009). Flood risk analyses - How detailed do we need to be? Natural Hazards, 49(1), 79–98. http://doi.org/10.1007/s11069-008-9277-8
Balbi, S., Giupponi, C., Olschewski, R., & Mojtahed, V. (2013). The economics of hydro-meteorological disasters : approaching the estimation of the total costs. BC3 Working Paper Series.
Beinat, E., & Nijkamp, P. (1998). Multicriteria analysis for land-use management. Environment & management. http://doi.org/10.1007/978-94-015-9058-7
Birkmann, J., Teichman, K. V., Welle, T., González, M., & Olabarrieta, M. (2010). The unperceived risk to Europe's coasts: Tsunamis and the vulnerability of Cadiz, Spain. Natural Hazards and Earth System Science, 10(12), 2659–2675. http://doi.org/10.5194/nhess-10-2659-2010
Bohensky, E. L., & Leitch, A. M. (2014). Framing the flood: A media analysis of themes of resilience in the 2011 Brisbane flood. Regional Environmental Change, 14(2), 475–488. http://doi.org/10.1007/s10113-013-0438-2
Burton, C., & Cutter, S. L. (2008). Levee Failures and Social Vulnerability in the Sacramento-San Joaquin Delta Area, California. Natural Hazards Review, 9(3), 136–149. http://doi.org/10.1061/(ASCE)1527-6988(2008)9:3(136)
Di Baldassarre, G., Kooy, M., Kemerink, J. S., & Brandimarte, L. (2013). Towards understanding the dynamic behaviour of floodplains as human-water systems. Hydrology and Earth System Sciences, 17(8), 3235–3244. http://doi.org/10.5194/hess-17-3235-2013
Di Baldassarre, G., Viglione, A., Carr, G., Kuil, L., Yan, K., Brandimarte, L., & Blöschl, G. (2015). Debates - Perspectives on socio-hydrology: Capturing feedbacks between physical and social processes. Water Resources Research, 4770–4781. http://doi.org/10.1002/2014WR016416
Di Baldassarre, G., Viglione, a., Carr, G., Kuil, L., Salinas, J. L., & Blöschl, G. (2013). Socio-

hydrology: conceptualising human-flood interactions. Hydrology and Earth System Sciences, 17(8), 3295–3303. http://doi.org/10.5194/hess-17-3295-2013
Gain, A. K., Mojtahed, V., & Biscaro, C. (2015). An integrated approach of flood risk assessment in the eastern part of Dhaka City. Natural Hazards, 79(3), 1499–1530. http://doi.org/10.1007/s11069-015-1911-7
Giupponi, C. (2013). Mojtahed , Animesh K . Gain and Stefano Balbi Integrated Assessment of Natural Hazards and Climate Change Adaptation : I . The KULTURisk Methodological Framework, (6).
Giupponi, C., Mojtahed, V., Gain, A. K., & Balbi, S. (2013). Integrated Assessment of Natural Hazards and Climate Change Adaptation : I . The KULTURisk Methodological Framework, (6).
Giupponi, C., Mojtahed, V., Gain, A. K., Biscaro, C., & Balbi, S. (2014). Integrated Risk Assessment of Water Related disasters, 163–200.
IPCC. (2012). Managing the Risks of Extreme Events and Disasters to Advance Climate Change Adaptation - SREX. (C. B. Field, V. Barros, T. F. Stocker, & Q. Dahe, Eds.). Cambridge: Cambridge University Press. http://doi.org/10.1017/CBO9781139177245
Johnson, C., Tunstall, S., & Penning-Rowsell, E. (2005). Floods as catalysts for policy change: historical lessons from England and Wales. International Journal of Water Resources Development, 21(4), 37–41. http://doi.org/10.1080/07900620500258133
Jonkman, S. N., Bočkarjova, M., Kok, M., & Bernardini, P. (2008). Integrated hydrodynamic and economic modelling of flood damage in the Netherlands. Ecological Economics, 66(1), 77–90. http://doi.org/10.1016/j.ecolecon.2007.12.022
Kates, R. W., Colten, C. E., Laska, S., & Leatherman, S. P. (2006). Reconstruction of New Orleans after Hurricane Katrina: a research perspective. Proceedings of the National Academy of Sciences of the United States of America, 103(40), 14653–60. http://doi.org/10.1073/pnas.0605726103
Liu, J., Dietz, T., Carpenter, S. R., Alberti, M., Folke, C., Moran, E., … Taylor, W. W. (2007). Complexity of Coupled Human and Natural Systems. Science, 317(5844), 1513–1516. http://doi.org/10.1126/science.1144004
Ludy, J., & Kondolf, G. M. (2012). Flood risk perception in lands “protected” by 100-year levees. Natural Hazards, 61(2), 829–842. http://doi.org/10.1007/s11069-011-0072-6
Marconcini, M., Metz, A., Zeidler, J., & Esch, T. (2015). Urban Monitoring in Support of Sustainable Cities. JURSE 2015, 0–3.
Mechler, R., & Bouwer, L. M. (2015). Understanding trends and projections of disaster losses and climate change: is vulnerability the missing link? Climatic Change, 133(1), 23–35. http://doi.org/10.1007/s10584-014-1141-0
Merz, B., Kreibich, H., Schwarze, R., & Thieken, a. (2010). Review article “assessment of economic flood damage.” Natural Hazards and Earth System Science, 10(8), 1697–1724. http://doi.org/10.5194/nhess-10-1697-2010
Mojtahed, V. (2013). Animesh K . Gain and Stefano Balbi Integrated Assessment of Natural Hazards and Climate Change Adaptation : II . The SERRA Methodology, (7).
Montanari, a., Young, G., Savenije, H. H. G., Hughes, D., Wagener, T., Ren, L. L., … Belyaev, V. (2013). “Panta Rhei—Everything Flows”: Change in hydrology and society—The IAHS Scientific Decade 2013–2022. Hydrological Sciences Journal, 58(6), 1256–1275. http://doi.org/10.1080/02626667.2013.809088
Montz, B. E., & Tobin, G. a. (2008). Livin’ Large with Levees: Lessons Learned and Lost. Natural Hazards Review, 9(3), 150–157. http://doi.org/10.1061/(ASCE)1527-6988(2008)9:3(150)
Ostrom, E. (2009). A general framework for analyzing sustainability of social-ecological systems. Science (New York, N.Y.), 325(5939), 419–22. http://doi.org/10.1126/science.1172133
Pahl-Wostl, C., Becker, G., Knieper, C., & Sendzimir, J. (2013). How multilevel societal learning processes facilitate transformative change: A comparative case study analysis on flood management. Ecology and Society, 18(4). http://doi.org/10.5751/ES-05779-180458
Penning-Rowsell, E. C. (1996). Flood-hazard response in {Argentina}. Geographical Review, 86(1), 72–90. http://doi.org/10.2307/215142
Penning-Rowsell, E., Johnson, C., & Tunstall, S. (2006). “Signals” from pre-crisis discourse: Lessons from UK flooding for global environmental policy change? Global Environmental Change, 16(4), 323–339. http://doi.org/10.1016/j.gloenvcha.2006.01.006
Srinivasan, V., Lambin, E. F., Gorelick, S. M., Thompson, B. H., & Rozelle, S. (2012). The nature and causes of the global water crisis: Syndromes from a meta-analysis of coupled human-water studies. Water Resources Research, 48(10). http://doi.org/10.1029/2011WR011087
Thieken, A. H., Müller, M., Kreibich, H., & Merz, B. (2005). Flood damage and influencing factors: New insights from the August 2002 flood in Germany. Water Resources Research, 41(12), n/a-n/a. http://doi.org/10.1029/2005WR004177
Werner, B. T., & McNamara, D. E. (2007). Dynamics of coupled human-landscape systems. Geomorphology, 91(3–4), 393–407. http://doi.org/10.1016/j.geomorph.2007.04.020
Wind, H. G., Nierop, T. M., De Blois, C. J., & De Kok, J. L. (1999). Analysis of flood damages

from the 1993 and 1995 Meuse floods. Water Resources Research, 35(11), 3459–3465. http://doi.org/10.1029/1999WR900192
Winsemius, H. C., Van Beek, L. P. H., Jongman, B., Ward, P. J., & Bouwman, A. (2013). A framework for global river flood risk assessments. Hydrology and Earth System Sciences, 17(5), 1871–1892. http://doi.org/10.5194/hess-17-1871-2013

CHAPTER 7

Balbi, S., Giupponi, C., Olschewski, R., & Mojtahed, V. (2013). The economics of hydro-meteorological disasters : approaching the estimation of the total costs. BC3 Working Paper Series.
Balbi, S., Villa, F., Mojtahed, V., Hegetschweiler, K. T., & Giupponi, C. (2016). A spatial Bayesian network model to assess the benefits of early warning for urban flood risk to people. Nat. Hazards Earth Syst. Sci, 16, 1323–1337. http://doi.org/10.5194/nhess-16-1323-2016
Di Baldassarre, G., Viglione, A., Carr, G., Kuil, L., Yan, K., Brandimarte, L., & Blöschl, G. (2015). Debates - Perspectives on socio-hydrology: Capturing feedbacks between physical and social processes. Water Resources Research, 4770–4781. http://doi.org/10.1002/2014WR016416
Evans, T., & Kelley, H. (2004). Multi-scale analysis of a household level agent-based model of landcover change. Journal of Environmental Management, 72, 57–72.
Gilbert, N. (2008). Agent-Based Models. SAGE Publications, 153(153), 98. http://doi.org/10.4135/9781412983259
Gilbert, N., & Terna, P. (2000). How to build and use agent-based models in social science. Mind & Society, 1(1), 57–72. http://doi.org/10.1007/bf02512229
Giupponi, C., Borsuk, M. E., de Vries, B. J. M., & Hasselmann, K. (2013). Innovative approaches to integrated global change modelling. Environmental Modelling & Software, 44, 1–9. http://doi.org/10.1016/j.envsoft.2013.01.013
Huang, C., Chen, Y., Wu, J., Chen, Z., Li, L., Liu, R., & Yu, J. (2014). Integration of remotely sensed inundation extent and high-precision topographic data for mapping inundation depth. 2014 The 3rd International Conference on Agro-Geoinformatics, Agro-Geoinformatics 2014, 1–4. http://doi.org/10.1109/Agro-Geoinformatics.2014.6910580
Liu, D., Tian, F., Lin, M., & Sivapalan, M. (2015). A conceptual socio-hydrological model of the co-evolution of humans and water: Case study of the Tarim River basin, western China. Hydrology and Earth System Sciences, 19(2), 1035–1054. http://doi.org/10.5194/hess-19-1035-2015
Mojtahed, V., Giupponi, C., Eboli, F., Busello, F., & Cararro, C. (2016). Integrated Spatio-temporal model of land-use change : a focus on Mediterranean agriculture under global changes.
Nefedov, S. (2003). A theory of demographic cycles and the social evolution of ancient and medieval oriental societies. Vostok-Oriens, 3, 5–22.
Turchin, P., & Korotayev, a V. (2006). Population Dynamics and Internal Warfare: A Reconsideration. Social Evolution and History, 5(2), 112–147.
Van Emmerik, T. H. M., Li, Z., Sivapalan, M., Pande, S., Kandasamy, J., Savenije, H. H. G., … Vigneswaran, S. (2014). Socio-hydrologic modeling to understand and mediate the competition for water between agriculture development and environmental health: Murrumbidgee River basin, Australia. Hydrology and Earth System Sciences, 18(10), 4239–4259. http://doi.org/10.5194/hess-18-4239-2014
Viglione, A., Di Baldassarre, G., Brandimarte, L., Kuil, L., Carr, G., Salinas, J. L., … Blo¨schl, G. (2014). Insights from socio-hydrology modelling on dealing with flood risk - Roles of collective memory, risk-taking attitude and trust. Journal of Hydrology, 518(PA), 71–82. http://doi.org/10.1016/j.jhydrol.2014.01.018

Università Ca'Foscari Venezia

DEPOSITO ELETTRONICO DELLA TESI DI DOTTORATO

DICHIARAZIONE SOSTITUTIVA DELL'ATTO DI NOTORIETA'

(Art. 47 D.P.R. 445 del 28/12/2000 e relative modifiche)

Io sottoscritto .Cian Fabio……

nat o. a .Camposampiero…… (prov. .PD.) il .25/12/1982……

residente a .Trebaseleghe…… in .Via C. Menotti…… n. .34/C

Matricola (se posseduta) .956095…… Autore della tesi di dottorato dal titolo:

…Social Vulnerability And Flood Risk Assessment Using Satellite Remote Sensing.……

…A support tool for decision making in a changing climate scenario……

……

Dottorato di ricerca in …Scienza e Gestione dei Cambiamenti Climatici……

(in cotutela con ……)

Ciclo ..29°……

Anno di conseguimento del titolo ..2017……

DICHIARO

di essere a conoscenza:

1) del fatto che in caso di dichiarazioni mendaci, oltre alle sanzioni previste dal codice penale e dalle Leggi speciali per l'ipotesi di falsità in atti ed uso di atti falsi, decado fin dall'inizio e senza necessità di nessuna formalità dai benefici conseguenti al provvedimento emanato sulla base di tali dichiarazioni;

2) dell'obbligo per l'Università di provvedere, per via telematica, al deposito di legge delle tesi di dottorato presso le Biblioteche Nazionali Centrali di Roma e di Firenze al fine di assicurarne la conservazione e la consultabilità da parte di terzi;

3) che l'Università si riserva i diritti di riproduzione per scopi didattici, con citazione della fonte;

4) del fatto che il testo integrale della tesi di dottorato di cui alla presente dichiarazione viene archiviato e reso consultabile via Internet attraverso l'Archivio Istituzionale ad Accesso Aperto dell'Università Ca' Foscari, oltre che attraverso i cataloghi delle Biblioteche Nazionali Centrali di Roma e Firenze;

5) del fatto che, ai sensi e per gli effetti di cui al D.Lgs. n. 196/2003, i dati personali raccolti saranno trattati, anche con strumenti informatici, esclusivamente nell'ambito del procedimento per il quale la presentazione viene resa;

6) del fatto che la copia della tesi in formato elettronico depositato nell'Archivio Istituzionale ad Accesso Aperto è del tutto corrispondente alla tesi in formato cartaceo, controfirmata dal tutor, consegnata presso la segreteria didattica del dipartimento di riferimento del corso di dottorato ai fini del deposito presso l'Archivio di Ateneo, e che di conseguenza va esclusa qualsiasi responsabilità dell'Ateneo stesso per quanto riguarda eventuali errori, imprecisioni o omissioni nei contenuti della tesi;

7) del fatto che la copia consegnata in formato cartaceo, controfirmata dal tutor, depositata nell'Archivio di Ateneo, è l'unica alla quale farà riferimento l'Università per rilasciare, a richiesta, la dichiarazione di conformità di eventuali copie;

Data 12 / 12 / 2016 **Firma** 

NON AUTORIZZO

l'Università a riprodurre ai fini dell'immissione in rete e a comunicare al pubblico tramite servizio on line entro l'Archivio Istituzionale ad Accesso Aperto la tesi depositata per un periodo di 12 (dodici) mesi a partire dalla data di conseguimento del titolo di dottore di ricerca.

DICHIARO

1) che la tesi, in quanto caratterizzata da vincoli di segretezza, non dovrà essere consultabile on line da terzi per un periodo di 12 (dodici) mesi a partire dalla data di conseguimento del titolo di dottore di ricerca;
2) di essere a conoscenza del fatto che la versione elettronica della tesi dovrà altresì essere depositata a cura dell'Ateneo presso le Biblioteche Nazionali Centrali di Roma e Firenze dove sarà comunque consultabile su PC privi di periferiche; la tesi sarà inoltre consultabile in formato cartaceo presso l'Archivio Tesi di Ateneo;
3) di essere a conoscenza che allo scadere del dodicesimo mese a partire dalla data di conseguimento del titolo di dottore di ricerca la tesi sarà immessa in rete e comunicata al pubblico tramite servizio on line entro l'Archivio Istituzionale ad Accesso Aperto.

Specificare la motivazione:
□ motivi di segretezza e/o di proprietà dei risultati e/o informazioni sensibili dell'Università Ca' Foscari di Venezia.
□ motivi di segretezza e/o di proprietà dei risultati e informazioni di enti esterni o aziende private che hanno partecipato alla realizzazione del lavoro di ricerca relativo alla tesi di dottorato.
□ dichiaro che la tesi di dottorato presenta elementi di innovazione per i quali è già stata attivata / si intende attivare la seguente procedura di tutela:

……;

☒ Altro (specificare):

I contenuti della tesi sono sotto processo di revisione peer-review per la pubblicazione ……

in riviste scientifiche di settore e perciò non condivisibili fino alla loro ufficiale pubblicazione. ……

……

A tal fine:
- dichiaro di aver consegnato la copia integrale della tesi in formato elettronico tramite auto-archiviazione (upload) nel sito dell'Università; la tesi in formato elettronico sarà caricata automaticamente nell'Archivio Istituzionale ad Accesso Aperto dell'Università Ca' Foscari, dove rimarrà non accessibile fino allo scadere dell'embargo, e verrà consegnata mediante procedura telematica per il deposito legale presso la Biblioteca Nazionale Centrale di Firenze;
- consegno la copia integrale della tesi in formato cartaceo presso la segreteria didattica del dipartimento di riferimento del corso di dottorato ai fini del deposito presso l'Archivio di Ateneo.

Data 12 -12 - 2016 **Firma** …… ……

La presente dichiarazione è sottoscritta dall'interessato in presenza del dipendente addetto, ovvero sottoscritta e inviata, unitamente a copia fotostatica non autenticata di un documento di identità del dichiarante, all'ufficio competente via fax, ovvero tramite un incaricato, oppure a mezzo posta.

Firma del dipendente addetto ……

Ai sensi dell'art. 13 del D.Lgs. n. 196/03 si informa che il titolare del trattamento dei dati forniti è l'Università Ca' Foscari - Venezia.
I dati sono acquisiti e trattati esclusivamente per l'espletamento delle finalità istituzionali d'Ateneo; l'eventuale rifiuto di fornire i propri dati personali potrebbe comportare il mancato espletamento degli adempimenti necessari e delle procedure amministrative di gestione delle carriere studenti. Sono comunque riconosciuti i diritti di cui all'art. 7 D. Lgs. n. 196/03.

Estratto per riassunto della tesi di dottorato

Studente: Cian Fabio matricola: 956095

Dottorato: Scienza e Gestione dei Cambiamenti Climatici

Ciclo: 29°

Titolo della tesi : Social Vulnerability and Flood Risk Assessment Using Satellite Remote Sensing. A support for decision making in a changing climate scenario

Abstract:

The potential of satellite remote sensing (active and passive) has been investigated, with the aim of improving the assessment of flood risk and social vulnerability, for defining the three components of risk: hazard, exposure and vulnerability.

A new method for flood mapping has been developed, based on multi-temporal statistics of radar images. Flood depth was estimated using a new method based on a statistical analysis of elevation data along the contours of flooded areas. Taking advantage of Earth observation big data, land cover maps have been derived from data fusion of optical and radar data, allowing urban growth analysis. Population density maps were derived by means of a dasymetric mapping technique, as well as indicators of social vulnerability by means of network analysis. The methodologies have been applied to floods in Italy and Malawi, with the objective of supporting decision makers in a context of climate change adaptation.

Estratto:

Con lo scopo di migliorare la valutazione del rischio idrico e della vulnerabilità sociale, si è esplorato il potenziale del telerilevamento satellitare, attivo e passivo, per definire le tre componenti del rischio: *hazard, exposure, vulnerability.*
Si è sviluppato un nuovo metodo per la mappatura di aree inondate basandosi su statistiche multi-temporali di immagini radar. La profondità dell'inondazione è stata stimata utilizzando un nuovo metodo basato sull'analisi statistica dell'elevazione lungo i contorni delle aree inondate. Sfruttando i *big data* di osservazione della Terra (ottici e radar), sono state ricavate mappe di *land cover*, permettendo l'analisi della crescita urbana. Sono state ricavate mappe di densità di popolazione utilizzando tecniche di *dasymetric mapping*, e indicatori di vulnerabilità sociale basandosi sull'analisi delle reti.
Le metodologie sono state applicate a inondazioni successe in Italia e in Malawi, con lo scopo di fornire un supporto ai *decision makers* in un contesto di adattamento ai cambiamenti climatici.

Firma dello studente